
Electronic Thesis and Dissertation Repository

9-10-2019 10:00 AM

The Hydrodynamics and Heat Transfer of Impinging Jet Flow and Circular Hydraulic Jump

Yunpeng Wang
The University of Western Ontario

Supervisor
Khayat, Roger E
The University of Western Ontario

Graduate Program in Mechanical and Materials Engineering
A thesis submitted in partial fulfillment of the requirements for the degree in Doctor of
Philosophy
© Yunpeng Wang 2019

Follow this and additional works at: <https://ir.lib.uwo.ca/etd>



Part of the [Applied Mechanics Commons](#)

Recommended Citation

Wang, Yunpeng, "The Hydrodynamics and Heat Transfer of Impinging Jet Flow and Circular Hydraulic Jump" (2019). *Electronic Thesis and Dissertation Repository*. 6526.
<https://ir.lib.uwo.ca/etd/6526>

This Dissertation/Thesis is brought to you for free and open access by Scholarship@Western. It has been accepted for inclusion in Electronic Thesis and Dissertation Repository by an authorized administrator of Scholarship@Western. For more information, please contact wlsadmin@uwo.ca.

Abstract

The laminar axisymmetric flow and heat transfer of a circular impinging jet and hydraulic jump on a solid surface is analyzed theoretically using boundary-layer and thin-film approaches. Liquid jet impingement features many applications such as jet rinsing, jet cooling, liquid atomization and chemical reactors. The associated hydraulic jump dramatically affects the performance of the heat and mass transfer in such applications. In the current thesis, the effects of inertia, surface tension, surface rotation, gravity and heat transfer are comprehensively explored for impinging jet flow and the formation of hydraulic jump.

The boundary-layer heights and film thickness are found to diminish with inertia. The wall shear stress is found to decrease with radial distance for on a stationary impingement surface but can increase for a rotary surface for large rotation speeds. When the surface is in rotation, a maximum liquid thickness occurs, reflecting the competition between inertia and rotation effects. The location of the hydraulic jump is determined for both low- and high-viscosity liquids. For low-viscosity liquid, the location of the jump is determined subject to the thickness near the trailing edge under static condition, reflecting the importance of surface tension. For high-viscosity liquids, the jump coincides with a singularity caused by gravity in the thin-film equation when surface tension is neglected. Downstream of the hydraulic jump, the recent finding of a constant ‘jump Froude number’ is also justified.

The heat transfer analysis of impinging jet flow involves a two-way coupling due to the temperature-dependent viscosity and surface tension. To consider this non-linear coupling which is largely missing in the existing theoretical approaches, we develop a simple and iteration-free model, making exploring the influence of heat transfer on the flow field and the hydraulic jump feasible theoretically. Both the hydrodynamic and thermal boundary layers are found to decrease with a higher heat input at the solid surface. Enhanced heating is also found to push the hydraulic jump in the downstream direction. The Marangoni stress causes the hydraulic jump to occur earlier. The hydraulic jump leads to shock-type drops in the Nusselt number, confirming previous findings in the literature.

Keywords

impinging jet, impinging jet heat transfer, thermal fluid, hydraulic jump, surface tension, free-surface flow, rotating flow, two-way coupling

Summary for Lay Audience

The current thesis presents a theoretical analysis on the flow and heat transfer of a column of liquid impacting a solid surface which is known as the impinging jet flow. Impinging flow is encountered in many applications such as jet rinsing, industrial cooling, combustion engine cooling, liquid atomization and chemical reactors. For impinging jet flow, the hydraulic jump is an abrupt increase in the depth of the liquid layer which can be daily observed at the bottom of a kitchen sink in tap water flow. The hydraulic jump can significantly affect the performance of the associated applications. It is not surprising that hydraulic jump moves further away from the impingement point for a larger speed of the incoming jet. But the quantitative dependence of jump location on the flow rate, including the heat transfer character, is still not completely settled due to complexity of fluid flow. For low-viscosity liquid, we find that surface tension is important on the location of the jump. But for a high-viscosity liquid, it turns out that gravity is more dominant on the hydraulic jump. It is also found that rotation of the solid surface can push the hydraulic jump further away from the impingement point. In the heat transfer analysis of impinging jet flow in cooling applications, the viscosity of a liquid depends on the temperature. However, this dependence is largely neglected in existing theoretical analyses due to the mathematical difficulty. In this regard, we develop a simple and efficient model that can incorporate this dependence so that heat transfer and flow field can be more accurately calculated. The current results show that a higher heat input from the solid surface can push the hydraulic jump further away. In addition to the hydraulic jump, the important features of the flow field and heat transfer are comprehensively presented in the thesis. For validation, our quantitative predictions are compared with existing measurements and good agreements are achieved.

Co-Authorship Statement

The current thesis is prepared in the Integrated-Article format in consistence with the regulations of the School of Graduate and Postdoctoral Studies at the University of Western Ontario. I hereby declare below the co-authorship and the explicit contribution of each author.

Chapter 2 is published in the Journal of Fluid Mechanics. Yunpeng Wang carried out the literature review, mathematical formulation and the computing work under the guidance of R.E. Khayat. Yunpeng Wang wrote the article. R.E. Khayat took the supervisory and editing role. The complete reference is:

Wang, Y. & Khayat, R.E. 2018 Impinging jet flow and hydraulic jump on a rotating disk. *J. Fluid Mech.* **839**, 525-560.

Chapter 3 is published in the Journal of Fluid Mechanics. Yunpeng Wang carried out the literature review, mathematical formulation and the computing work under the guidance of R.E. Khayat. Yunpeng Wang wrote the article. R.E. Khayat took the supervisory and editing role. The complete reference is:

Wang, Y. & Khayat, R.E. 2019 The role of gravity in the prediction of the circular hydraulic jump radius for high-viscosity liquids. *J. Fluid Mech.* **862**, 128-161.

Chapter 4 has been submitted to the Journal of Fluid Mechanics in 2019 and is currently under review. Yunpeng Wang carried out the literature review, mathematical formulation and the computing work under the guidance of R.E. Khayat. Yunpeng Wang wrote the article. R.E. Khayat took the supervisory and editing role.

Acknowledgments

I would like to first thank my supervisor Dr. Roger Khayat for his great support during my research. I am grateful for his constant encouragement and patience in the process of finishing this thesis. More importantly, I would like to thank him for pushing me to expand my knowledge and guiding me through all the difficulties in this research.

I would also like to thank my former colleagues Md. Asif Zobaer and Mohammad Tanvir Hossain for their valuable help and companionship during the first two years of my research.

Finally, I would like to thank my parents and friends for constantly supporting and encouraging me through all the difficulties in life.

Table of Contents

Abstract	ii
Summary for Lay Audience	iii
Co-Authorship Statement.....	iv
Acknowledgments.....	v
Table of Contents	vi
List of Tables	x
List of Figures	xi
List of Appendices	xviii
Nomenclature	xix
Chapter 1	1
1 Introduction	1
1.1 Background and applications	1
1.2 Modeling of the flow and thermal fields of a spreading jet and a circular hydraulic jump	6
1.2.1 Dimensionless numbers	6
1.2.2 Boundary layer theory and the thin-film approach	7
1.2.3 The Kármán–Pohlhausen (K–P) approach.....	9
1.2.4 Momentum-force relation across the hydraulic jump.....	11
1.3 Literature review	13
1.3.1 The hydrodynamics of the impinging jet and circular hydraulic jump.....	13
1.3.2 The influence of a rotating surface on the impinging jet flow and hydraulic jump	19
1.3.3 Impinging jet heat transfer and its influence on the hydraulic jump	22
1.4 The objectives and the thesis outline	25
1.4.1 The research gap	25

1.4.2	The objectives of the thesis.....	26
1.4.3	Thesis outline	26
1.5	References.....	27
Chapter 2	36
2	Impinging jet flow and hydraulic jump on a stationary and a rotating disk	36
2.1	Introduction.....	36
2.2	Physical domain and problem statement.....	39
2.2.1	The physical domain	42
2.2.2	Governing equations and boundary conditions.....	43
2.2.3	Overall solution strategy	46
2.3	Influence of rotation on the developing boundary-layer and transition.....	48
2.3.1	The developing boundary-layer in region (ii).....	48
2.3.2	Influence of rotation on the transition location and film thickness	52
2.4	Influence of rotation on the flow in the fully-viscous region	54
2.5	Influence of rotation on the hydraulic jump	67
2.5.1	General formulation	68
2.5.2	The hydraulic jump over a stationary disk.....	70
2.5.3	The hydraulic jump over a rotating disk.....	79
2.6	Concluding remarks	85
2.7	References.....	88
Chapter 3	94
3	The circular hydraulic jump for high-viscosity liquids.....	94
3.1	Introduction.....	94
3.2	Physical domain and problem statement.....	97
3.2.1	The physical domain	98
3.2.2	Governing equations and boundary conditions.....	99

3.3	The flow in the developing boundary-layer and the transition location	102
3.4	The fully-viscous region and prediction of the jump location	108
3.4.1	The equation for the film thickness	108
3.4.2	The supercritical flow and the location of the hydraulic jump	109
3.4.3	Comparison with experiment	116
3.4.4	Further validation	119
3.5	The influence of gravity on the hydraulic jump height and the subcritical flow	122
3.5.1	Conservation of momentum across the jump	122
3.5.2	The influence of disk radius and edge thickness	126
3.6	Concluding remarks and discussion	136
3.7	References	139
Chapter 4		144
4	The influence of heat transfer on liquid jet spreading and hydraulic jump formation	144
4.1	Introduction	144
4.2	Physical domain and problem statement	149
4.2.1	The physical domain	151
4.2.2	Governing equations and boundary conditions	152
4.2.3	The viscosity and surface tension model	155
4.3	The influence of heat transfer on the flow in the supercritical region and transition locations	158
4.3.1	The general supercritical integral formulation	158
4.3.2	The influence of wall temperature	165
4.3.3	The influence of constant wall heat flux on the flow	170
4.4	The influence of heat transfer on the hydraulic jump and subcritical flow	175
4.4.1	The subcritical velocity and temperature profiles	176
4.4.2	The influence of the wall temperature on the hydraulic jump	181

4.4.3 The influence of the wall heat flux on the hydraulic jump	187
4.5 Conclusion	189
4.6 References	192
Chapter 5	197
5 Conclusions and recommendations for future works	197
5.1 Conclusions	197
5.2 Recommendations for future works	198
Appendices	200
Curriculum Vitae	203

List of Tables

Table 1: Viscosity and surface tension fitting parameters for three common liquids. 156

List of Figures

Figure 1-1: Schematic illustration of impinging liquid jet and a circular hydraulic jump.	1
Figure 1-2: Planar hydraulic jump.	2
Figure 1-3: Different types of circular hydraulic jump.	3
Figure 1-4: Boundary-layer and thin-film flow.	9
Figure 1-5: A numerical view of the K-P approach.	10
Figure 1-6: A schematic view of the control volume across the hydraulic jump: (a) 3-dimensional view; (b) axisymmetric view.	11
Figure 2-1: Schematic illustration of the axisymmetric jet flow impinging on a flat rotating disk. Illustrated are the stagnation region (i), the developing boundary-layer region (ii), the fully viscous region (iii) and the hydraulic jump region (iv). All notations are dimensionless.	41
Figure 2-2: Marginal stability curves based on the analysis of Charwat <i>et al.</i> (1972) reproduced here in the (Re, Ω) plane. The stable (unstable) region below (above) each curve that corresponds to axisymmetric (wavy) flow is indicated here for iso-propyl alcohol.	43
Figure 2-3: Influence of rotation in the developing boundary-layer region (ii). The boundary-layer thickness is plotted against the radial distance for different rotation speed.	51
Figure 2-4: Dependence of location and film thickness at the transition point between the developing boundary-layer and fully-viscous regions (ii) and (iii).	53
Figure 2-5: Influence of rotation on the developing boundary-layer height and film thickness. The transition location coincides with the intersection of the two heights.	56

Figure 2-6: Influence of rotation on the thickness distribution upstream and downstream of the transition point $r = r_0$. The inner, intermediate and outer subregions are shown for $Re^{1/3} \Omega = 0.1$ 57

Figure 2-7: Influence of rotation on the velocity at the film surface upstream and downstream of the transition point $r = r_0$. The transition point coincides with the location at which the velocity first deviates from 1. 59

Figure 2-8: Influence of rotation on the wall shear stress upstream and downstream of the transition point $r = r_0$ 62

Figure 2-9: Influence of inertia on the film thickness upstream and downstream of the transition point. Here $\Omega = 0.02$. The inner, intermediate and outer subregions are indicated for the $Re = 200$ curve. 64

Figure 2-10: Influence of inertia and centrifugal effects on the minimum film thickness and its location. Arrows indicate direction of increasing rotation speed. 65

Figure 2-11: Influence of inertia and centrifugal effects on the maximum film thickness and its location. Arrows indicate direction of increasing rotation speed. 66

Figure 2-12: Influence of rotation speed on the maximum film thickness and its location. Comparison between theory and the measurements of Ozar *et al.* (2003). The data correspond to $Q = 3$ L/min. 67

Figure 2-13: Dependence of hydraulic jump location on flow rate (Froude number) for a stationary disk. The figure shows the comparison between the current theoretical predictions and the measurements of Dressaire *et al.* (2010) for a water. 73

Figure 2-14: Dependence of Fr_j on the flow rate (Froude number) for a stationary disk. The solid and dashed lines show the results corresponding to the configuration of Dressaire *et al.* (2010) for water, based on the current cubic and similarity profiles, respectively. The data corresponding to silicon oil from Duchesne *et al.* (2014) are also included. 75

Figure 2-15: Dependence of hydraulic jump location on flow rate (Froude number) for a stationary disk. The figure shows the comparison between the current theoretical predictions and the measurements of Hansen *et al.* (1997) for a water jet on a glass disk. The distribution of Fr_j is also included. 76

Figure 2-16: Comparison between theory and the measurements of Ozar *et al.* (2003) for the hydraulic jump of a thin film flowing on a stationary disk for $Q = 7$ L/min (a) and $Q = 15$ L/min (b). 78

Figure 2-17: Final film thickness as function of rotation speed in the spin coating of AZ6600 photoresist liquid films. The values of β are given for a best fit of Equation (2.5.11). Data are reproduced from MicroChemicals (2013). Inset shows data amplified in the small thickness range. 81

Figure 2-18: Influence of rotation on the hydraulic jump location, plotted against the Froude number (flow rate) for the AZ6612 photoresist fluid. 82

Figure 2-19: Influence of rotation on the hydraulic jump height, plotted against the Froude number (flow rate) for the AZ6612 photoresist fluid. 83

Figure 2-20: Influence of rotation on the film thickness plotted against radial distance in regions (ii), (iii) and (iv) for the AZ6612 fluid. 84

Figure 2-21: Influence of rotation on the film free-surface velocity plotted against radial distance in regions (ii), (iii) and (iv) for the AZ6612 fluid. Inset shows the amplification around the jump. 85

Figure 3-1: Schematic illustration of the axisymmetric jet flow impinging on a flat stationary disk and the hydraulic jump of type I. Shown are the stagnation region (i), the developing boundary-layer region (ii), the fully-viscous region (iii), and the hydraulic jump region (iv). All notations are dimensionless. 98

Figure 3-2: Influence of gravity in the developing boundary-layer region (ii). The rescaled boundary-layer height, δ , and film thickness, h , are plotted against the normalized radial

distance. The transition location coincides with the intersection of the two heights (at the cusps in the figure). We only indicate the transition location by a vertical line for $\alpha = 10$. 106

Figure 3-3: Dependence of the location and film thickness at the transition point between the developing boundary-layer and fully-viscous regions (ii) and (iii) on gravity. 107

Figure 3-4: Influence of gravity on the developing boundary layer height and film thickness for supercritical flow. Also indicated in vertical lines are the locations of the hydraulic jump location $Re^{-1/3} r_J$ for different α values..... 113

Figure 3-5: Influence of gravity on the free surface velocity for supercritical flow..... 114

Figure 3-6: Influence of gravity on the wall shear stress for supercritical flow. 115

Figure 3-7: Dependence on the jump location and height immediately upstream of the jump on α 116

Figure 3-8: Dependence of the hydraulic jump radius on the flow rate. The figure shows the comparison between the present theoretical predictions and the measurements of Hansen *et al.* (1997) for two silicon oils of viscosities $\nu = 15$ cSt and 95 cSt. The numerical predictions of Rojas *et al.* (2010) are also included. 117

Figure 3-9: Dependence of the hydraulic jump radius on the flow rate. The figure shows the comparison between the present theoretical predictions (solid lines) and the ones based on the scaling law (dashed lines) of Rojas *et al.* (2013) for two silicon oils of viscosities $\nu = 15$ cSt and 95 cSt..... 118

Figure 3-10: Dependence of Fr_J on the flow rate (Froude number). The solid line corresponds to predictions based on Equations (3.4.4) and (3.5.13). The experimental data corresponding to silicon oil from Duchesne *et al.* (2014). Also added as dashed and dash-dotted lines the result based on Equations (3.5.5) and (3.5.9), respectively..... 128

Figure 3-11: Free-surface velocity in the supercritical and subcritical domains. Comparison between the present theory (solid line), the numerical results of Rojas *et al.* (2015), as well as

the experimental data of Ellegaard *et al.* (1996). Also added is the velocity distribution based on the parabolic profile. 130

Figure 3-12: Influence of gravity on the film thickness plotted against radial distance in regions (ii), (iii) and (iv). 131

Figure 3-13: Influence of the disk radius on the film thickness plotted against the radial distance in regions (ii), (iii) and (iv). Solution in solid line based on Equations (3.4.4) and (3.5.11). Dashed line shows the subcritical profile based on (3.4.4). 133

Figure 3-14: Free surface profile. Comparison between theoretical predictions and the measurements of Duchesne *et al.* (2014) for silicon oil (20 cSt). Results plotted in dimensionless form with $Re = 169$, $Fr = 14.88$, $Bo = 1.19$, $\theta_Y = 55^\circ$ and $r_\infty = 94$. Theoretical profiles based on current theory or Equation (3.4.4) (solid lines) and asymptotic subcritical Equation (3.5.11) (dashed line). 135

Figure 4-1: Schematic illustration of the axisymmetric jet flow impinging on a heated disk. The four sub-regions of the physical domain are also shown. All notations are dimensionless. 150

Figure 4-2: The dependence of viscosity on temperature for three common liquids. Solid lines indicate the fitting using the parameters in Table 1. The markers are experimental data from various sources (Korson *et al.* 1969 for water, Segur & Oberstar 1951 for glycerol, and Peleg 2017 for soybean oil). 156

Figure 4-3: The dependence of surface tension on temperature for three common liquids. Solid lines indicate the fitting using the parameters in table 1. The markers are experimental data from various sources (Agrawal & Menon 1992 for water, Takamura *et al.* 2012 for glycerol, Sahasrabudhe *et al.* 2017 for soybean oil). 157

Figure 4-4: Comparison of Watson's similarity solution with the cubic and parabolic velocity profiles. 162

Figure 4-5: Influence of the wall temperature on the film thickness and boundary-layer heights for $\hat{T}_0 = 278\text{K}$ and $\text{Ca Re}^{2/3} = 10$ in the super-critical region. Also indicated are the values of (rescaled) transition locations in light vertical lines for $T_w = 1.05$ 166

Figure 4-6: Influence of the wall temperature on the surface temperature and velocity in the super-critical region for $\hat{T}_0 = 278\text{K}$ and $\text{Ca Re}^{2/3} = 10$ 167

Figure 4-7: Influence of the wall temperature on the wall shear stress and Marangoni stress (surface shear stress) in the super-critical region for $\hat{T}_0 = 278\text{K}$ and $\text{Ca Re}^{2/3} = 10$. Vertical lines indicate second transition locations..... 168

Figure 4-8: Influence of the wall temperature on the average Nusselt number (no surface tension effect). Also shown in the figure is the predictions of Chaudhury (1964) for water without surface tension effect. Here, $\text{Pr}=3$ corresponds to $\hat{T}_0 = 329.45\text{K}$ and $\text{Pr}=10$ corresponds to $\hat{T}_0 = 279.15\text{K}$ 169

Figure 4-9: Influence of the wall temperature on the Nusselt number (no surface tension effect). The data for constant fluid property is from Searle *et al.* (2017). The Reynolds number is maintained at $\text{Re} = 4300$, $\hat{T}_0 = 278\text{K}$ 170

Figure 4-10: Influence of the wall heat flux on the boundary-layer heights and the film thickness for $\hat{T}_0 = 300\text{K}$ and $\text{Ca Re}^{2/3} = 10$ 171

Figure 4-11: Influence of the wall-heat flux on the effective Prandtl number along the wall and the free surface for super-critical flow for $\hat{T}_0 = 300\text{K}$ and $\text{Ca Re}^{2/3} = 10$ 172

Figure 4-12: Influence of inertia and the wall heat flux on the transition locations for $\hat{T}_0 = 300\text{K}$. Inset shows the rescaled transition locations..... 173

Figure 4-13: Influence of the Reynolds number on the local Nusselt number distribution). The comparison with the measurements and numerical results of Liu & Lienhard (1989) is also included. 175

Figure 4-14: Influence of the wall temperature on the film height in the super- and sub-critical regions for $\hat{T}_0 = 300\text{K}$. Here $\text{Ca Re}^{2/3} = 100$, $\text{Fr Re}^{-1/2} = 3$ and $r_\infty \text{Re}^{-1/3} = 6$.. 182

Figure 4-15: Influence of the wall temperature on the jump location and height for $\hat{T}_0 = 278\text{K}$, $\text{Fr Re}^{-1/2} = 3$ and $r_\infty \text{Re}^{-1/3} = 6$ 183

Figure 4-16: . Comparison of the film thickness over the entire domain with the predictions of Sung *et al.* (1999) for different wall temperatures ($\hat{T}_0 = 293\text{K}$, $\text{Re} = 16000$, $\text{Pe} = 112000$, $\text{Fr} = 5$, $\text{Ca} = 0.022$)..... 184

Figure 4-17: Influence of the jet flow rate on the profiles of the Nusselt number. Comparison between our results and the predictions of Sung *et al.* (1999)..... 185

Figure 4-18: Influence of the wall heat flux on the film profile in the super- and sub-critical regions for $\hat{T}_0 = 300\text{K}$. Here $\text{Ca Re}^{2/3} = 100$, $\text{Fr Re}^{-1/2} = 3$ and $r_\infty \text{Re}^{-1/3} = 6$ 188

Figure 4-19: Influence of the wall heat flux on the Nusselt number in the super- and sub-critical regions for $\hat{T}_0 = 300\text{K}$. Here $\text{Ca Re}^{2/3} = 100$, $\text{Fr Re}^{-1/2} = 3$ and $r_\infty \text{Re}^{-1/3} = 6$.. 189

List of Appendices

Appendix A: The thin-film equations and boundary conditions	200
---	-----

Nomenclature

a	Radius of the jet, m
Bo	Bond number $\rho g a^2 / \gamma_0$
C_p	Specific heat, $J \cdot kg^{-1} \cdot K^{-1}$
Fr	Froude number, $Q / \pi \sqrt{a^5 g}$
Fr_h	Depth Froude number $V / \sqrt{g \hat{h}}$
Fr_J	Jump Froude number, $Fr / 2r_J h_J^{+3/2}$
g	Gravitational acceleration, $m \cdot s^{-2}$
G	Gravity number, Re / Fr^2
h	Film thickness, dimensionless
\bar{h}	Rescaled film thickness, dimensionless
\hat{h}	Film thickness, m
\tilde{h}	Heat transfer coefficient, $W / (m^2 \cdot K)$
h_0	Film thickness at $r = r_0$, dimensionless
h_1	Film thickness at $r = r_1$, dimensionless
h_f	Final film thickness of spin coating, m
h_i	Initial Film thickness, dimensionless

h_J^-	Film thickness immediately upstream of the jump, dimensionless
h_J^+	Film thickness immediately downstream of the jump, dimensionless
h_{\max}	Film thickness at $r = r_{\max}$, dimensionless
h_{\min}	Film thickness at $r = r_{\min}$, dimensionless
h_∞	Film thickness at the edge of the disk, dimensionless
H	Function of the free surface, $z - h$
k	Thermal conductivity, $W \cdot m^{-1} \cdot s^{-1}$
M	Mach number, V / V_c
Nu	Nusselt number, $\tilde{h}a / k$
p	Pressure, dimensionless
\hat{p}	Pressure, $N \cdot m^{-2}$
Pe	Peclet number, $Q / \pi a \kappa$
Pr	Prandtl number, ν_0 / κ
q	Heat flux, dimensionless
q_w	Wall heat flux, dimensionless
\hat{q}_w	Wall heat flux, $W \cdot m^{-2}$
Q	Volume flow rate, $m^3 \cdot s^{-1}$
r	Radial coordinate, dimensionless

\bar{r}	Rescaled radial coordinate, dimensionless
\hat{r}	Radial coordinate, m
r_0	Transition location of the hydrodynamic boundary layer, dimensionless
r_1	Transition location of the thermal boundary layer, dimensionless
r_{\max}	Maximum film thickness location in supercritical flow, dimensionless
r_{\min}	Minimum film thickness location in supercritical flow, dimensionless
r_∞	Disk radius, dimensionless
r_J	Radius of the hydraulic jump, dimensionless
Re	Reynolds number, $Q / \pi a v_0$
s	Arclength, m
T	Temperature, dimensionless
\hat{T}_0	Incoming jet temperature, K
T_s	Free-surface temperature, dimensionless
T_s^-	Free-surface temperature immediately upstream of the jump, dimensionless
T_s^+	Free-surface temperature immediately downstream of the jump, dimensionless
T_w	Wall temperature, dimensionless
\hat{T}_w	Wall temperature, K
u	Horizontal velocity, dimensionless

\hat{u}	Horizontal velocity, m/s
u_s	Free-surface velocity, dimensionless
v	Azimuthal velocity, dimensionless
\hat{v}	Azimuthal velocity, m/s
V	Velocity, $\text{m} \cdot \text{s}^{-1}$
V_c	Speed of sound, $\text{m} \cdot \text{s}^{-1}$
w	Vertical velocity, dimensionless
\hat{w}	Vertical velocity, m/s
z	vertical coordinate, dimensionless
\hat{z}	Vertical coordinate, m

Greek Symbols

α	Dimensionless parameter, $\text{Re}^{1/3} \text{Fr}^2$
γ	Surface tension, dimensionless
$\hat{\gamma}$	Surface tension (variable), $\text{N} \cdot \text{m}^{-1}$
γ_0	Surface tension (constant), $\text{N} \cdot \text{m}^{-1}$
δ	Hydrodynamic boundary layer thickness, dimensionless
$\bar{\delta}$	Rescaled hydrodynamic boundary layer thickness, dimensionless
δ_{\max}	Hydrodynamic Boundary layer thickness at $r = \rho_{\max}$, dimensionless
δ_T	Thermal boundary layer thickness, dimensionless

ε	Perturbation parameter, dimensionless
η	Scaled vertical coordinate, z/h
$\bar{\eta}$	Mapped vertical coordinate, \bar{z}/\bar{h}
θ	azimuthal coordinate
θ_Y	Static contact angle
κ	Thermal diffusivity, $\text{m}^2 \cdot \text{s}^{-1}$
ν	Kinematic viscosity, dimensionless
$\hat{\nu}$	Kinematic viscosity (variable), $\text{m}^2 \cdot \text{s}^{-1}$
ν_0	Kinematic viscosity (constant), $\text{m}^2 \cdot \text{s}^{-1}$
$\bar{\xi}$	Mapped radial coordinate (equal to \bar{r})
ρ	Density of liquid, $\text{kg} \cdot \text{m}^{-3}$
ρ_{\max}	Maximum hydrodynamic boundary layer thickness location, dimensionless
τ_w	Wall shear stress, dimensionless
ω	Rotating speed, s^{-1}
Ω	Rotation parameter, $\pi a^3 \omega / Q$

Chapter 1

1 Introduction

The circular impinging jet flow and hydraulic jump will be introduced including the applications, practical relevance and analogies to other physical phenomena. The major theoretical tools and theories are then introduced followed by an introduction to the existing literatures on the hydrodynamics and heat transfer of impinging jet flow and circular hydraulic jump. The objectives and thesis outline are given at the end of the chapter.

1.1 Background and applications

When a circular liquid jet impacts a solid surface, it spreads out radially as a thin film. The thickness of the liquid develops gradually until reaching a radial location where the height of the liquid rises abruptly as illustrated in Figure 1-1a. The sudden increase of the liquid depth is known as the circular hydraulic jump that can be daily observed when the tap water hits the bottom of a kitchen sink (Figure 1-1b). The region before the hydraulic jump is formally known as the supercritical region characterized by having high velocity. In the post-jump field, known as the subcritical region, the velocity of the liquid significantly drops due to the sudden increase of the liquid depth.

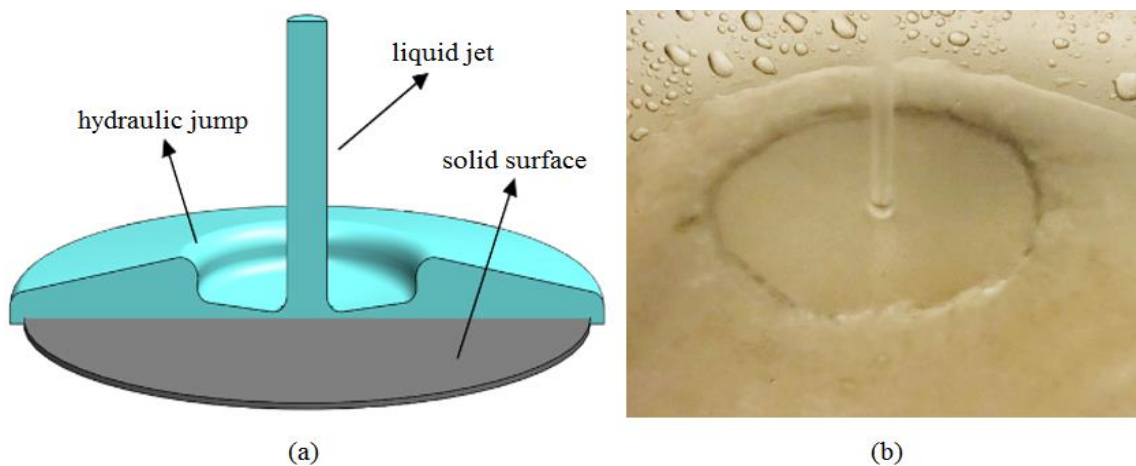


Figure 1-1: Schematic illustration of impinging liquid jet and a circular hydraulic jump.

It is worth noting that the hydraulic jump can also occur on a much larger scale and non-circular shape, which is generally known as planar jump. The planar hydraulic jump usually occurs when a fast discharging flow meets a slowly moving stream or an obstacle. Figure 1-2 illustrates a 2-D hydraulic jump in a discharging flow from a dam. For both circular and planar hydraulic jumps, a depth Froude number can be defined as

$$Fr_h = \frac{V}{\sqrt{g\hat{h}}}, \quad (1.1.1)$$

with V being the flow velocity, g the gravitational acceleration and \hat{h} the depth of the liquid. In the current thesis, a hat is used to denote a dimensional variable or parameter when necessary. The supercritical flow is characterized by having $Fr_h > 1$ while the subcritical flow has $Fr_h < 1$ (Crowe 2009).

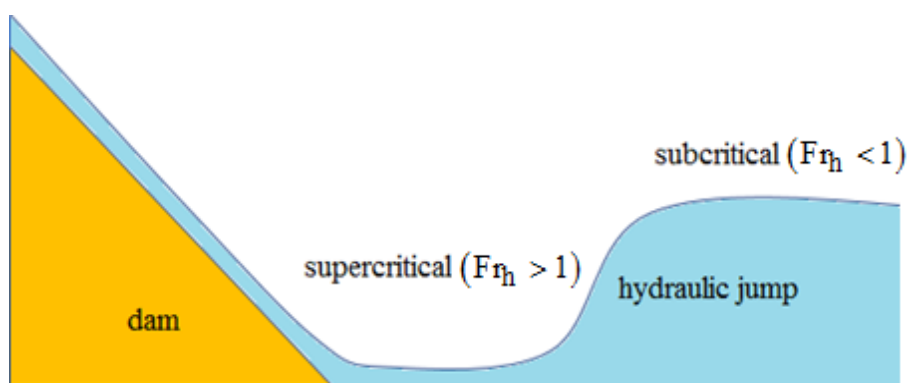


Figure 1-2: Planar hydraulic jump.

Introductions to planar hydraulic jump can be found in undergraduate textbooks on fluid mechanics or open-channel flows. This type of hydraulic jump is often artificially created by engineers to dissipate energy below spillways and discharging outlets. A proper design can destruct large amounts of energy and reduce the scouring and damage to the channel bed. For this reason, there is extensive research on the planar hydraulic jump. However, the focus of the current thesis will be on the circular hydraulic jump.

The circular hydraulic jump was first described by Leonardo da Vinci in the 1500s in one of his paintings and it is intriguing to find that such a common and simple-looking

phenomenon is still far from being fully understood today after such a long time of research and hundreds of publications. Based on the observation of Bush *et al.* (2006), there are three basic types of circular hydraulic jump as illustrated by Figure 1-3. In the absence of downstream obstacle, the height of the jump is relatively small and there is only a separation roller downstream of the jump. This is the standard hydraulic jump known as the type I jump (Figure 1-3a). If the downstream depth is increased by mounting an obstacle, a second roller near the free surface will appear as some of the liquid falls back on the coming flow from the supercritical region, which features a type IIa jump (Figure 1-3b). If the downstream depth increases further, the type IIa jump transforms into a type IIb jump (Figure 1-3c) marked by having a ‘double-jump’ structure. The current thesis focuses only on the standard type I jump.

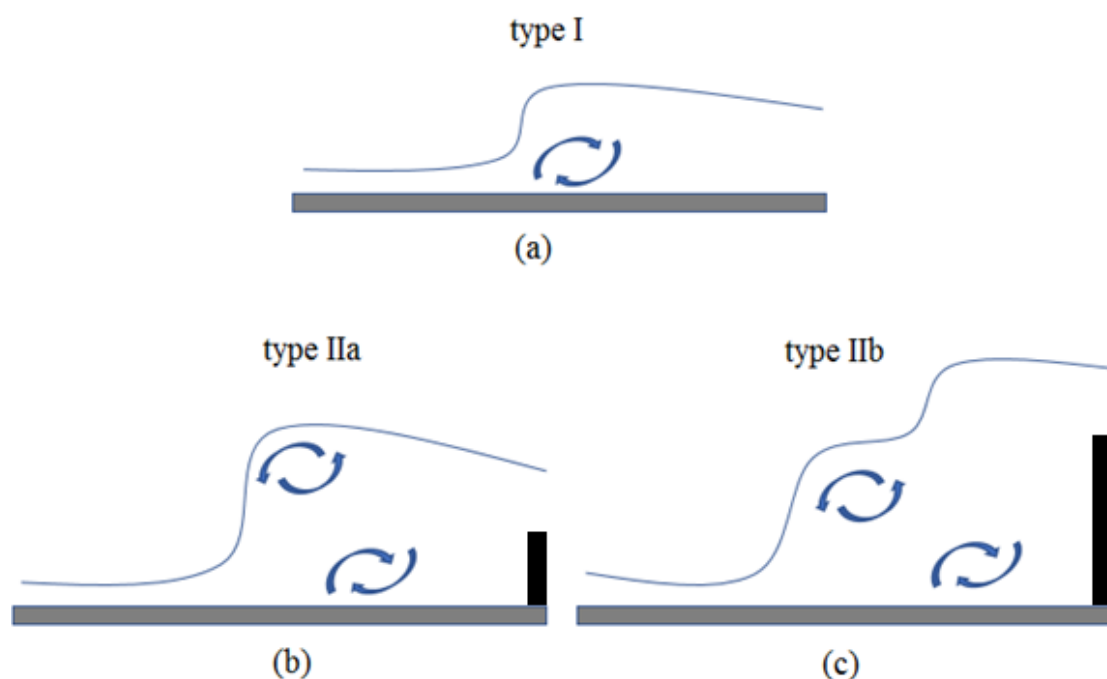


Figure 1-3: Different types of circular hydraulic jump.

Before giving a detailed introduction and discussing outstanding issues, it is important to discuss first some of the many applications of impinging jet flow and heat transfer, and the practical relevance of the hydraulic jump to engineers and scientists. Apart from its common use as rinsing flow in many applications (Hsu *et al.* 2011; Walker *et al.* 2012),

the impinging jet flow is important in numerous industrial cooling applications. For example, liquid jet impingement is the major cooling method in machining process, where the cutting liquid (coolant) is directed to impinge at the target area to control the local temperature which affects significantly the mechanical properties of the product (DBMR 2019). Liquid oil jet cooling is also used in the car engine's piston room (Melaniff 2003), on the other side of which is the combustion chamber where a large amount of heat is generated. A proper design of the cooling system helps to avoid the overheating the piston and its accessories. In addition, liquid jet impingement is always used in the jet quenching and jet cooling process in the heat treatment of steel and hot strip rolling production lines (Linz 2011).

The impingement target can also be a rotating surface, for which a common application is the spinning disk reactor (SDR) for chemical reactions (Reay 2013). Usually one or more liquids can be fed at the centre of a rotating disk which can be either cooled or heated. The liquid spreads over the disc (and mixes if more than one liquid is present) and the produced liquids are collected from the outlet. The intensity of mixing, heat and mass transfer rate can be precisely controlled by adjusting the rotating speed. Moreover, by rotation, the liquid layer can be made ultra thin, providing good characteristics for isothermal heating, chemical reaction and liquid atomization.

Recently, micro electronic devices became increasingly popular and compact power modules are widely used in varieties of power control and conversion applications with increasing trends in the operating voltage and current (Bhunia *et al.* 2007). Consequently, temperature control of such high-thermal-density systems becomes quite challenging. In this case, traditional air fan cooling of electronic devices often falls short, begging more efficient liquid cooling systems. In recent decades, increasing attention has been drawn to the high performance of liquid jet cooling on electronic devices, making crucial the understanding of the hydrodynamics and heat transfer of liquid jet spreading.

The hydraulic jump is a phenomenon often encountered in impinging jet flow, except for high-speed jets. The fast motion of a liquid inside the jump provides a high rate of heat and mass transfer as well as a large shear stress, whereas the low velocity in the

subcritical region (downstream of the jump), caused by the hydraulic jump, dramatically harms the performance (Mohajer & Li 2015). Consequently, the prediction of the jump location (radius) is crucial in the design of relevant processes.

Apart from the direct relevance to practical applications, the problem is also of scientific interest, particularly the understanding of the transition from the supercritical to the subcritical flow along free surface flow. Due to its fundamental and practical importance, circular jet impingement and hydraulic jump has become the focuses of many studies in the recent decades.

Before discussing existing theories and methodologies, there are two interesting analogies of the circular hydraulic jump worth discussing. The first one is the analogy to a white hole (the reverse of a black hole), which is a hypothetical region that light wave cannot enter but can always escape from. As mentioned above, Fr_h is greater than 1 in the supercritical region so that $v > \sqrt{gh}$, where \sqrt{gh} is the speed of the shallow-water wave (Kundu *et al.* 2016). Consequently, the flow is faster than the shallow-water wave in the supercritical region. In this case, the wave can only travel downstream. In the subcritical region, however, the wave can travel in both directions as Fr_h is smaller than 1. In this sense, the region upstream of the hydraulic jump can be viewed as a hydrodynamic white hole since the wave is always trapped outside (Jannes *et al.* 2011).

The second analogy of the circular hydraulic jump is the similarity to the transition from supersonic to subsonic flow in aerodynamics. The Mach number is defined by

$$M = \frac{V}{V_c}, \quad (1.1.2)$$

with V being the velocity of an object and V_c being the speed of sound. If an object is traveling with a speed greater than the speed of sound (e.g. a supersonic jet), the air around the object will experience a transition from the supersonic ($M > 1$) to the subsonic state ($M < 1$). Therefore the circular hydraulic jump can be an important tool to study other problems involving transition effects.

1.2 Modeling of the flow and thermal fields of a spreading jet and a circular hydraulic jump

The dimensionless numbers associated with the flow and thermal field in the impinging jet problem will be first introduced. The major theories and assumptions are then discussed followed by the introduction of the theoretical tools in the current thesis.

1.2.1 Dimensionless numbers

Dimensionless numbers are important parameters in the similarity analysis of hydrodynamic and thermal systems. We have already defined two dimensionless numbers as per Equations (1.1.1) and (1.1.2). In fact, for any problem of viscous flow, the first important dimensionless number is the Reynolds number, which is defined in the current thesis by

$$\text{Re} = \frac{Q}{\pi a v_0}, \quad (1.2.1)$$

with Q , a and v_0 being the incoming volume flow rate, the jet radius and the kinematic viscosity, respectively. The Reynolds number reflects the strength of the inertial over the viscous effects or the strength of the convective momentum transfer to the diffusive momentum transfer.

When heat transfer is involved, it is always convenient to introduce the Peclet number, defined by

$$\text{Pe} = \frac{Q}{\pi a \kappa}, \quad (1.2.2)$$

where κ is the thermal diffusivity, defined by

$$\kappa = \frac{k}{\rho C_p}, \quad (1.2.3)$$

with k , ρ and C_p being the thermal conductivity, density and specific heat respectively. By analogy, the Peclet number can be viewed as the counterpart of the Reynolds number as it reflects the strength of convective heat transfer over conductive heat transfer. The ratio of Peclet number to Reynolds number defines the Prandtl number, namely

$$\text{Pr} = \frac{v_0}{\kappa}, \quad (1.2.4)$$

which reflects the ratio of viscous diffusion to thermal diffusion. The Prandtl number is generally greater than 1 for non-metallic liquids but smaller than 1 for liquid metals.

In thermal convection, another important dimensionless number characterising the heat transfer performance is the Nusselt number, defined by

$$\text{Nu} = \frac{\hat{q}_w a}{k(\hat{T}_w - \hat{T}_0)}, \quad (1.2.5)$$

with \hat{q}_w being the wall heat flux, \hat{T}_w being the wall temperature and \hat{T}_0 being the jet temperature.

It should be noted that only some important dimensionless number are introduced here for convenience of discussion in the current chapter. Other dimensionless numbers will be introduced in later chapters when needed.

1.2.2 Boundary layer theory and the thin-film approach

The laminar boundary layer equations for axisymmetric flow and heat transfer can be written as

$$\frac{\partial \hat{u}}{\partial \hat{r}} + \frac{\hat{u}}{\hat{r}} + \frac{\partial \hat{w}}{\partial \hat{z}} = 0, \quad (1.2.6a)$$

$$\left(\hat{u} \frac{\partial \hat{u}}{\partial \hat{r}} + \hat{v} \frac{\partial \hat{u}}{\partial \hat{z}} \right) = -\frac{1}{\rho} \frac{\partial \hat{p}}{\partial \hat{r}} + \nu_0 \frac{\partial^2 \hat{u}}{\partial \hat{z}^2}, \quad (1.2.6b)$$

$$\hat{u} \frac{\partial \hat{v}}{\partial \hat{r}} + \hat{w} \frac{\partial \hat{v}}{\partial \hat{z}} + \frac{\hat{u}\hat{v}}{\hat{r}} = \nu_0 \frac{\partial^2 \hat{v}}{\partial \hat{z}^2}, \quad (1.2.6c)$$

$$-\frac{1}{\rho} \frac{\partial \hat{p}}{\partial \hat{y}} + g = 0, \quad (1.2.6d)$$

$$\left(\hat{u} \frac{\partial \hat{T}}{\partial \hat{r}} + \hat{v} \frac{\partial \hat{T}}{\partial \hat{z}} \right) = \kappa \frac{\partial^2 \hat{T}}{\partial \hat{z}^2}, \quad (1.2.6e)$$

Here a hat denotes a dimensional variable. \hat{u} , \hat{v} and \hat{w} are the velocities in \hat{r} , $\hat{\theta}$ and \hat{z} directions. \hat{p} and \hat{T} are the flow pressure and temperature. ρ, g, ν_0 and κ are physical parameters representing the density, gravitational acceleration, kinematic viscosity and thermal diffusivity respectively. As the flow is assumed to be axisymmetric, azimuthal dependence on the tangential coordinate is not involved.

In fluid dynamics, the main idea behind the boundary layer theory is that the effect of viscosity is only important within a thin layer of fluid in the immediate vicinity of a solid boundary (Prandtl 1904), especially at moderate to large flow rate (i.e. a large Reynolds number). Therefore, the boundary layer is in nature a viscous layer, outside of which the fluid is of inviscid character as illustrated by Figure 1-4a. It is worth noting that there is no clear-cut border between the viscous and the inviscid regions. It is generally acceptable that the upper edge of the boundary layer can be defined at the position where the velocity approaches 99% of the free stream velocity (Schlichting & Gersten 2000) where the velocity gradient is negligibly small. It is also noted that, even inside the boundary layer region, the velocity gradient is the largest at the wall and continuously decreases until it almost vanishes near the edge of the boundary layer.

Particularly for the boundary layer on a flat plate, it is observed that the streamwise velocity varies much slower along the plate than in the direction normal to it according to a scaling analysis of the Navier-Stokes equations (Schlichting & Gersten 2000, see also Appendix A). This theory in fact constitutes the leading order solution of a matched asymptotic expansion analysis for the whole flow field. Higher order boundary layers are

not of concern in the current thesis and interested readers are referred to the works of Van Dyke (1964) and Sobey (2000).

While the general boundary layer is bounded by the same fluid, the thin-film theory is specifically applicable to the flow of a thin liquid layer on a solid surface, characterised by having a liquid-air interface, known as the free-surface thin-film flow, as shown in Figure 1-4b. The velocity distribution within the thin liquid film is also of the boundary-layer type. As the air has a much smaller viscosity compared to the liquid, the velocity gradient and thus the shear stress of the liquid near the free surface is also negligible. A pressure boundary condition is generally obtained at the liquid-air interface based on the air pressure (and surface tension when a large surface curvature is present). In the present thesis, the boundary-layer equations and the thin-film theory constitute the major assumptions of the theoretical analysis.

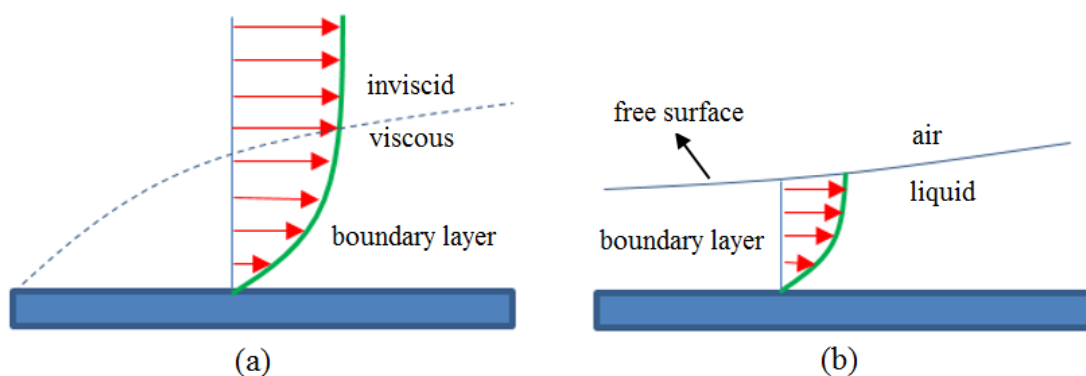


Figure 1-4: Boundary-layer and thin-film flow.

1.2.3 The Kármán–Pohlhausen (K–P) approach

One important observation regarding Equations (1.2.6) is that the partial derivatives with respect to the radial coordinate are of first order. This is not surprising since the large velocity (Reynolds number) makes the flow a one-way problem (i.e. only one boundary condition is needed) in the streamwise direction. The boundary-layer equations admit an exact solution in the absence of transverse pressure gradient (Watson 1964; Schlichting & Gersten 2000). Therefore, it is also not surprising that an exact solution would not exist in the presence of a hydrostatic pressure. Consequently, the convenient Kármán–

Pohlhausen (K–P) approach will be adopted due to its proven efficiency and accuracy (Schlichting & Gersten 2000).

The K-P approach is, to the best of the author’s knowledge, the earliest and still the most widely used method for solving the boundary layer equations, originally due to the works of Kármán (1921) and Pohlhausen (1921). It is essentially an integration of the boundary-layer equations between the solid surface and the upper edge of the boundary layer or the free surface. By approximating the velocity profile, the boundary-layer thickness, film thickness and wall shear stress can be obtained. In fact, the K-P approach can also be understood from a numerical point of view as illustrated in Figure 1-5.

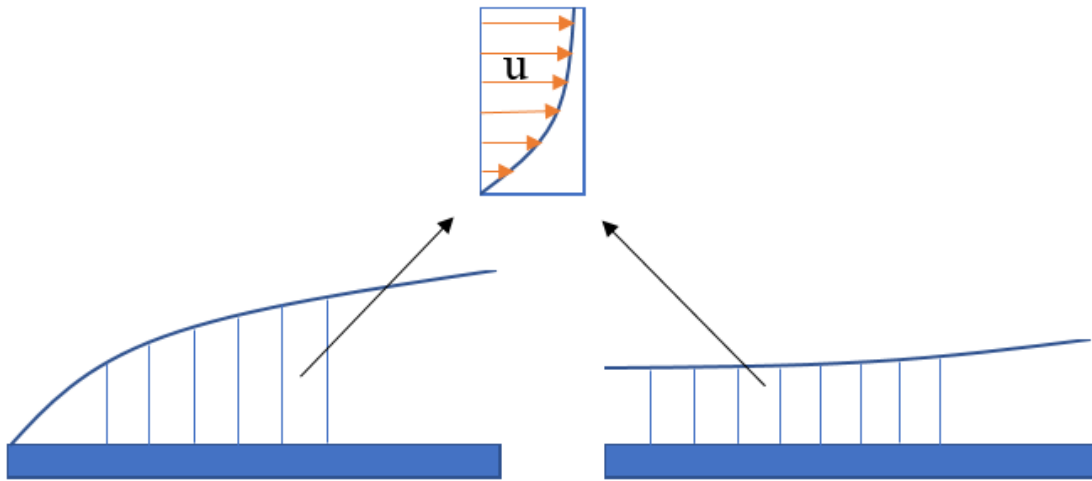


Figure 1-5: A numerical view of the K-P approach.

In a formal numerical method, the discretization (and meshing) in both the horizontal and the vertical direction are necessary. However, with the K-P approach, the discretization in the vertical direction is eliminated by imposing a certain profile for velocity distribution. The profile is designed as to satisfy the physical boundary conditions and mass conservation. This is equivalently to deploying one layer of mesh cells (Figure 1-5) with variable heights of each control volume. Then the solution can be obtained by an integration in the horizontal direction, which either admits an analytical solution or can be accurately obtained with a high-order Runge-Kutta method. It should be noted that the

boundary-layer equations and the K-P method are equally applicable to the energy equation and heat transfer problems as will be discussed in later chapters.

1.2.4 Momentum-force relation across the hydraulic jump

From many aspects in the studies of hydraulic jump, predicting its location is undoubtedly the most important aspect and is still an open issue due to its influence on the heat and mass transfer performance. Therefore, understanding the changes in velocity and pressure before and after the jump is crucial to compute the hydraulic jump profile and predict its location. The basic relation to use is derived from Newton's second law that the rate of change of linear momentum equals to the total applied force in the direction of interest. In the current problem, the rate of destruction of momentum across the jump equals the reverse hydrostatic pressure force due to the jump in depth (Crowe 2009). To demonstrate this method, a control volume of angle $\Delta\theta$ across the jump is taken as shown in Figure 1-6a. Assuming inviscid flow for convenience for now, the relation per unit circumferential length between the velocity and pressure is given by

$$\rho \hat{u}_2 \hat{h}_2 \hat{u}_2 - \rho \hat{u}_1 \hat{h}_1 \hat{u}_1 = \hat{p}_1 \hat{h}_1 - \hat{p}_2 \hat{h}_2 + f(\gamma_0), \quad (1.2.7)$$

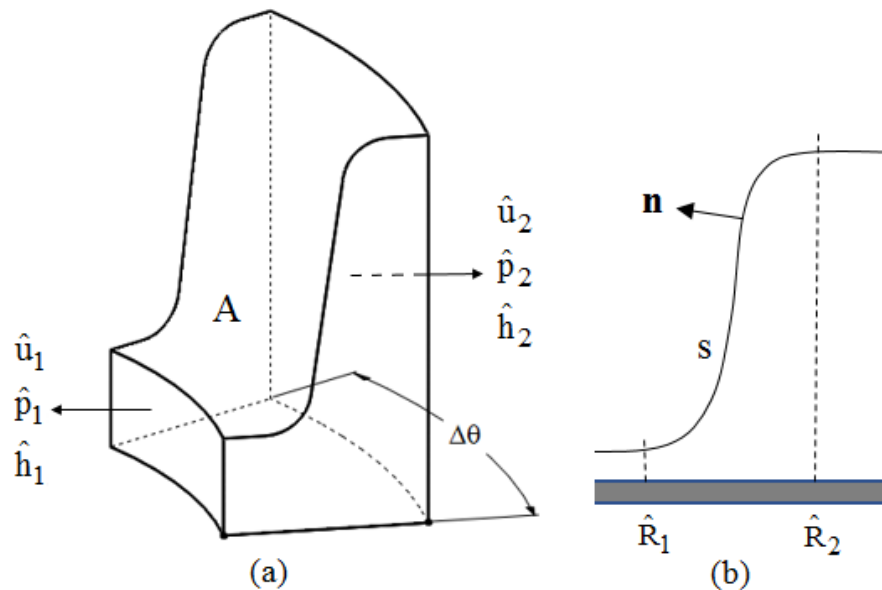


Figure 1-6: A schematic view of the control volume across the hydraulic jump: (a) 3-dimensional view; (b) axisymmetric view.

where \hat{u} , \hat{p} and \hat{h} are the velocity, the average hydrostatic pressure and the height of the cross sections before and after the jump. It should be emphasized that for a viscous liquid, the left-hand-side of Equation (1.2.7) should be an integration over the cross section of the liquid as the velocity varies in the vertical direction. The viscous force at the bottom surface will be neglected anyway as the width of the jump is negligibly small (Watson 1964; Prince *et al.* 2012). Based on Equation (1.2.7), the hydrodynamic character on one side of the jump can be determined if the information on the other side is known. The additional term $f(\gamma_0)$ represents the force per unit circumferential length due to surface tension in the presence of large curvature (i.e. small jump radius) exclusively for circular jumps. We here give a brief derivation below for this additional term.

Considering the shape of the jump in the axisymmetric plane as illustrated in Figure 1-6b, we write the force per unit circumferential length due to surface tension as

$$f(\gamma_0) = \frac{1}{\hat{r}_j \Delta\theta} \int_A \gamma_0 (\nabla \cdot \mathbf{n})(\mathbf{n} \cdot \mathbf{r}) dA, \quad (1.2.8)$$

where \hat{r}_j is the radius of the jump, A is the area of the free surface within the control volume, $dA = \hat{r} d\theta d\hat{r} \sqrt{1 + \hat{h}'^2}$ and $\hat{R}_1 < \hat{r} < \hat{R}_2$. Here a prime denotes a total differentiation. It should be noted that $\hat{h}' \approx 0$ at $\hat{r} = \hat{R}_1$ and $\hat{r} = \hat{R}_2$. The free surface is defined by $H(\hat{r}, \hat{z}) = \hat{z} - \hat{h}(\hat{r}) = 0$, so that the outward unit surface normal can be written as

$$\mathbf{n} = \frac{\nabla H}{|\nabla H|} = \left(\frac{-\hat{h}'}{\sqrt{1 + \hat{h}'^2}}, \frac{1}{\sqrt{\sqrt{1 + \hat{h}'^2}}} \right). \quad (1.2.9)$$

Upon using Equation (1.2.9), the force due to surface tension, as per Equation (1.2.8), finally takes the following form

$$f(\gamma_0) = \frac{\gamma_0}{\hat{r}_j} \left(\hat{r} \sqrt{1 + \hat{h}'^2} \Big|_{\hat{R}_1}^{\hat{R}_2} - \int_{\hat{R}_1}^{\hat{R}_2} \sqrt{1 + \hat{h}'^2} d\hat{r} \right). \quad (1.2.10)$$

It is not difficult to realize that the second term in Equation (1.2.10) represents the total arclength s of the free surface in the axisymmetric plane between $\hat{r} = \hat{R}_1$ and $\hat{r} = \hat{R}_2$. In this case, for a sharp jump, the first term vanishes since at $\hat{R}_1 = \hat{R}_2$, and the second term becomes $\hat{h}_2 - \hat{h}_1$. Therefore,

$$f(\gamma_0) = -\frac{\gamma_0}{\hat{r}_j} (\hat{h}_2 - \hat{h}_1), \quad (1.2.11)$$

Equations (1.2.10) and (1.2.11) were first derived by Bush & Aristoff (2003). In fact, for a sharp jump, Equation (1.2.11) can be directly obtained by analysing the pressure jump across the cylindrical surface of radius \hat{r}_j and length $(\hat{h}_2 - \hat{h}_1)$.

1.3 Literature review

In this section, the existing studies relevant to the hydrodynamics and heat transfer of an impinging jet and hydraulic jump are introduced. The advantages and limitations of these works are also discussed.

1.3.1 The hydrodynamics of the impinging jet and circular hydraulic jump

Two major branches of studies exist on the circular impinging jet and hydraulic jump. To start with, it is natural to expect that the height after the jump should have a tangible effect on the location of the jump. In other words, a larger subcritical depth would result in a smaller jump radius due to the larger reverse hydrostatic pressure gradient at the jump. The first major contribution to the prediction of the circular hydraulic jump structure based on this idea is due to Watson (1964). In his work on the liquid jet spreading on a horizontal plate, Watson assumed that a boundary layer develops near the impingement point and grows until reaching the free surface at some transition location

(not the jump location) making the liquid layer fully-viscous. The thickness of the boundary layer is determined by the K-P approach and the fully-viscous region is solved by a similarity transformation method (Watson 1964). In the fully-viscous region, the film thickness continues to grow until reaching the hydraulic jump. Gravity was neglected in the supercritical region due to the small liquid thickness. Assuming the height of the liquid after the jump is known, the location of the jump was obtained using the force and momentum balance approach as discussed in Section 1.2.4. Watson (1964) made an approximation that the velocity is uniform across the subcritical depth due to the slow motion of the liquid.

Watson's (1964) approach yielded a reasonably good agreement with his own experiments on the location of the jump. In his experiment, the subcritical thickness is controlled by barrier downstream. Olsson & Turkdogan (1966) carried out experimental measurements on the free-surface velocity by dropping small corps on the surface of the liquid and taking photos using a high-speed camera. They found that the free-surface velocity is about 10% lower than the free stream velocity predicted by Watson (1964). In contrast, the experiments of Azuma & Hoshino (1984a,b) did support the theory of Watson (1964). It should be noted that, in the measurements of Olsson & Turkdogan (1966), it was not evident that those corps would accurately follow the speed of the free surface (Liu *et al.* 1991). Watson's theory was later also tested by Errico (1986), Vasista (1989), Stevens & Webb (1992), Liu & Lienhard (1993), Bush & Aristoff (2003) and Baonga *et al.* (2006). It was observed that Watson's prediction is generally satisfying for a large jump radius. Liu & Lienhard (1993) observed that Watson's predictions are least satisfactory in the limit of relatively small jump radius for which surface tension effect becomes important. In this regard, Bush & Aristoff (2003) included the surface tension effect in the force and momentum balance relation, leading to a better agreement with experiment.

Watson's method laid out the foundation for numerous later extensions. Craik *et al.* (1981) observed a separation eddy precisely behind the hydraulic jump and attributed the cause of hydraulic jump to flow separation caused by the subcritical depth. Kate *et al.* (2007) experimentally studied the formation of the hydraulic jump on an inclined plane.

They observed that the hydraulic jump is bounded by a smooth curve or a curve with sharp corners depending on the inclination angle. Zhao & Khayat (2008) extended Watson's theory to non-Newtonian liquids for both shear-thinning and shear-thickening fluids of the power-law type, and found that only the overall viscosity influences the location of the hydraulic jump. The influence of slip was examined by Dressaire *et al.* (2010) with a combination of experiment and theoretical analysis but no quantitative relation between the slip length and the hydraulic jump was given. Later the effect of slip was also examined by Prince *et al.* (2012, 2014) using a K-P approach, and by Khayat (2016) using a numerical approach. Both Prince *et al.* (2012, 2014) and Khayat (2016) observed that the location of the jump moves downstream for a larger slip length. The influence of the nozzle-to-disk distance on the hydraulic jump radius was investigated experimentally by Brechet & Neda (1999), who observed that the nozzle-to-disk distance has little influence on the jump location. Kuraan *et al.* (2017) however in their experiments found that when the ratio of nozzle-to-disk distance to the nozzle diameter is less than 0.4, the radius of the hydraulic jump increases.

It is worth noting that the relation between the momentum and the force across the jump requires the knowledge of the height immediately downstream of the jump, which is usually artificially fixed by mounting a barrier downstream (Watson 1964; Bush & Aristoff 2003; Prince *et al.* 2012, 2014; Zhao & Khayat 2008; Khayat 2016). In fact, such barriers can give rise to both type I and type II jumps depending on the subcritical height (see Section 1.1). In practical applications, however, the target surface is often free of such controlled height and the flow is often allowed to drain freely at some edge far away from the impingement point. Therefore, the jump is most likely of type I. This constitutes the major drawback of Watson's approach that the downstream depth has to be prescribed. Another consideration is that the velocity of the flow after the jump was assumed to be uniform (i.e. inviscid) across the liquid depth in most of these studies, but the fluid is viscous in reality (Duchesne *et al.* 2014).

The other branch of studies initially began with the theoretical approach of Tani (1949), which assumes that the flow separation (and thus the hydraulic jump) is caused by the accumulating liquid thickness from the supercritical region, which explains the

occurrence of type I jump without a downstream confinement. Taking guidance from the pioneering work of Tani (1949), Bohr *et al.* (1993) incorporated the hydrostatic pressure in the shallow-water equations, and, by averaging the axisymmetric Navier–Stokes equations in the vertical direction, they obtained an ordinary differential equation for the average velocity. They found that the average velocity can exhibit a singularity at some finite distance, indicating a potential separation. They argued that the jump location is close to the singularity point of their averaged equation, and deduced that the jump radius scales as $Q^{5/8} \nu_0^{-3/8} g^{-1/8}$, where Q is the flow rate, ν_0 is the kinematic viscosity and g is the acceleration due to gravity. The scaling constant depends on the velocity profile of choice. In their scaling law however, the radius of the jump depends only on the overall flow rate, not on the specific impinging velocity. The results of Bohr *et al.* (1993) predict well the trend from experiment but also shows some discrepancy quantitatively. In addition, their scaling cannot yield the shape of the jump. Later, Bohr *et al.* (1997) and Watanabe *et al.* (2003) adopted a non-self-similar velocity that allowed them to predict the shape of the jump. However, two experimental points are needed in their solution to fix the boundary conditions. Also, those two points must be close to the jump, otherwise would drive the solution to unstable states. Therefore, some prior knowledge of the jump location is required. More importantly, as the boundary-layer equations do not strictly hold across the jump, the validity of their solution is questionable. Kasimov (2008) modified the formulation of Bohr *et al.* (1993) by adding surface tension effect and incorporating a falling edge of the plate. However, no comparison against experiment was reported.

Gajjar & Smith (1983) showed the relevance of hydraulic jump to the hypersonic separation/free interaction problem and concluded that viscous-inviscid interaction is the cause of hydraulic jump. They also showed that it is only in a viscous sub-sublayer where the flow reacts to the reverse hydrostatic pressure gradient and separates. Bowles & Smith (1992) analyzed the hydraulic jump caused by a bump using the ‘viscous-inviscid interaction’ theory and achieved a good agreement with the measured jump profile of Craik *et al.* (1981). They showed that the hydraulic jumps are due to the flow separation caused by a viscous-inviscid interaction resulted from downstream conditions (at locally

large but globally small Froude number). They also proposed that the hydraulic jump is governed by surface tension and viscosity upstream, and viscosity and hydrostatic pressure gradient downstream. Higuera (1994) numerically solved the location and structure of the planar jump using boundary-layer approach. The boundary condition near the edge was fixed by matching the downstream flow with the flow that turns around the trailing edge under gravity. Later Higuera (1997) also extended his work to the circular case for the flow entering the jump for large values of Reynolds number and Froude number. The reader is also referred to the work of Scheichl (2018, 2019) for the case of a rotating disk using asymptotic and numerical analysis.

The recent measurements of Duchesne *et al.* (2014) indicate that, for a steady hydraulic jump, the flow in the subcritical region is essentially of the lubrication type. More importantly, they found a constant jump Froude number based on the jump height and the depth-averaged velocity downstream of the jump. The constancy reflects the independence of the flow rate and a weak dependence on other parameters. With this jump Froude number, they deduced that the location of the hydraulic jump can be fully determined using the lubrication flow from downstream given the liquid thickness near the plate's trailing edge. They also observed that the thickness near the trailing edge is almost constant with a weak dependence on the incoming flow rate. Therefore, its value can be taken from experiment for a given liquid. However, the mechanism behind the constant jump Froude number is unknown according to Duchesne *et al.* (2014). More recently, the measurements of Mohajer & Li (2015) indeed supported the claim of Duchesne *et al.* (2014), but they found that the jump Froude number is not independent of the surface tension. In the current thesis, the constancy of the jump Froude number will be justified in multiple ways for both low- and high-viscosity liquids.

Most of the hydraulic jumps considered in the literature are steady, and the current thesis will also focus on the steady hydraulic jump. Nevertheless, the hydraulic jump can become unstable as well. Craik *et al.* (1981) reported the instability of circular hydraulic jump and showed that the jump becomes unstable once the Reynolds number immediately upstream of the jump exceeds a critical value. A growth of the separation eddy downstream of the jump was also observed prior to the instability. Ellegaard *et al.*

(1998) observed that the axial symmetry breaks after the jump becomes unstable. Stable polygonal jumps may form after the instability occurs. Bush *et al.* (2006) confirmed the findings of Ellegaard *et al.* (1998) with experiment and highlighted the influence of surface tension in causing the polygonal hydraulic jump. Kasimov (2008) also studied the influence of surface tension on the stability of the hydraulic jump, and found that a steady jump may not exist at high surface tension. The polygonal regime was recently examined theoretically by Martens *et al.* (2012) and numerically by Rojas & Tirapegui (2015). Experimental work was also reported by Teymourtash & Mokhlesi (2015).

Numerical predictions on the formation of hydraulic jump were not so many in the literature. Ellegaard *et al.* (1996) studied the flow separation under the hydraulic jump. To circumvent the difficulties caused by the unknown free surface, they replaced the liquid-air interface by a fixed, but stress-free boundary at prescribed locations based on experiment. In other words, they imposed the free surface profile and only solved for the flow. As expected, the flow separation was captured behind the hydraulic jump due to the strong reverse pressure gradient. Passandideh-Fard *et al.* (2011) proposed a numerical approach to compute the hydraulic jump using the volume-of-fluid approach (Hirt & Nichols 1981). The location of the jump was accurately predicted. In their calculation domain however, the thickness near the trailing edge was artificially controlled. Passandideh-Fard *et al.* (2011) observed that, for high-viscosity liquids, the hydraulic jump is more stable and its location less sensitive to the subcritical thickness. Rojas *et al.* (2010, 2013, 2015) developed and implemented a spectral representation for the velocity profile in the vertical direction in their studies on the circular hydraulic jump. Both the location and the height of the jump were captured using their ‘inertia-lubrication theory’. The thickness of the liquid was imposed at the plate’s trailing edge based on experiment. In addition, two other parameters need to be artificially adjusted to match the experiments. Rohlfes *et al.* (2014) recently also investigated numerically the impinging jet flow. Their prediction of the shape of the free surface generally agrees with the prediction of Watson (1964). However, the hydraulic jump region is not included.

As discussed earlier, it is generally agreed that the cause of the circular hydraulic jump is largely due to gravity. However, Bhagat *et al.* (2018) very recently observed that a hydraulic jump still forms when a horizontal jet impacts a vertical wall. They have also

proposed a scaling law using a surface energy approach in an approximate manner. Based on their scaling analysis, Bhagat *et al.* (2018) concluded that for a circular hydraulic jump, surface tension is the only dominant effect and gravity plays almost no role. Their findings seem to overthrow most of the existing studies. However, due to the nature of their approximate method, their findings are not conclusive. More recently, Duchesne *et al.* (2019) also pointed out that the approach of Bhagat *et al.* (2018) was “wrong”. Instead of using the approximate surface energy approach, Duchesne *et al.* (2019) rigorously derived a corrected energy equation based on the Laplace pressure and the effect of surface curvature, which reflects the only effect of surface tension. They showed that their corrected formulation reduces significantly the influence of surface tension, invalidating the conclusion of Bhagat *et al.* (2018). More rigorous analysis on the issue of Bhagat *et al.* (2018) can be found in Scheichl (2018, 2019). This recent dispute will also be addressed in the current thesis.

1.3.2 The influence of a rotating surface on the impinging jet flow and hydraulic jump

The influence of a rotating surface on impinging jet flow has also been explored in the literature. Dorfman (1967) investigated the boundary layer flow on a rotating surface using a similarity transformation. However, the flow field is infinite, without a free surface (see also Schlichting & Gersten 2000). The early film thickness measurements of Charwat *et al.* (1972) for the flow on a rotating disk showed that the film thickness \hat{h} decays with rotation speed ω and radial distance \hat{r} like $\hat{h} \sim \hat{r}^{-1} \left(Qv_0 / \omega^2 \right)^{2/5}$. Charwat’s scaling law reflects the dominance of centrifugal effects over inertia to balance with the viscous effects. Rauscher *et al.* (1973) later proposed a similar scaling $\hat{h} \sim \hat{r}^{-2/3} \left(Qv_0 / \omega^2 \right)^{1/3}$ which also indicates a monotonic decay with radial distance. Miyasaka (1974) reported a maximum thickness at some location away from the impingement point, in contrast to the monotonic decay previously reported. The hydraulic jump was not involved in his work. Hung (1982) studied the impinging jet flow using an integral method. Both a radial and a tangential boundary layers are assumed. However, the physical origin of the tangential boundary layer development was not clear.

The hydraulic jump region was not included. Thomas *et al.* (1990) performed a numerical analysis on the axisymmetric film flow on a rotating surface and predicted a significant thinning of the film with increased speed of rotation. The radial velocity was assumed to be uniform across the thickness of the liquid. The hydraulic jump was found to disappear at a high rotating speed or in the absence of gravity.

Later, Thomas *et al.* (1991) conducted thickness measurements of a film emerging from a collar on a rotating disk and found that the jump location depends on the rotation speed and the flow rate. However, no quantitative information was given for the rotating hydraulic jump. In addition, a local maximum in the film thickness was also observed in their experiments. They found that the local maximum moves downstream with increasing inertia but upstream with increasing rotation speed. They also identified three distinct flow regions: an inner inertia-dominated region near the centre of the disk, a transition region where inertia and rotation are of the same strength, and an outer rotation-dominated region near the perimeter of the disk. Rahman & Faghri (1992) investigated numerically the thin-film flow over a rotating disk using the same flow configuration of Thomas *et al.* (1991). The computed film thickness agreed reasonably with the measurements of Thomas *et al.* (1991). They also concluded that the flow is dominated by inertia near the collar and by rotation near the trailing edge of the disk confirming the findings of Thomas *et al.* (1990). But the hydraulic jump was not investigated in their numerical domain. Zhao *et al.* (2000) numerically simulated the flow field on a rotating surface downstream of the hydraulic jump in their study on liquid metal atomization. A monotonic decrease of the film surface was observed. Convective terms were not included in the governing equations.

Ozar *et al.* (2003) examined experimentally again the radial spread of water emerging from a collar onto a rotating disk following the work of Thomas *et al.* (1991). They reported a similar behavior of the local maximum thickness as in the work of Thomas *et al.* (1991). Later, Rice *et al.* (2005) examined numerically the flow in a two-dimensional axisymmetric domain using the configuration of Ozar *et al.* (2003). The film thickness was determined using the volume-of-fluid method. Their results agreed reasonably with the measurements of Ozar *et al.* (2003). The formation of a hydraulic jump was not

included. An approximate approach for the emerging flow between a collar and rotating disk was also developed by Basu & Cetegen (2007) using a parabolic approximation for the velocity. The computed film thickness agreed with the numerical results of Rice *et al.* (2005). It should be noted that in most of these works, the thickness of the liquid is known at some upstream location since the flow is emitted from the gap between a collar and a rotating surface. Deng & Ouyang (2011) investigated the vibration of spinning disks and the powder formation in centrifugal atomization process. The information on hydraulic jump is not reported. Prieling & Steiner (2013) applied a transient integral approach in his study on axisymmetric flow over a rotating surface. Both an upstream maximum and a downstream waviness were observed. They also found that the difference between the steady and unsteady formulations is small. The results from their integral method generally agreed with the 2-D CFD model. Scheichl & Kluwick (2019) applied an asymptotic method to study the supercritical flow on a rotating disk with a large Reynolds number assumption. They captured a maximum film thickness that weakens with rotation, simultaneously with its location moving toward the center of the disk, confirming the findings of Thomas *et al.* (1991) and Ozar *et al.* (2003).

In the works of both Thomas *et al.* (1991) and Ozar *et al.* (2003), waviness of the free surface was observed. Indeed, Surface waves of axisymmetric and non-axisymmetric shapes can form depending on the flow rate and rotation speed indicating the instability of the axisymmetric flow. Charwat *et al.* (1972) found that the smooth axisymmetric flow exists within a regime defined by the flow rate, rotation speed and surface tension of the liquid. Outside this regime, surface waves can form in concentric, spiral or irregular shapes depending the flow parameters. A linear stability analysis of the film was also given and found to agree with his experiment. Sisoiev *et al.* (2003) developed a system of nonlinear evolution equations to model the axisymmetric capillary waves in rotating flow. Approximate solutions were presented and qualitative agreement with experiments was achieved with some quantitative discrepancies. Martar *et al.* (2005) numerically investigated the evolution equations for thin-film flow on a rotating surface. The formation of large finite-amplitude waves was observed and leads to deformations of the boundary layer. More aspects on the stability of rotating flow and wave formation can be

found in the work Sisoiev *et al.* (2010) and the references therein. The current thesis will focus only on the smooth axisymmetric regime.

1.3.3 Impinging jet heat transfer and its influence on the hydraulic jump

For the heat transfer problem associated with a spreading jet, most existing studies focused only on the influence of the flow on the heat transfer. Chaudhury (1964) adopted Watson's similarity approach for the impinging liquid jet on a heated wall. The temperature within the thermal boundary layer was approximated by a quartic profile. The convective heat transfer efficiency was found to exhibit a monotonic decrease with radial distance. As the stagnation zone was neglected, the solution is not valid near the impingement point. In fact, it leads to an infinite heat transfer rate (i.e. infinite Nusselt number). Chaudhury (1964) assumed that the fluid properties do not vary with temperature and there is no heat loss from the free surface due to the dominance of convection. These assumptions essentially lead to the independence of the Nusselt number of the temperature of the wall. Chaudhury's (1964) work and assumptions became the basis for many later studies. Brdlik & Savin (1965) solved the thermal field of a liquid jet impinging on a solid surface at constant temperature using the K-P integral approach. In their model, it was assumed that the thickness ratio of the thermal and the hydrodynamic boundary layers remains equal to $Pr^{-1/3}$ so that the momentum equation was conveniently eliminated. Saad *et al.* (1977) numerically investigated a submerged jet impinging on a surface at constant temperature using an upwind finite-difference scheme. It was found that for a parabolic inlet velocity profile, the maximum Nusselt number is larger and closer to the center of the jet compared to a flat velocity profile.

Wang *et al.* (1989a) considered the heat transfer in the stagnation zone and predicted a nearly constant Nusselt number. Later Wang *et al.* (1989b) also considered the heat transfer downstream of the stagnation region and extended their analysis to the case of distributed (varying with distance) wall temperature and heat flux condition using a series approach. Liu *et al.* (1993) numerically studied the effect of the surface tension on the stagnation heat transfer for inviscid liquids. They observed that at a very low flow rate, the inclusion of surface tension can slightly increase the Nusselt number. However, the

effect of surface tension is almost negligible for practical configurations. Gabour & Lienhard (1994) investigated experimentally the effect of surface roughness on the stagnation Nusselt number. The flow was found to be turbulent and the local Nusselt number could be increased by a maximum 50 percent compared to a smooth surface. Other studies on the stagnation zone heat transfer can be found in the review paper of Lienhard (2006).

Baonga *et al.* (2006) showed that a smaller nozzle-to-disk distance slightly lowers the Nusselt number. In contrast, Kuraan *et al.* (2017) observed that at very low nozzle-to-disk spacing, the heat transfer can be enhanced due to the increase in the entrance velocity. Rohlf's *et al.* (2014) numerically investigated the heat transfer of an impinging free-surface jet and found that a maximum Nusselt number can occur depending on the inlet velocity profile and the spacing between the nozzle the solid surface. Searle *et al.* (2017) studied impinging jet heat transfer of the axisymmetric flow over a slipping surface of constant temperature using a K-P approach. Their results suggested a drop in both the hydrodynamic and thermal boundary layers with increasing slip and temperature jump length. However, the effects of the temperature jump length was not conclusive since it was set equal to the slip length.

The heat transfer of the thin film flow on a rotating disk was also explored. The effects of rotation were investigated by Ozar *et al.* (2004) experimentally, by Hung (1982), Thomas *et al.* (1990), Shevchuk (2003) and Basu & Cetegen (2006, 2007) using K-P methods, and by Rahman & Faghri (1992) by numerical simulation. In those studies, both the flow rate and rotation were found to increase the local heat transfer rate. Those works considered only the heat transfer of the flow field and assumed no heat loss from the free surface. The evaporation and conjugate effects (i.e. the heat transfer in the solid) were considered numerically by Rice *et al.* (2005) who observed that the conjugate effect can make 10% to 15% difference on the Nusselt number compared to the non-conjugated cases.

For a large surface area or surface temperature, jet boiling may occur. In such cases, it is often necessary to deploy multiple jets to achieve the desired cooling performance. This

constitutes another hot area of research where most of the works are experimental and numerical due to the phase change in the physical domain. Such works can be found in the review papers of Ma *et al.* (1993), Lienhard (2006), and Molana & Banooni (2013). They are not detailed here as the focus of the current thesis is on the single jet impingement without boiling effects.

We emphasize that all the studies mentioned above assume constant fluid properties. Other theoretical and numerical works using such assumptions can also be found in the recent review paper of Jagtap *et al.* (2017). Nevertheless, it should be noted that even though the heat capacity and thermal conductivity do not change significantly with temperature for most liquids (Okhotin *et al.* 1992; Granato 2002), their viscosity decreases moderately or even significantly with temperature as a result of the decrease of the cohesive forces among liquid molecules (Kundu *et al.* 2016). For instance, water has a kinematic viscosity of 1.79 cSt at 0°C which drops to 0.29 cSt when the temperature rises to 100°C (Korson *et al.* 1969). The viscosity of other non-metallic liquids can have even larger variations of multiple orders of magnitude (Seeton 2006). It is therefore important to consider the dependence of viscosity on temperature, and consequently the influence of heat transfer on the flow. However, this two-way coupling consideration has largely been ignored in the existing theoretical and even in numerical works for jet impingement heat transfer problem.

Currently the only known theoretical contribution to the two-way coupling for an impinging jet was carried out by Liu & Lienhard (1989). They adopted a K-P approach to solve the energy equation and obtained the thermal boundary layer thickness based on the established velocity and viscous boundary layer thickness. In their problem, the solid surface is heated by a uniform heat flux, and the Prandtl number is greater than unity. To account for the change of viscosity with temperature, they implemented a numerical iterative algorithm to solve the coupled problem. The viscosity was evaluated based on the locally averaged temperature. Later Liu *et al.* (1991) also extended their work to the regime where Prandtl number is smaller than unity. We note that the influence of heat transfer on the hydraulic jump region was not included in the work of Liu & Lienhard (1989) and Liu *et al.* (1991). In this regard, Sung *et al.* (1999), adopting a finite-element

implementation, solved the coupled problem and investigated the influence of heat transfer on the location and height of the hydraulic jump. The thickness of the liquid at the trailing edge was imposed with an empirical formula. The location of the hydraulic jump was found to move downstream with increasing wall temperature and heat flux. In addition, a sharp drop in the Nusselt number was reported in the hydraulic jump region. In the current thesis, a simple and efficient two-coupling method will be developed, allowing us to investigate the influence of heat transfer on the hydrodynamics of the spreading jet and the circular hydraulic jump.

1.4 The objectives and the thesis outline

1.4.1 The research gap

First, as already discussed, the momentum and force balance approach across the jump requires the knowledge of the depth of the jump immediately after the jump. Previously it was usually taken from experimental measurements. Therefore a coherent theoretical model for the prediction of the jump without empirical input is still missing. In addition, the theoretical mechanism behind the constant jump Froude number (Duchesne *et al.* 2014) is still not reported yet.

Furthermore, the influence of surface rotation on a free impinging jet and hydraulic jump has rarely been reported even though there are works on the flow emerging from the slot between a collar and a rotational disk (Thomas *et al.* 1991; Ozar *et al.* 2003; Rice *et al.* 2005).

Recalling that the viscous force is neglected in momentum and force balance relation, one would anticipate that the accuracy of this method will drop if the width of the jump is not small. In other words, the viscous force at the bottom of the jump cannot be neglected if the jump is not steep. Indeed, the steep jump only occurs for low-viscosity liquid like water. For a high-viscosity liquid, the location of the jump is not always identifiable. The numerical simulation of Rojas *et al.* (2010) indeed depicts the ambiguity in the jump location. Their numerical film profiles illustrate how the abrupt jump ceases to exist with increasing viscosity, giving way to a smoother jump over a relatively large distance. It should also be noted that gravity is neglected before the jump in Watson's (1964) method

and all the works following him. For a liquid with high viscosity however, gravity should not be omitted since the strong viscous effect often causes a large increase in the supercritical thickness, which in fact causes the smooth jump. Consequently, there should be a separate method specifically for high-viscosity liquids. But no such attempts have been made in the literature.

For impinging jet heat transfer problem, extensive studies exist in literature. However, there is a lack in the consideration of the temperature-dependent viscosity as discussed. In the only couple of works where the two-way is considered, numerical iterations are unavoidable. In this case, the influence of the heat transfer on the hydraulic jump and the subcritical flow and thermal field are still missing theoretically.

1.4.2 The objectives of the thesis

The first objective of the thesis is to establish a theoretical model to determine the location of the jump without measuring the height of the jump. Consequently, the mechanism behind the constancy of the jump Froude number can also be justified. In addition, the influence of surface rotation on the flow and the hydraulic jump will also be investigated.

A separated model for high-viscosity jump will be designed separately. And, since Bhagat *et al.* (2018) argued that surface tension is the dominant effect on formation of the circular hydraulic jump and gravity plays almost no role regardless of viscosity, it is desirable to isolate the effect of gravity (neglecting surface tension) to either validate or invalidate their arguments.

For the thermal coupling problem, a simple iteration-free model will be developed to account for the temperature-dependent viscosity. Consequently, the influence of heat transfer on the flow and hydraulic jump will be quantified.

1.4.3 Thesis outline

In Chapter, to locate the hydraulic jump without empirical parameters, a theoretical model will be designed by directly connecting the inertia-dominated supercritical flow and the lubrication-type subcritical flow through a shock using the relation between the

momentum and pressure force. The mechanism behind the constancy of the jump Froude number will be investigated. The effects of rotation of the impingement surface will be also pursued. In Chapter 3, a specific model for high-viscosity hydraulic jump will be presented. We shall isolate the effects of gravity by neglecting surface tension so as to either validate or invalidate the recent arguments of Bhagat *et al.* (2018). In Chapter 4, a simple iteration-free model will be developed and tested. The influence of heating on the flow and hydraulic jump will be comprehensively explored. In Chapter 5, the overall concluding remarks and suggestions for future works will be given.

1.5 References

Azuma, T. & Hoshino, T. 1984a The radial flow of a thin liquid film: 2nd report, liquid film thickness. *Bulletin of JSME* **27**, 2747-2754.

Azuma, T. & Hoshino, T. 1984b The radial flow of a thin liquid film: 3rd report, velocity profile. *Bulletin of JSME* **27**, 2755-2762.

Baonga, J. B., Gualous, H. L. & Imbert, M. 2006 Experimental study of hydrodynamic and heat transfer of free liquid jet impinging a flat circular heated disk. *Appl. Therm. Engng* **26**, 1125–1138.

Bhagat, R. K., Jha, N. K., Linden, P. F. & Wilson, D. I. 2018 On the origin of the circular hydraulic jump in a thin liquid film. *J. Fluid Mech.* **851**, R5 1-11.

Bhunja, A., Chandrasekaran, S. & Chen, C. L. 2007 Performance improvement of a power conversion module by liquid micro-jet impingement cooling. *IEEE Trans. Components Packag. Technol.* **30**, 309-316.

Basu, S. & Cetegen, B. M. 2006 Analysis of hydrodynamics and heat transfer in a thin liquid film flow flowing over a rotating disk by the integral method. *Trans. ASME J. Heat Transfer* **128** (3), 217–225.

Basu, S. & Cetegen, B. M. 2007 Effect of hydraulic jump on hydrodynamics and heat transfer in a thin liquid film flowing over a rotating disk analyzed by integral method. *Trans. ASME J. Heat Transfer* **129**, 657–663.

Bohr, T., Dimon, P. & Putzkaradze, V. 1993 Shallow-water approach to the circular hydraulic jump. *J. Fluid Mech.* **254**, 635-648.

Bohr, T., Putkaradze, V. & Watanabe, S. 1997 Averaging theory for the structure of hydraulic jumps and separation in laminar free-surface flows. *Phys. Rev. Lett.* **79**, 1038-1041.

Bowles, R. I. & Smith, F. T. 1992 The standing hydraulic jump: theory, computations and comparisons with experiments. *J. Fluid Mech.* **242**, 145–168.

Brdlik, P. M. & Savin, V. K. 1965 Heat transfer between an axisymmetric jet and a plate normal to the flow. *J. Engng Phys.* **8**, 91-98.

Brechet, Y. & Neda, Z. 1999 On the circular hydraulic jump. *Am. J. Phys.* **67**, 723–731.

Bush, J. W. M. & Aristoff, J. M. 2003 The influence of surface tension on the circular hydraulic jump. *J. Fluid Mech.* **489**, 229-238.

Bush, J.W.M., Aristoff, J.M., & Hosoi, A.E. 2006. An experimental investigation of the stability of the circular hydraulic jump. *J. Fluid Mech.* **558**, 33-52.

Charwat, A., Kelly, R. & Gazley, C. 1972 The flow and stability of thin liquid films on a rotating disk. *J. Fluid Mech.* **53**, 227–255.

Chaudhury, Z. H. 1964 Heat transfer in a radial liquid jet. *J. Fluid Mech.* **20**, 501-511.

Craik, A., Latham, R., Fawkes, M. & Gibbon, P. 1981 The circular hydraulic jump. *J. Fluid Mech.* **112**, 347-362.

Crowe, C. T. 2009 *Engineering Fluid Mechanics*, 9th edn. Wiley.

DBMR 2019 Fuel Additives and Lubricants Market 2026 | Analysis by Chevron Corporation, Exxon Mobil Corporation, The Lubrizol Corporation, Afton Chemical, Fuel Performance Solutions, Evonik Industries AG, BASF SE, LANXESS <https://stocknewsmagazine.com/fuel-additives-lubricants-market-2026-analysis-chevron-corporation-exxon-mobil-corporation-lubrizol-corporation-afton-chemical-fuel-performance-solutions-evonik-industries-ag-basf-s/>

- Dorfman, L. A. 1967 Flow and heat transfer in a viscous layer on a spinning disc. *J. Engng Phys.* **12** (3), 309–316.
- Dressaire, E., Courbin, L., Crest, J. & Stone H. A. 2010 Inertia dominated thin-film flows over microdecorated surfaces. *Phys. Fluids* **22**, 073602-07
- Duchesne, A., Lebon, L. & Limat, L. 2014 Constant Froude number in a circular hydraulic jump and its implication on the jump radius selection. *Europhys. Lett.* **107**, 54002.
- Duchesne, A., Anderson, A. & Bohr, T. 2019 Surface tension and the origin of the circular hydraulic jump in a thin liquid film. arXiv:1903.11495
- Ellegaard, C., Hansen, A., Haaning, A., Hansen, K. & Bohr, T. 1996 Experimental results on flow separation and transitions in the circular hydraulic jump. *Phys. Scr.* **T67**, 105–110.
- Ellegaard, C, Hansen, A.E., Haaning, A., Marcussen, A., Bohr, T., Hansen, J.L. & Watanabe, S. 1998 Creating corners in kitchen sink flows. *Nature* **392**, 767-768.
- Errico, M. 1986 A study of the interaction of liquid jets with solid surfaces. PhD thesis, University of California, San Diego.
- Gabour, L. A. & Lienhard, J. 1994 Wall roughness effects on stagnation-point heat transfer beneath an impinging liquid jet. *ASME J. Heat Transfer* **116**, 81–87.
- Gajjar, J. S. B. & Smith, F. T. 1983 On hypersonic self-induced separation, hydraulic jumps and boundary layers with algebraic growth. *Mathematika* **30**, 77-91.
- Granato, A. V. 2002 The specific heat of simple liquids. *J. Non-Cryst. Solids* **307–310**, 376-386.
- Higuera, F. J. 1994 The hydraulic jump in a viscous laminar flow. *J. Fluid Mech.* **274**, 69–92.
- Higuera, F. J. 1997 The circular hydraulic jump. *Phys. Fluids* **9** (5), 1476–1478; Brief communications.

Hirt, C. W. & Nichols, B. D. 1981 Volume of Fluid (VOF) Method for the Dynamics of Free Boundaries. *J. Comput. Phys.* **39**, 201–225.

Hsu, T. T., Walker, T. W., Frank, C. W. & Fuller, G. G. 2011 Role of fluid elasticity on the dynamics of rinsing flow by an impinging jet. *Phys. Fluids* **23**, 033101.

Hung, Y. T. 1982 A numerical analysis of jet impingement cooling of a rotating disk. M.S. Thesis, Texas Tech University, Lubbock, TX.

Jagtap, K. C., Kale, N. B., Kale, V. V., Pawar, K. S. & Deshmukh, S. A. 2017 Heat transfer enhancement through liquid jet impingement. *IRJET.* **4**, 1365-1369.

Jannes, G., Piquet, R., Maissa, P., Mathis, C. & Rousseaux, G. 2011 Experimental demonstration of the supersonic–subsonic bifurcation in the circular jump: a hydrodynamic white hole. *Phys. Rev. E* **83**, 056312.

Kármán, T. V. 1921 Uber laminare und turbulente Reibung, *Z. angew. Math. Mech.* **1**, 233-252; translated as On laminar and turbulent friction, *Nut, Adv. Comm. Aero., Wash., Tech. Mem.* no. 1092, 1946.

Kate, R. P., Das, P. K. & Chakraborty, S. 2007 Hydraulic jumps due to oblique impingement of circular liquid jets on a flat horizontal surface. *J. Fluid Mech.* **573**, 247–263.

Kasimov, A. R. 2008 A stationary circular hydraulic jump, the limits of its existence and its gasdynamic analogue. *J. Fluid Mech.* **601**, 189–198.

Khayat, R. E. 2016 Impinging planar jet flow and hydraulic jump on a horizontal surface with slip. *J. Fluid Mech.* **808**, 258-289.

Korson, L., Dorst-Hansen, W. & Millero, F. J. 1969 Viscosity of Water at Various Temperatures. *J. Phys. Chem.* **73**, 34-39.

Kundu, P.K., Cohen, I.M. & Bowling, D.R. 2016 Fluid Mechanics. 6th edn. Elsevier.

Kuraan, A. M., Moldovan, S. I. & Choo, K. 2017 Heat transfer and hydrodynamics of free water jet impingement at low nozzle-to-plate spacings, *Int. J. Heat Mass Transfer.* **108**, 2211–2216.

Lienhard, J. 2006 Heat transfer by impingement of circular free-surface liquid jets. *18th National & 7th ISHMT-ASME Heat and Mass Transfer Conference* (IIT Guwahati, India) 1-17.

Linz 2011 Siemens to modernize process control system in Wuhan Iron & Steel's hot rolling mill
https://www.siemens.com/press/en/pressrelease/?press=/en/pressrelease/2011/industry_solutions/iis201103939.htm

Liu, X. & Lienhard, J. 1989 Liquid jet impingement heat transfer on a uniform flux surface. *ASME Heat Transfer Phenomena in Radiation, Combustion, and Fires* **106**, 523-530.

Liu, X., Lienhard V. & Lombara, J. S. 1991 Convective heat transfer by impingement of circular liquid jets. *ASME J. Heat Transfer* **113**, 517-582.

Liu, X. & Lienhard, J. 1993 The hydraulic jump in circular jet impingement and in other thin liquid films. *Experiments in Fluids* **15**, 108-116.

Liu, X., Gabour, L. A. & Lienhard, J. 1993 Stagnation-point heat transfer during impingement of laminar liquid jets: analysis Including surface tension. *ASME J. Heat Transfer* **115**, 99-105.

Ma, C. F., Gan, Y. P., Tian, Y. C., Lei, D. H. & Gomi, T. 1993 Liquid jet impingement heat transfer with or without boiling. *J. Thermal Sci.* **2**, 32-49.

Martens, E. A., Watanabe, S. & Bohr, T. 2012 Model for polygonal hydraulic jumps. *Phys. Rev. E* **85**, 036316.

Melaniff 2003 Secrets of Dodge's new mini-muscle turbo car
http://www.melaniff.com/srt-4/hot%20rod/hot_rod_2003_09.htm

Miyasaka Y. 1974 On the flow of a viscous free boundary jet on a rotating disk. *Bull J. Soc. Mech. Eng.* **17**, 1469-1475.

Mohajer, B. & Li, R. 2015 Circular hydraulic jump on finite surfaces with capillary limit. *Phys. Fluids* **27**, 117102.

Molana, M. & Banooni, S. 2013 Investigation of heat transfer processes involved liquid impingement jets: a review. *Braz. J. Chem. Eng.* **30**, 413-435.

Okhotin, A. S., Zhmakin, L. I. & Ivanyuk, A. P. 1992 Universal temperature dependence of the thermal conductivity and viscosity coefficients. *Int. J. Heat Mass Transfer* **35**, 3059-3067.

Olsson, R. G. & Turkdogan, E. T. 1966 Radial spread of a liquid stream on a horizontal plate. *Nature* **211**, 813-816.

- Ozar, B., Cetegen, B. M. & Faghri, A. 2003 Experiments on the flow of a thin liquid film over a horizontal stationary and rotating disk surface. *Experiments in Fluids* **34**, 556–565.
- Ozar, B., Cetegen, B. M. & Faghri, A. 2004 Experiments on heat transfer in a thin liquid film flowing over a rotating disk. *Trans. ASME J. Heat Transfer* **126**, 184–192.
- Passandideh-Fard, M., Teymourtash, A. R. & Khavari, M. 2011 Numerical study of circular hydraulic jump using volume-of-fluid method. *J. Fluids Eng.* **133**, 011401.
- Prieling, D. & Steiner, H. 2013 Unsteady thin film flow on spinning disks at large Ekman numbers using an integral boundary layer method. *Intl J. Heat Mass Transfer* **65**, 10–22.
- Pohlhausen, K. 1921 Zur näherungsweise Integration der Differentialgleichung der laminaren Grenzschicht. *Z. Angew. Math. Mech.* **1**, 252–268.
- Prandtl, L. 1904 Motion of fluid with very little viscosity. English Translation: N.A.S.A. TM 452. 1928.
- Prince, J. F., Maynes, D. & Crockett, J. 2012 Analysis of laminar jet impingement and hydraulic jump on a horizontal surface with slip. *Phys. Fluids* **24**, 102103.
- Prince, J. F., Maynes, D. & Crockett, J. 2014 Jet impingement and the hydraulic jump on horizontal surfaces with anisotropic slip. *Phys. Fluids* **26**, 042104.
- Rahman M. & Faghri A. 1992 Numerical simulation of fluid flow and heat transfer in a thin liquid film over a rotating disk. *Int. J. Heat Mass transfer* **35**, 1441–1453.
- Rauscher, J., Kelly, R. & Cole, J. 1973 An asymptotic solution for the laminar flow of a thin film on a rotating disk. *J. Applied Mech.* **40**, 43–47.
- Reay, D. 2013 *Process Intensification*, 2nd, edn. Elsevier.
- Rice, J., Faghri, A. & Cetegen, B. 2005 Analysis of a free surface film from a controlled liquid impinging jet over a rotating disk including conjugate effects, with and without evaporation. *Int. J. Heat Mass Transfer* **48**, 5192–5204.
- Rohlf, W., Ehrenpreis, C., Haustein, H. D. & Kneer, R. 2014b Influence of viscous flow relaxation time on self-similarity in free-surface jet impingement. *Int. J. Heat Mass Transfer*. **78**, 435-446.

Rojas, N., Argentina, M. & Tirapegui, E. 2010 Inertial lubrication theory. *Phys. Rev. Letts.* **104**, 187801-4

Rojas, N., Argentina, M. & Tirapegui, E. 2013 A progressive correction to the circular hydraulic jump scaling. *Phys. Fluids* **25**, 042105-9

Rojas, N. & Tirapegui, E. 2015 Harmonic solutions for polygonal hydraulic jumps in thin fluid films. *J. Fluid Mech.* **780**, 99-119.

Saad, N. R., Douglas, W. J. M. & Mujumdar, A. S. 1977 Prediction of heat transfer under an axisymmetric laminar impinging jet. *Ind. Eng. Chem., Fundam.* **16**, 148–154.

Scheichl, B. “Centred splash of a vertical jet on a horizontal rotating disc: the thin radial film in the parabolic and weakly elliptic limit”; accepted as talk for: BAIL 2018 - International Conference on Boundary and Interior Layers, University of Strathclyde, Glasgow, UK; 2018-06-18 - 2018-06-22; in: "Boundary and Interior Layers, Computational and Asymptotic Methods - BAIL 2018", G. Barrenechea et al. (ed.); Springer, Lecture Notes in Computational Science and Engineering / ?? / Berlin, Heidelberg (2019), ISSN: 1439-7358.

Scheichl, B. & Kluwick, A. 2019 Laminar spread of a circular liquid jet impinging axially on a rotating disc. *J. Fluid Mech.* **864**, 449-489.

Schlichting, H. & Gersten, K. 2000 *Boundary-layer theory* (Springer, Berlin).

Searle, M., Maynes, D. & Crockett, J. 2017 Thermal transport due to liquid jet impingement on super hydrophobic surfaces with isotropic slip. *Int. J. Heat Mass Transfer* **110**, 680–691.

Seeton, C. J. 2006 Viscosity–temperature correlation for liquids. *Tribol Lett.* **22**, 67-78.

Shevchuk, I. V. 2003 Impingement heat transfer over a rotating disk: integral Method. *J. Thermalphysics* **17**, 291-293.

Sisoev, G. M., Matar, O. K. & Lawrence, C. J. 2003 Axisymmetric wave regimes in viscous liquid film flow over a spinning disk. *J. Fluid Mech.* **495**, 385-411.

Sisoev, G. M., Goldgof, D. B. & Korzhova, V. N. 2010 Stationary spiral waves in film flow over a spinning disk. *Phys. Fluids.* **22**, 052106-6.

- Sobey, I. J. 2000 *Introduction to interactive boundary-layer theory*. (Oxford University Press, Oxford).
- Stevens, J. & Webb, B. W. 1992 Measurements of the free surface flow structure under an impinging free liquid jet. *Trans. ASME J. Heat Transfer* **114**, 79–83.
- Sung, J., Choi, H. G. & Yoo, J. Y. 1999 Finite element simulation of thin liquid film flow and heat transfer including a hydraulic jump. *Int. J. Numer. Methods Eng.* **46**, 83-101.
- Tani, I. 1949 Water jump in the boundary layer. *J. Phys. Soc. Japan* **4**, 212–215.
- Teymourash, A. R. & Mokhlesi, M. 2015 Experimental investigation of stationary and rotational structures in non-circular hydraulic jumps. **762**, 344-360.
- Thomas, S., Faghri, A. & Hankey, W. 1991 Experimental analysis and flow visualization of a thin liquid film on a stationary and rotating disk. *J. Fluids Eng.* **113**, 73–80.
- Thomas, S., Hankey, W., Faghri, A. & Swanson T. 1990 One-dimensional analysis of the hydrodynamic and thermal characteristics of thin film flows including hydraulic jump and rotation. *J. Heat Transfer* **112**, 728–735.
- Van Dyke, M. D. 1964 *Perturbation methods in fluid mechanics* (Academic Press, New York).
- Vasista, V. 1989 Experimental study of the hydrodynamics of an impinging liquid jet. B. Eng. thesis, MIT.
- Walker, T. W., Hsu, T. T., Frank, C. W. & Fuller, G. G. 2012 Role of shear-thinning on the dynamics of rinsing flow by an impinging jet. *Phys. Fluids* **24**, 093102.
- Wang, X. S., Dagan, Z. & Jiji, L. M. 1989a Heat transfer between a circular free impinging jet and a solid surface with nonuniform wall temperature or wall heat flux—1. solution for the stagnation region. *Int. J. Heat Mass Transfer* **32**, 1351-1360.
- Wang, X. S., Dagan, Z. & Jiji, L. M. 1989b Heat transfer between a circular free impinging jet and a solid surface with nonuniform wall temperature or wall heat flux—2. solution for the boundary layer region. *Int. J. Heat Mass Transfer* **32**, 1361-1371.

Watanabe, S., Putkaradze, V. & Bohr, T. 2003 Integral methods for shallow free-surface flows with separation. *J. Fluid Mech.* **480**, 233–265.

Watson, E. 1964 The spread of a liquid jet over a horizontal plane. *J. Fluid Mech.* **20**, 481-499.

Zhao, Y. Y., Dowson, A. L. & Jacobs, M. H. 2000 Modelling of liquid flow after a hydraulic jump on a rotating disk prior to centrifugal atomization. *Modelling Simul. Mater. Sci. Eng.* **8**, 55-65.

Zhao, J. & Khayat, R.E. 2008 Spread of a non-Newtonian liquid jet over a horizontal plate. *J. Fluid Mech.* **613**, 411-443.

Chapter 2

2 Impinging jet flow and hydraulic jump on a stationary and a rotating disk

The impinging jet flow and hydraulic jump on both a stationary and a rotational surface will be treated in this chapter. The problem is formulated with the inclusion of a rotation parameter Ω . The stationary case is obtained by setting $\Omega = 0$.

2.1 Introduction

When a circular liquid jet impacts a solid surface, the fluid is expelled radially as a thin film until reaching a critical location where the layer depth increases abruptly, and a hydraulic jump occurs. The regions before and after the jump are known as the supercritical and subcritical regions respectively. The impinging jet flow on solid surface is important in numerous industrial applications such as the jet cooling, jet rinsing, spinning disk reactor, spray and atomization and powder production (Lawley 1992; Uma & Usha 2009; Mohajer & Li 2015). The hydraulic jump can significantly influence the performance of such processes. The impingement surface can either be stationary or rotational depending on the application.

For stationary disk, Watson (1964) developed an appropriate description of supercritical flow using boundary layer approach and a similarity transformation. The location of the jump was determined by a force and momentum balance method. Watson's (1964) theory was tested in a number of experimental investigations, including those of Watson himself, Craik *et al.* (1981), Stevens & Webb (1992). Liu & Lienhard (1993) observed that Watson's predictions are least satisfactory for small jump radius for which surface tension is important. In this regard, Bush & Aristoff (2003) included the influence of surface tension for small circular jump radius, leading to better predictions. It is generally agreed that Watson's theory is adequate for a circular jump with relatively large radius and height.

The influence of slip was examined by Prince *et al.* (2012) and Khayat (2016) and found to push the jump downstream. Watson's theory was also extended to non-Newtonian jet by Zhao & Khayat (2008) who found that only the overall viscosity influences the location of the jump. The liquid height downstream of the jump were artificially prescribed in these studies. In experiments, the downstream depth can be controlled by a downstream barrier. Passandideh-Fard *et al.* (2011) proposed a numerical approach to determine the hydraulic jump location using volume-of-fluid approach (Hirt & Nichols 1981). The hydraulic jump was successfully captured. However, the downstream depth must be imposed at the disk edge.

Bohr *et al.* (1993) deduced that the jump radius scales as $Q^{5/8}v_0^{-3/8}g^{-1/8}$ based on the critical point of the averaged shallow-water equations. However, their scaling only depends on the overall flow rate and cannot predict the shape of the jump. Later, Bohr *et al.* (1997) and Watanabe *et al.* (2003) obtained a solution that can resolve the shape of the jump using a non-self-similar velocity, but two experimental points were needed in their solution to fix the boundary conditions. Kasimov (2008) modified the formulation of Bohr *et al.* (1993) by incorporating a falling edge of the plate but no comparison was attempted against experiments.

The recent measurements of Duchesne *et al.* (2014) showed that the subcritical flow is essentially of lubrication character. In addition, they observed that, for a stationary disk, the jump Froude number, based on the jump height and velocity, remains constant with varying flow rates. The constant jump Froude number together with the lubrication equation should in principle provide the desired relation for problem completion but the theoretical mechanism behind this constancy is unclear according to Duchesne *et al.* (2014).

Regarding the influence of rotation, the film thickness was the main focus in experiments using mechanical, optical or electrical techniques. The early film thickness measurements of Charwat *et al.* (1972) suggested that the film thickness \hat{h} decays with rotation speed ω and radial distance \hat{r} like $\hat{h} \sim \hat{r}^{-1} \left(Qv_0 / \omega^2 \right)^{2/5}$. In fact, when rotation is dominant

over inertia, the balance between the centrifugal and viscous terms in the radial momentum equation yields $\hat{h} \sim \hat{r}^{-2/3} \left(Qv_0 / \omega^2 \right)^{1/3}$, which also corresponds to the asymptotic form obtained by Rauscher *et al.* (1973). However, these scaling relations indicate only the strong rotational case. Miyasaka (1974) reported a maximum thickness at some location away from the impingement point, in contrast to the monotonic decrease reported before. Good agreements were achieved with experiments. However, the focus was only on the neighbourhood of the impingement region without the consideration of hydraulic jump.

Thomas and coworkers (1990, 1991) conducted both theoretical analysis and experiments on the radial flow emerging from a collar on a rotating disk. A local maximum in the film thickness was also observed. They identified three distinct flow regions: an inner inertia-dominated region near the centre of the disk, a transition region where the maximum appears, and an outer rotation-dominated region. They found that hydraulic jump can appear at very low rotation speed, however quantitative information was not given. Rahman & Faghri (1992) investigated numerically the same problem. The computed film thickness agreed qualitatively with the measurements of Thomas *et al.* (1991). More recently, Burns *et al.* (2003) found similar results to those of Thomas *et al.* (1991). We shall assess these observations against our own findings in the current study.

Ozar *et al.* (2003) also examined experimentally the emerging flow from the gap between a collar and a rotating disk. They provided detailed descriptions on the behavior of the maximum thickness. They observed that the strength of the maximum thickness weakens with both rotation and inertia. On the other hand, its location moves upstream with increasing rotation speed but travels downstream with increasing inertia. Later, Rice *et al.* (2005) examined numerically the same problem using the volume-of-fluid method and achieved a reasonable agreement with Ozar *et al.* (2003) at low rotation speed range. They did not consider the formation of a hydraulic jump.

Both Thomas *et al.* (1991) and Ozar *et al.* (2003) observed strong surface waves at high rotation speeds, indicating the instability of the flow. Analyses on the rotating film stability can be found in the studies of Charwat *et al.* (1972), Sisoiev *et al.* (2003), Matar

et al. (2004) and Sisoev *et al.* (2010). The current work focuses on the smooth axisymmetric flow regime. More discussions on the flow instability and wave formation will be given in Section 2.2.

As discussed, most existing works for the rotational case are on the emerging flow between a collar and a rotating surface, in contrast to the present impinging jet problem. In addition, little is reported on the quantitative information of hydraulic jump. Therefore, it is important to examine how the impinging jet flow would behave in the presence of rotation. Moreover, a coherent theoretical model for the hydraulic jump is still lacking even in the stationary case since most of the existing models require experimental input. In this case, we shall directly connect the supercritical flow and the lubrication flow through a shock to locate the jump. Consequently, we can predict the height of the jump instead of imposing experimental values, and, provide a theoretical justification for the constancy of the jump Froude number (Duchesne *et al.* 2014).

The current problem is formulated with the inclusion of a rotation parameter Ω and the stationary case is obtained by setting $\Omega = 0$. Since axisymmetric flow is examined, the surface-tension effect will be included when calculating the hydraulic jump. In Section 2.2, we outline the problem formulation by giving the governing equations and boundary conditions in each region. The overall solution strategy is also discussed. In Section 2.3, the Kármán–Pohlhausen (K–P) approach is adopted to determine the boundary-layer structure and the film thickness upstream of the jump. The transition point is also located. In Section 2.4, the K–P approach is employed again to examine the fully-viscous region and assess the influence of rotation on the thin-film flow. In Section 2.5, the location of the hydraulic jump is determined by a momentum balance across the jump, and the effect of rotation on the jump is analyzed. The liquid thickness near the edge of the disk is established for a stationary disk to calculate the downstream flow and then extended to a rotating disk. Finally, concluding remarks are given in Section 2.6.

2.2 Physical domain and problem statement

Consider the steady laminar incompressible flow of a circular axisymmetric jet of a Newtonian fluid of radius a , impinging at a volume flow rate Q on a flat disk lying

normal to the jet direction and rotating at an angular velocity ω . The flow configuration is depicted schematically in Figure 2-1, where dimensionless variables and parameters are used. The problem is formulated in the (r, θ, z) fixed coordinates, with the origin coinciding with the disk centre. In this case $u(r, z)$, $v(r, z)$ and $w(r, z)$ are the corresponding dimensionless velocity components in the radial, azimuthal and vertical directions, respectively. The r -axis is taken along the disk radius and the z -axis is taken parallel to the jet. Since the flow is assumed to be axisymmetric, there is no dependence on the azimuthal angle θ . The length and velocity scales are conveniently taken to be a and $Q/\pi a^2$ in the radial, azimuthal and vertical directions. A more suitable scaling is used in the appendix where the thin-film problem is formulated. Since the pressure is expected to be predominantly hydrostatic for a thin film, it will be scaled by $\rho g a$. Four dimensionless groups emerge in this case: the Reynolds number $Re = Q/\pi a \nu_0$, where ν_0 is the kinematic viscosity, the rotation parameter, $\Omega = \pi a^3 \omega / Q$, the Froude number, $Fr = Q/\pi \sqrt{a^5 g}$, g being the acceleration due to gravity, and the Bond number, $Bo = \rho g a^2 / \gamma_0$, ρ being the density and γ_0 being surface tension. We note that Ω^{-1} may be introduced as the Rossby number. A Gravity number: $G \equiv Re/Fr^2$ is useful to introduce, which reflects the effect of gravity relative to inertia and viscous effect.

In this study, the flow is assumed to remain steady and axisymmetric. Therefore, surface waves that may be present on the liquid film under some conditions are not accounted for. When the flow rate or rotation speed is relatively small, or the apparent surface tension of a liquid is below a critical value, the flow is smooth and axisymmetric without any sign of wave (Charwat *et al.* 1972). Otherwise, surface waves of axisymmetric and non-axisymmetric shapes can be present, depending on flow rate and rotation speed. Charwat *et al.* (1972) carried out experimental measurements and linear stability analysis for a thin film formed on a rotating disk. Smooth flow was found to occur in a region defined by the flow rate, rotational speed and physical properties of the liquid. Outside this region various wave patterns were observed: concentric, spiral and irregular waves. In their experiments with water and glycerine solution, Butuzov & Pukhovi (1976)

observed that a laminar film with no signs of wave formation is possible over the entire disk for angular velocities below 400 rpm and low flow rates. The second situation corresponds to a flow with low surface tension. In their experiment, Charwat *et al.* (1972) observed that for a fluid with surface tension coefficient less than approximately 57 mN/m, the film becomes absolutely stable, with no waves of any kind observed throughout the entire range of flow rates and rotational speeds covered. Figure 2-2 depicts the marginal stability curves, reproduced from Charwat *et al.* (1972) in the (Re, Ω) plane for three liquids: methyl alcohol, iso-propyl alcohol and water with a wetting agent. The region of stable axisymmetric flow lies below each curve while the region for the onset of spiral waves lies above. Clearly, axisymmetric flow is predicted over a wide range of Reynolds number and rotation speed. This range widens for liquids with lesser surface tension, which seem to exhibit wavy flow only if Re is of order 10^3 . The current calculations for the flow over a rotating disk are essentially limited to $Re < 500$ and $\Omega \ll 1$ (see figures 2-9 to 2-11), which ensures the validity of the assumption of flow axisymmetry.

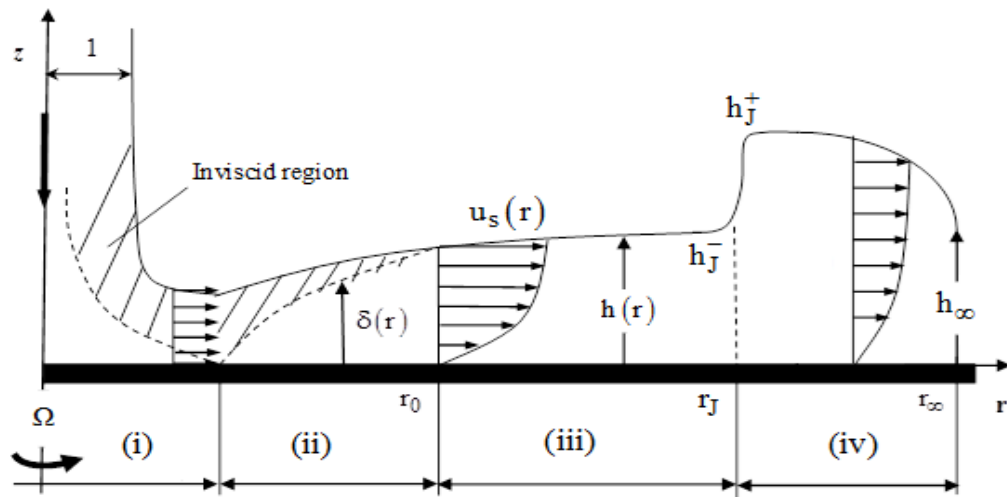


Figure 2-1: Schematic illustration of the axisymmetric jet flow impinging on a flat rotating disk. Illustrated are the stagnation region (i), the developing boundary-layer region (ii), the fully viscous region (iii) and the hydraulic jump region (iv). All notations are dimensionless.

2.2.1 The physical domain

Following the treatment of Watson (1964) of the flow over a flat plate, we identify four distinct flow regions for the jet over a rotating disk, with smooth passage from one region to the next (see Figure 2-1): a stagnation flow region (i), a developing boundary-layer region (ii), where the boundary layer grows until it reaches the film surface at $r = r_0$, and a fully viscous thin-film region (iii). Under some flow conditions, a hydraulic jump may form in region (iv), starting at $r = r_J$. In the vicinity of the stagnation point, in region (i), $r = O(1)$. The velocity outside the boundary layer rises rapidly from 0 at the stagnation point to the impingement velocity in the inviscid far region. In region (ii), the boundary layer is expected to grow like $\sqrt{r/Re}$, at a rate that diminishes with Ω . The speed outside the boundary layer remains almost constant, equal to 1 (in units of $Q/\pi a^2$), as the fluid here is unaffected by the viscous stresses. For $r \gg 1$, the flow field in region (ii) is not significantly affected by the stagnation flow of region (i). The region $1 \ll r \ll r_0$ will be referred to as the developing boundary-layer region, with boundary-layer thickness $\delta(r)$, outside which the flow is inviscid and constant. Here r_0 is the location of the transition point at which viscous stresses become appreciable right up to the free surface, where the whole flow is of the boundary-layer type. At this point, the velocity profile changes from the Blasius type to the similarity profile for a stationary disk. In contrast, a similarity profile does not exist for a jet impinging on a rotating disk. The flow in region (iii), $r > r_0$, which will be referred to as the fully-viscous region, is bounded by the disk and the free surface $z = h(r)$.

Finally, the hydraulic jump in region (iv) occurs at a location $r = r_J$. The height immediately upstream of the jump is denoted by h_J^- , and the height immediately downstream of the jump is denoted by h_J^+ . In this study, the fluid is assumed to be drained at the edge of the disk $r = r_\infty$ to maintain steady flow, with the film thickness denoted by $h_\infty = h(r = r_\infty)$. Although it is common practice to assume the jump height to remain equal to h_J^+ , this assumption is valid for fluids of low viscosity on a stationary

disk. The edge thickness is expected to depend heavily on the rotation speed and surface tension, but not so much on the flow rate (Mohajer & Li 2015). In this study, we consider a viscous lubrication flow downstream of the jump.

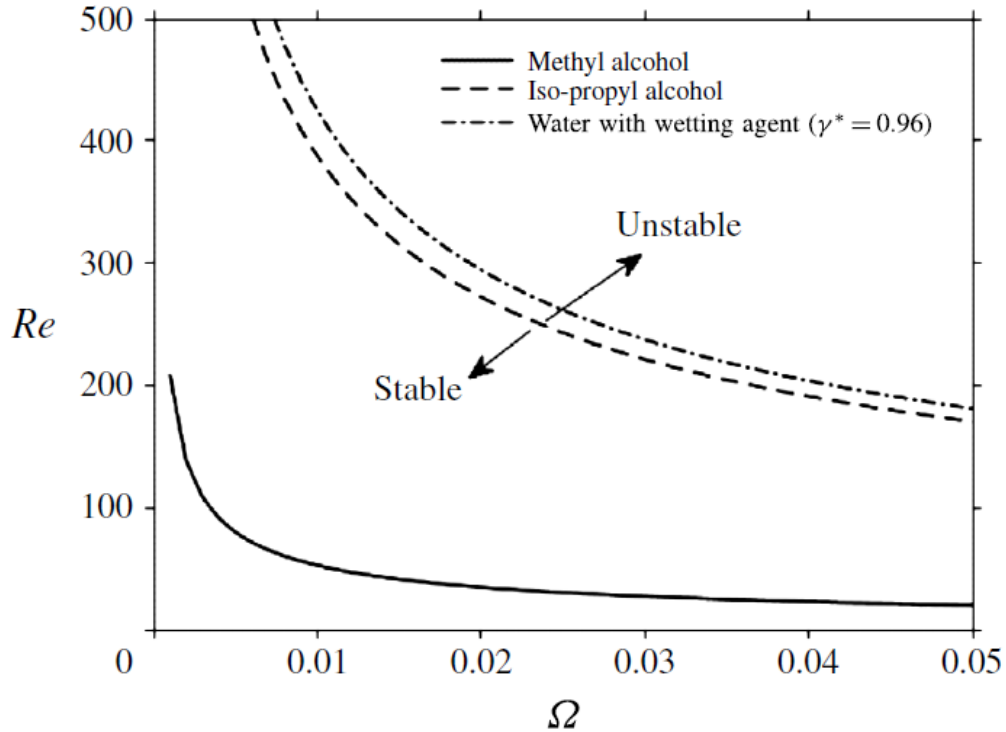


Figure 2-2: Marginal stability curves based on the analysis of Charwat *et al.* (1972) reproduced here in the (Re, Ω) plane. The stable (unstable) region below (above) each curve that corresponds to axisymmetric (wavy) flow is indicated here for iso-propyl alcohol.

2.2.2 Governing equations and boundary conditions

Unless otherwise specified, the Reynolds number is assumed to be large but without causing turbulence. Consequently, for steady axisymmetric thin-film flow, in the presence of rotation, the mass and momentum conservation equations are formulated using a thin-film or Prandtl boundary-layer approach, which amounts to assuming that the radial flow varies much slower than the vertical flow (Schlichting & Gersten 2000). The thin-film problem is formulated in the appendix. By letting a subscript with respect

to r or z denote partial differentiation, the reduced dimensionless conservation equations become

$$u_r + \frac{u}{r} + w_z = 0, \quad (2.2.1a)$$

$$\text{Re} \left(uu_r + wu_z - \frac{v^2}{r} \right) = -\frac{\text{Re}}{\text{Fr}^2} p_r + u_{zz}, \quad (2.2.1b)$$

$$\text{Re} \left(uv_r + wv_z + \frac{uv}{r} \right) = v_{zz}, \quad (2.2.1c)$$

$$p_z = \begin{cases} 0 & r < r_j \\ -1 & r > r_j \end{cases} \quad (2.2.1d)$$

These equations are essentially the same as those used by Bohr *et al.* (1996). We observe that the pressure for a thin film is essentially hydrostatic as a result of its vanishing at the film surface (in the absence of surface tension) and the small thickness of the film. In addition, upstream of the jump, the variation of the film thickness with the radius is expected to be smooth and gradual. In this case, the radial variation of the hydrostatic pressure is also small. According to the calculations of Prince *et al.* (2012), the hydrostatic pressure exerts less than 0.4% cumulative influence on the dynamics of the thin film and is thus neglected upstream of the hydraulic jump. This is generally commonly assumed in modelling hydraulic jump flow, where the hydrostatic pressure is included only downstream of the jump where the film is relatively thicker (Watson 1964; Bush & Aristoff 2003; Dressaire *et al.* 2010; Prince *et al.* 2012). At the disk, the no-slip and no-penetration conditions are assumed to hold for any r . In this case:

$$u(r, z = 0) = 0, \quad v(r, z = 0) = \Omega r, \quad w(r, z = 0) = 0. \quad (2.2.2a-c)$$

At the free surface $z = h(r)$, the kinematic condition for steady flow takes the form

$$w(r, z = h) = u(r, z = h)h'(r). \quad (2.2.3)$$

Here a prime denotes total differentiation. In addition, the radial and tangential shear stress components as well as the pressure must vanish everywhere ($0 < r < r_\infty$), so that

$$u_z(r, z = h) = v_z(r, z = h) = p(r, z = h) = 0. \quad (2.2.4a-c)$$

The flow field is sought separately in the developing boundary-layer region (ii) for $0 < r < r_0$, the fully-viscous region (iii) for $r_0 < r < r_J$ and the hydraulic jump region (iv) for $r_J < r < r_\infty$. We observe that region (i) is negligible, and the leading edge of the boundary layer in region (ii) coincides with the disk centre (see Section 2.2.3). Consequently, the additional boundary conditions are as follows. In region (ii), the flow is assumed to be sufficiently inertial for inviscid flow to prevail between the boundary-layer outer edge and the free surface (see Figure 2-1). In this case, the following condition at the outer edge of the boundary layer and beyond must hold:

$$u(r < r_0, z = \delta) = 1, \quad u_z(r < r_0, z = \delta) = 0, \quad u(r < r_0, \delta \leq z < h) = 1, \quad (2.2.5a-c)$$

Integrating Equation (2.2.1d) subject to condition (2.2.4c), the pressure becomes

$$p(r, z) = \begin{cases} 0 & r < r_J \\ h(r) - z & r \geq r_J. \end{cases} \quad (2.2.6)$$

To satisfy Equations (2.2.1b) and (2.2.1c) at the disk surface, we have

$$u_{zz}(r, z = 0) = -\text{Re}\Omega^2 r + \begin{cases} 0 & r < r_J \\ G \frac{dh}{dr} & r > r_J, \end{cases} \quad (2.2.7a)$$

$$v_{zz}(r, z = 0) = 0, \quad (2.2.7b)$$

which are obtained subject to conditions (2.2.2) and (2.2.6). It is not difficult to see that, regardless of the distributions of $u(r, z)$ and $w(r, z)$, and subject to conditions (2.2.2b), (2.2.4b) and (2.2.7b), Equation (2.2.1c) admits the following exact solution for the tangential velocity component:

$$v(r, z) = \Omega r. \quad (2.2.8)$$

This simple behaviour is not unexpected for a thin film flowing with a free surface and adhering to the rotating disk. We note that Equation (2.2.8) holds throughout the flow domain. Finally, the conservation of mass at any location upstream and downstream of the jump yields the following relation in dimensionless form:

$$\frac{1}{2r} = \int_0^{h(r)} u(r, z) dz. \quad (2.2.9)$$

We note that this relation follows from the mass conservation relation in dimensional

form: $Q = 2\pi\hat{r} \int_0^{\hat{h}(\hat{r})} \hat{u}(\hat{r}, \hat{z}) d\hat{z}$, where a hat variable denotes a dimensional quantity.

2.2.3 Overall solution strategy

Throughout this study, the stagnation region (i) under the impinging jet is assumed to be negligibly small. The velocity outside the boundary layer rises rapidly from 0 at the stagnation point to the impingement velocity in the inviscid far region. For a jet on a stationary as well as a rotating disk, the impinging jet is predominantly inviscid close to the stagnation point, and the boundary-layer thickness remains negligibly small. Obviously, this is the case for a jet at relatively large Reynolds number. Disk rotation adds to the inviscid character of the flow upon impingement. Ideally, the flow at the boundary-layer edge should correspond to the potential flow near the stagnating point, with the boundary-layer leading edge coinciding with the stagnation point (Liu *et al.* 1993). However, the assumption of uniform horizontal flow near the wall and outside the boundary layer (as illustrated in Figure 2-1) is reasonable since distance from the stagnation point for the inviscid flow to reach uniform horizontal velocity is small, of the order of the jet radius (Lienhard 2006). In addition, for a jet on a stationary disk, the flow acquires a similarity character. In this case, the position or effect of the leading edge is irrelevant. This is not the case for the jet on a rotating disk, where, as we shall see, a non-similarity solution is sought subject to initial conditions at the leading edge. However, as

argued above, the dominance of inertia near the stagnation point, which is further enhanced by disk rotation, should make plausible the assumption of uniform horizontal flow and negligible stagnation region (i). This assumption, which was adopted initially by Watson (1964), is commonly used in the modelling of impinging jet flow (see, for instance, Bush & Aristoff 2003; Dressaire *et al.* 2010; Prince *et al.* 2012).

The pressure due to gravitational effect is neglected upstream of the hydraulic jump. We shall calculate the flow of a liquid jet impinging on a stationary disk for reference, for which the similarity solution developed by Watson (1964) applies. In contrast, the rotation of the disk causes the flow to be non-similar in character. Therefore, in the present problem, approximate solutions are sought in each region. An integral approach of the Kármán–Pohlhausen type (Schlichting & Gersten 2000) with a cubic profile is adopted upstream of the jump, similar to the formulation of Prince *et al.* (2012) for a jet impinging on a slippery disk. The cubic profile may also be considered as the leading-order solution in a comprehensive spectral approach when inertia is included (Khayat & Kim 2006; Rojas *et al.* 2010). The cubic profile seems to be amply adequate as it leads to close agreement with Watson's (1964) similarity solution for a jet impinging on a stationary disk (Prince *et al.* 2012). The validity of such a profile was also assessed by Khayat (2016) for a planar jet impinging on a slippery stationary surface; the cubic profile was found to yield good agreement against his numerical solution. See also Rao & Arakeri (1998) for an integral analysis of a rotating film. Higher-order polynomial velocity profiles were also used. In their study on flow separation and wave breaking, Bohr *et al.* (1996) used a quartic profile to illustrate the emergence of a singularity at the separation point for a thin film. The coefficients in the polynomial expansion were not obtained explicitly. Later, Bohr *et al.* (1997) adopted a cubic velocity profile in an averaging boundary-layer approach that accounts for regions of separation, yielding the structures of hydraulic jumps.

Different forms of cubic profiles are used in region (ii) and region (iii) due to the difference in surface velocity. The flow in the entire supercritical domain is obtained upon matching the flows at the transition point r_0 . Downstream of the hydraulic jump, inertia is neglected, but the centrifugal effect is included. However, in contrast to the flow

over a stationary disk, an analytical solution is not possible for a rotating case, and the solution will be sought numerically. In an effort to obtain the location and height of the jump uniquely, we impose the value of the film thickness at the edge of the disk. Its value is estimated by applying the minimum energy principle at the disk edge. An additional contribution is included to account for rotation in the absence of radial flow as encountered in spin coating.

2.3 Influence of rotation on the developing boundary-layer and transition

Given the non-similar character of the rotating flow, an approximate solution is sought in region (ii). We note that, in their study of a circular jet impinging onto a slip surface, Prince *et al.* (2012) assumed a cubic profile for the radial velocity. However, they used a three-coefficient profile with the z^2 term missing. This would have been indeed the case for an adhering fluid but not rigorous for a slipping film though it should not affect much the accuracy in an averaged method. In the current work, we impose a cubic velocity profile for $u(r, z)$, with four unknown coefficients in the z direction.

2.3.1 The developing boundary-layer in region (ii)

In region (ii), the inviscid flow dominates the upper layer ($\delta \leq z < h$) of the film in the radial direction; therefore, the radial velocity above the boundary layer remains equal to one. In addition, the tangential component of the inviscid flow outside the boundary-layer edge is negligible near the stagnation point where the Coriolis force is dominated by the impinging flow, which results in a dominant radial flow. A cubic profile is sought for the radial velocity component $u(r, z)$, which is obtained using conditions (2.2.2a), (2.2.5a,b) and (2.2.7a), that is

$$u(r < r_0, z) = \left(\frac{3}{2\delta} + \frac{\text{Re}\Omega^2}{4} r\delta \right) z - \frac{\text{Re}\Omega^2}{2} rz^2 + \left(\frac{\text{Re}\Omega^2}{4} \frac{r}{\delta} - \frac{1}{2\delta^3} \right) z^3. \quad (2.3.1)$$

The boundary-layer height δ is determined by considering the mass and momentum balance over the boundary-layer region (ii). Therefore, consider first the integral form of

the convective term in Equation (2.2.1b). The vertical velocity component is eliminated by noting from Equation (2.2.1a) that $w(r, z) = -(1/r)(\partial/\partial r)\left(r\int_0^z u(r, z)dz\right)$. In this

$$\text{case,} \quad uu_r + wu_z = \partial u^2 / \partial r + u^2 / r - (1/r)(\partial/\partial z)\left(u(r, z)\int_0^z (\partial u(r, \bar{z})/\partial r)d\bar{z}\right) \quad .$$

Consequently, upon integrating Equation (2.2.1b) over the boundary-layer thickness, and neglecting the radial pressure gradient, we obtain the integral form of the momentum equation upstream of the jump:

$$\left(\frac{d}{dr} + \frac{1}{r}\right)\int_0^\delta (u^2 - u)dz - \frac{1}{r}\int_0^\delta v^2 dz = -\frac{1}{\text{Re}}u_z(r, z=0), \quad (2.3.2)$$

Upon substituting the velocity profiles (2.2.8) and (2.3.1), we obtain the desired differential equation for the boundary-layer height:

$$\frac{d\delta}{dr} = -\frac{C_1 r^2 \delta^6 + C_2 r \delta^4 + (C_3 + C_4 r^2)\delta^2 + 2520r}{C_5 r^3 \delta^5 + C_6 r^2 \delta^3 + C_7 r \delta}, \quad (2.3.3)$$

where the constant coefficients are $C_1 = 3\text{Re}^3 \Omega^4$, $C_2 = 6\text{Re}^2 \Omega^2$, $C_3 = -234\text{Re}$, $C_4 = -420(4\text{Re}-1)\text{Re}\Omega^2$, $C_5 = 5\text{Re}^3 \Omega^4$, $C_6 = 9\text{Re}^2 \Omega^2$ and $C_7 = -234\text{Re}$.

Equation (2.3.3) is solved numerically subject to $\delta(r=0)=0$. In the limit $\Omega = 0$, the equation admits the solution $\delta = 2\sqrt{(70/39)(r/\text{Re})}$, which agrees with the $\delta \approx \sqrt{r/\text{Re}}$ behaviour established from dimensional argument of Equation (2.2.1b).

Figure 2-3 illustrates the influence of rotation on the boundary-layer height. In the limit of $\Omega = 0$, the classical boundary-layer result is recovered (Watson 1964; Schlichting & Gersten 2000). As expected, the rotation can have a tangible effect as it tends to lower the boundary-layer height. This is clearly reflected in Equation (2.2.1b) when Equation (2.2.8) is used. We see that the centrifugal effect, which enhances inertial effect by growing like $\text{Re}\Omega^2 r$, tends to compete with the radial convective effect, which is

reflected by the term Reu_r . An estimate of the order of magnitude of this term is reached upon taking u to correspond to the free-surface value. In this case, we see that Reu_r decays like Re/r . Thus, close to the impingement point, the convective and viscous effects must balance in Equation (2.2.1b), and the boundary-layer height grows like $\delta \approx \sqrt{r/Re}$ regardless of the rotation speed. This is clearly depicted in Figure 2-3 where all curves merge for $Re^{-1/3}r < 0.1$. Far from the impingement point, the centrifugal and viscous effects must balance, and the height decays like $\delta \approx \sqrt{1/Re\Omega^2r}$. Therefore, rotation has a similar effect of thinning the boundary layer like slip (Khayat 2016, Prince *et al.* 2012) or shear thinning (Khayat 2014). Interestingly, unlike slip flow, where the boundary-layer height invariably increases in the radial direction, a high rotation rate causes the boundary layer height to decrease with radial distance after reaching a maximum as shown in Figure 2-3.

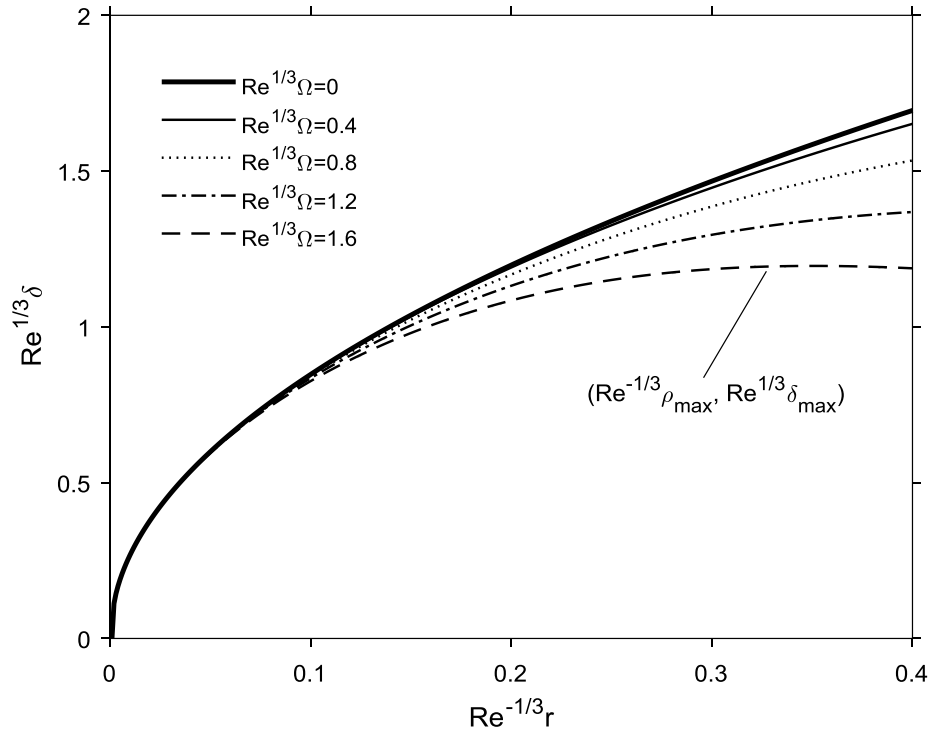


Figure 2-3: Influence of rotation in the developing boundary-layer region (ii). The boundary-layer thickness is plotted against the radial distance for different rotation speed.

A maximum in the boundary-layer height is therefore expected to emerge as a result of the growing centrifugal effect with radial distance. The maximum height δ_{max} coincides with the balance between the radial convective and the centrifugal effects, at a distance that is roughly dictated by $1/r \sim \Omega^2 r$. Thus, the location ρ_{max} of the maximum decreases rather rapidly with rotation speed, like $1/\Omega$, and the maximum height behaves like $\Omega^{-1/2}$. Considering that the inherent reason of the boundary-layer growth is due to accumulating viscous effect, the location of the maximum boundary-layer height occurs closer to the disk center when Ω increases. We now examine the transition point and film thickness.

2.3.2 Influence of rotation on the transition location and film thickness

As the boundary layer grows with radial distance, it eventually invades the entire film width, merging with the jet free surface at $r = r_0$. For $r < r_0$ and above the boundary-layer, at some height $z = h(r) > \delta(r)$, lies the free surface. The height of the free surface in region (ii) is then determined from mass conservation inside and outside the boundary layer. Therefore, for $r < r_0$,

$$\int_0^{\delta(r)} u(r, z) dz + h(r) - \delta(r) = \frac{1}{2r}. \quad (2.3.4)$$

Upon substituting the velocity profile (2.3.1), the film thickness is obtained as

$$h(r < r_0) = \frac{1}{48} \frac{24 + 18r\delta - \text{Re}\Omega^2 r^2 \delta^3}{r}. \quad (2.3.5)$$

The term $\text{Re}\Omega^2 r^2 \delta^3$ reflects the thinning effect of rotation on the film thickness. In the stationary case, we recall that $\delta = 2\sqrt{(70/39)(r/\text{Re})}$, so that

$$h(r < r_0; \Omega = 0) = \frac{1}{4} \left(\frac{2}{r} + \sqrt{\frac{210}{13} \frac{r}{\text{Re}}} \right). \quad (2.3.6)$$

Hence, in the stationary case, h decreases rapidly, like $1/r$, near the disk center, reaching a minimum, and increases like \sqrt{r} further downstream. In contrast, in the presence of strong centrifugal effect, upon recalling that $\delta \sim \sqrt{1/\text{Re}\Omega^2 r}$, we find that the film thickness also behaves like $h(r < r_0) \sim \sqrt{1/\text{Re}\Omega^2 r}$. This will be discussed further later.

Figure 2-4 depicts the influence of rotation on the transition location r_0 and corresponding film thickness $h_0 \equiv h(r_0)$, which are determined by setting $h(r_0) = \delta(r_0)$. The transition location increases as the film becomes thinner with increasing rotation

speed as inertia is enhanced by rotation. This is the same trend predicted for the effect of slip (see figure 8 of Khayat 2016). However, in contrast to the effect of slip, the rotation speed does not exhibit an asymptotic behaviour for large Ω . Another interesting contrasting behaviour is the slow deviation from the $\Omega = 0$ level for small Ω in Figure 2-4 as opposed to the strong departure for small slip.

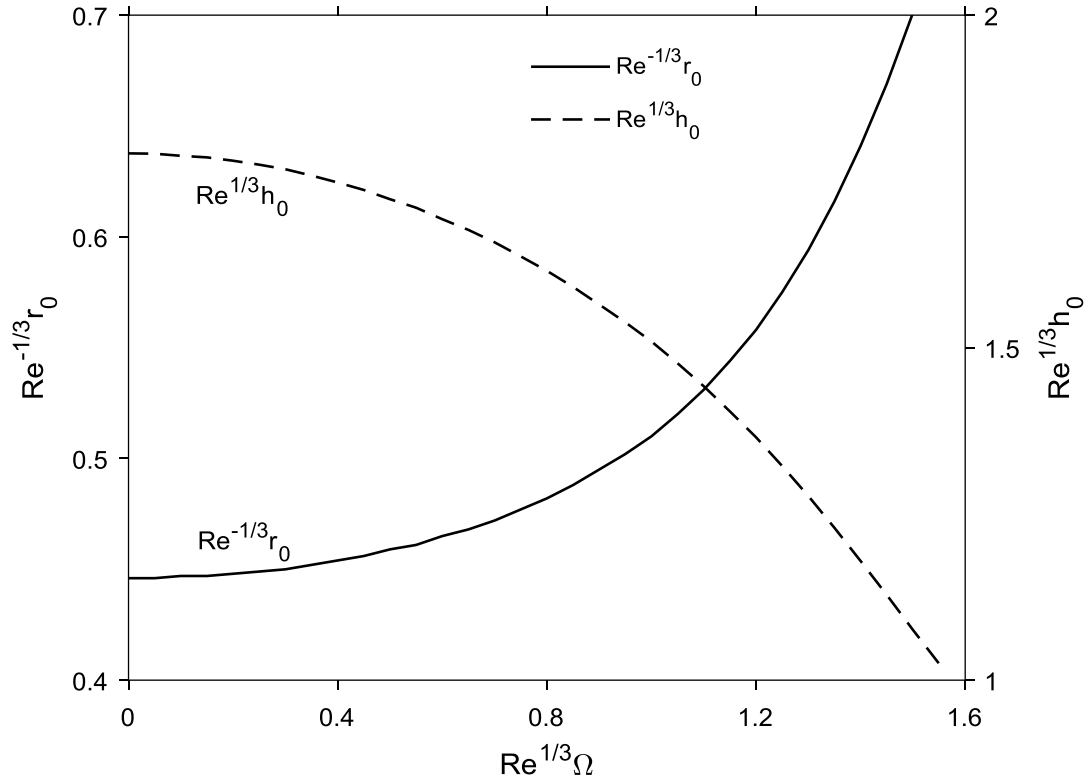


Figure 2-4: Dependence of location and film thickness at the transition point between the developing boundary-layer and fully-viscous regions (ii) and (iii).

In the stationary case, upon equating $h(r_0; \Omega = 0) = 1/4 \left(2/r_0 + \sqrt{(210/13)(r_0/Re)} \right)$ and

$\delta(r_0; \Omega = 0) = 2\sqrt{(70/39)(r_0/Re)}$, we obtain

$$r_0(\Omega = 0) = \left(\frac{78}{875} Re \right)^{1/3}. \quad (2.3.7)$$

In particular, $\text{Re}^{-1/3} r_0 = 0.447$ and $\text{Re}^{1/3} h(r_0) = 1.791$ are the limit values reflected in Figure 2-4. In comparison, Watson's transition location is given by $\text{Re}^{-1/3} r_0 = 9\sqrt{3}c(\pi - c\sqrt{3})/16\pi^2 = 0.463$, where $c = 1.402$ (Watson 1964), which reflects a discrepancy less than 3%.

2.4 Influence of rotation on the flow in the fully-viscous region

In region (iii), the potential flow in the radial direction ceases to exist, with the velocity $u_s(r) = u(r, z = h)$ at the free surface becoming dependent on r . We again assume a cubic velocity profile, subject to conditions (2.2.2a), (2.2.4a) and (2.2.7a), which amounts to setting $\delta = h$ in Equation (2.3.1) for $u(r, z)/u_s(r)$. In this case, $u_s(r)$ is determined by using the mass conservation Equation (2.2.9), yielding the following relation:

$$u_s(r > r_0) = \frac{24}{hr(\text{Re}\Omega^2 rh^2 + 30)}. \quad (2.4.1)$$

For $\Omega = 0$, this equation agrees with equation (15) of Prince *et al.* (2012) upon setting their slip parameter equal to zero. The radial velocity profile is given as function of the surface velocity $u_s(r)$:

$$u(r > r_0, z) = \frac{u_s}{4h^3} \left[h^2 (\text{Re}\Omega^2 h^2 r + 6)z - 2\text{Re}\Omega^2 h^3 r z^2 + (\text{Re}\Omega^2 h^2 r - 2)z^3 \right]. \quad (2.4.2)$$

This equation is equivalent to equation (3) of Bohr *et al.* (1997) for a stationary disk. In that case, the r -dependent coefficients were also obtained using the same boundary conditions at the disk and the film surface.

Similar to Equation (2.3.2), the integral form of the momentum equation reads:

$$\left(\frac{d}{dr} + \frac{1}{r} \right) \int_0^h (u^2 - u) dz - \Omega^2 hr = -\frac{1}{\text{Re}} u_z(r, z = 0). \quad (2.4.3)$$

Substituting Equation (2.4.2) into Equation (2.4.3), we obtain the equation for the film thickness in the fully-viscous region, which is integrated numerically for $r \geq r_0$ subject to $h(r=r_0) = \delta(r_0)$. The resulting differential equation for h is algebraically complicated and will not be displayed here. It takes a particularly simple form in the stationary case. Thus, for $\Omega = 0$ and $r \geq r_0$, the problem reduces to the following equation and boundary condition:

$$\frac{dh}{dr} = -\frac{h}{r} + \frac{525}{136} \frac{r}{\text{Re}}, \quad h(r_0, \Omega = 0) = 2\sqrt{\frac{70}{39} \frac{r_0}{\text{Re}}}, \quad (2.4.4a,b)$$

which admits

$$h(r > r_0; \Omega = 0) = \frac{175}{136 \text{Re} r} (r^3 - r_0^3) + 2 \frac{r_0}{r} \sqrt{\frac{70}{39} \frac{r_0}{\text{Re}}} = \frac{175}{136} \frac{r^2}{\text{Re}} + \frac{1}{5} \left(4 - \frac{39}{68} \right) \frac{1}{r}, \quad (2.4.5)$$

as solution, where we recall $r_0 = (78/875 \text{Re})^{1/3}$ from Equation (2.3.7). Clearly, Equation (2.4.5) indicates that the thickness increases like $h \sim r^2$ at large distance. The limit of large rotation speed will be discussed shortly. Figure 2-5 depicts the influence of rotation on the film thickness in the transition region. Results are shown for $\text{Re}^{1/3} \Omega$, ranging from 0 to 1.6. In the limit $\Omega = 0$, Watson's film thickness profile is essentially recovered, which is the only profile that increases with r after exhibiting a strong minimum, as per Equation (2.4.5). For comparison, Watson's expression is reproduced here in dimensionless form:

$$h(r > r_0) = \frac{2\pi}{3\sqrt{3}} \frac{r^2}{\text{Re}} + \frac{3c(3\sqrt{3}c - \pi)}{8\pi} \frac{1}{r}. \quad (2.4.6)$$

Thus, we have $h \approx 1.21r^2 / \text{Re} + 0.685(1/r)$ from Equation (2.4.5) compared to Watson's $h \approx 1.28r^2 / \text{Re} + 0.69(1/r)$ from Equation (2.4.6), showing a surprisingly close agreement.

The minimum film thickness weakens considerably as the rotation speed is slightly increased. The transition occurs upstream of the minimum, with unmatched slopes between h and δ at $r = r_0$. For a faster spinning disk, the film acquires additional radial momentum, with relatively reduced viscous effect (friction). The film thickness as well as the boundary-layer height decrease overall, and the minimum weakens further. As rotation intensifies further, the film does no longer exhibit a minimum in thickness. In the case of an infinite rotation speed, Figure 2-5 indicates that the film thickness saturates to a finite value, which is practical since the film thickness cannot vanish. Also shown in this figure is the location of the minimum height pushed outward as effects of viscosity decrease, which is a combined effect of Reynolds number and rotation speed.

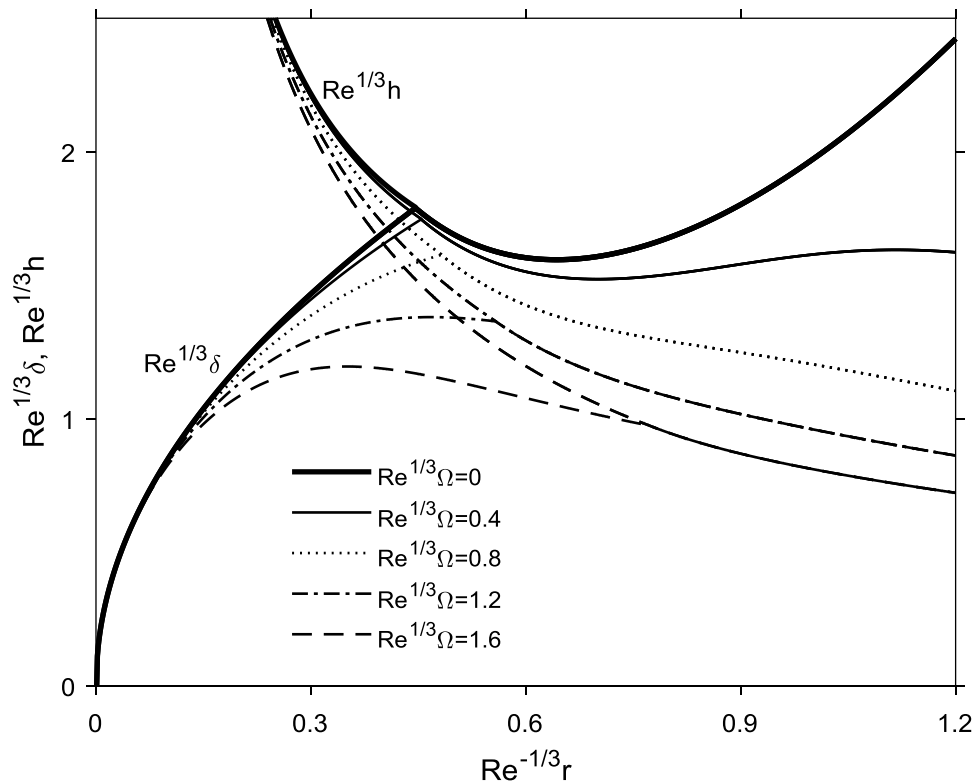


Figure 2-5: Influence of rotation on the developing boundary-layer height and film thickness. The transition location coincides with the intersection of the two heights.

Figure 2-6 gives an overall view of the film thickness distribution. In addition to the minimum film thickness, there is also a maximum height whose location and strength

depend on the interplay between convective and centrifugal effects. This was also observed by Thomas *et al.* (1991) and Ozar *et al.* (2003) in their experimental studies on the radial film flow over a rotating disk. Downstream of the transition location, the liquid film behaviour can be divided into three zones: the inner inertia-dominated region, the outer rotation-dominated region and the intermediate region in between. In the inertia-dominated region, the inertia and friction forces are dominant. The liquid film tends to slow down as a result of friction, and the film thickness increases as reported by Thomas *et al.* (1991). In the rotation-dominated region, centrifugal forces come into play, causing a thinning of the liquid film. Meanwhile in the transition region, both the viscous effect and centrifugal effect come into play and are in balance. Thus, the film thickness reaches a maximum in the transition region, where deceleration of the flow due to friction is compensated and eventually balanced by the acceleration due to centrifugal effect.

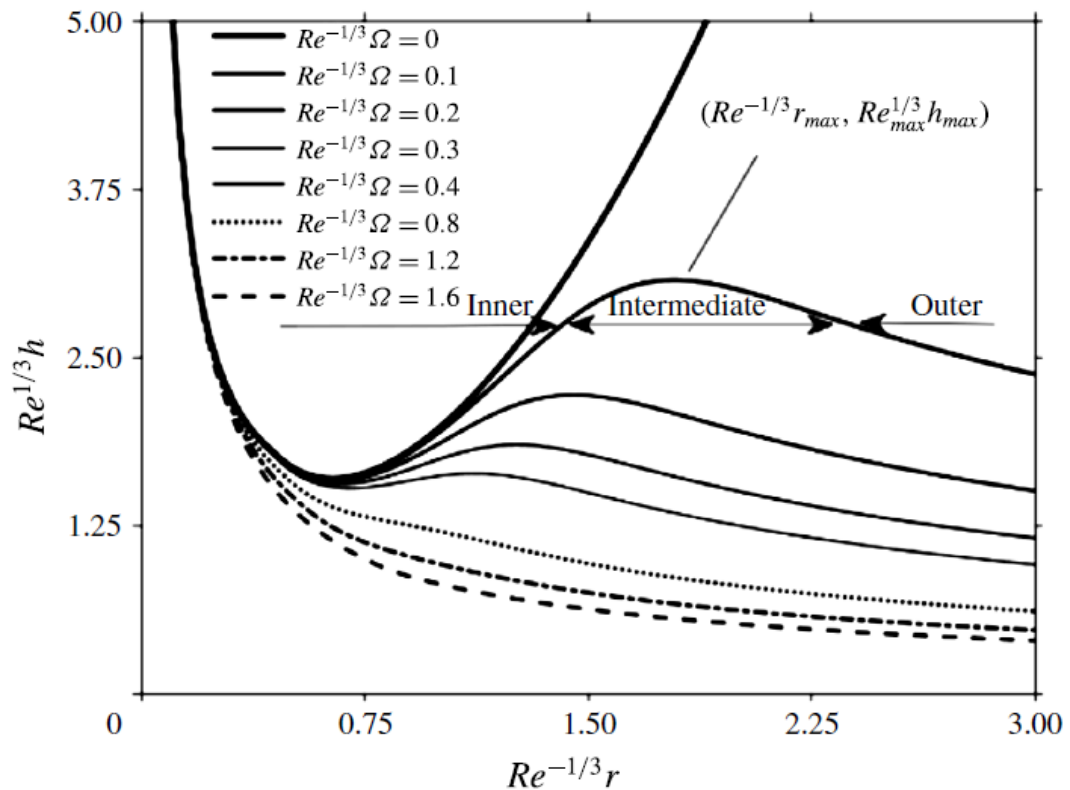


Figure 2-6: Influence of rotation on the thickness distribution upstream and downstream of the transition point $r = r_0$. The inner, intermediate and outer

subregions are shown for $Re^{1/3}\Omega = 0.1$.

As is apparent from Figure 2-6, at a given Reynolds number, the location where the maximum film thickness occurs, moves towards the center of the disk as the rotation speed increases, which indicates that the centrifugal effect gradually dominates inertia. This is illustrated through the curves corresponding to $Re^{1/3} \Omega = 0.1, 0.2, 0.3$. Eventually, upon further increase of the rotation speed, the centrifugal effect becomes dominant over the entire disk, except in region (i) where convective effects appear to be always present. The film thickness decreases monotonically as the rotation speed increases and becomes essentially independent of the radial distance far downstream. Also, the thickness becomes gradually insensitive to the rotation speed as indicated by the curve saturation in Figure 2-6. This behaviour agrees closely with the measurements and leading-order asymptotic solution of Burns *et al.* (2003). The development from inertial to centrifugal dominance will be further examined below once the surface velocity is discussed.

The influence of rotation on the corresponding free surface velocity profiles is depicted in Figure 2-7. Here the velocity in the developing boundary-layer region (ii) outside the boundary layer is equal to the uniform jet velocity, which then decreases monotonically with distance downstream of the transition location. We can see the significant effect of rotation on the surface velocity as it tends to enhance the radial flow but diminishes the rate at which the surface velocity decreases with radial distance, which is similar to the effect of slip (Prince *et al.* 2012, Khayat 2016). However, the effect of rotation seems stronger than that of slip since slip is nothing but a release in surface resistance, whereas rotation has an obvious effect of accelerating the flow. That is, the momentum dissipated by viscous stress is gradually recovered by the centrifugal force. The figure also suggests that when the rotation speed tends to infinity, the developing boundary-layer region dominates the entire flow, and the free surface velocity saturates to a horizontal line which is the free jet velocity, which is artificial since the flow becomes unstable for super large rotation speeds.

In the stationary case, the surface velocity decreases rapidly. This behaviour is easily deduced from Equation (2.4.1) upon setting $\Omega = 0$ and substituting Equation (2.4.5) to obtain

$$u_s(r > r_0; \Omega = 0) = \frac{4}{5} \left(\frac{175}{136 \text{Re}} (r^3 - r_0^3) + 2r_0 \sqrt{\frac{70 r_0}{39 \text{Re}}} \right)^{-1}. \quad (2.4.7)$$

In this case, u_s decreases like r^{-3} at large distance.

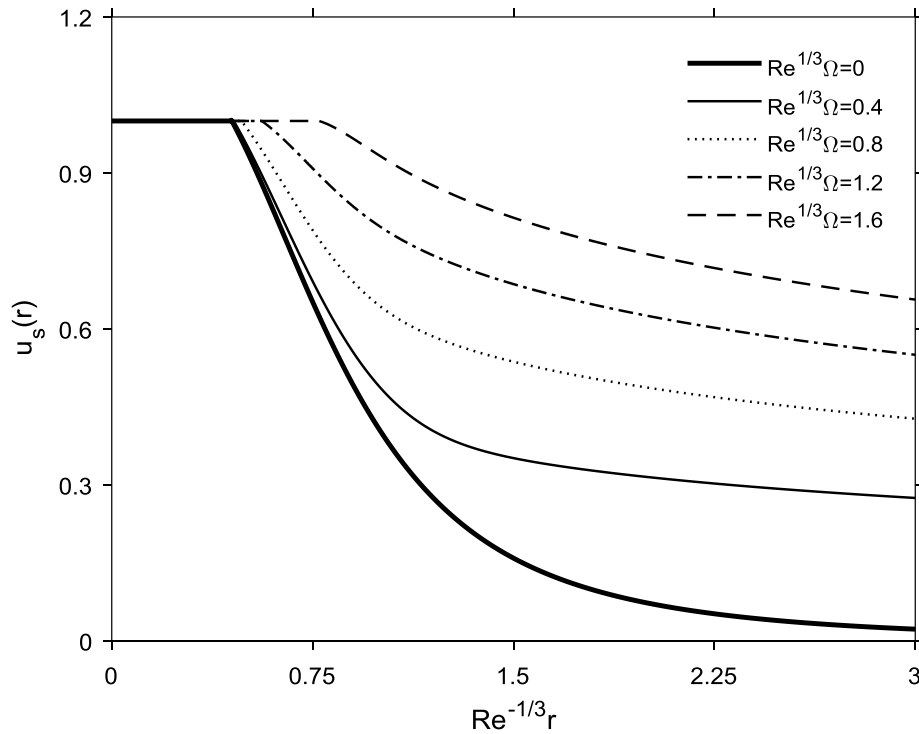


Figure 2-7: Influence of rotation on the velocity at the film surface upstream and downstream of the transition point $r = r_0$. The transition point coincides with the location at which the velocity first deviates from 1.

Although the explicit dependence of the film thickness and surface velocity on rotation speed and radial distance is complex, further insight is gained by examining the limits of negligible and dominant centrifugal effect. Figures 2-6 and 2-7 suggest the existence of three distinct sub regions downstream of the transition point in the fully-viscous region: an inner sub-region close to the transition point where the convective effect dominates the centrifugal effect, an intermediate sub-region where these two effects are comparable, and a sub-region far from the transition point where the centrifugal effect is dominant.

We observe that in all three sub-regions, the viscous effects are significant. An approximate relation between u_s and h may be deduced from the mass conservation Equation (2.2.9):

$$u_s h \approx \frac{1}{2r}. \quad (2.4.8)$$

Consider first the inner sub-region where inertia and viscous effects are dominant. In this case, Equation (2.2.1b) suggests that

$$\text{Re} \frac{u_s^2}{r} \sim \frac{u_s}{h^2}. \quad (2.4.9)$$

Using Equation (2.4.8), we obtain

$$u_s \sim \frac{\text{Re}}{r^3}, \quad h \sim \frac{r^2}{\text{Re}}. \quad (2.4.10a,b)$$

This behaviour corresponds to the more explicit expression (2.4.5) for h derived earlier in the stationary case and based on the cubic profile for velocity. The behaviour in Equation (2.4.10) clearly corroborates the trends reported in Figures 2-6 and 2-7 for the region close to the transition point $r = r_0$.

Next, consider the situation in the intermediate subregion where both the convective and centrifugal effects, along with the viscous effects are significant. In this case, we have

$$\text{Re} \frac{u_s^2}{r} \sim \text{Re} \Omega^2 r \sim \frac{u_s}{h^2}. \quad (2.4.11)$$

These relations, along with Equation (2.4.8), yield the following estimates for the maximum thickness, and corresponding location and velocity:

$$h_{\max} \sim \frac{1}{\sqrt{\text{Re} \Omega}}, \quad r_{\max} \sim \left(\frac{\text{Re}}{\Omega} \right)^{1/4}, \quad u_{\max} \sim \left(\text{Re} \Omega^3 \right)^{1/4}. \quad (2.4.12a-c)$$

Clearly, these estimates agree with the trends observed in Figures 2-6 and 2-7 in the intermediate region. Thus, Equations (2.4.12a-c) indicates that, with increasing rotation speed, the radial location of the maximum thickness decreases towards the center like $\Omega^{-1/4}$ and the maximum thickness weakens and saturates like $\Omega^{-1/2}$, eventually disappearing altogether as shown in Figure 2-6. This behaviour will be confirmed further below.

In the outer sub-region, at large radial distance, the centrifugal effect becomes particularly dominant whereas inertia becomes insignificant. In this case, and in the absence of gravity, the centrifugal term must balance the viscous term in the radial momentum Equation (2.2.1b), suggesting that $\text{Re}\Omega^2 r \sim u_s / h^2$. Consequently, upon using Equation (2.4.8), the behaviours of the film thickness and surface velocity for large centrifugal effect become:

$$h \sim (\text{Re}\Omega^2 r^2)^{-1/3}, \quad u_s \sim \left(\frac{\text{Re}\Omega^2}{r} \right)^{1/3}. \quad (2.4.13a,b)$$

These limit expressions closely corroborate the profiles reported in Figures 2-6 and 2-7. In particular, the $h \sim \Omega^{-2/3}$ behaviour reflects the saturation at large rotation speed in Figure 2-6. Also, Equation (2.4.13) reflects the faster decay with distance of the thickness compared to that of the velocity. Finally, we note that Equation (2.4.13a) is equivalent to the asymptotic behaviour obtained by Rauscher *et al.* (1973).

Figure 2-8 illustrates the development of the dimensionless wall shear stress at the disk (skin friction) for the same rotation speeds as in Figures 2-6 and 2-7. From Equation (2.4.1) and Equation (2.4.2), we have

$$\tau_w (r > r_0) = 6 \frac{\text{Re}\Omega^2 h^2 r + 6}{h^2 r (\text{Re}\Omega^2 h^2 r + 30)}. \quad (2.4.14)$$

The figure shows that the wall shear stress is always larger for a higher rotation speed anywhere along the disk. This larger shear stress, which reflects a larger shear rate at the

disk, is the result of a thinner film thickness and a greater free-surface velocity caused by higher rotation speed as already reported in Figures 2-6 and 2-7. The shear stress decreases rapidly in the developing boundary-layer region. For a stationary disk:

$$\tau_w (r > r_0; \Omega = 0) = \frac{6}{5} r \left[\frac{175}{136 \text{Re}} (r^3 - r_0^3) + 2r_0 \sqrt{\frac{70}{39} \frac{r_0}{\text{Re}}} \right]^{-2}. \quad (2.4.15)$$

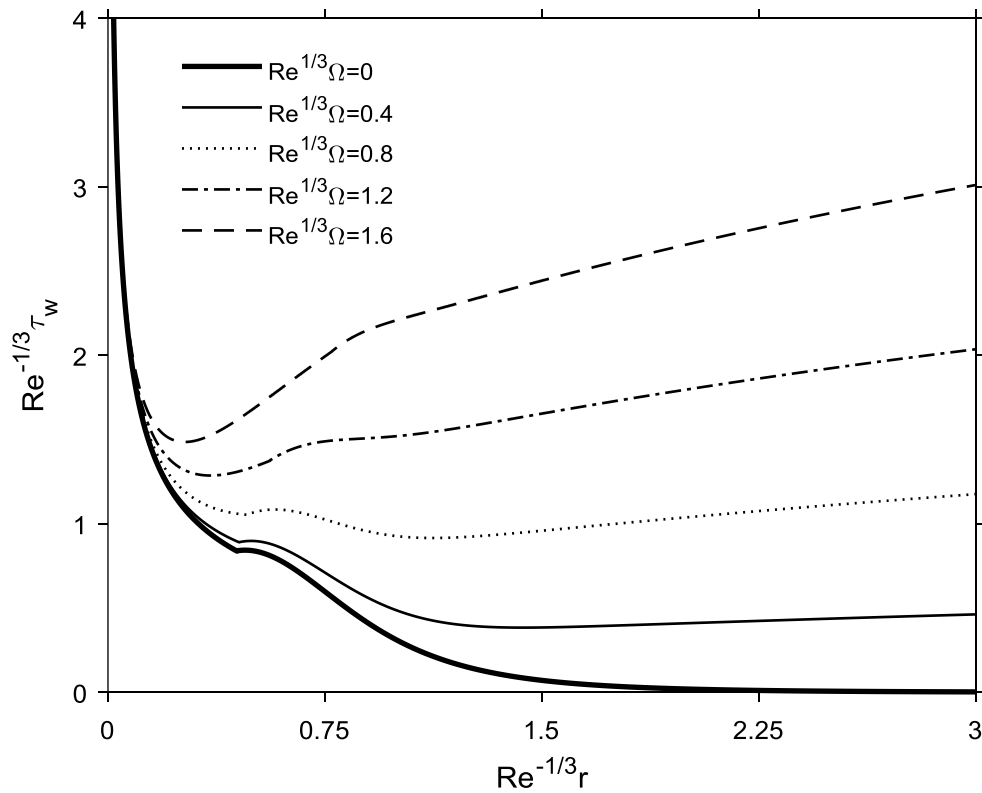


Figure 2-8: Influence of rotation on the wall shear stress upstream and downstream of the transition point $r = r_0$.

In this case, after the rapid drop, τ_w exhibits a maximum before decaying monotonically.

At large radial distance, the shear stress decays like r^{-5} for a stationary disk as a result of film thickening and absence of flow (see $\Omega = 0$ curves in Figures 6 and 7). In contrast, the shear stress on a rotating disk decreases to a minimum after which τ_w increases relatively slowly with r . The minimum strengthens and moves towards the center of the

disk with increasing rotation speed, signalling the increasing dominance of centrifugal effect over the entire viscous boundary-layer region.

Figure 2-8 suggests that τ_w increases essentially linearly with radial distance for moderate rotation speed. In the outer region, upon substituting Equation (2.4.13a) into Equation (2.4.15), we have

$$\tau_w \sim \left(\text{Re}^2 \Omega^4 r \right)^{1/3}. \quad (2.4.16)$$

We also arrive at the same result if we write $\tau_w \sim u_s / h$ and use Equation (2.4.10). This shows that the shear stress deviates from the linear growth with radial distance and behaves closer to $r^{1/3}$, which is also noticeable from Figure 2-8 for $\text{Re} \Omega^2 = 1.6$. Also, the behaviour $\tau_w \sim \Omega^{4/3}$ reflects the mildly nonlinear (slightly faster than linear) growth of the shear stress with rotation speed depicted in Figure 2-8.

We next consider the effect of inertia by varying the Reynolds number and fixing the rotation speed to $\Omega = 0.02$. Figure 2-9 shows the film thickness for Re between 200 and 500. An increase in the Reynolds number causes an increase in film inertia. Therefore, a higher centrifugal force is required to overcome the higher inertial force to maintain the flow. If the rotation speed is kept constant and the Reynolds number is increased, then the maximum film thickness location travels towards the edge of the disk while the maximum weakens. This is in agreement with Equations (2.4.12a-c). Since the radial location influences the magnitude of centrifugal effects, the region where the centrifugal and inertia forces are comparable, moves towards the edge of the disk.

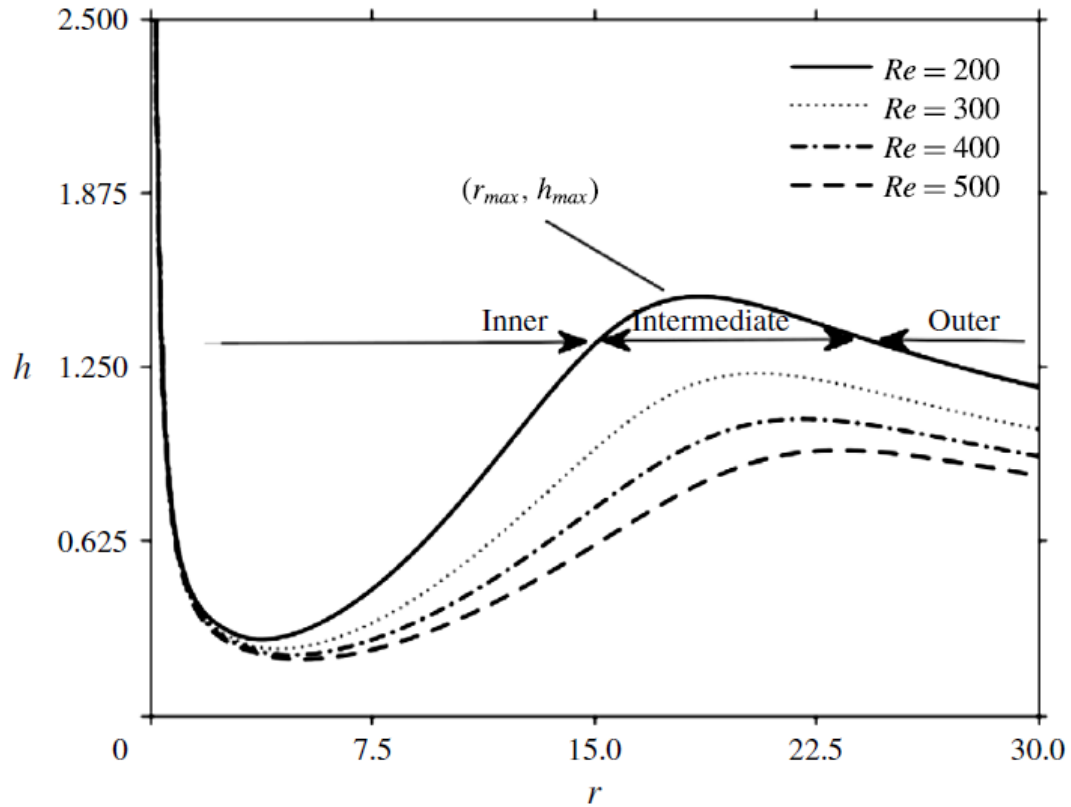


Figure 2-9: Influence of inertia on the film thickness upstream and downstream of the transition point. Here $\Omega = 0.02$. The inner, intermediate and outer subregions are indicated for the $Re = 200$ curve.

A more explicit illustration is given in Figures 2-10 and 2-11, where both the location and the values of the minimum thickness as well as the maximum thickness are reported. Figure 2-10 indicates that the location of the minimum thickness moves outwards with rotation as well as inertia, whereas the minimum height decreases as argued earlier. In Figure 2-11, however, the location and the magnitude of the maximum height behave differently as emphasized by the arrows.

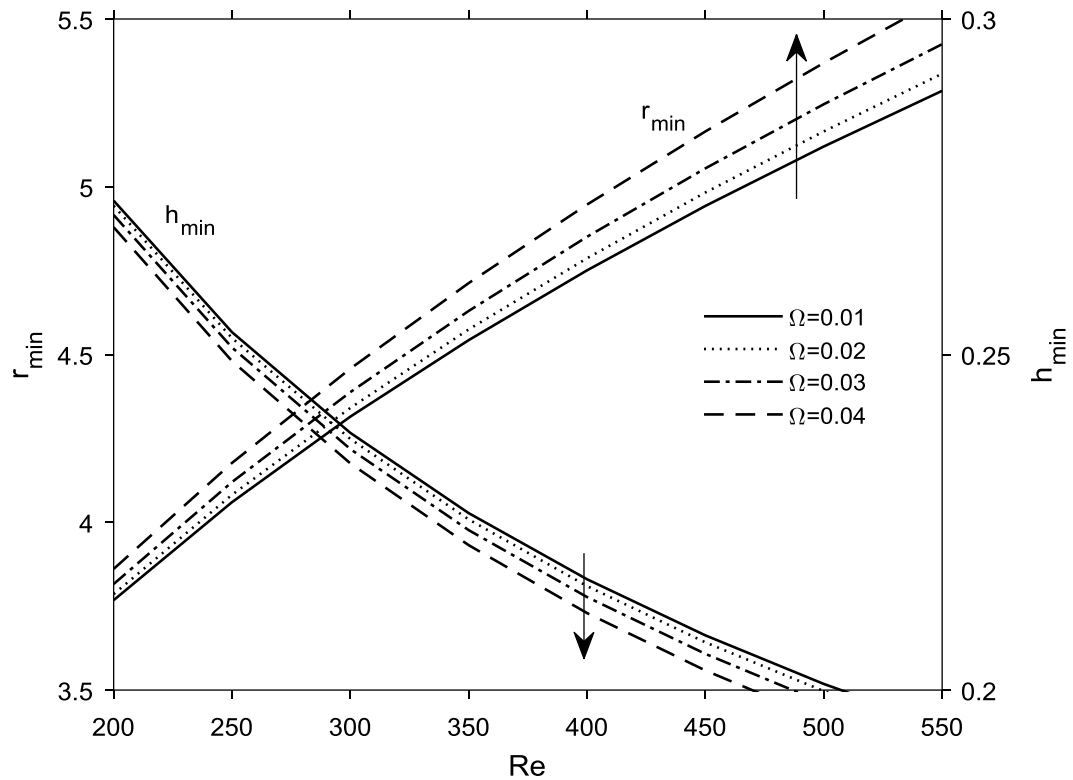


Figure 2-10: Influence of inertia and centrifugal effects on the minimum film thickness and its location. Arrows indicate direction of increasing rotation speed.

The trends in Figure 2-10 are well reflected by the earlier analysis and Equations (2.4.12a-c). In particular, $r_{max} \sim (Re/\Omega)^{1/4}$ suggests that the location of the maximum increases with inertia like $Re^{1/4}$ and decreases with rotation speed like $\Omega^{-1/4}$, reflecting the saturation in Figure 2-11 with respect to Re and Ω , respectively. Similarly, the behaviour $h_{max} \sim 1/\sqrt{Re\Omega}$ is well represented in Figure 2-11

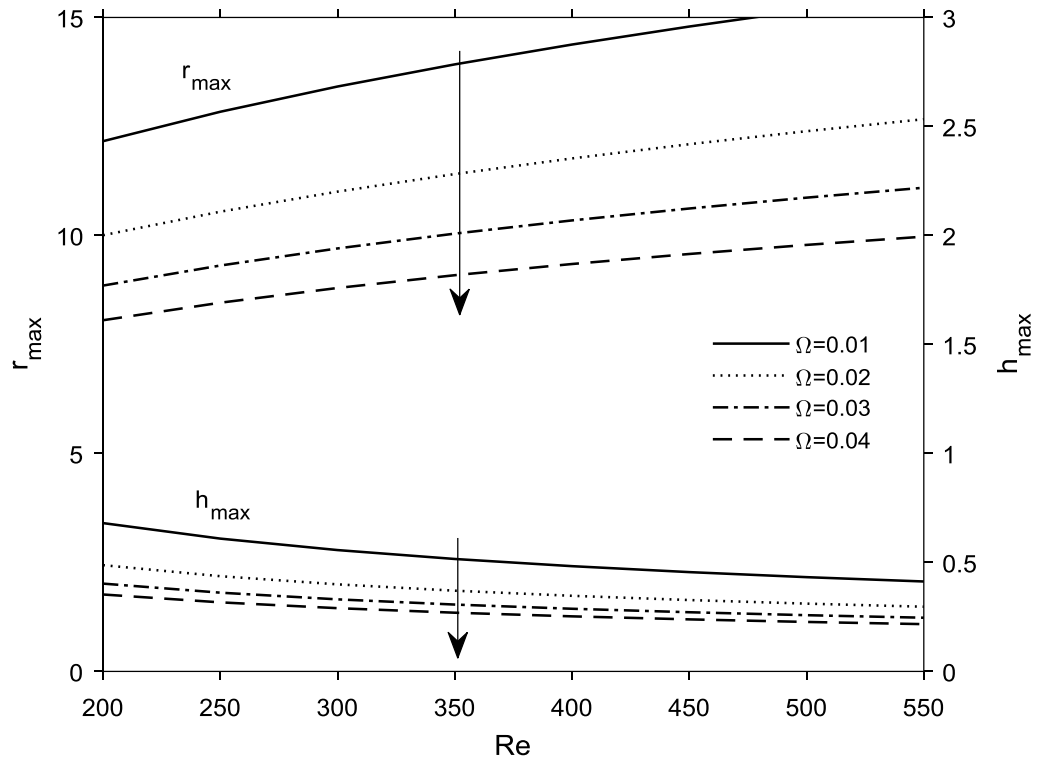


Figure 2-11: Influence of inertia and centrifugal effects on the maximum film thickness and its location. Arrows indicate direction of increasing rotation speed.

Although there are no film thickness measurements for the flow impinging on a rotating disk, some data exist for a thin film emanating radially on a rotating disk. In particular Ozar *et al.* (2003) examined the flow of water emerging from a collar. In an effort to validate the observed behaviour in the viscous region (iii), we carry out a direct comparison with their measurements by solving Equation (2.4.3) for the thickness distribution. We choose the initial thickness and location to correspond to the height and radius of the collar, respectively. Figure 2-12 depicts the influence of rotation on the thickness distribution. The figure shows that the flow features predicted by our formulation in region (iii) are realistic as they are also observed experimentally. In particular, Figure 2-12 shows a good agreement between theory and experiment regarding the emergence of the thickness maximum and its location. As theory suggests (see also Figure 2-11), the observed maximum height and location decrease with increasing rotation speed. It is also worth noting that the discrepancies become larger

further downstream, and also when rotation speed increases. The reason for this is twofold: First, the flow configuration in the experiment (Ozar *et al.* 2003) is not strictly the same as ours since the flow is emitted from the gap between a collar and a rotating disk, which we mimic by our fully-viscous flow, taking the height of the gap as the initial condition; Second, there can be some turbulence occurring further downstream and the flow also becomes unstable when rotation speed increases to a higher level (Charwat *et al.* 1972).

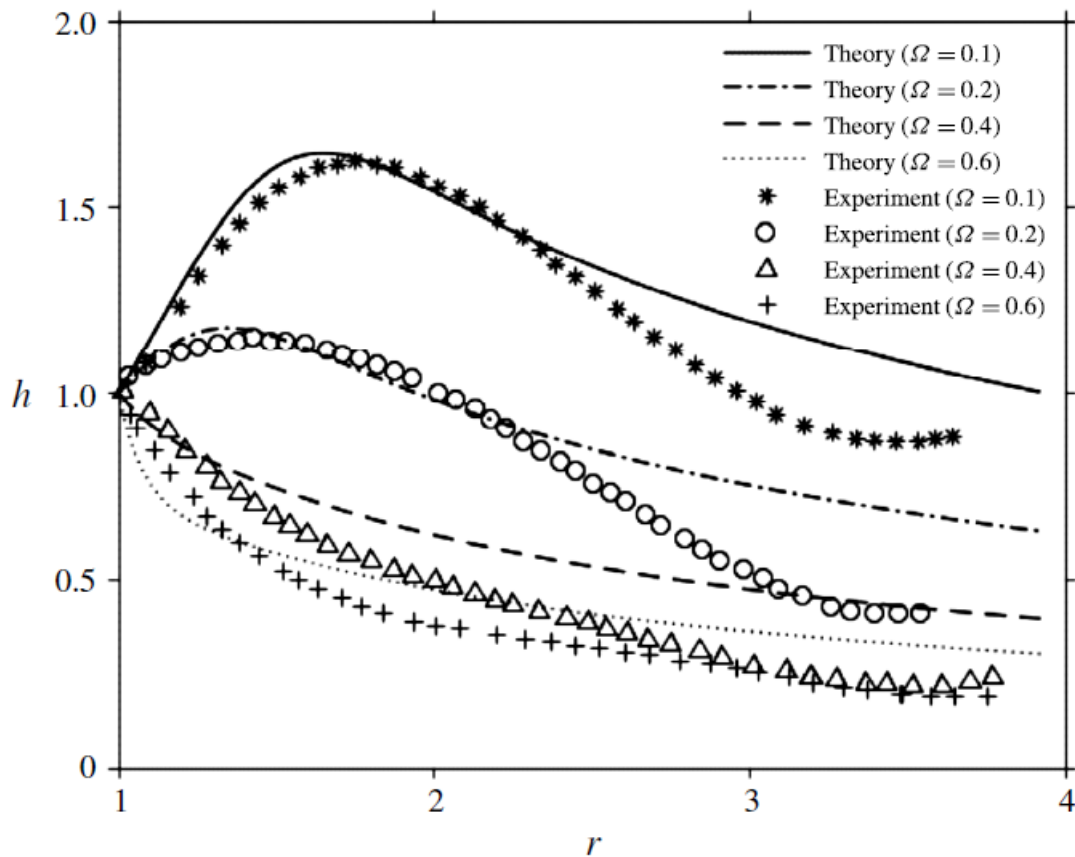


Figure 2-12: Influence of rotation speed on the maximum film thickness and its location. Comparison between theory and the measurements of Ozar *et al.* (2003).

The data correspond to $Q = 3$ L/min.

2.5 Influence of rotation on the hydraulic jump

In this section, we consider the axisymmetric flow in region (iv), the hydraulic jump region. The flow on a stationary disk will be presented first, with discussion focused on

the prediction or determination of the thickness at the edge of the disk, which will be used as a boundary condition. The resulting arguments will be extended for the flow over a rotating disk. Although the flow downstream of the jump may be assumed to be inviscid or viscous, only the viscous flow will be examined as it seems to reflect closer the real flow (Duchesne *et al.* 2014). In fact, the hydraulic jump is associated with a considerable energy loss which is traditionally difficult to determine. As such, the energy equation is not suitable for the analysis of the hydraulic jump (Crowe 2009). Consequently, a momentum balance approach is applied across the jump. In addition, the surface tension effect will be included although a large jump radius is anticipated in the presence of rotation.

2.5.1 General formulation

Using Equation (2.2.1a), the integral form of Equation (2.2.1b) at any location becomes

$$\frac{1}{r} \frac{d}{dr} r \int_0^h (u^2 - u) dz - \frac{1}{r} \int_0^h v^2 dz = -\frac{1}{Fr^2} \int_0^h \frac{\partial p}{\partial r} dz - \frac{1}{Re} \left. \frac{\partial u}{\partial z} \right|_{z=0}. \quad (2.5.1)$$

We recall the position of the hydraulic jump as being $r = r_J$. We observe that the azimuthal velocity component at the jump is given by $v_J = \Omega r_J$ as per Equation (2.2.8). Across the jump, Equation (2.5.1) is applied to a control volume of width Δr in the radial direction, yielding

$$\begin{aligned} & \int_0^{h_J^+} \left((u_J^+)^2 - u_J^+ \right) dz - \int_0^{h_J^-} \left((u_J^-)^2 - u_J^- \right) dz - \frac{\Delta r}{r_J} \int_0^{h_J} v_J^2 dz \\ & = -\frac{1}{Fr^2} \left(\int_0^{h_J^+} p_J^+ dz - \int_0^{h_J^-} p_J^- dz \right) - \frac{\Delta r}{Re} \left. \frac{\partial u_J}{\partial z} \right|_{z=0}. \end{aligned} \quad (2.5.2)$$

From here on, a ‘-’ and a ‘+’ superscript denotes a value immediately upstream and downstream of the jump, respectively. Since the width of the jump Δr is assumed to be small, the terms in Equation (2.5.2) containing Δr become negligible. In this case, we

recall the pressure terms from Equation (2.2.6) and use Equation (2.2.9) for mass conservation. In addition, following Bush & Aristoff (2003), we include the effect of surface tension. The resulting equation takes the same form as in the case of a stationary disk, namely

$$\frac{1}{2} \left((h_J^+)^2 - (h_J^-)^2 \right) + \frac{1}{\text{Bo}} \frac{(h_J^+ - h_J^-)}{r_J} = \text{Fr}^2 \int_0^{h_J^-} (u_J^-)^2 dz - \text{Fr}^2 \int_0^{h_J^+} (u_J^+)^2 dz. \quad (2.5.3)$$

We observe that the effect of rotation is reflected implicitly in Equation (2.5.3) in the height and velocity upstream and downstream of the jump. As in the case of a stationary disk, some assumptions are made regarding the nature of the flow downstream of the jump.

In this work, we follow Duchesne *et al.* (2014), and adopt a lubrication flow assumption in the presence of rotation. In this case, a differential equation for $h(r > r_J)$ can be obtained by neglecting the first two inertia terms in Equation (2.2.1b). This is not unreasonable as the rotation effects is even stronger downstream. We note that the hydrostatic pressure term is not negligible due to the large film thickness downstream of the jump. Consequently, the remaining terms in Equation (2.2.1b), the hydrostatic pressure, the viscous and the centrifugal effects, must balance:

$$\text{Re} \Omega^2 r = \frac{\text{Re}}{\text{Fr}^2} \frac{dh}{dr} - u_{zz}. \quad (2.5.4)$$

By applying the no-slip condition at the fluid–disk interface and the no-shear condition at the free surface, Equation (2.5.4) can be integrated to yield the velocity downstream of the jump:

$$u(r > r_J, z) = \text{Re} \left(\frac{1}{\text{Fr}^2} \frac{dh}{dr} - \Omega^2 r \right) \left(\frac{z^2}{2} - hz \right). \quad (2.5.5)$$

Upon inserting Equation (2.5.5) into the mass conservation Equation (2.2.9) and integrating, the governing equation for the film thickness downstream of the jump becomes

$$\frac{dh}{dr} = -\frac{3}{2} \frac{Fr^2}{Re} \frac{h^{-3}}{r} + Fr^2 \Omega^2 r. \quad (2.5.6)$$

The corresponding velocity reduces to

$$u(r > r_J, z) = -\frac{3}{2r} h^{-3} \left(\frac{z^2}{2} - hz \right). \quad (2.5.7)$$

The problem remains open as to the existence of an additional relation, which would allow us to determine uniquely the height and the location of the jump. This additional relation can be based on a boundary condition for the film height specified at the edge of the disk, that is $h(r = r_\infty) = h_\infty$. However, the specification of the height at the edge is theoretically not a simple matter. We discuss this issue by first examine the flow over a stationary disk.

2.5.2 The hydraulic jump over a stationary disk

In the stationary case, and subject to $h(r = r_\infty) = h_\infty$, an analytical solution exists for Equation (2.5.6):

$$h(r > r_J) = \left(h_\infty^4 + 6 \frac{Fr^2}{Re} \ln \left(\frac{r_\infty}{r} \right) \right)^{\frac{1}{4}}. \quad (2.5.8)$$

Obviously, in the presence of radial flow, the film thickness at the edge of the disk cannot be zero. Direct measurements by Duchesne *et al.* (2014) of this edge thickness, performed at nearly 5 mm of the disk perimeter in their experiment, give a nearly constant value with a weak power-law variation not exceeding a few per cent. This constant thickness value is very close to the capillary length $\sqrt{\gamma_0 / \rho g}$ of the fluid, which results from the balance of forces between the hydrostatic pressure and the surface

tension at the disk perimeter. This value is also consistent with the measurements of Dressaire *et al.* (2013). Similarly, we assume here that the film thickness at the edge of the disk is essentially equal to the film thickness the liquid exhibits under static conditions. This is not an unreasonable assumption since the flow downstream of the jump has predominantly the character of gradually varied flow. This static thickness is governed by the minimum free energy and was given by Lubarda & Talke (2011) as $h_s = 2\sqrt{\gamma_0 / \rho g} \sin(\theta_Y / 2)$, where θ_Y is the contact angle.

We note that the contact line is not present if the liquid flows off the edge evenly in ideal axisymmetric flow. In that case, the thickness near the edge of the disk should be pursued following the treatment of Higuera (1994). For realistic surface tension effect, however, the liquid film always breaks into several rivulets when falling off the edge, or even flows off the edge at only one spot in the capillary limit (Mohajer & Li 2015). Therefore, the film is mostly quasi static and stable along the rim of the disk and the thickness can be approximated by the quasi-static condition. Existing measurements show that the edge thickness is almost constant and on the order of the capillary length, which reflects the static film condition (Dressaire *et al.* 2010, Duchesne *et al.* 2014, Mohajer & Li 2015). We also observe that, even though the flow breaks into rivulets when flowing off the edge, the flow remains axisymmetric until getting very close to the rim of the disk where some weak azimuthal flow appears (Mohajer & Li 2015). In this case, the axisymmetric assumption should remain valid throughout most part of the domain, and this is the assumption we have made in the current work.

In addition, in order to explore the small variation of edge thickness with flow rate as observed by Duchesne *et al.* (2014), we resort to a minimum mechanical energy principle (Yang & Chen 1992; Yang, Chen & Hsu 1997). This principle states that a fluid flowing over the edge of a disk under the influence of a hydrostatic pressure gradient will adjust itself so that the mechanical energy within the fluid will be minimum with respect to the film thickness at the disk edge. We note that this approach originates from open-channel hydraulics (Bakhmeteff 1966). Consequently, the contribution on the thickness at the edge of the disk can be calculated by setting the derivative of the mechanical energy with respect to the film thickness equal to zero, that is

$$\frac{\partial}{\partial h} \int_0^h \left(Fr^2 \frac{u^2}{2} + h \right) dz = 0. \quad (2.5.9)$$

After substituting for $u(r > r_j, z)$ from Equation (2.5.7) into Equation (2.5.9), we obtain the variation of the thickness with the Froude number (flow rate) at the edge of the disk $(3/40)^{1/3} (Fr/r_\infty)^{2/3}$.

Taking into consideration this small dependence, we obtain the dimensionless film thickness at the edge as

$$h_\infty = 2\sqrt{\frac{1}{Bo}} \sin\left(\frac{\theta_Y}{2}\right) + \left(\frac{3}{40}\right)^{1/3} \left(\frac{Fr}{r_\infty}\right)^{2/3}. \quad (2.5.10)$$

Upon specifying the thickness $h(r = r_\infty) = h_\infty$ at the edge of the disk as per Equation (2.5.10), we obtain the film thickness distribution downstream of the jump from Equation (2.5.8), which is then substituted into the momentum balance Equation (2.5.3) to determine the location of the jump. For the current problem, we achieve a good agreement with the measurements of Dressaire *et al.* (2010) by taking $\theta_Y = 90^\circ$. This value is well within the range of values measured for water on polydimethylsiloxane (Diversified Enterprises 2009), which is the material used by Dressaire *et al.* (2010) for their disk.

The dependence of the jump location on the Froude number is reported in Figure 2-13, where a comparison with experiment is presented based on the data of Dressaire *et al.* (2010) for water, leading to good agreement. The original experimental data were reported in terms of the flow rate for a jet radius of 1 mm and a speed ranging approximately from 3 to 16 m/s. In this case, taking $g \approx 10 \text{ m/s}^2$, $\nu = 10^{-6} \text{ m}^2/\text{s}$ and $\gamma = 70 \text{ mN/m}$, we have $Bo = 0.13$ and $G = 10^{-2}$.

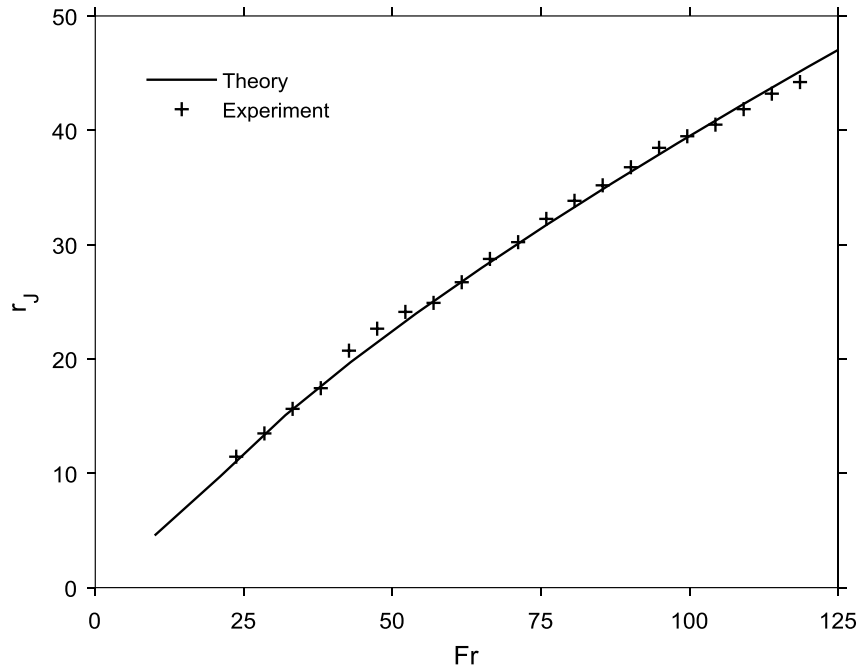


Figure 2-13: Dependence of hydraulic jump location on flow rate (Froude number) for a stationary disk. The figure shows the comparison between the current theoretical predictions and the measurements of Dressaire *et al.* (2010) for a water.

Bohr *et al.* (1993) and Rojas *et al.* (2013) found that the jump radius scales approximately as $Q^{5/8}v_0^{-3/8}g^{-1/8}$. Avedisian & Zhao (2000) investigated the circular hydraulic jump experimentally for normal and reduced gravity conditions. They measured the jump diameter and shape at the free liquid surface for an impinging jet on a stationary disk. Based on the reported two values of the flow rate and two gravitational acceleration data provided, we find that the location of the jump behaves close to $g^{-1/9}$, roughly confirming the scaling of Bohr *et al.* (1993) for low gravity. Using the current scaling, the dimensionless form of Bohr *et al.* estimate can be written in terms of the transition location and the Froude number as $r_J \sim r_0^{9/8}Fr^{1/4}$, where we recall $r_0(\Omega=0) = (78/875Re)^{1/3}$ from Equation (2.3.7). More recently, Duchesne *et al.* (2014) derived a more accurate estimate involving a logarithmic correction based on the thin-film approach. When cast in dimensionless form, we find that the jump location

behaves like $r_J \sim Fr_J^{-1} Fr^{5/8} G^{-3/8}$, where Fr_J is the jump Froude number defined in terms of the jump height and the average velocity immediately after the jump. In our notation, $Fr_J = Fr / 2r_J (h_J^+)^{3/2}$. Duchesne *et al.* (2014) found that Fr_J remains sensibly independent of the flow rate (constant with respect to Fr), especially for a jet of fluid of low viscosity or at relatively large flow rate. Figure 2-14 shows the behaviour of Fr_J against Fr , corresponding to the prediction in Figure 2-13, based on the current formulation. It is found that Fr_J remains sensibly equal to 0.15. As a way to validate the current approach based on the cubic velocity profile, we also included in Figure 2-14 the result based on Watson's similarity solution, which indicates that both approaches yield essentially the same value for Fr_J . As a reference, we also reproduced the measurements of Duchesne *et al.* (2014) for silicon oil. In this case, it turns out that we essentially have $Fr_J \approx 0.33$. However, the data also suggest a deviation from the constant level at very low flow rate. This issue is further explored next by comparing the location of the jump in the low flow rate range.

It appears that in order to determine both the location and the height of the jump, we seem to have two alternatives: fixing the value of Fr_J or imposing the film thickness at the edge. Based on the results reported in Figures 2-13 and 2-14, the two alternatives are essentially equivalent. It is therefore important to further examine conditions where Fr_J may not remain independent of the flow rate. This is likely the case for impinging flow at low flow rate. For this purpose, we conduct a comparison against the data of Hansen *et al.* (1997), who measured the position of the hydraulic jump against the flow rate, ranging from 0 to 60 cm³/s. In this case, the contact angle in Equation (2.5.10) was taken for water and glass as 35° (Vicente *et al.* 2012). Figure 2-15 depicts the comparison between our formulation and experiment. The experimental data are reproduced in dimensionless form. The distribution of Fr_J versus Fr is also included for reference. The figure clearly confirms that Fr_J remains constant over the large Froude

number (flow rate) range. At small flow rate, Fr_J increases rather rapidly as Fr tends to zero.

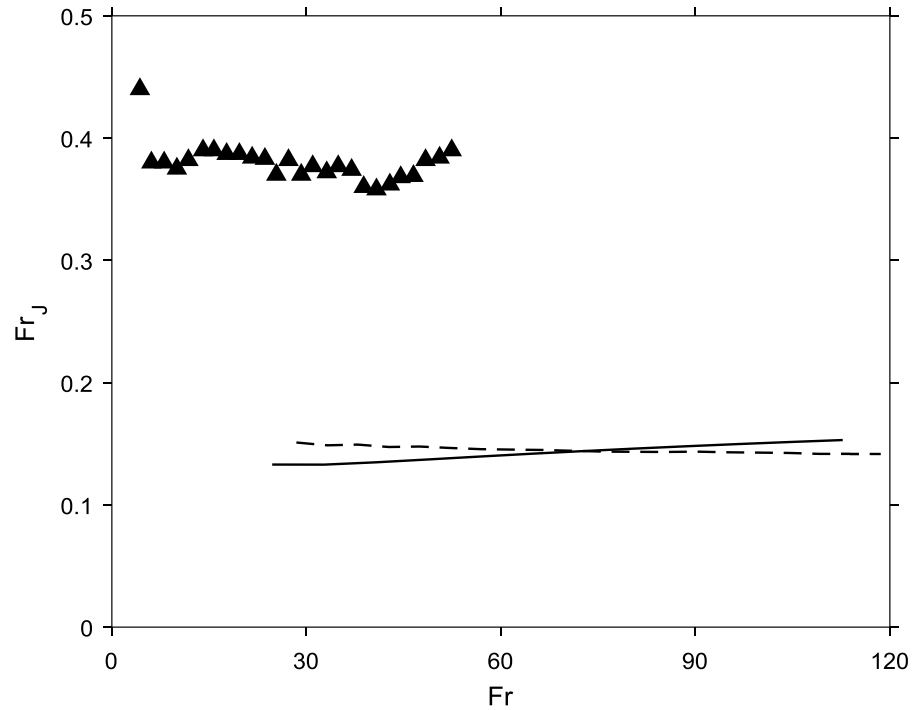


Figure 2-14: Dependence of Fr_J on the flow rate (Froude number) for a stationary disk. The solid and dashed lines show the results corresponding to the configuration of Dressaire *et al.* (2010) for water, based on the current cubic and similarity profiles, respectively. The data corresponding to silicon oil from Duchesne *et al.* (2014) are also included.

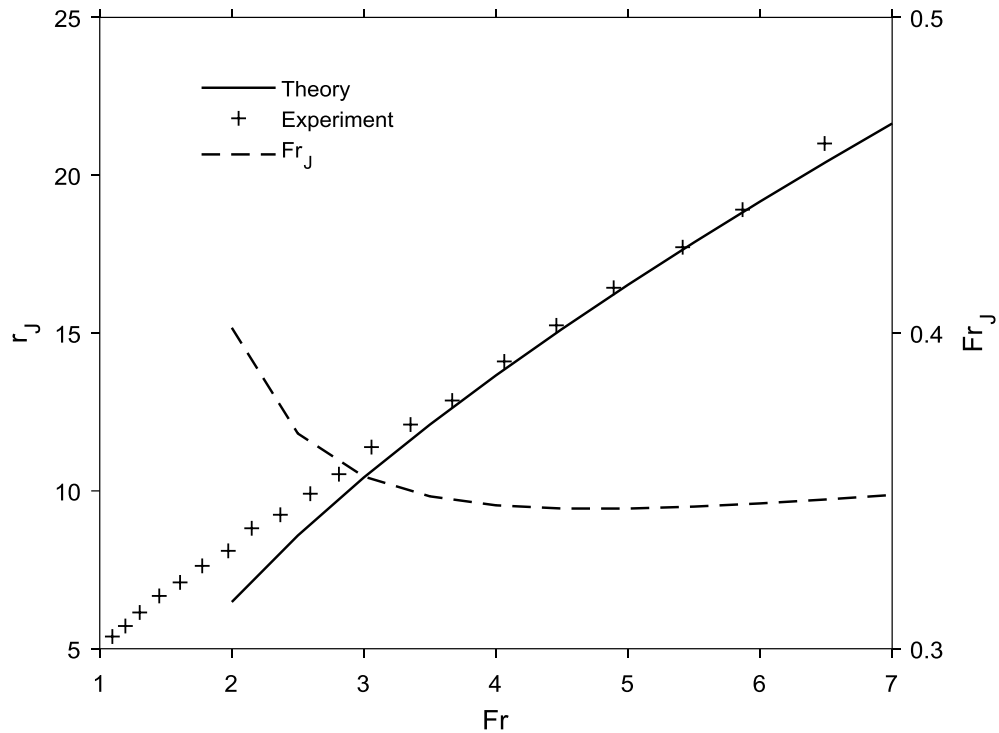


Figure 2-15: Dependence of hydraulic jump location on flow rate (Froude number) for a stationary disk. The figure shows the comparison between the current theoretical predictions and the measurements of Hansen *et al.* (1997) for a water jet on a glass disk. The distribution of Fr_j is also included.

It is clear from Figures 2-13 and 2-15 that the range of Froude numbers is not the same. The data of Hansen *et al.* (1997) are restricted to the very low range with no overlap with the data of Dressaire *et al.* (2010). Therefore, we confirm from the observations of Duchesne *et al.* (2014) as well as from their data in Figure 2-14, that Fr_j is not expected to remain constant in the low Froude number range.

Finally, we examine the validity of our approach regarding the actual size and shape of the jump. In their experiment of the flow of a thin film, Ozar *et al.* (2003) measured the jump profile against the radial distance on a stationary aluminium disk. The comparison between theory and experiment is reported in Figure 2-16 for two different flow rates for a disk of radius 203mm or $r_\infty = 4$. In this case, we take the contact angle for water and

aluminium to be 70° (Majeed 2014). For $Q = 7$ L/min, Figure 2-16a shows that the jump is located far upstream of the disk edge ($r_j \approx 2$), whereas for $Q = 15$ L/min, Figure 2-16b shows that the jump is located close to the edge. In both cases, the jump height exhibits a maximum and tapers rather rapidly near the edge. The comparison shows a rough agreement for the thickness distribution upstream of the jump as well as for the (average) location and height of the jump for the two flow rates. Again, due to the difference in flow configuration, the agreements should be acceptable.

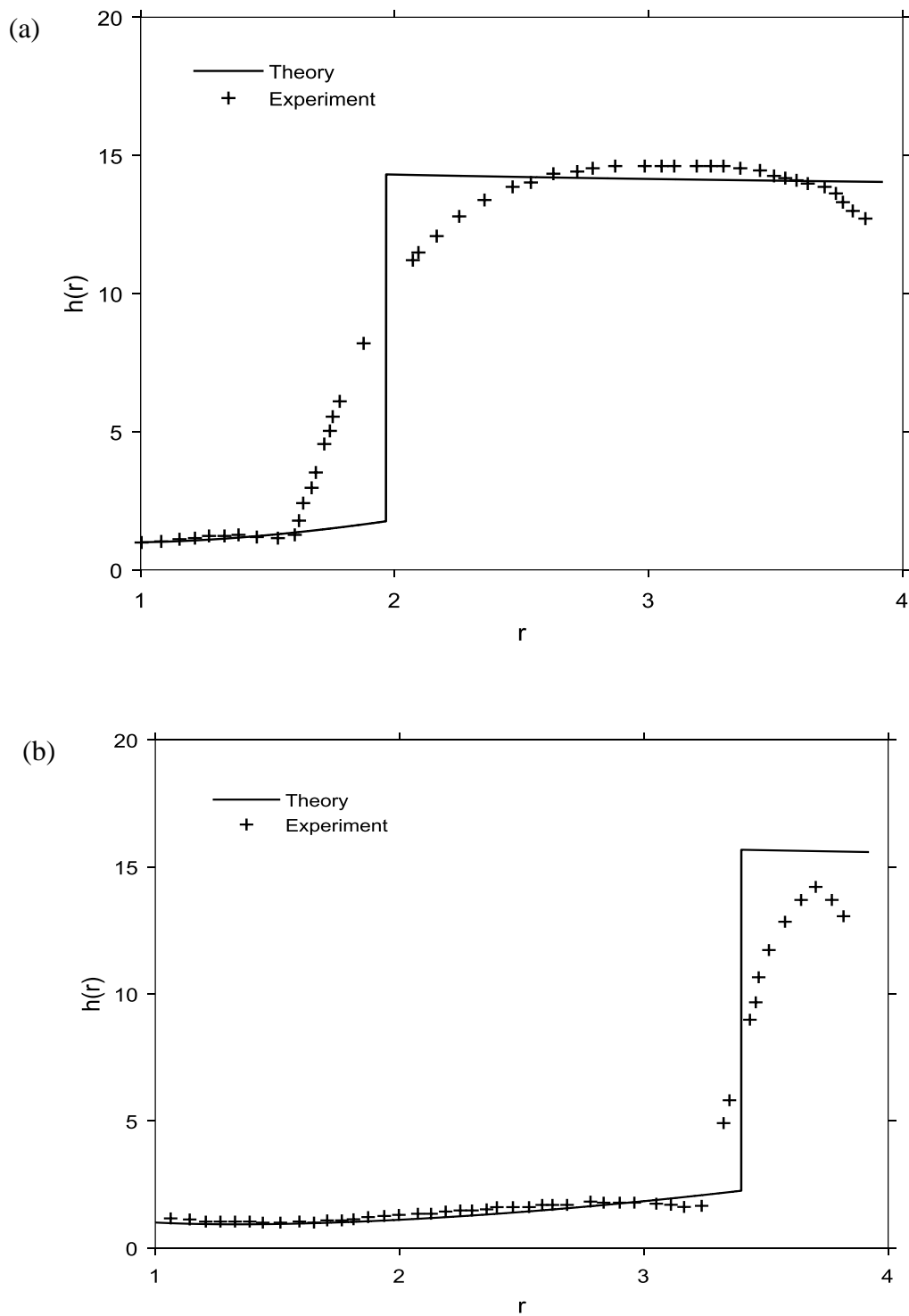


Figure 2-16: Comparison between theory and the measurements of Ozar *et al.* (2003) for the hydraulic jump of a thin film flowing on a stationary disk for $Q = 7$ L/min (a) and $Q = 15$ L/min (b).

2.5.3 The hydraulic jump over a rotating disk

In the case of a rotating disk, the thickness at the edge is expected to vary with the speed of rotation as well as the jet flow rate and surface tension. In this case, while the minimum energy principle is expected to hold, the static film thickness must be adjusted to account for rotation. We expect the thickness at the edge to decrease with rotation speed and increase with the flow rate as it should somehow reflect a balance between the centrifugal acceleration, the hydrostatic pressure and the surface tension. However, the measurements of Duchesne *et al.* (2014) as well as those of Dressaire *et al.* (2010) seem to suggest little influence of the flow rate, which is also supported by our predictions in Section 2.5.2 above. Although these observations are conclusive for a stationary disk, we expect them to hold for a rotating disk.

However, the influence of rotation speed on the thickness at the edge of a rotating disk remains unaddressed. Here, we examine the effect of rotation by taking guidance from the extensive existing insight in thin-film spin coating. In this process, a drop of liquid solution is deposited onto a rotating substrate (wafer). After an initial acceleration, the liquid reaches a uniform thickness that is sufficiently small for the viscous shear drag to balance the centrifugal acceleration. At this stage, the film begins to dry up as the solvent evaporates, ultimately exhibiting a constant and steady thickness. Theory as well as experiment suggest that the final thickness varies with rotation speed like $h_f \sim \nu_0^{1/3} \omega^{-2/3}$ (Hall *et al.* 1998), where the kinematic viscosity ν_0 appears to be the main influencing liquid property. This behaviour is observed at relatively large spin speed and does not take into account the static limit that corresponds to $\omega = 0$. We find the overall behaviour that seems to fit well experiment to be of the form:

$$h_f = \frac{h_s}{1 + \beta h_s \left(\frac{\omega^2}{\nu} \right)^{1/3}}. \quad (2.5.11)$$

Here β is an empirical coefficient in units of $(s/m)^{1/3}$. To illustrate the applicability of Equation (2.5.11), we examine the flow of photoresist AZ6600 liquid series, which are

liquid films used as resistant substance applied as a coating to protect a surface during some process, for example to prevent dye or glaze adhering (MicroChemicals 2013). Figure 2-17 shows the data and curves based on Equation (2.5.11) for five AZ6600 liquid films based on measurements reported by Clariant GmbH (see reference source below). In this case, all five liquid films have sensibly the same surface tension for a contact angle of 90° , namely 10 mN/m . (Bauer *et al.* 1997), yielding $h_s = 1.7 \text{ mm}$. The kinematic viscosities are as follows: 19 cSt (AZ6612), 27.7 cSt (AZ6615), 34.3 cSt (AZ6618), 58.5 cSt (AZ6624) and 82 cSt (AZ6632). Figure 2-17 shows a significant drop in the film thickness from the static level at low spin speed, reflecting the difficulty of the liquid to spread initially. Figure 2-17 also shows the final film thickness as function of rotation speed in the spin coating of AZ6600 photoresist liquid films. The values of β are given for a best fit of expression Equation (2.5.11). The data are reproduced from MicroChemicals (2013). The inset shows data amplified in the small thickness range.

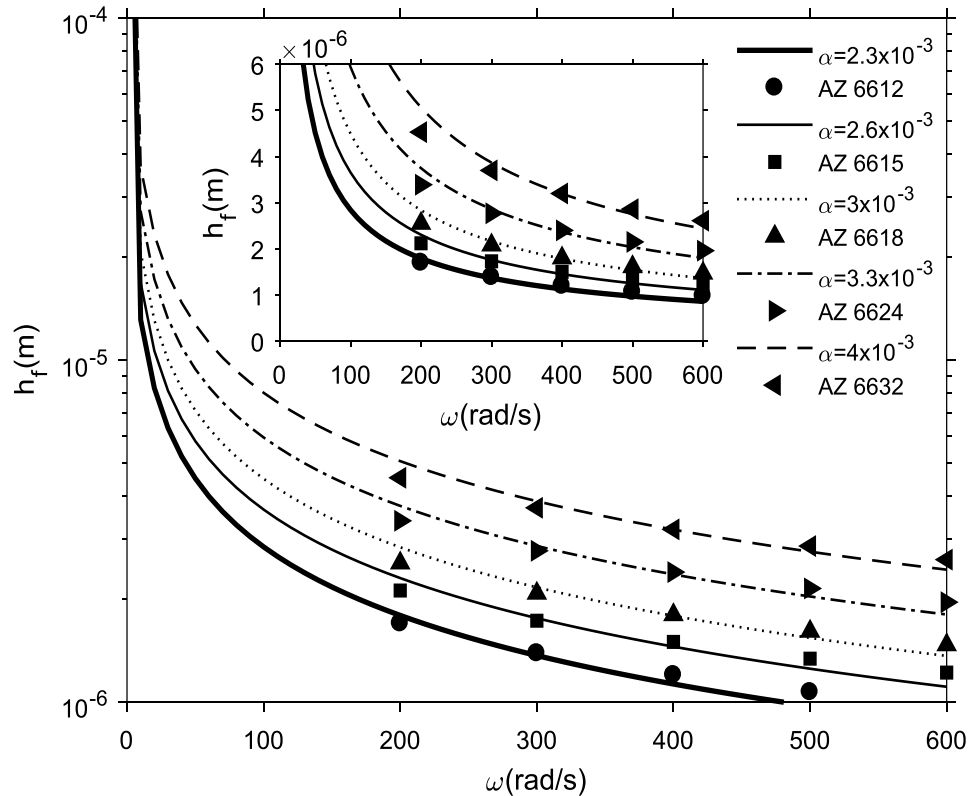


Figure 2-17: Final film thickness as function of rotation speed in the spin coating of AZ6600 photoresist liquid films. The values of β are given for a best fit of Equation (2.5.11). Data are reproduced from MicroChemicals (2013). Inset shows data amplified in the small thickness range.

We now illustrate the influence of rotation on the jet flow and hydraulic jump by examining the behaviour of the AZ6612 liquid. The flow configuration is the same as that of Dressaire *et al.* (2010) discussed in Section 2.5.2 for the stationary disk; only the fluid is now AZ6612 instead of water and the jet radius is 4 mm instead of 1 mm. The location of the jump and corresponding height are shown respectively in Figures 2-18 and 2-19 against the Froude number (flow rate). We can see that the location of the jump is pushed outwards with higher rotating speed as well as higher flow rate, which is consistent with existing experimental findings (Ozar *et al.* 2003; Deng & Ouyang 2011). Here, the Coriolis acceleration associated with rotation can be seen as weakening the effect of gravity. Indeed, an interesting parallel can be established between rotation and body

forces. The measurements of Avedisian & Zhao (2000) show that the steady state diameter of the jump under reduced gravity is larger than the diameter of the same jump under normal gravity conditions. Similar to the current case of a rotating disk, they predicted that the hydraulic jump would also disappear in the absence of gravity.

For a stationary disk ($\Omega = 0$), Figure 2-18 suggests that the location of the jump grows essentially linearly with flow rate. On a rotating disk, the growth rate increases for large rotating speeds.

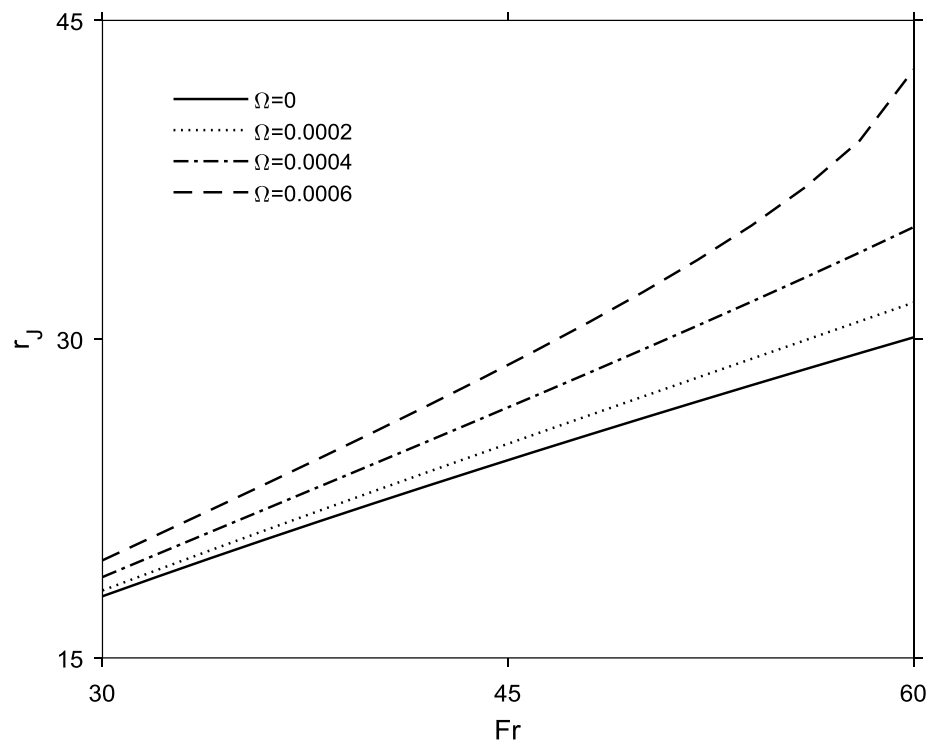


Figure 2-18: Influence of rotation on the hydraulic jump location, plotted against the Froude number (flow rate) for the AZ6612 photoresist fluid.

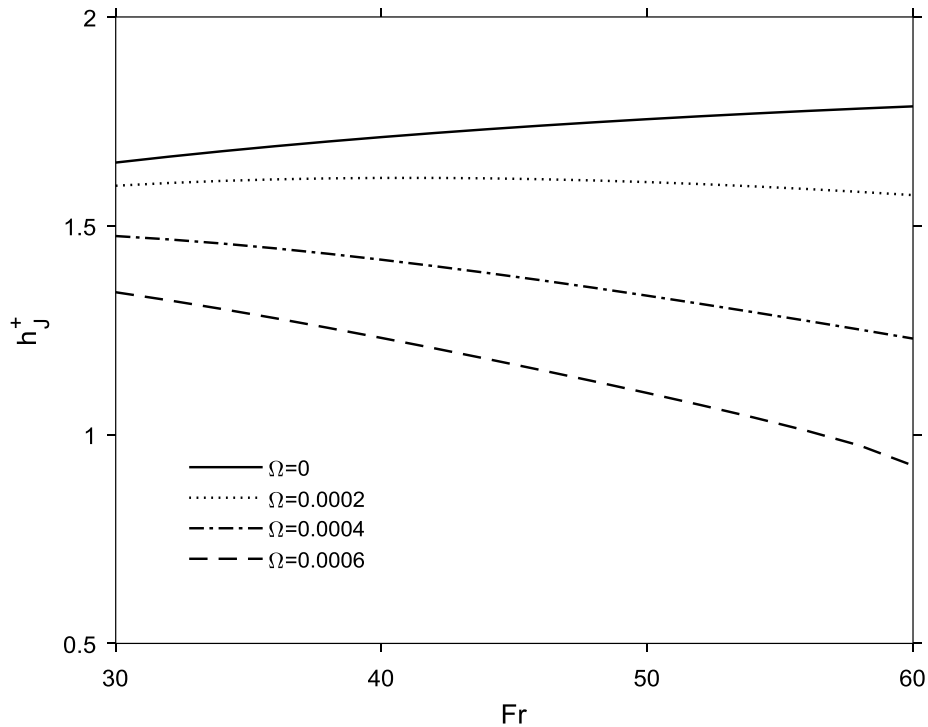


Figure 2-19: Influence of rotation on the hydraulic jump height, plotted against the Froude number (flow rate) for the AZ6612 photoresist fluid.

The jump height in Figure 2-19 is shown to grow monotonically with flow rate for a stationary disk but tends to exhibit a maximum at low rotation speed. At higher rotation speed, the jump decreases with flow rate, suggesting that the jump weakens as it is being pushed towards the disk edge. Although there is no indication from the figure that the jump has reached the edge of the disk ($r_{\infty} = 90$), this may not be the case in reality. A more accurate prediction would have to be based on a formulation that includes inertia since convective effects are bound to become more significant at higher flow rate.

The overall effect of rotation is illustrated in Figures 2-20 and 2-21, which depict the film thickness (Figure 2-20) and the corresponding surface velocity (Figure 2-21) over the entire disk for $Fr = 30$. For very small Ω , the jump saturates to the stationary case. The jump height decreases with increasing rotation rate, simultaneously as the jump location is pushed outwards toward the edge of the disk. However, the film thickness and surface

velocity upstream of the jump do not seem to vary significantly with Ω over the range reported here.

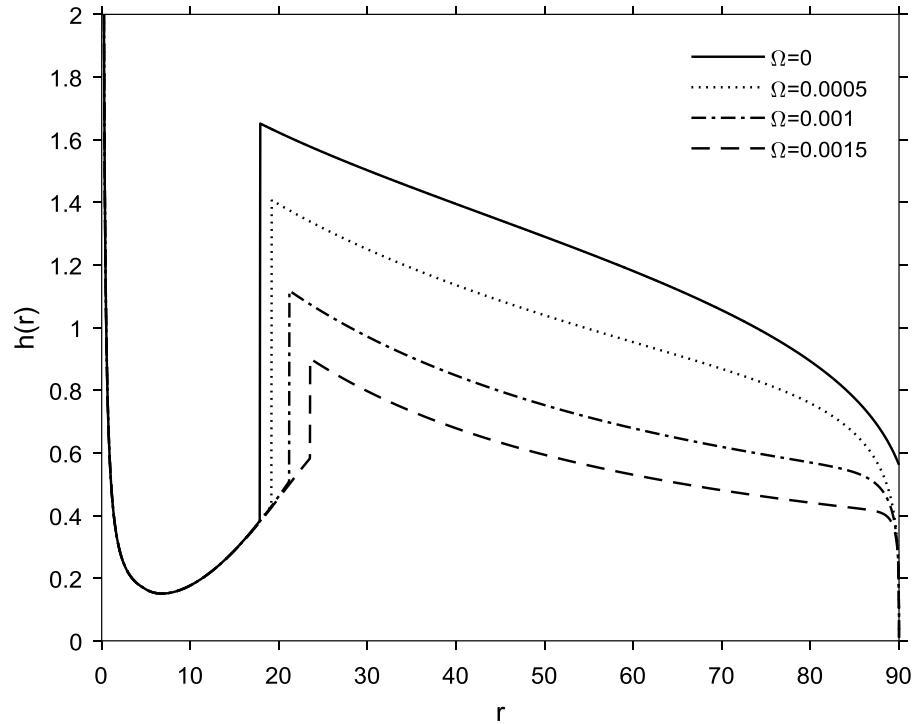


Figure 2-20: Influence of rotation on the film thickness plotted against radial distance in regions (ii), (iii) and (iv) for the AZ6612 fluid.

Overall, the velocity in Figure 2-21 is much less influenced by the rotation speed than the film thickness. For a stationary and low rotation speed ($\Omega = 0.001$), the existence of the jump is unquestionable. However, with higher rotation speed, the jump becomes weaker, which may signal the beginning of the vanishing of hydraulic jump. Both the thickness and velocity decrease monotonically with radial distance, followed by a drastic thinning near the edge of the disk that is enhanced by centrifugal effect.

Finally, we observe from Figures 2-20 and 2-21 that the flow appears insensitive to the variation of the rotation speed. This insensitivity corroborates well with experiment at least for the range of speeds reported here.

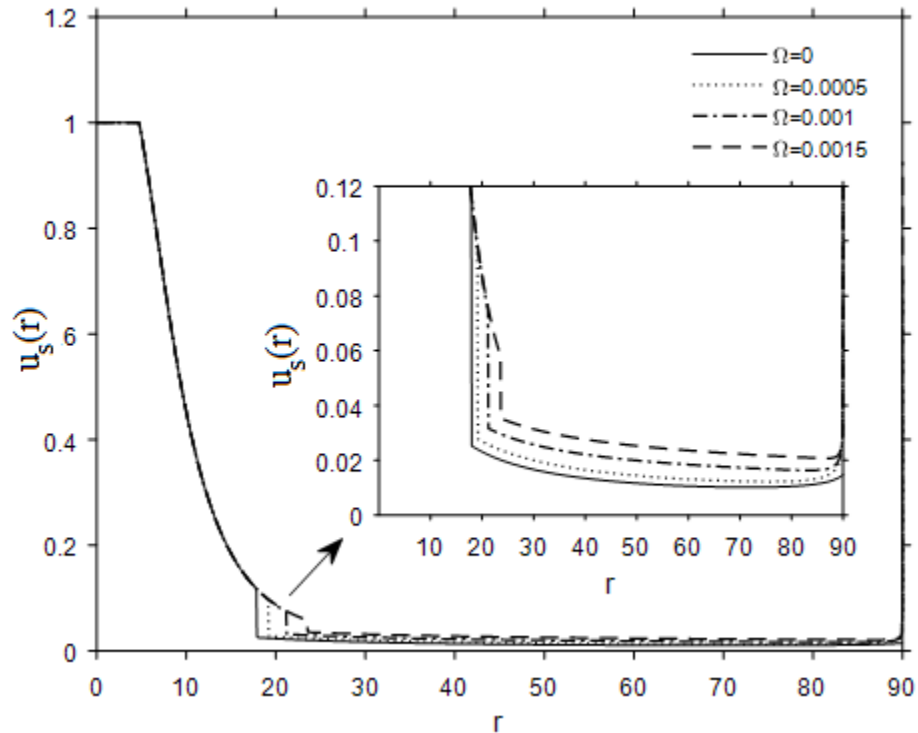


Figure 2-21: Influence of rotation on the film free-surface velocity plotted against radial distance in regions (ii), (iii) and (iv) for the AZ6612 fluid. Inset shows the amplification around the jump.

2.6 Concluding remarks

In this study, the flow of a jet impinging on both a stationary and rotating disk is examined theoretically. The flow is assumed to remain steady and axisymmetric (Figure 2-1). The range of Reynolds number and rotation speed for which axisymmetric flow is expected is established from existing linear stability analysis (Figure 2-2). A model is developed based on the Kármán–Pohlhausen integral approach to describe the behaviour of the flow in the developing boundary-layer region (ii) and the fully-viscous region (iii). The integral form of the continuity and momentum equations is treated numerically separately in each region, and the flow is matched at the transition point. Unlike the flow on a stationary disk, the radial velocity does not admit a similarity profile. A cubic profile is assumed for the velocity, which is commonly used and was shown to be accurate. A momentum balance is taken across the hydraulic jump, including the centrifugal effect

and surface tension, and the flow is assumed to be non-convective (non-inertial) downstream of the jump, where a lubrication flow is assumed with the rotational effect accounted for.

We find that rotation tends to enhance inertia, leading to a drop in the boundary layer height as well as the film thickness in region (ii). Near the stagnation point, the boundary layer grows like $\sqrt{r/\text{Re}}$, which is expected since the centrifugal effect is dominated by convective inertia. Further downstream, a maximum develops before the boundary-layer thickness decreases as a result of strong centrifugal effect (Figure 2-3). The transition point, where the outer edge of the boundary layer intersects the film surface, moves towards the perimeter of the disk with increasing rotation speed while the film thickness at the transition location diminishes (Figure 2-4).

The development of a maximum also occurs for the thickness in the fully-viscous region (iii), which is a behaviour observed only for the flow of a film on a rotating disk. Closer to impingement, the film thickness decreases rapidly and exhibits a minimum that weakens with rotation speed before experiencing the maximum. Simultaneously, a significant effect of the rotation speed is predicted on the surface velocity as it tends to increase and decay at a lower rate with radial distance (Figures 2-5 and 2-6). Interestingly, unlike the film thickness, the surface velocity decays monotonically with distance (Figure 2-7). In contrast, the shear stress along the wall exhibits a minimum for a rotating disk, which strengthens and becomes located closer to impingement as the rotation speed increases (Figure 2-8).

The numerical results clearly confirm the presence of an inner region that is inertia dominated where the film thickness grows with radial distance like $h \sim r^2/\text{Re}$ until it reaches the maximum height where convective and centrifugal effects are of the same order, at a location given approximately as $r_{\text{max}} \sim (\text{Re}/\Omega)^{1/4}$ and a value $h_{\text{max}} \sim 1/\sqrt{\text{Re}\Omega}$. Further downstream, in the outer region where the centrifugal effect dominates, the film thickness decreases like $h \sim (\text{Re}\Omega^2 r^2)^{-1/3}$. Meanwhile, the wall

shear stress is found to decay like $\tau_w \sim \text{Re}^2 r^{-5}$ in the inner region. Further downstream, and in contrast to the flow on a stationary disk, the shear stress experiences a minimum and then increases like $\tau_w \sim (\text{Re}^2 \Omega^4 r)^{1/3}$ as a result of film thinning. Our numerical results corroborate well existing measurements in the published literature.

An important issue that remains unaddressed in the literature is the prediction of the hydraulic jump without experimental input. In this study, we specify the thickness h_∞ of the film at the edge of the disk based on a static and a dynamic contribution to the thickness at the edge of the disk. Comparison between our predictions and published measurements of the jump location against the flow rate for water lead to excellent agreement (Figures 2-13, 2-15 and 2-16), especially in the higher range of Froude number (high flow rate or low viscosity), where the jump is clearly identified (i.e. a sharp jump). These arguments are then extended to account for disk rotation, taking guidance from existing analyses and measurements on the influence of rotation on the film thickness in spin coating (Figure 2-17). The hydraulic jump is found to be pushed outwards with rotation speed as well as with flow rate. The existence of the jump is obvious for a stationary disk and at low rotation speed. However, the jump weakens with increasing rotation speed, and for very large rotating speed (small Rossby number), should eventually disappear (Figure 2-20).

Finally, we observe that, downstream of the hydraulic jump, the change in liquid thickness with radial distance for low-viscosity liquids (e.g. water) is very small (Figure 2-16a). This phenomenon is also reported by Dressaire *et al.* (2010). In fact, the hydrostatic pressure gradient is driving force of the flow in the subcritical region. Due to the small viscosity and thus wall resistance, the decrease in the height of the free surface is not expected to be large. In this case, the thickness immediately downstream of the jump is also very close to the static thickness of a large flat droplet, which in nature reflects the dominance of the surface tension effect. This to some extent confirms the finding of Bhagat *et al.* (2018). However, they went too far to argue that surface tension is the main reason for any circular hydraulic jump and gravity is irrelevant. In fact, the effect of gravity depends on the viscosity of the liquid and should be more dominant for

high-viscosity liquids. More rigorous analysis on the issue can be found in Scheichl (2018, 2019).

On the other hand, it is also important to note that the viscous force is neglected in the momentum and force balance relation in Equation (2.5.3). This is surely a reasonable assumption provided the width of the jump is negligible. However, one would anticipate that the accuracy of this method should drop if the width of the jump is not small. In other words, the momentum destruction due to the viscous force at the bottom of the jump cannot be neglected if the jump is not sharp. Indeed, the sharp jump only occurs for low-viscosity liquid like water. For a high-viscosity liquid, the location of the jump is not always identifiable in reality, especially for high-viscosity liquids (Rojas *et al.* 2010). Moreover, gravity is neglected before the jump in the current chapter. For a liquid with high viscosity however, gravity should not be omitted before the jump since the strong viscous effect generally causes a large increase in the liquid thickness leading to a smooth jump. Consequently, there should be a more suitable method for high-viscosity liquids. These issues will be addressed in the next chapter.

2.7 References

Avedisian, C. T. & Zhao, Z. 2000 The circular hydraulic jump in low gravity. *Proc. R. Soc. London, Ser. A* **456**, 2127–2151.

Bakhmeteff, B. A. 1966 *Hydraulics of Open Channels* (McGrawHill, New York).

Bauer, J., Drescher, G., Silz, H., Frankenfeld, H. & Illig, M. 1997 Surface tension and adhesion of photo and electron-beam resists. *Proc. SPIE* 3049, Advances in Resist Technology and Processing XIV, 640 (July 7).

Bohr, T., Dimon, P. & Putzkaradze, V. 1993 Shallow-water approach to the circular hydraulic jump. *J. Fluid Mech.* **254**, 635-648.

Bohr, T., Ellegaard, C., Hansen, A. E. & Haaning, A. 1996 Hydraulic jumps, flow separation and wave breaking: An experimental study. *Physica B* **228**, 1-10.

- Bohr, T., Putkaradze, V. & Watanabe, S. 1997 Averaging theory for the structure of hydraulic jumps and separation in laminar free-surface flows. *Phys. Rev. Lett.* **79**, 1038-1041.
- Burns, J., Ramshaw, C. & Jachuck, R. 2003 Measurement of liquid film thickness and the determination of spin-up radius on a rotating disc using an electrical resistance technique. *Chem. Eng. Sci.* **58**, 2245–2253.
- Bush, J. W. M. & Aristoff, J. M. 2003 The influence of surface tension on the circular hydraulic jump. *J. Fluid Mech.* **489**, 229-238.
- Butuzov, A. I. & Pukhovoi. I. I. 1976 Liquid film flow regimes on a rotating surface. *J. Eng. Phys.* **31**, 886-891.
- Charwat, A., Kelly, R. & Gazley, C. 1972 The flow and stability of thin liquid films on a rotating disk. *J. Fluid Mech.* **53**, 227–255.
- Clariant GmbH. n.d. AZ 6600 Series General-Purpose Photoresists. https://www.microchemicals.com/micro/tds_az_6600_series.pdf
- Craik, A., Latham, R., Fawkes, M. & Gibbon, P. 1981 The circular hydraulic jump. *J. Fluid Mech.* **112**, 347-362.
- Crowe, C. T. 2009 *Engineering Fluid Mechanics*. (9th edition, John Wiley & Sons, Inc.).
- Deng, H. & Ouyang, H. 2011 Vibration of spinning discs and powder formation in centrifugal atomization. *Proc. R. Soc. A.* **467**, 361–380.
- Diversified Enterprises (2009) Surface Energy Data for PDMS (Polydimethylsiloxane): http://www.accudynetest.com/polymer_surface_data/polydimethylsiloxane.pdf
- Dressaire, E., Courbin, L., Crest, J. & Stone H. A. 2010 Inertia dominated thin-film flows over microdecorated surfaces. *Phys. Fluids* **22**, 073602-07

Duchesne, A., Lebon, L. & Limat, L. 2014 Constant Froude number in a circular hydraulic jump and its implication on the jump radius selection. *Europhys. Lett.* **107**, 54002.

Hall, D. B., Underhill, P. & Torkelson, J. M. 1998 Spin coating of thin and ultrathin polymers. *Polym. Eng. Sci.* **38**, 2039-2045.

Hansen, S. H., Horluck, S., Zauner, D., Dimon, P., Ellegaard, C. & Creagh, S. C. 1997 Geometric orbits of surface waves from a circular hydraulic jump. *Phys. Rev. E* **55**, 7048-7061.

Higuera, F. J. 1994 The hydraulic jump in a viscous laminar flow. *J. Fluid Mech.* **274**, 69-92.

Kasimov, A. R. 2008 A stationary circular hydraulic jump, the limits of its existence and its gasdynamic analogue. *J. Fluid Mech.* **601**, 189-198.

Khayat, R. E. 2016 Impinging planar jet flow and hydraulic jump on a horizontal surface with slip. *J. Fluid Mech.* **808**, 258-289.

Khayat, R. E. & Kim, K. 2006 Thin-film flow of a viscoelastic fluid on an axisymmetric substrate of arbitrary shape. *J. Fluid Mech.* **552**, 37-71.

Lawley, A. 1992 *Atomization: The Production of Metal Powders*. Metal Powder Industries Federation.

Lienhard, J. 2006 Heat transfer by impingement of circular free-surface liquid jets. *18th National & 7th ISHMT-ASME Heat and Mass Transfer Conference* (IIT Guwahati, India) 1-17.

Liu, X. & Lienhard, J. 1993 The hydraulic jump in circular jet impingement and in other thin liquid films. *Experiments in Fluids* **15**, 108-116.

Liu, X., Gabour, L. A. & Lienhard, J. 1993 Stagnation-point heat transfer during impingement of laminar liquid jets: Analysis including surface tension. *ASME J. Heat Transfer* **115**, 99-105.

Lubarda, V. & Talke, K. A. 2011 Analysis of the equilibrium droplet shape based on an ellipsoidal droplet Model. *Langmuir* **27**, 10705–10713.

Majeed, M. H. 2014 Static contact angle and large water droplet thickness measurements with the change of water temperature. *Nahrain Univ. College Eng. J.* **17** (1), 114–128.

Matar, O. K., Sisoiev, G. M. & Lawrence, C. J. 2004 Evolution scales for wave regimes in liquid film flow over a spinning disk. *Phys. Fluids*. **16**, 1532-1545.

MicroChemicals 2013 Spin coating of photoresists:
http://www.microchemicals.com/technical_information/spin_coating_photoresist.pdf.

Miyasaka Y. 1974 On the flow of a viscous free boundary jet on a rotating disk. *Bull J. Soc. Mech. Eng.* **17**, 1469–1475.

Mohajer, B. & Li, R. 2015 Circular hydraulic jump on finite surfaces with capillary limit. *Phys. Fluids* **27**, 117102.

Ozar, B., Cetegen, B. M. & Faghri, A. 2003 Experiments on the flow of a thin liquid film over a horizontal stationary and rotating disk surface. *Experiments in Fluids* **34**, 556–565.

Passandideh-Fard, M., Teymourtash, A. R. & Khavari, M. 2011 Numerical study of circular hydraulic jump using volume-of-fluid method. *J. Fluids Eng.* **133**, 011401.

Prince, J. F., Maynes, D. & Crockett, J. 2012 Analysis of laminar jet impingement and hydraulic jump on a horizontal surface with slip. *Phys. Fluids* **24**, 102103.

Rahman M. & Faghri A. 1992 Numerical simulation of fluid flow and heat transfer in a thin liquid film over a rotating disk. *Int. J. Heat Mass transfer* **35**, 1441–1453.

Rao, A. & Arakeri, J. H. 1998 Integral Analysis Applied to Radial Film Flows. *Int. J. Heat Mass Transfer* **41**, 2757–2767.

Rauscher, J., Kelly, R. & Cole, J. 1973 An asymptotic solution for the laminar flow of a thin film on a rotating disk. *J. Applied Mech.* **40**, 43–47.

Rice, J., Faghri, A. & Cetegen, B. 2005 Analysis of a free surface film from a controlled liquid impinging jet over a rotating disk including conjugate effects, with and without evaporation. *Int. J. Heat Mass Transfer* **48**, 5192–5204.

Rojas, N., Argentina, M. & Tirapegui, E. 2010 Inertial lubrication theory. *Phys. Rev. Letts.* **104**, 187801-4

Rojas, N., Argentina, M. & Tirapegui, E. 2013 A progressive correction to the circular hydraulic jump scaling. *Phys. Fluids* **25**, 042105-9

Scheichl, B. “Centred splash of a vertical jet on a horizontal rotating disc: the thin radial film in the parabolic and weakly elliptic limit”; accepted as talk for: BAIL 2018 - International Conference on Boundary and Interior Layers, University of Strathclyde, Glasgow, UK; 2018-06-18 - 2018-06-22; in: "Boundary and Interior Layers, Computational and Asymptotic Methods - BAIL 2018", G. Barrenechea et al. (ed.); Springer, Lecture Notes in Computational Science and Engineering / ?? / Berlin, Heidelberg (2019), ISSN: 1439-7358.

Schlichting, H. & Gersten, K. 2000 *Boundary-layer theory* (Springer, Berlin).

Sisoev, G. M., Matar, O. K. & Lawrence, C. J. 2003 Axisymmetric wave regimes in viscous liquid film flow over a spinning disk. *J. Fluid Mech.* **495**, 385-411.

Sisoev, G. M., Goldgof, D. B. & Korzhova, V. N. 2010 Stationary spiral waves in film flow over a spinning disk. *Phys. Fluids.* **22**, 052106-6.

Stevens, J. & Webb, B. W. 1992 Measurements of the free surface flow structure under an impinging free liquid jet. *Trans. ASME J. Heat Transfer* **114**, 79–83.

Thomas, S., Faghri, A. & Hankey, W. 1991 Experimental analysis and flow visualization of a thin liquid film on a stationary and rotating disk. *J. Fluids Eng.* **113**, 73–80.

Thomas, S., Hankey, W., Faghri, A. & Swanson T. 1990 One-dimensional analysis of the hydrodynamic and thermal characteristics of thin film flows including hydraulic jump and rotation. *J. Heat Transfer* **112**, 728–735.

- Uma, B. & Usha, R. 2009 A thin conducting liquid film on a spinning disk in the presence of a magnetic field: dynamics and stability. *Trans. ASME J. Appl. Mech.* **76**, 041002.
- Vicente, C. M. S., Andre, P. S. & Ferreira, R. A. S. 2012 Simple measurement of surface free energy using a web cam. *Rev. Brasil. Ens. Fisica* **34**, 3312.
- Watson, E. 1964 The spread of a liquid jet over a horizontal plane. *J. Fluid Mech.* **20**, 481-499.
- Yang, S. & Chen, C. 1992 Laminar film condensation on a finite-size horizontal plate with suction at the wall. *Appl. Math. Modelling* **16**, 325-329.
- Yang, Y., Chen, C. & Hsu, P. 1997 Laminar film condensation on a finite-size wavy disk. *Appl. Math. Modelling* **21**, 139-144.
- Zhao, J. & Khayat, R.E. 2008 Spread of a non-Newtonian liquid jet over a horizontal plate. *J. Fluid Mech.* **613**, 411-443.

Chapter 3

3 The circular hydraulic jump for high-viscosity liquids

As discussed at the end of last chapter, the force and momentum balance would become less accurate if the width of the jump is not negligible (i.e. a smooth jump) which is usually the case for liquids of high viscosity. Also, gravity effects will dominate the flow upstream of the jump and thus become non-negligible. In this chapter, we will include gravity in the supercritical region and illustrate the effects of gravity on the boundary layer, the liquid thickness and the hydraulic jump for high-viscosity liquids.

3.1 Introduction

A circular hydraulic jump is expected to arise when a fluid jet falling vertically at high Reynolds number impacts the disk. The fluid spreads radially as a thin film until reaching a critical radius at which the film rises abruptly. The regions before and after the jump are known as the supercritical and subcritical regions respectively. Impinging jet flow is important in numerous industrial applications such as jet cooling, jet quenching and surface cleaning etc. The fast motion of liquid inside the jump provides high rate of heat and mass transfer whereas the low velocity caused by hydraulic jump dramatically harms the performance (Mohajer & Li 2015). Although the impingement of a circular jet has been extensively considered, there remain important issues as to a fully theoretical formulation, particularly concerning the prediction of the jump location and height for high-viscosity liquids.

Watson (1964) formulated an appropriate description of the supercritical flow using boundary layer equations. Gravity was neglected before the jump due to the small thickness. The location of the jump was determined by a force and momentum balance method given the downstream height of the liquid. Watson's theory was tested in many experimental investigations, including those of Watson himself, Craik *et al.* (1981), Stevens & Webb (1992), Bush & Aristoff (2003) and Baonga *et al.* (2006). Bush & Aristoff (2003) improved Watson's theory by including the effect of surface tension and achieved better agreements with experiments.

We note that in the force and momentum balance proposed by Watson (1964), the shear stress at the bottom of the jump is neglected since the width of the jump is assumed to be small. This approximation is generally satisfying for sharp (steep) hydraulic jumps. However, smooth jumps can also occur, and the location of the jump is not always identifiable in such cases, especially for high-viscosity liquids and flow at low speed. The numerical simulation of Rojas *et al.* (2010) also depicts the ambiguity in the jump location. Their numerical film profiles in their figure 2 illustrate how the abrupt jump ceases to exist with increasing viscosity, giving way to a smoother profile. We also note that gravity is neglected before the jump in Watson's theory. For a liquid with high viscosity however, gravity should not be neglected in the supercritical region since the strong viscous effect often causes a large slope of the free surface.

Several studies have considered the gravitational effect in the supercritical region. Tani (1949) first proposed the idea that the hydraulic jump is a result of flow separation caused by the accumulating hydrostatic pressure in the supercritical region. He incorporated gravity before the jump and obtained a differential equation governing the film thickness using the K-P approach. However, an upstream condition has to be artificially given or taken from the experiments. Following the idea of Tani (1949), Bohr *et al.* (1993) derived an ordinary differential equation for the average velocity using shallow-water theory (i.e. thin-film approximation). The equation turned out to have a single critical point which is a spiral (see Tani 1949) and can exhibit an essential singularity at some finite distance. Bohr *et al.* (1993) argued that the jump location is close to the critical spiral point of their averaged equation and deduced that the jump radius scales as $Q^{5/8} v_0^{-3/8} g^{-1/8}$. However, this scaling only depends on the overall flow rate, not the specific velocity. The influence of nozzle-to-disk distance on the hydraulic jump radius was investigated experimentally by Brechet & Neda (1999), who reached a scaling law similar to that proposed by Bohr *et al.* (1993). They also observed that the nozzle-to-disk distance has no influence on the jump location. We also note that the scaling law of Bohr *et al.* (1993) cannot predict the shape of the jump. In this regard, Bohr *et al.* (1997) and Watanabe *et al.* (2003) proposed a new model that can cross the jump and predict the shape of the jump using a non-self-similar velocity. However, two experimental points are needed in their solution to fix the

boundary conditions. In addition, the two points should be close to the jump, otherwise making the solution unstable. Therefore, some prior knowledge of the location of the jump was also required. More importantly, as the boundary layer equations do not strictly hold across the jump, the validity of their solution is questionable. Kasimov (2008) modified the formulation of Bohr *et al.* (1993) by adding the effect of surface tension and incorporating the shape of a flat plate with a falling edge, however no comparison with experiments were attempted.

Duchesne *et al.* (2014) showed experimentally that the jump Froude number based on the jump height and velocity is independent of the flow rate. This constant jump Froude number should in principle provide the desired relation for the full prediction of the jump location and height. However, no theoretical justification was provided. More recently, the measurements of Mohajer & Li (2015) do indeed support the claim of Duchesne *et al.* (2014) but found that the jump Froude number is not independent of the surface tension. Chapter 2 addressed this issue and provided some theoretical arguments and comparisons with experiment in support of the claim of Duchesne *et al.* (2014). The thickness at the edge of the disk was determined as a combination of static and dynamic contributions based on the local minimization of energy. The jump Froude number was found to remain essentially independent of the flow rate. However, the predictions were limited to low-viscosity liquids and high flow rates. We will revisit this issue in this chapter and prove that the constancy still holds for high-viscosity liquids.

The main objective of the present study is the theoretical prediction of the jump location and height for liquids of high viscosity. In particular, we explore the role of gravity and its influence on the location and height of the jump. We demonstrate the crucial role of gravity for liquids of relatively large viscosity and low surface tension. In Section 3.2, we outline the problem by giving the governing equations and boundary conditions in each region of the physical domain. The overall solution strategy is also discussed. In Section 3.3, the Kármán–Pohlhausen (K-P) approach is adopted to determine the boundary-layer structure and the film thickness upstream of the jump. The transition point is also located, where the boundary-layer edge and the free surface meet. In Section 3.4, the K-P approach is employed again to examine the viscous boundary-layer region and assess the

influence of gravity on the thin-film flow and jump location. Comparison with experiment is also carried out. In Section 3.5, the height of the hydraulic jump is first calculated using the momentum and force balance method, and the effect of gravity on the jump is analyzed. The drawback of this approach is then discussed. Alternatively, we propose an approach based on the knowledge of the edge thickness from Chapter 2. Finally, concluding remarks and discussion are given in Section 3.6.

3.2 Physical domain and problem statement

Consider the steady laminar incompressible flow of a circular (axisymmetric) jet of a Newtonian fluid emerging from a nozzle of radius a , impinging at a volume flow rate Q on a flat disk lying normal to the jet direction. The flow configuration is depicted schematically in Figure 3-1, where dimensionless variables and parameters are used. The problem is formulated in the (r, θ, z) fixed coordinates, with the origin coinciding with the disk center. The flow is assumed to be independent of θ , thus excluding polygonal flow. In this case, $u(r, z)$ and $w(r, z)$ are the corresponding dimensionless velocity components in the radial and vertical directions, respectively. The r -axis is taken along the disk radius and the z -axis is taken parallel to the jet. The length and the velocity scales are conveniently taken to be the radius of the jet, a , and $Q/\pi a^2$ both in the radial and vertical directions. Since the pressure is expected to be predominantly hydrostatic for a thin film, it will be scaled by $\rho g a$. Two main dimensionless groups emerge in this case: the Reynolds number $Re = Q/\pi a \nu_0$, where ν_0 is the kinematic viscosity, and the Froude number $Fr = Q/\pi \sqrt{a^5 g}$, g being the acceleration due to gravity. We shall see that the problem can be reduced to a one-parameter problem, but the two parameters remain useful when comparing with experiment.

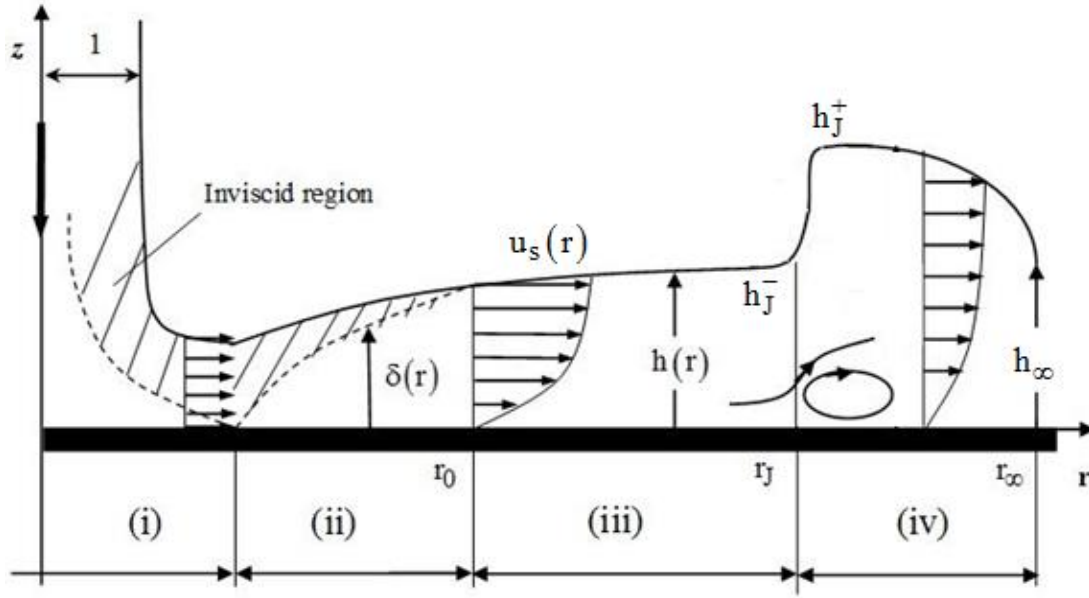


Figure 3-1: Schematic illustration of the axisymmetric jet flow impinging on a flat stationary disk and the hydraulic jump of type I. Shown are the stagnation region (i), the developing boundary-layer region (ii), the fully-viscous region (iii), and the hydraulic jump region (iv). All notations are dimensionless.

3.2.1 The physical domain

Following the treatment of Watson (1964), we identify four distinct flow regions for the jet over a circular disk, with smooth passage from one region to the next (see Figure 3-1): a stagnation flow region (i), a developing boundary-layer region (ii), where the boundary layer grows until it reaches the film surface at the transition location $r = r_0$ and a fully-viscous region (iii). A hydraulic jump emerges in region (iv), located at a radius $r = r_J$. We observe that $r = O(1)$ near the stagnation point in region (i). The velocity outside the boundary layer rises rapidly from 0 at the stagnation point to the impingement velocity in the inviscid far region. In region (ii), and as we shall confirm, the boundary layer is not expected to grow like $\sqrt{r/\text{Re}}$ in the presence of gravity. The speed outside the boundary layer remains almost constant, as the fluid here is unaffected by the viscous stresses. For $r \gg 1$, the flow field in region (ii) is not significantly affected by the stagnation flow of region (i). The region $1 \ll r < r_0$ will be referred to as the developing boundary-layer

region, with boundary-layer thickness $\delta(r)$, outside which the flow is inviscid and uniform. Here r_0 is the location of the transition point at which the viscous stresses become appreciable right up to the free surface, where the whole flow is of the boundary-layer type. At this point, in the absence of gravity, the velocity profile changes from the Blasius type to the self-similar profile. In contrast, in the presence of gravity, a similarity profile does not exist. The flow in region (iii), $r < r_0$, which will be referred to as the fully-viscous region, is bounded by the disk and the free surface $z = h(r)$.

Finally, the hydraulic jump in region (iv) occurs at a location $r = r_J$, which is larger than r_0 since the jump typically occurs downstream of the transition point. Referring to Figure 3-1, the height immediately upstream of the jump is denoted by h_J^- , and the height immediately downstream of the jump is denoted by h_J^+ . The subcritical height $h(r > r_J)$ is generally not constant and is different from the jump height h_J^+ . In this study, the fluid is assumed to be drained at the edge of the disk $r = r_\infty$ to maintain steady flow, with the film thickness denoted by $h_\infty = h(r = r_\infty)$. The edge thickness is not expected to depend heavily on the flow rate (Rojas *et al.* 2013, Mohajer & Li 2015).

3.2.2 Governing equations and boundary conditions

Unless otherwise specified, the Reynolds number is assumed to be large but without causing turbulence. Consequently, for steady axisymmetric thin-film flow, in the presence of gravity, the mass and momentum conservation equations are formulated using a thin-film or Prandtl boundary-layer approach, which amounts to assuming that the radial flow varies much slower than the vertical flow (Schlichting & Gersten 2000). By letting a subscript with respect to r or z denote partial differentiation, the reduced dimensionless conservation equations become

$$u_r + \frac{u}{r} + w_z = 0, \quad (3.2.1a)$$

$$\text{Re}(uu_r + wu_z) = -\frac{\text{Re}}{\text{Fr}^2} p_r + u_{zz}, \quad (3.2.1b)$$

$$p_z = -1. \quad (3.2.1c)$$

Here, p is the dimensionless pressure.

These are the thin-film equations commonly used to model the spreading liquid flow (Tani 1949; Bohr *et al.* 1993, 1996; Kasimov 2008). We observe that the pressure for a thin film is hydrostatic as a result of its vanishing at the film surface (in the absence of surface tension) and the small thickness of the film. In addition, upstream of the jump, the variation of the film thickness with the radius is expected to be smooth and gradual. In this case, the radial variation of the hydrostatic pressure is also small. Unlike the case of liquids of low viscosity, gravity cannot be neglected in the supercritical range. At the disk, the no-slip and no-penetration conditions are assumed to hold for any r . In this case:

$$u(r, z = 0) = w(r, z = 0) = 0. \quad (3.2.2)$$

At the free surface $z = h(r < r_j)$, the kinematic and dynamic conditions for steady flow take the form

$$w(r, z = h) = u(r, z = h)h'(r), \quad u_z(r, z = h) = p(r, z = h) = 0. \quad (3.2.3a,b)$$

Here a prime denotes total differentiation. The flow field is sought separately in the developing boundary-layer region (ii) for $0 < r < r_0$, the fully-viscous region (iii) for $r_0 < r < r_j$ and the hydraulic jump region (iv) for $r_j < r < r_\infty$. We observe that region (i) is neglected here as per Chapter 2. In this case, the leading edge of the boundary layer in region (ii) is taken to coincide with the disk center. Consequently, the additional boundary conditions are as follows. In region (ii), the flow is assumed to be sufficiently inertial for inviscid flow to prevail between the boundary-layer outer edge and the free surface (see Figure 3-1). In this case, the following conditions at the outer edge of the boundary layer and beyond must hold:

$$u_z(r < r_0, z = \delta) = 0, \quad u(r < r_0, \delta \leq z < h) = 1. \quad (3.2.4a,b)$$

Integrating Equation (3.2.1c) subject to condition (3.2.3b), the pressure becomes $p(r, z) = h(r) - z$, which is then eliminated so that Equation (3.2.1b) reduces to

$$\text{Re}(uu_r + wu_z) = -\frac{\text{Re}}{\text{Fr}^2} h' + u_{zz}. \quad (3.2.5)$$

Finally, the conservation of mass at any location upstream and downstream of the jump yields the following relation in dimensionless form:

$$\frac{1}{2r} = \int_0^{h(r)} u(r < r_j, z) dz \quad (3.2.6)$$

The presence of gravity causes the flow to be non-self-similar in character. Therefore, in the present study, approximate solutions are sought in each region. An integral approach of the Kármán -Pohlhausen (K-P) type (Schlichting & Gersten 2000) is adopted upstream of the jump. The cubic profile is used for the velocity, which is considered to be the leading-order solution in a comprehensive spectral approach when inertia is included (Khayat 2006, Rojas *et al.* 2010). The cubic profile seems to be amply adequate as it leads to close agreement with Watson's (1964) similarity solution for a jet impinging on a stationary disk (Prince *et al.* 2012). The cubic profile was also assessed by Khayat (2016) for a planar jet impinging on a surface with slip and was found to yield a good agreement against his numerical solution. See also Rao & Arakeri (1998) for an integral analysis of a rotating film. Higher-order polynomial velocity profiles were also used. In their study on flow separation and wave breaking, Bohr *et al.* (1996) used a quartic profile to illustrate the emergence of a singularity at the separation point for a thin film. A cubic velocity profile was later adopted by Bohr *et al.* (1997), accounting for regions of separation. The cubic profile was also adopted in Chapter 2 and was found to yield close agreement with experiment.

3.3 The flow in the developing boundary-layer and the transition location

Throughout this study, the stagnation region (i) under the impinging jet will not be considered. The velocity outside the boundary layer rises rapidly from 0 at the stagnation point to the impingement velocity in the inviscid far region. The impinging jet is predominantly inviscid close to the stagnation point, and the boundary-layer thickness remains negligibly small. Obviously, this is the case for a jet at relatively large Reynolds number. Ideally, the flow at the boundary-layer edge should correspond to the potential flow near the stagnating jet, with the boundary-layer leading edge coinciding with the stagnation point (Liu *et al.* 1993). However, the assumption of uniform horizontal flow near the wall and outside the boundary layer (as illustrated in Figure 3-1) is reasonable. The distance from the stagnation point for the inviscid flow to reach uniform horizontal velocity is small, of the order of the jet radius (Lienhard 2006). Also, the dominance of inertia near the stagnation point, albeit weakened by gravity, should make plausible the assumption of uniform horizontal flow near the impingement point. This assumption was adopted initially by Watson (1964) and is commonly used in the existing theories (see Bush & Aristoff 2003; Dressaire *et al.* 2010; Prince *et al.* 2012).

We therefore start by examining the flow in region (ii), where the inviscid flow dominates the upper layer ($\delta \leq z < h$) of the film in the radial direction. Consequently, the radial velocity above the boundary layer remains equal to one: $u_s(r) = 1$. The boundary-layer height δ is determined by considering the mass and momentum balance over the boundary-layer region (ii). Therefore, we consider first the integral form of the convective term in Equation (3.2.5). The vertical velocity component is eliminated by noting from Equation (3.2.1a) that $w(r, z) = -(1/r) \partial / \partial r \left(r \int_0^z u(r, z) dz \right)$. In this case,

$$uu_r + wu_z = \frac{\partial u^2}{\partial r} + \frac{u^2}{r} - \frac{1}{r} \frac{\partial}{\partial z} \left(u(r, z) \int_0^z \frac{\partial ru(r, \bar{z})}{\partial r} d\bar{z} \right) \quad (3.3.1)$$

Consequently, upon integrating Equation (3.3.1) across the boundary-layer thickness, we obtain the integral form of the momentum equation in the boundary-layer region:

$$\frac{\text{Re}}{r} \left[\frac{d}{dr} \int_0^{\delta} r u (u-1) dz \right] = -\frac{\text{Re}}{\text{Fr}^2} h' \delta - u_z (r, z=0). \quad (3.3.2)$$

The boundary layer grows with radial distance, eventually invading the entire film width, reaching the jet free surface at $r = r_0$. For $r < r_0$ and above the boundary-layer outer edge, at some height $z = h(r) > \delta(r)$, lies the free surface. The height of the free surface in region (ii) is then determined from mass conservation inside and outside the boundary layer. Therefore, for $r < r_0$,

$$\int_0^{\delta(r)} u(r, z) dz + h(r) - \delta(r) = \frac{1}{2r}. \quad (3.3.3)$$

For simplicity, we choose a cubic profile for the velocity. Thus, we let

$$u(r < r_0, z) = \frac{3}{2} \left(\frac{z}{\delta} \right) - \frac{1}{2} \left(\frac{z}{\delta} \right)^3 = \frac{1}{2} \eta (3 - \eta^2) \equiv f(\eta), \quad (3.3.4)$$

where $\eta = z/\delta$. The cubic profile (3.3.4) is obviously one of many that can be used. The cubic profile, which will also be modified and implemented in the fully-viscous region (iii), does not satisfy the momentum equation at $z = 0$ but so do many profiles used in the literature, including the parabolic profile used by Bohr *et al.* (1993) and Kasimov (2008). Indeed, it is not necessary to force to profile to satisfy the momentum equations at specific locations for an averaged method. For this reason, simple profiles are often adopted in the literature, including the cubic profile used by Prince *et al.* for a flow on a disk with isotropic (2012) and anisotropic (2014) slip, Watson's (axisymmetric) similarity profile used by Dressaire *et al.* (2010) to simulate non-axisymmetric hydraulic jump patterns. None of these profiles satisfy the momentum equation at the disk, yet they all lead to an accurate description. See, for instance, the comparisons of Dressaire *et al.*

(2010), Prince *et al.* (2012) and Khayat (2016). The profile (3.3.4) fulfils desirable criteria as it is simple and, and as we shall see, yields accurate results.

Upon inserting Equation (3.3.4) into Equation (3.3.2) and Equation (3.3.3), we obtain the following coupled equations for the boundary-layer and free-surface heights:

$$h - \frac{3}{8}\delta = \frac{1}{2r}, \quad (3.3.5a)$$

$$\frac{39}{280} \frac{\text{Re}}{r} \delta \frac{d}{dr}(r\delta) = \frac{\text{Re}}{\text{Fr}^2} h' \delta^2 + \frac{3}{2}. \quad (3.3.5b)$$

These equations are solved subject to $\delta(r=0)=0$. In the absence of gravity ($\text{Fr} \rightarrow \infty$), Equations (3.3.5) are easily solved to yield the following boundary-layer and film thicknesses:

$$\delta(r < r_0) = 2\sqrt{\frac{70}{39} \frac{r}{\text{Re}}}, \quad h(r < r_0) = \frac{1}{4} \left(\frac{2}{r} + \sqrt{\frac{210}{13} \frac{r}{\text{Re}}} \right), \quad (3.3.6a,b)$$

which agree with the $\delta \approx \sqrt{r/\text{Re}}$ behaviour established from the dimensional argument of Equation (3.2.5). In this case, h decreases rapidly, like $1/r$, near the disk center, reaching a minimum, and increases like \sqrt{r} further downstream. The transition location is determined by equating $h(r_0)$ and $\delta(r_0)$ to obtain $r_0 = ((78/875)\text{Re})^{1/3}$.

In the presence of gravity, Equations (3.3.5) must be solved numerically. The problem can be reduced to a one-parameter problem by introducing the following transformation:

$$r = \text{Re}^{1/3} \bar{r}, \quad (h, \delta) = \text{Re}^{-1/3} (\bar{h}, \bar{\delta}). \quad (3.3.7a,b)$$

Eliminating the film height and using Equation (3.3.7), the equation for the boundary-layer height reduces to, along with the film thickness:

$$\frac{3}{4} \left(\frac{1}{\alpha} \bar{\delta} - \frac{13}{35} \right) \bar{\delta} \bar{\delta}' = \frac{39}{140} \left(\frac{\bar{\delta}^2}{\bar{r}} \right) + \frac{1}{\alpha} \frac{\bar{\delta}^2}{\bar{r}^2} - 3, \quad \bar{h} = \frac{3}{8} \bar{\delta} + \frac{1}{2\bar{r}}. \quad (3.3.8a,b)$$

Here, we introduce

$$\alpha \equiv \text{Re}^{1/3} \text{Fr}^2, \quad (3.3.9)$$

which becomes the only parameter in the problem. Equation (3.3.8a) is solved numerically subject to $\bar{\delta}(\bar{r} = 0) = 0$, yielding in turn the height from Equation (3.3.8b).

Figure 3-2 illustrates the influence of gravity on the boundary-layer height. In the limit of infinite Froude number, the classical boundary-layer result is recovered (Watson 1964, Schlichting & Gersten 2000). As expected, gravity can have a tangible effect as the profiles in Figure 3-2 show a departure from the classical parabolic character of the boundary layer height. In fact, it is not difficult to show that the asymptotic solution of Equation (3.3.8a) for small r that the behaviour of the boundary-layer height near impingement is linear with distance. More precisely, $\bar{\delta} = \sqrt{3\alpha\bar{r}} + O(\bar{r}^2)$, or $\delta \approx \sqrt{3}(\text{Fr}/\sqrt{\text{Re}})r$ as opposed to $\delta = 2\sqrt{(70/39)r/\text{Re}}$ in the absence of gravity. The linear growth is clearly reflected by the $\alpha=10$ curve. Thus, the boundary-layer height approaches the linear behaviour with a diminishing slope as the level of gravity increases. We observe from Equation (3.3.8b) that, since the boundary-layer height is small near the origin, the film height decays like $\bar{h} \sim 1/2\bar{r}$ regardless of the level of gravity. This behaviour is also reflected by the h curves in Figure 3-2, showing a narrow spread when α is varied compared to δ . Gravity tends to lower the boundary-layer height.

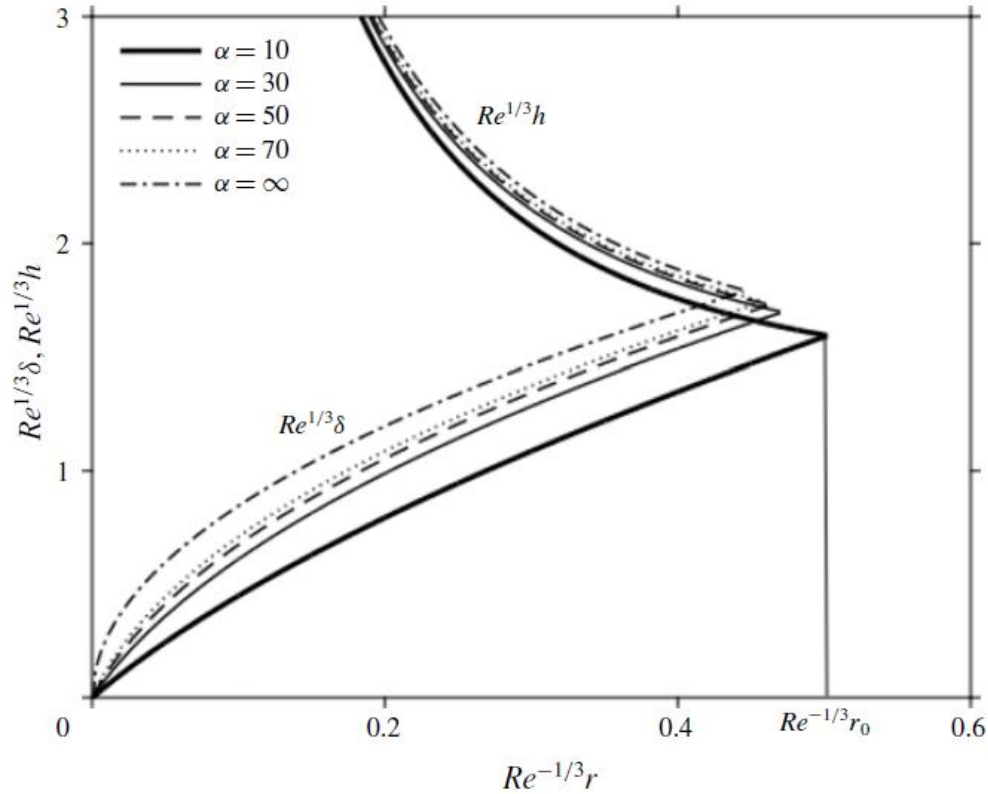


Figure 3-2: Influence of gravity in the developing boundary-layer region (ii). The rescaled boundary-layer height, δ , and film thickness, h , are plotted against the normalized radial distance. The transition location coincides with the intersection of the two heights (at the cusps in the figure). We only indicate the transition location by a vertical line for $\alpha = 10$.

The behaviour in Figure 3-2 can also be deduced qualitatively from Equation (3.2.5), where the effect of gravity tends to enhance the effect of inertia as a result of the decaying film thickness with distance. The level of inertia is reflected by the radial convective term $Re u u_r$. An estimate of the order of magnitude of this term is reached by taking u to correspond to the free-surface value. In this case, we see that $Re u u_r$ decays with distance like $Re r^{-1}$. There is an additional contribution to inertia stemming from gravity, namely through $-(Re/ Fr^2) h' \sim (Re/ 2Fr^2) r^{-2}$ for small r , making the boundary-layer height behaves roughly like $\delta \sim \sqrt{r/ Re} \left(1 + 1/ 2Fr^2 r\right)^{-1/2}$, which clearly

shows the diminishing influence of gravity on the boundary-layer height. Thus, for dominant gravity, this relation reduces to $\delta \sim (Fr/Re)r$, which is the linear behaviour based on Equation (3.3.8).

Figure 3-3 depicts the influence of gravity on the transition location r_0 and corresponding film thickness $h(r_0)$, which are determined by setting $h(r_0) = \delta(r_0)$. The transition location is further from impingement for a thinner film with increasing gravity as inertia is enhanced by gravity. This is the same trend predicted for the effect of slip. Similar to slip, gravity results in an asymptotic behaviour of the thickness for large α .

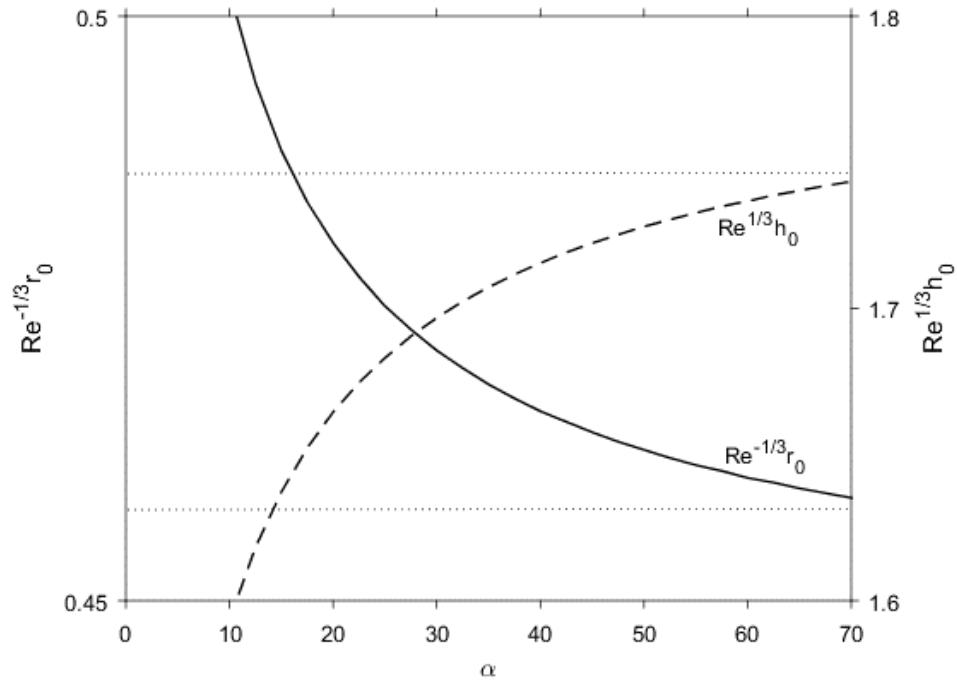


Figure 3-3: Dependence of the location and film thickness at the transition point between the developing boundary-layer and fully-viscous regions (ii) and (iii) on gravity.

3.4 The fully-viscous region and prediction of the jump location

In this section, we formulate the problem for the film thickness in region (iii) and examine the flow field in this region. We then determine the location of the jump based on the supercritical flow without recourse to the subcritical solution. The approach is validated against existing measurements of the jump radius and its dependence on the flow rate.

3.4.1 The equation for the film thickness

In region (iii), the potential flow in the radial direction ceases to exist, with the velocity $u_s(r) = u(r, z = h)$ at the free surface becoming dependent on r . We again assume a cubic velocity profile subject to conditions (3.2.3a) and (3.2.3b). In this case, the radial velocity profile is given as function of the surface velocity $u_s(r)$ as

$$u(r_0 < r < r_J, z) = u_s(r)f(\eta), \quad \eta = \frac{z}{h(r)}. \quad (3.4.1a,b)$$

Here, we observe that $f(\eta)$ is still given by Equation (3.3.4). Using the mass conservation Equation (3.2.6) yields the following relation:

$$u_s(r_0 < r < r_J) = \frac{4}{5hr}. \quad (3.4.2)$$

This equation agrees with equation (15) of Prince *et al.* (2012) when setting their slip parameter equal to zero.

Similar to Equation (3.3.2), the integral form of the momentum equation reads:

$$\frac{\text{Re}}{r} \frac{d}{dr} \int_0^h ru^2 dz = -\frac{\text{Re}}{\text{Fr}^2} hh' - u_z(r, z = 0). \quad (3.4.3)$$

Substituting Equation (3.4.1) into Equation (3.4.3) and using Equation (3.4.2) to eliminate u_s , we obtain the equation for the film thickness in the fully-viscous region:

$$\text{Re} \left(\frac{1}{\text{Fr}^2} - \frac{272}{875r^2h^3} \right) h' = \frac{4}{5rh^2} \left(\frac{68\text{Re}}{175} \frac{1}{r^2} - \frac{3}{2h} \right), \quad (3.4.4)$$

which is solved for $r \geq r_0$ subject to $h(r=r_0) = \delta(r_0)$. We observe that the flow in the absence of gravity is recovered in the limit $\text{Fr} \rightarrow \infty$. In this case, the problem reduces to the following equation and boundary condition:

$$\frac{dh}{dr} = -\frac{h}{r} + \frac{525}{136} \frac{r}{\text{Re}}, \quad h(r_0) = 2\sqrt{\frac{70}{39} \frac{r_0}{\text{Re}}}, \quad (3.4.5a,b)$$

which admits

$$h(r > r_0) = \frac{175}{136\text{Re}r} (r^3 - r_0^3) + 2\frac{r_0}{r} \sqrt{\frac{70}{39} \frac{r_0}{\text{Re}}} = \frac{175}{136} \frac{r^2}{\text{Re}} + \frac{233}{340} \frac{1}{r}, \quad (3.4.6)$$

as solution, where we recall $r_0 = ((78/875)\text{Re})^{1/3}$. For comparison, Watson's expression is reproduced here in dimensionless form:

$$h(r > r_0) = \frac{2\pi}{3\sqrt{3}} \frac{r^2}{\text{Re}} + \frac{3c(3\sqrt{3}c - \pi)}{8\pi} \frac{1}{r}. \quad (3.4.7)$$

Thus, we have $h \approx 1.21(r^2/\text{Re}) + 0.685(1/r)$ from Equation (3.4.6) compared to Watson's $h \approx 1.28(r^2/\text{Re}) + 0.69(1/r)$ from Equation (3.4.7), showing a close agreement, and validity of the cubic profile.

3.4.2 The supercritical flow and the location of the hydraulic jump

Equation (3.4.4) indicates that a singularity exists, occurring at some distance where the slope of the free surface becomes infinite. An equation similar to Equation (3.4.4) was

obtained by Bohr *et al.* (1993) by approximating the mean of the derivative of u^2 in the averaged momentum Equation (3.4.3) in terms of the derivative of the mean square. They showed that the singularity is not an artefact of the averaging process but is inherent to the thin-film equations. Of closer relevance is the equation obtained by Kasimov (2008) using a parabolic velocity profile, incorporating the shape of a finite disk with a sudden falling edge.

We conjecture that the location of the singularity coincides with the radius of the jump. Consequently, we now have a relation between the jump radius r_J and the film height \bar{h} immediately upstream of the jump:

$$\text{Fr}^{-2} = \frac{272}{875} \frac{1}{r_J^2 \bar{h}^3}. \quad (3.4.8)$$

We therefore identify the jump location or radius to occur when the slope of the free surface upstream of the jump becomes infinite, that is $h'(r = r_J) \rightarrow \infty$, which coincides with the occurrence of the singularity of Equation (3.4.4). At this location the relation between the jump radius and height is given by Equation (3.4.8). Obviously, this claim is bold and needs to be validated, which we shall do shortly. The jump location is found by simply integrating Equation (3.4.4) numerically subject to $h(r_0) = \delta(r_0)$ from r_0 to a distance r_J until Equation (3.4.8) is satisfied to within a certain tolerance. More details on the numerical treatment are given below.

Before comparing the predicted jump radius with existing measurements, it is helpful to explore the general supercritical flow behaviour (upstream of the jump). Once again, the flow becomes governed by a one-parameter problem when transformation (3.3.7) is used. In this case, Equation (3.4.4) reduces to

$$\left(\frac{1}{\alpha} - \frac{272}{875} \frac{1}{\bar{r}^2 \bar{h}^3} \right) \bar{h}' = \frac{1}{\bar{r} \bar{h}^2} \left(\frac{272}{875} \frac{1}{\bar{r}^2} - \frac{6}{5\bar{h}} \right), \quad (3.4.9)$$

where we recall α from Equation (3.3.9). In this case, Equation (3.4.8) becomes

$$\bar{r}_J^2 \left(\bar{h}_J^- \right)^3 = \frac{272}{875} \alpha. \quad (3.4.10)$$

We observe that the velocity at the free surface remains invariant under transformation (3.3.7). Equation (3.4.9) is integrated numerically subject to the condition $\bar{h}(\bar{r} = \bar{r}_0) = \bar{\delta}(\bar{r}_0)$ at the transition point, using MATLAB forth-order Runge-Kutta scheme. The integration is carried out at equal steps in the distance taken equal to 10^{-3} , until the turning point is reached at the singularity. The program is terminated when the slope $h' > 10^2$, giving an accuracy in the jump location r_J to the third decimal. The pre-jump height h_J is then deduced from (3.4.10).

We observe that Equation (3.4.9), similar to equation (33) of Bohr *et al.* (1993) and equation (3.1) of Kasimov (2008) for a flat disk, has only one critical point $\bar{h}_c = 6\alpha/5^{1/4}$, $\bar{r}_c = \sqrt{272/875} (5/6)^{3/8} \alpha^{1/8}$, which is the root of the system $1/\alpha - (272/875) \left(1/\bar{r}^2 \bar{h}^3 \right) = (272/875) \left(1/\bar{r}^2 \right) - 6/5\bar{h} = 0$, corresponding to a pair of complex conjugate eigenvalues of the Jacobian of the linearized two-dimensional dynamical system (Kasimov 2008). The real part is positive, indicating that the critical point is an unstable spiral, which in turn indicates that the solution cannot pass through the critical point. Bohr *et al.* (1993) estimated that the jump is located close to the critical point. They computed the flow and the free surface by choosing the pre-jump (inner) branch to correspond to a constant average velocity and chose the post-jump (outer) branch that emanates from the point of singularity. The two branches are then joined by the shock when they reach the same radial position, at a point that is identified as the jump radius (see their figure 3). This method led them to deduce the scaling for the jump radius to be $r_J \approx Q^{5/8} v_0^{-3/8} g^{-1/8}$. In fact, if we assume the jump to occur at or near the critical point and recall Equation (3.3.9), we obtain $\bar{r}_J \approx \bar{r}_c = \sqrt{272/875} (5/6)^{3/8} \left(\text{Re}^3 \text{Fr}^2 \right)^{1/8}$, which is the dimensionless form of the scaling deduced by Bohr *et al.* (1993).

Later, Kasimov (2008) derived an equation of closer similarity to Equation (3.4.9) but introduced the shape of a flat disk with a cutoff at the edge. See his equation (3.1) and figure 2. The addition of the variable disk shape led to the existence of a critical saddle point near the disk edge, in addition to the spiral critical point. Kasimov determined the flow and the surface height on the two sides of the jump. The upstream branch is sought by solving his equation (3.1) subject to an initial condition corresponding the location where the jet velocity at impact equals the free-surface velocity. The downstream branch is sought by integrating (3.1) inward toward the jump starting at the far critical saddle point through which the solution effectively must pass. The integration is terminated on each side at the turning points, corresponding to an infinite slope in the surface height or the singularity in (3.1). The two heights computed on either side are subsequently used to determine the location of the jump by applying the discretized momentum equation.

Figure 3-4 gives an overview of the influence of gravity on the film thickness distribution up to the jump location. The film thickness exhibits a minimum typically downstream of the transition location. The film growth stops at the location where the slope becomes infinite.

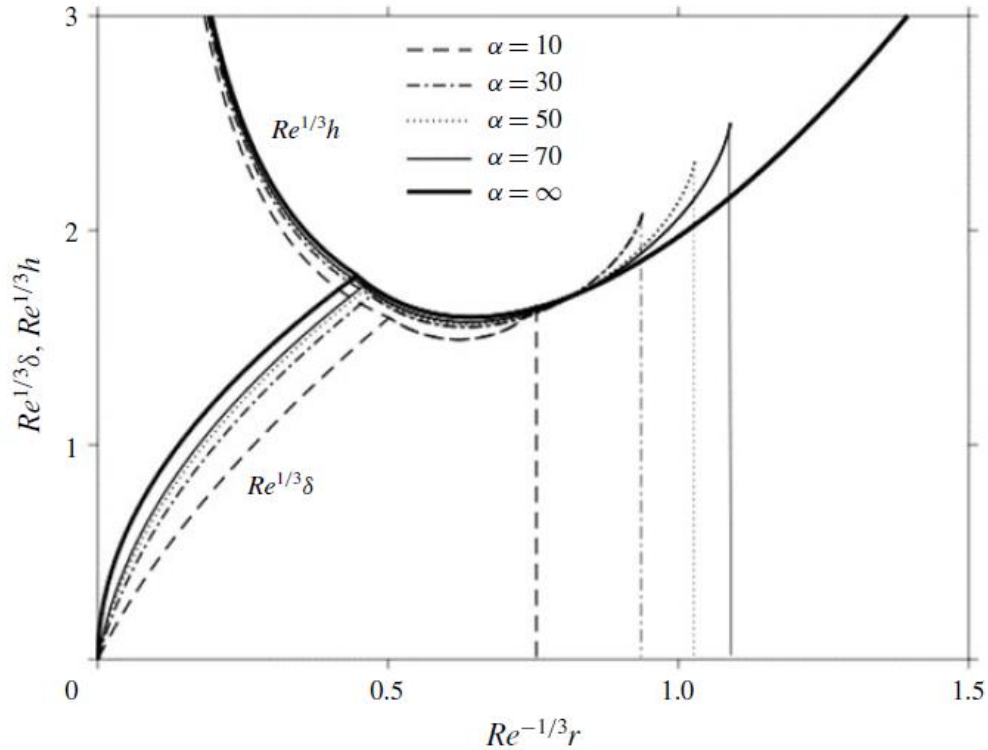


Figure 3-4: Influence of gravity on the developing boundary layer height and film thickness for supercritical flow. Also indicated in vertical lines are the locations of the hydraulic jump location $Re^{-1/3}r_j$ for different α values.

The influence of gravity on the corresponding free-surface velocity profiles is depicted in Figure 3-5. Here the velocity in the developing boundary-layer region (ii) outside the boundary layer is equal to 1 (the uniform jet velocity), which then decreases monotonically with distance downstream of the transition location. In the absence of gravity ($\alpha \rightarrow \infty$), the surface velocity decreases rapidly. This behaviour is easily deduced from Equation (3.4.2) by substituting Equation (3.4.6) to obtain

$$\bar{u}_s(\bar{r}_0 < \bar{r} < \bar{r}_J) \sim \frac{4}{5} \left(\frac{175}{136} (\bar{r}^3 - \bar{r}_0^3) + 2\bar{r}_0 \sqrt{\frac{70}{39} \bar{r}_0} \right)^{-1}, \quad \text{as } \alpha \rightarrow \infty. \quad (3.4.11)$$

In this case, u_s decreases like r^{-3} at large distance. The figure indicates that gravity tends to enhance the radial flow near the transition point similar to the effects of disk

rotation (Chapter 2) and slip (Prince *et al.* 2012, Khayat 2016). The rate at which the surface velocity decays with radial distance is also enhanced by gravity. However, further downstream, gravity inhibits flow movement as the film thickens ahead of the jump.

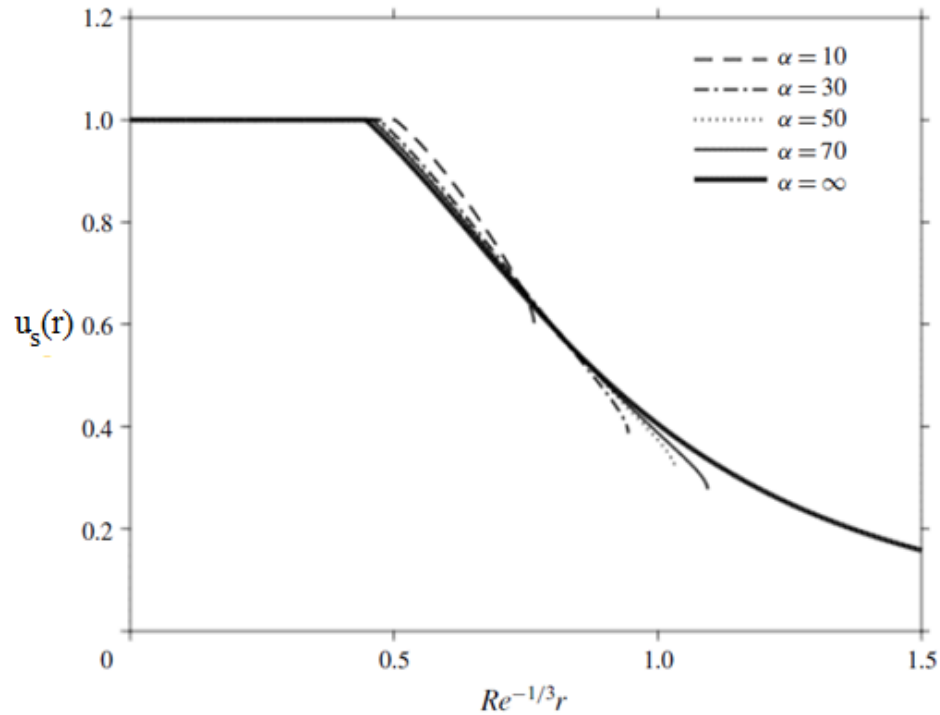


Figure 3-5: Influence of gravity on the free surface velocity for supercritical flow.

For any gravity level, after the rapid drop, τ_w exhibits a maximum before decaying monotonically. At large radial distance, the shear stress decays like r^{-5} in the absence of gravity effect. The strength of the maximum is essentially uninfluenced by gravity but tends to occur further downstream with increasing gravity effect. We emphasize that this maximum value might be an artificial effect due to the matching of the flow the slope of the free surface and the boundary layer are not smoothly connected.

Figure 3-6 illustrates the development of the dimensionless wall shear stress at the disk (skin friction) for the same gravity levels as in Figures 3-4 and 3-5. The figure shows that the wall shear stress is always larger for higher gravity except near the jump. This larger shear stress, which reflects a larger shear rate at the disk, is the result of a thinner film

thickness and a greater free-surface velocity caused by a higher gravity effect as already reported in Figures 3-4 and 3-5. The shear stress decays rapidly with radial distance in the developing boundary-layer region. In the absence of gravity,

$$\bar{\tau}_w (\bar{r}_0 < \bar{r} < \bar{r}_j) \sim \frac{6}{5} \bar{r} \left[\frac{175}{136} (\bar{r}^3 - \bar{r}_0^3) + 2\bar{r}_0 \sqrt{\frac{70}{39} \bar{r}_0} \right]^{-2}, \quad \text{as } \alpha \rightarrow \infty. \quad (3.4.12)$$

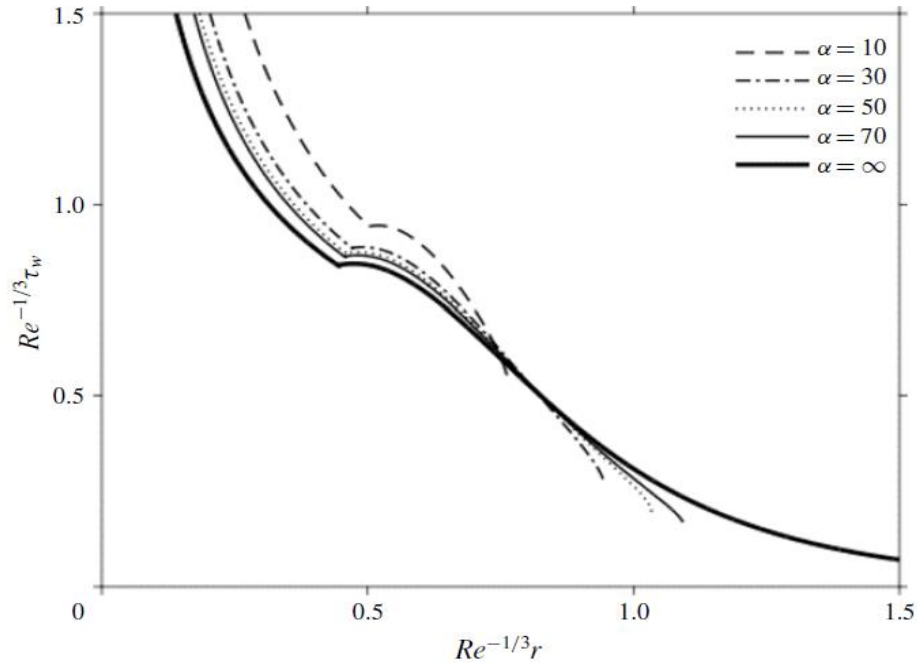


Figure 3-6: Influence of gravity on the wall shear stress for supercritical flow.

Although both the film height in Figure 3-4 and the free-surface velocity in Figure 3-5 are not significantly influenced by gravity, the location of the jump reflects a significant influence. This is depicted in Figure 3-7 where the jump radius and corresponding film thickness immediately upstream of the jump are plotted against α . The growth of the jump radius and the height closely follows the overall behaviour $\bar{r}_j \approx \alpha^{1/6}$ and $\bar{h}_j \approx \alpha^{2/9}$, yielding $\bar{r}_j^2 \bar{h}_j^3 \approx \alpha$, which agrees with the original Equation (3.4.10). The fractional power growth is also reflected from the position of the vertical lines in Figure 3-4 as well.

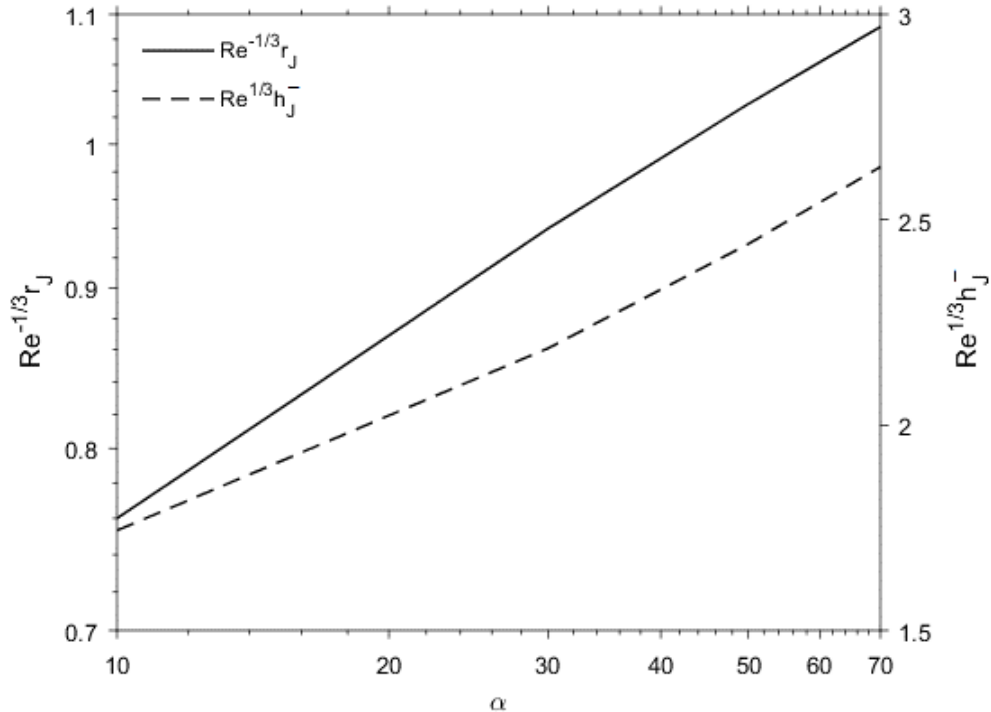


Figure 3-7: Dependence on the jump location and height immediately upstream of the jump on α .

3.4.3 Comparison with experiment

Figure 3-8 shows the dependence of the dimensional jump location on the flow rate, where comparison is carried out with the measurements of Hansen *et al.* (1997) as well as the numerical predictions of Rojas *et al.* (2010) for silicon oils of two different viscosities. The same experimental data were also used by Rojas *et al.* (2010) when they validated their spectral solution. We have included our results using the same log-log ranges used by Rojas *et al.* (2010) in their figure 2. Our predictions are in excellent agreement with their numerical results. The qualitative and quantitative agreement for the highest-viscosity case $\nu = 95 \text{ cSt}$ is especially encouraging given the simplicity of the present approach compared to their spectral approach. In particular, and in contrast to the numerical approach, the present formulation does not require imposing a boundary condition downstream of the jump. The agreement with experiment appears to suggest that the location of the jump can be determined without knowledge of downstream conditions such as the disk diameter or the thickness at the edge of the disk. This

observation corroborates well the experimental findings of Brechet & Neda (1999). We recall that Rojas *et al.* (2010) had to impose the thickness at the edge of the disk as measured by Hansen *et al.* (1997). Both the present theoretical and existing numerical predictions tend to overestimate slightly the jump radius compared to experiment. The discrepancy appears to be higher for low flow rates, for a given liquid. A plausible explanation for the discrepancy is the difficulty to accurately locate the jump radius in reality when it occurs very close to the jet, where the accuracy also drops due to the neglect of the stagnation region.

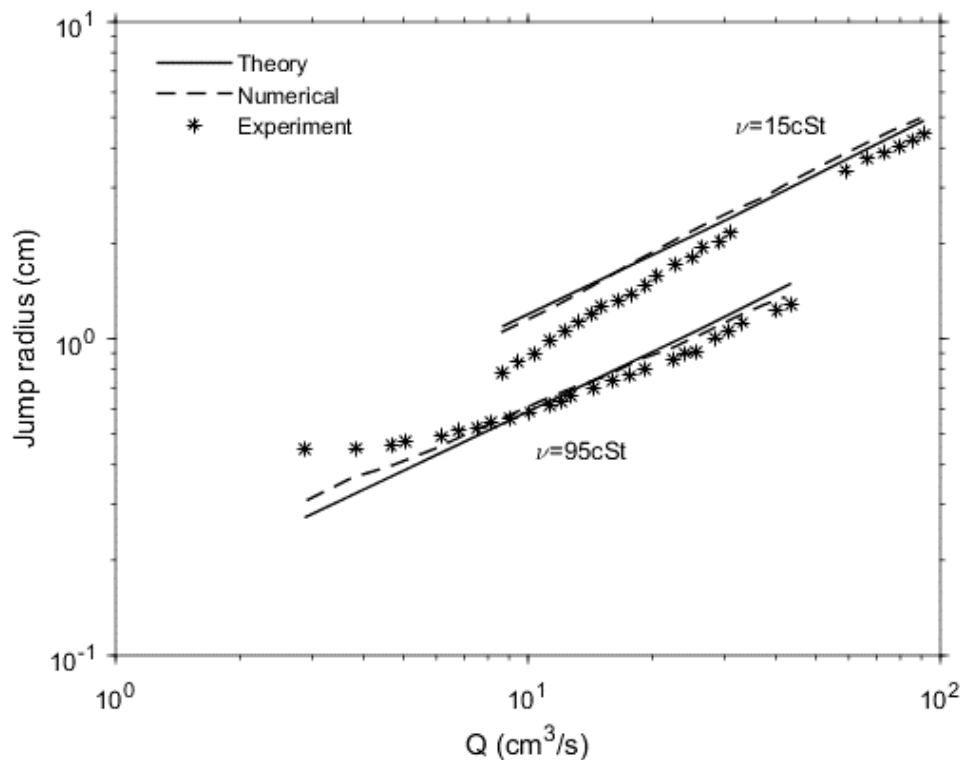


Figure 3-8: Dependence of the hydraulic jump radius on the flow rate. The figure shows the comparison between the present theoretical predictions and the measurements of Hansen *et al.* (1997) for two silicon oils of viscosities $\nu = 15$ cSt and 95 cSt. The numerical predictions of Rojas *et al.* (2010) are also included.

We further assess the validity of our approach by comparison against the scaling law proposed by Rojas *et al.* (2013), which relates the radius of the jump, in particular, to the height downstream of the jump (see their relation (15)). In the absence of surface tension,

the relation, written here as $r_J \approx \left((9/70) \left(Q^3 / \pi^3 \nu g h_\infty \right) \right)^{1/4}$, becomes based on their spectral approach for inertial lubrication flow (Rojas *et al.* 2010) and the inviscid Belanger equation (White 2006). Figure 3-9 shows the comparison between our predictions and the scaling law.

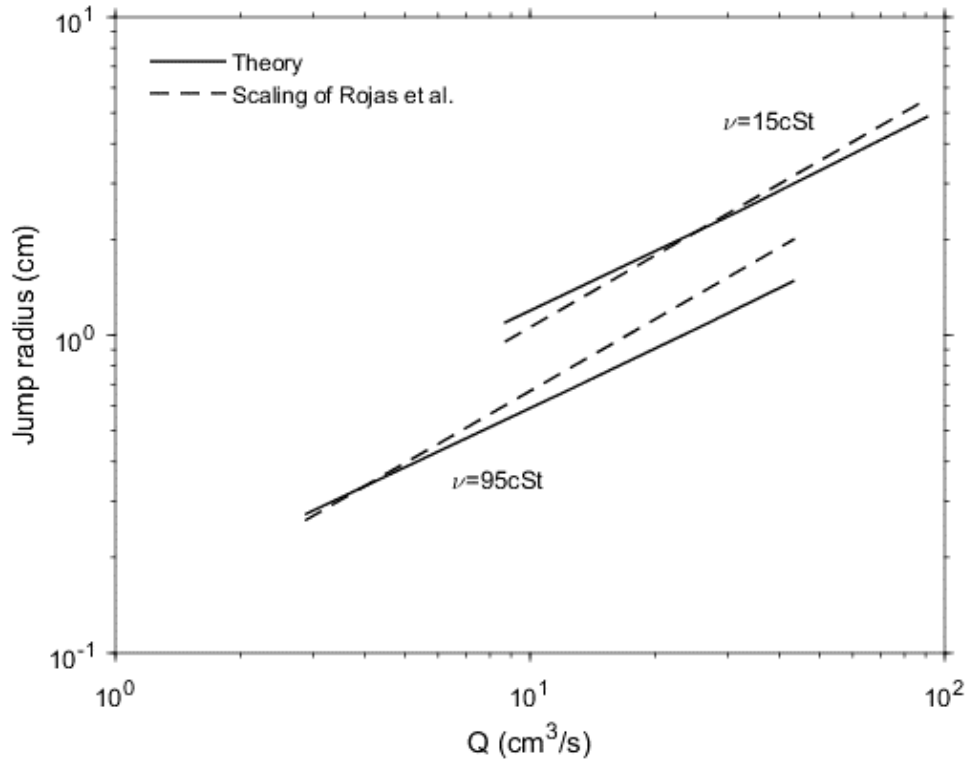


Figure 3-9: Dependence of the hydraulic jump radius on the flow rate. The figure shows the comparison between the present theoretical predictions (solid lines) and the ones based on the scaling law (dashed lines) of Rojas *et al.* (2013) for two silicon oils of viscosities $\nu = 15$ cSt and 95 cSt.

Finally, we observe that the approach in Chapter 2, where gravity is neglected in the supercritical regime, could not accurately locate the jump in comparison to experiment for heavily viscous liquids. On the other hand, the case of water is not considered here, not just because of the low viscosity but also due to the high surface tension. We have considered the case of water in Chapter 2. In the present work, we neglect surface tension upstream in order to investigate the role of gravity on the hydraulic jump. Our objective

is to also confirm or dismiss the claim and observation of Duchesne *et al.* (2014) for highly viscous liquids and Bhagat *et al.* (2018) who claimed that gravity is almost irrelevant in circular hydraulic jump. More comparisons with other existing measurements, including those of Duchesne *et al.* (2014), will be carried out in Section 3.5.

3.4.4 Further validation

As further general assessment of the validity of Equation (3.4.9), we examine its solution against that of the shallow-water equations for weak gravity. Thus, we set $\varepsilon \equiv \alpha^{-1}$ as the small parameter and expand the thickness as $\bar{h}(\bar{r}) = \sum_{m=0} \varepsilon^m \bar{h}_m(\bar{r})$. To leading order,

Equation (3.4.9) yields the following equation for \bar{h}_0 :

$$(\bar{r}\bar{h}_0)' = \frac{525}{136} \bar{r}^2, \quad (3.4.13)$$

which corresponds to the thickness in the absence of gravity. The solution of this equation was already given earlier and is equivalent to Equation (3.4.6). To next order:

$$(\bar{r}\bar{h}_1)' = \frac{875}{272} \bar{r}^3 \bar{h}_0' \bar{h}_0. \quad (3.4.14)$$

We next examine the corresponding solution of the shallow-water equations, which are first rescaled to involve the only parameter $\alpha = \text{Re}^{1/3} \text{Fr}^2$ by recalling Equation (3.3.7) and introducing all the barred variables as

$$r = \text{Re}^{1/3} \bar{r}, \quad h = \text{Re}^{-1/3} \bar{h}, \quad z = \text{Re}^{-1/3} \bar{z}, \quad u = \bar{u}, \quad w = \text{Re}^{-2/3} \bar{w}. \quad (3.4.15a-e)$$

In this case, Equations (3.2.1a), (3.2.5) and (3.2.6) become

$$\bar{u}_{\bar{r}} + \frac{\bar{u}}{\bar{r}} + \bar{w}_{\bar{z}} = 0, \quad \bar{u}\bar{u}_{\bar{r}} + \bar{w}\bar{u}_{\bar{z}} = -\alpha^{-1} \bar{h}' + \bar{u}_{\bar{z}\bar{z}}, \quad \int_0^{\bar{h}} \bar{u} \, d\bar{z} = \frac{1}{2\bar{r}}. \quad (3.4.16a-c)$$

In the presence of gravity, a similarity solution is possible only under some conditions.

Starting with the mapping $\bar{\xi}(\bar{r}, \bar{z}) = \bar{r}$, $\bar{\eta}(\bar{r}, \bar{z}) = \bar{z} / \bar{h}(\bar{r})$, and taking $\bar{u}(\bar{r}, \bar{z}) = \bar{u}_s(\bar{\xi})g(\bar{\eta})$, Equation (3.4.16a) becomes

$$\bar{u}'_s g - \frac{\bar{h}'}{\bar{h}} \bar{\eta} \bar{U} g_{\bar{\eta}} + \frac{\bar{u}_s g}{\bar{\xi}} + \frac{1}{\bar{h}} \bar{w}_{\bar{\eta}} = 0. \quad (3.4.17)$$

Isolating $\bar{w}_{\bar{\eta}}$ and rearranging terms:

$$\bar{w}_{\bar{\eta}} = \bar{\xi}^{-1} \left[-(\bar{\xi} \bar{h} \bar{u}'_s)' g + \bar{\xi} \bar{h}' \bar{u}_s (\bar{\eta} g)_{\bar{\eta}} \right]. \quad (3.4.18)$$

Now, from conservation of mass or Equation (3.4.16c), we have

$$\bar{u}_s \bar{h} \bar{r} = \frac{1}{2 \int_0^{\bar{\eta}} g d\bar{\eta}} = \text{Const, yielding } (\bar{\xi} \bar{h} \bar{u}'_s)' = 0. \quad (3.4.19)$$

Consequently, Equation (3.4.18) reduces to $\bar{w}_{\bar{\eta}} = \bar{h}' \bar{u}_s (\bar{\eta} g)_{\bar{\eta}}$. Integrating and recalling

that $\bar{w}(\bar{\xi}, \bar{\eta} = 0) = 0$, we get $\bar{w} = \bar{h}' \bar{u}_s \bar{\eta} g(\bar{\eta})$.

We thus have so far

$$\bar{u} = \bar{U} g(\bar{\eta}), \quad \bar{w} = \bar{h}' \bar{U} \bar{\eta} g(\bar{\eta}), \quad \bar{r} \bar{U} \bar{h} = C \equiv \left(2 \int_0^{\bar{\eta}} g(\eta) d\eta \right)^{-1}, \quad (3.4.20a-c)$$

where Equation (3.4.20c) is deduced from Equation (3.4.16c). Substituting the velocity components from Equations (3.4.20a,b) into Equation (3.4.16b), and eliminating \bar{U} using Equation (3.4.20c), yields the following problem for g :

$$C^2 (\bar{r} \bar{h})' g^2 - \bar{\epsilon} \bar{h}^3 \bar{r}^3 \bar{h}' + Cr^2 g_{\bar{\eta} \bar{\eta}} = 0, \quad g(0) = g_{\bar{\eta}}(1) = 0, \quad g(1) = 1. \quad (3.4.21a-c)$$

We again seek the solution by expanding the thickness as $\bar{h}(\bar{r}) = \sum_{m=0} \varepsilon^m \bar{h}_m(\bar{r})$. To

leading order, we recover the classical equation of Watson (1964):

$$C(\bar{r}h_0)' g^2 + \bar{r}^2 g_{\bar{\eta}\bar{\eta}} = 0, \quad (3.4.22)$$

which suggests that $\bar{r}^{-2}(\bar{r}h_0)'$ must be constant. Multiplying Equation (3.4.22) by $g_{\bar{\eta}}$, and integrating using the conditions in Equation (3.4.21), yields the following equation:

$$(\bar{r}h_0)' = \frac{3c^2}{2C} r^2, \text{ where } c = \int_0^1 \frac{dg}{\sqrt{1-g^3}} = 1.402. \quad (3.4.23)$$

The value of C is determined by noting that $c = g_{\bar{\eta}} / \sqrt{1-g^3}$, yielding

$\int_0^1 g dg = \int_0^1 g dg / \sqrt{1-g^3} = 0.615$, so that $C = 0.813$. To the next order in ε , Equation (4.21) gives

$$(\bar{r}h_1)' = \frac{3c}{2C^2} \bar{r}^3 h_0^3 h_0', \quad (3.4.24)$$

where $c \int_0^1 g^2 d\eta = (1/3) \int_0^1 dg^3 / \sqrt{1-g^3} = 2/3$ was used. Comparison between the numerical coefficients of Equation (3.4.14) and Equation (3.4.24) indicates a discrepancy of 6%. The discrepancy for the first-order contribution is 1% when Equation (3.4.15) is compared with Equation (3.4.24).

Avedisian & Zhao (2000) investigated the circular hydraulic jump experimentally for normal and reduced gravity conditions. They measured the jump diameter and shape at the free liquid surface for an impinging jet on a stationary disk. Based on the reported two values of the flow rate and two gravitational acceleration data provided, we find that the location of the jump behaves close to $g^{-1/9}$, roughly confirming the scaling of Bohr *et al.* (1993) for low gravity. We can also estimate the behaviour of the jump radius from

Equation (3.4.8) by assuming the thickness from Equation (3.4.6) or (3.4.7) for large distance or $h_J^- \approx r_J^2 / \text{Re}$. When inserted in Equation (3.4.8), we obtain $r_J \approx \text{Re}^{3/8} \text{Fr}^{1/4}$, which is precisely the scaling suggested by Bohr *et al.* (1993) cast in dimensionless form. Interestingly, this scaling law can also be expressed in terms of only one parameter as $\bar{r}_J \approx \alpha^{1/8}$.

3.5 The influence of gravity on the hydraulic jump height and the subcritical flow

Now that the jump location has been determined, we are in a position to examine the flow and the film height in the subcritical region downstream of the jump, in particular the height of the jump. Here, we consider two alternatives and assess their validity, the first consisting of applying the conservation of momentum across the jump though we expect it will give less accuracy for high-viscosity liquids, and the second involving the use of the film thickness at the edge of the disk and integrating the momentum equation (backwards) to determine the jump height.

3.5.1 Conservation of momentum across the jump

We first recall the integral form Equation (3.4.3) of the momentum conservation equation, which holds for any position $r > r_0$ in the super- and subcritical regions. Across the jump, Equation (3.4.3) is applied for a control volume of width Δr in the radial direction, taking the following discretized form:

$$\text{Re} \Delta \int_0^h u^2 dz = -\frac{\text{Re}}{\text{Fr}^2} \frac{\Delta h^2}{2} - \Delta r u_z(r_J, z=0). \quad (3.5.1)$$

Since the width of the jump Δr is assumed to be small, Equation (3.5.1) reduces to

$$\frac{1}{2} \left((h_J^+)^2 - (h_J^-)^2 \right) = \text{Fr}^2 \left(\int_0^{h_J^-} (u_J^-)^2 dz - \int_0^{h_J^+} (u_J^+)^2 dz \right). \quad (3.5.2)$$

We observe that the supercritical velocity is already available from Equation (3.4.1) and Equation (3.4.2), yielding $u_J^-(r_J, z) = \left(4/5r_J h_J^-\right) f(\eta)$, where $\eta = z/h_J^-$ and $f(\eta)$ is given in Equation (3.3.4). We also use relation (3.4.8) to eliminate h_J , In this case, Equation (3.5.2) becomes

$$h_J^{+2} - 3 \left(\frac{272}{875} \frac{Fr^2}{r_J^2} \right)^{2/3} + 2Fr^2 \int_0^{h_J^+} (u_J^+)^2 dz = 0. \quad (3.5.3)$$

Thus, the jump height is completely determined as a function of the Froude and the Reynolds numbers once the subcritical velocity profile u_J^+ is imposed. Various assumptions have been adopted in the literature, ranging from inviscid to fully viscous flows. Both regimes will be explored next.

We first consider the flow to be inviscid downstream of the jump. Although the present work is focused on heavily viscous liquids, the inviscid simply corresponds to uniform velocity assumption across the depth due to the slow motion of liquids. This is an assumption that has been widely adopted in the literature in various contexts (see, for instance, Watson 1964, Bush & Aristoff 2003, Dressaire *et al.* 2010, Prince *et al.* 2012). At the very least, the inclusion of the uniform subcritical flow is helpful as a reference limit.

Thus, assuming uniform flow downstream of the jump, and using the mass conservation Equation (3.2.6), Equation (3.5.3) reduces to

$$h_J^{+2} - 3 \left(\frac{272}{875} \frac{Fr^2}{r_J^2} \right)^{2/3} + \frac{Fr^2}{2r_J^2 h_J^+} = 0. \quad (3.5.4)$$

Equation (3.5.4) takes an interesting form when cast in terms of the jump Froude number based on the jump radius and height. In this regard, there is a close connection with the recent experimental findings and claim of Duchesne *et al.* (2014), which we will now explore.

Duchesne *et al.* (2014) introduced the jump Froude number defined in terms of the jump height and the average velocity immediately after the jump, namely $Fr_J = Fr / \left(2r_J (h_J^+)^{3/2} \right)$ in our notations. Their measurements suggest that Fr_J remains sensibly independent of the flow rate (constant with respect to Fr). However, they could not explain or theoretically support this observation, which, in turn, begs the question whether the constancy of Fr_J has any theoretical basis. This turns out to be indeed the case as we shall now demonstrate.

It is easy to see that Equation (3.5.4) yields the following equation for Fr_J :

$$Fr_J^2 - \frac{24}{25} \left(\frac{17}{7} \right)^{2/3} Fr_J^{4/3} + \frac{1}{2} = 0. \quad (3.5.5)$$

This equation indicates that Fr_J is indeed a constant that is independent of the Fr or, equivalently, of the flow rate, confirming the observation of Duchesne *et al.* (2014). This is a cubic equation in $Fr_J^{2/3}$, admitting $Fr_J = 0.58$ as a solution. Thus, we have established the constancy of Fr_J when the subcritical flow is inviscid.

We next address the question whether Fr_J remains actually independent of the flow rate if the subcritical flow is assumed to be viscous. We follow Duchesne *et al.* (2014) and adopt a lubrication flow approach. In this case, a differential equation for h can be obtained by neglecting the inertial terms in Equation (3.2.5), yielding the following profile for the radial velocity:

$$u(r > r_J, z) = \frac{Re}{Fr^2} \frac{dh}{dr} \left(\frac{z^2}{2} - hz \right). \quad (3.5.6)$$

Inserting u into the mass conservation Equation (3.2.6) and integrating, the equation governing the film thickness downstream of the jump becomes

$$\frac{dh}{dr} = -\frac{3 \text{Fr}^2 h^{-3}}{2 \text{Re} r}, \quad (3.5.7)$$

which leads to the velocity profile just downstream of the jump as

$$u_J^+(r_J, z) = -\frac{3}{2r_J h_J^{+3}} \left(\frac{z^2}{2} - h_J^+ z \right). \quad (3.5.8)$$

Finally, inserting Equation (3.5.8) into Equation (3.5.3), we obtain the following equation for Fr_J :

$$\text{Fr}_J^2 - \frac{4}{5} \left(\frac{17}{7} \right)^{2/3} \text{Fr}_J^{4/3} + \frac{5}{12} = 0. \quad (3.5.9)$$

Similar to Equation (3.5.5), Equation (3.5.9) also confirms that Fr_J is independent of Fr (flow rate), with $\text{Fr}_J = 0.71$.

What we have established so far, based on the discretized mass and momentum equations across the jump, is that Fr_J is indeed constant (independent of the flow rate) as Duchesne *et al.* (2014) claim from their measurements. Surprisingly, this is the case whether the subcritical flow is assumed to be inviscid or viscous obeying the lubrication regime, thus covering a wide range of viscosity and flow rate. The value of Fr_J is found to be slightly lower for inviscid compared to viscous subcritical flow. However, both values remain higher than the measured value by Duchesne *et al.* (2014): $\text{Fr}_J \approx 0.35$ to 0.40 . It is important to observe that the values of Fr_J can be found theoretically without the knowledge of downstream conditions of the jump such as the disk radius or the thickness at the edge of the disk. Such conditions are not needed when the discretized conservation equations are invoked. Another important observation to make is whether the discretized Equation (3.5.2) itself is valid. It is expected that Equation (3.5.2) remains reasonably valid for low-viscosity liquids or at high flow rate since the jump is of negligible thickness and its location is well defined. However, for high-viscosity liquids such as the silicon oils used by Duchesne *et al.* (2014), the jump is expected to be wide, and

Equation (3.5.2) cannot be entirely valid. This brings us to the second alternative when seeking the subcritical flow.

3.5.2 The influence of disk radius and edge thickness

We proceed by examining the flow in the subcritical range, downstream of the jump, without invoking Equation (3.5.3). In this case, an approximate or asymptotic solution of Equation (3.4,4) can be found by keeping the three dominant terms for large distance, reducing it to a lubrication-like equation for h :

$$\frac{dh}{dr} = -\frac{6 Fr^2}{5 Re} \frac{h^{-3}}{r}. \quad (3.5.10)$$

Subject to $h(r = r_\infty) = h_\infty$, Equation (3.5.10) can be integrated analytically to give

$$h(r > r_J) = \left(h_\infty^4 + \frac{24 Fr^2}{5 Re} \ln\left(\frac{r_\infty}{r}\right) \right)^{\frac{1}{4}}. \quad (3.5.11)$$

The prediction of the edge thickness was already considered in Chapter 2. Both static and dynamic contributions were considered, which yielded an accurate prediction established by comparing against experiment for the edge thickness. Direct measurements by Duchesne *et al.* (2014) of the edge thickness, performed at nearly 5 mm of the disk perimeter in their experiment, give a nearly constant value with a weak power-law variation with the flow rate, not exceeding a few per cent. This constant thickness value is very close to the capillary length $\sqrt{\gamma_0 / \rho g}$ of the fluid, which results from the balance of forces between the hydrostatic pressure and the surface tension (γ_0) at the disk perimeter. This value is also consistent with the measurements of Dressaire *et al.* (2010). Consequently, we assumed that the film thickness at the edge of the disk is essentially equal to the film thickness the liquid exhibits under static conditions. Lubarda & Talke (2011) proposed an expression for this static thickness as $h_s = 2\sqrt{\gamma_0 / \rho g} \sin(\theta_Y / 2)$, based on the minimum free energy principle. Here θ_Y is the contact angle, which depends on both the liquid and the solid, and may then be deduced from experiment.

In addition to the static contribution, and in order to explore the small variation of edge thickness with flow rate as observed by Duchesne *et al.* (2014), we resorted to a minimum mechanical energy principle (Yang & Chen 1992; Yang, Chen & Hsu 1997), which states that a fluid flowing over the edge of a disk under the influence of a hydrostatic pressure gradient will adjust itself so that the mechanical energy within the fluid will be minimum with respect to the film thickness at the disk edge. Consequently, the contribution to the thickness at the edge of the disk is determined by setting the derivative of the mechanical energy with respect to the film thickness equal to zero. The thickness near the edge of the disk is finally given by

$$h_{\infty} = 2\sqrt{\frac{1}{\text{Bo}}} \sin\left(\frac{\theta_Y}{2}\right) + \left(\frac{3}{40}\right)^{\frac{1}{3}} \left(\frac{\text{Fr}}{r_{\infty}}\right)^{\frac{2}{3}}. \quad (3.5.12)$$

Here the Bond number is given by $\text{Bo} = \rho g a^2 / \gamma_0$, with γ_0 being the surface tension. Clearly, in the presence of relatively strong gravity or surface tension and large disk radius, the second term tends to be dominated by the static contribution. As we shall see next, even the static contribution will turn out to be unimportant for the heavily viscous liquids considered in the present work.

Indeed, once the thickness $h(r = r_{\infty}) = h_{\infty}$ at the edge of the disk is determined as per Equation (3.5.12), we obtain the film thickness distribution downstream of the jump from Equation (3.5.10). In particular, and given that the jump location has already been determined, the jump height is now obtained through

$$h_J^+ = \left(h_{\infty}^4 + \frac{24}{5} \frac{\text{Fr}^2}{\text{Re}} \ln\left(\frac{r_{\infty}}{r_J}\right) \right)^{\frac{1}{4}}. \quad (3.5.13)$$

In this case, it is not difficult to confirm that, for a large disk and relatively small Reynolds number, the logarithmic term dominates on the right-hand side of Equation (3.5.13). This is obviously the case of very viscous liquids. As a comparison, the Reynolds number for the flow of silicon oils (Duchesne *et al.* 2014) is of the order of 10^2

, whereas for water (Dressaire *et al.* 2010) its order is closer to 10^4 . It is important to note that the range of Froude number in both sets of measurements is essentially the same. Based on the range of Froude numbers in Figure 3-10 below, it is not difficult to deduce that the static contribution to the edge thickness is also dominated. In fact, experiments (Duchesne *et al.* 2014) indicate that $h_\infty = O(1)$ at most, and $h_\infty \approx 0$ for a liquid of high viscosity.

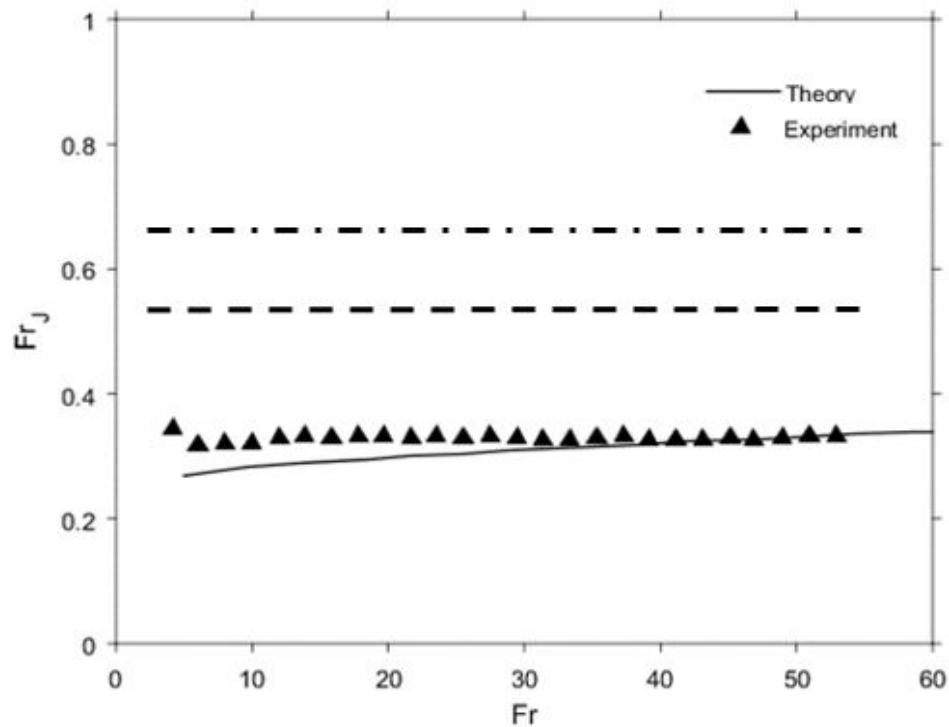


Figure 3-10: Dependence of Fr_J on the flow rate (Froude number). The solid line corresponds to predictions based on Equations (3.4.4) and (3.5.13). The experimental data corresponding to silicon oil from Duchesne *et al.* (2014). Also added as dashed and dash-dotted lines the result based on Equations (3.5.5) and (3.5.9), respectively.

We now turn, once again, to examining conditions where Fr_J may remain independent of the flow rate. This time, Equation (3.5.13) is used instead of Equation (3.5.3). In this case, since the pre-jump height h_j^- and the jump radius r_j must be computed

numerically, it is not possible to derive a closed form equation similar to Equation (3.5.5) or Equation (3.5.9), confirming that Fr_J is constant. In fact, Equation (3.5.13) suggests that Fr_J is not independent of Fr . However, the dependence on Fr turns out to be weak, as Figure 3-10 suggests. The figure shows the variation of Fr_J against Fr for the silicon oil of viscosity 20 cSt used by Duchesne *et al.* (2014) in their measurements, which are also shown in the Figure 3-10. The experimental data are reproduced in dimensionless form. Surprisingly, the figure indicates that Fr_J not only is indeed sensibly constant but agrees closely with experiment. Some discrepancy is, however, noted for low flow rates, which is not surprising given the difficulty in measuring accurately the jump radius and height.

Now that the solution is available in the supercritical and subcritical regions, we are in a position to validate our model over the entire domain, against existing numerical results and experiment. We also take the opportunity to assess the validity of the parabolic profile. For the supercritical range, an equation similar to Equation (3.4.4) is obtained when using the parabolic profile: $f(\eta) = 2\eta - \eta^2$, namely

$$\text{Re} \left(\frac{1}{Fr^2} - \frac{3}{10r^2h^3} \right) h' = \frac{3}{10rh^2} \left(\frac{\text{Re}}{r^2} - \frac{5}{h} \right). \quad (3.5.14)$$

We observe that the asymptotic form of Equation (3.5.14) for large r is precisely the lubrication Equation (3.5.7), which when integrated yields

$$h(r > r_J) = \left(h_\infty^4 + 6 \frac{Fr^2}{\text{Re}} \ln \left(\frac{r_\infty}{r} \right) \right)^{\frac{1}{4}}. \quad (3.5.15)$$

Figure 3-11 shows the comparison between the present theory and the numerical results of Rojas *et al.* (2015) as well as the measurements of Ellegaard *et al.* (1996) for ethylene glycol. Both formulations based on the parabolic and cubic profiles are represented. The results for the free-surface velocity are reported in dimensionless form, with corresponding parameters being $\text{Re} = 334$, $Fr = 14.4$ and $\text{Bo} = 1.21$. The contact angle

used to determine the edge thickness is $\theta_Y = 70^\circ$, yielding a total edge thickness of $h_\infty = 1.7$, including the height of the vertical edge. While the position of the jump is well reproduced by the present theory based on the cubic profile and the numerical method, Figure 3-11 shows that the theory tends to slightly underestimate the level of the surface velocity in both the super- and subcritical ranges. Figure 3-11 indicates that the numerical approach of Rojas *et al.* tends to agree slightly better with experiment than the present theory. The figure also indicates a larger discrepancy when the parabolic profile is used.

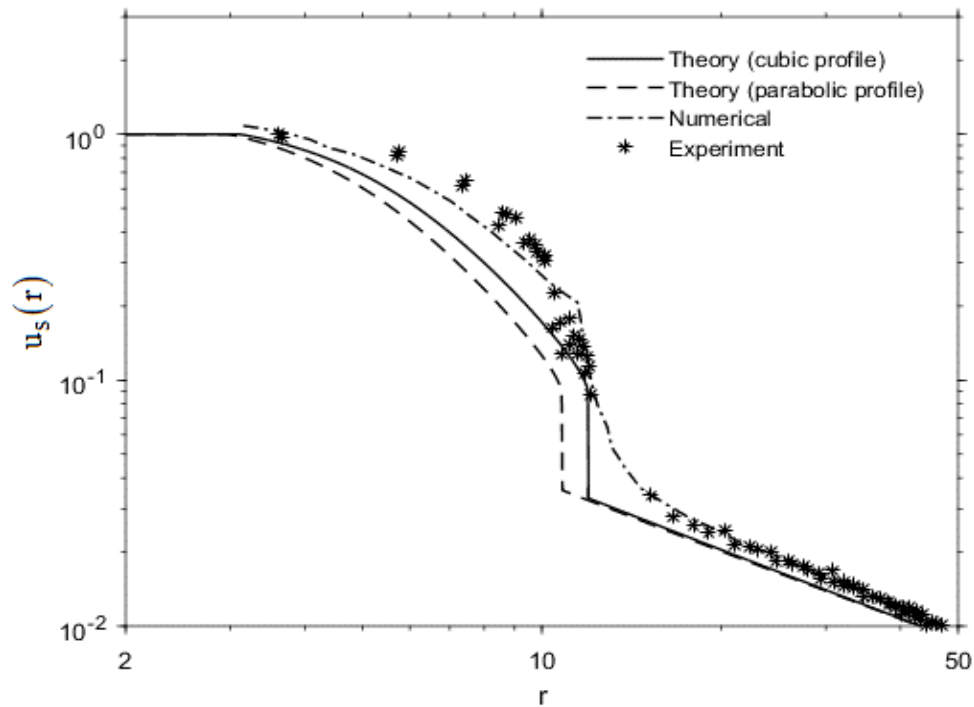


Figure 3-11: Free-surface velocity in the supercritical and subcritical domains.

Comparison between the present theory (solid line), the numerical results of Rojas *et al.* (2015), as well as the experimental data of Ellegaard *et al.* (1996). Also added is the velocity distribution based on the parabolic profile.

We next examine the shape of the entire film under general flow conditions. For this, we rescale Equation (3.5.11) using Equation (3.3.7) to reduce the problem in terms of the parameter α :

$$\bar{h}(\bar{r} > \bar{r}_j) = \left(\bar{h}_\infty^4 + \frac{24}{5} \alpha \ln \left(\frac{\bar{r}_\infty}{\bar{r}} \right) \right)^{\frac{1}{4}}. \quad (3.5.16)$$

Here $\bar{h}_\infty = 2\sqrt{\text{Re}^{2/3}/\text{Bo} \sin(\theta_Y/2)} + \left((3/40)/\bar{r}_\infty^2 \right)^{1/3}$ from Equation (3.5.12). The overall effect of gravity is illustrated in Figure 3-12, which depicts the film thickness over the entire disk. The jump height decreases with increasing gravity, simultaneously as the jump location is pushed upstream toward the stagnation point and away from the edge of the disk. We can also observe the logarithmic increase in height reported earlier in Figure 3-7.

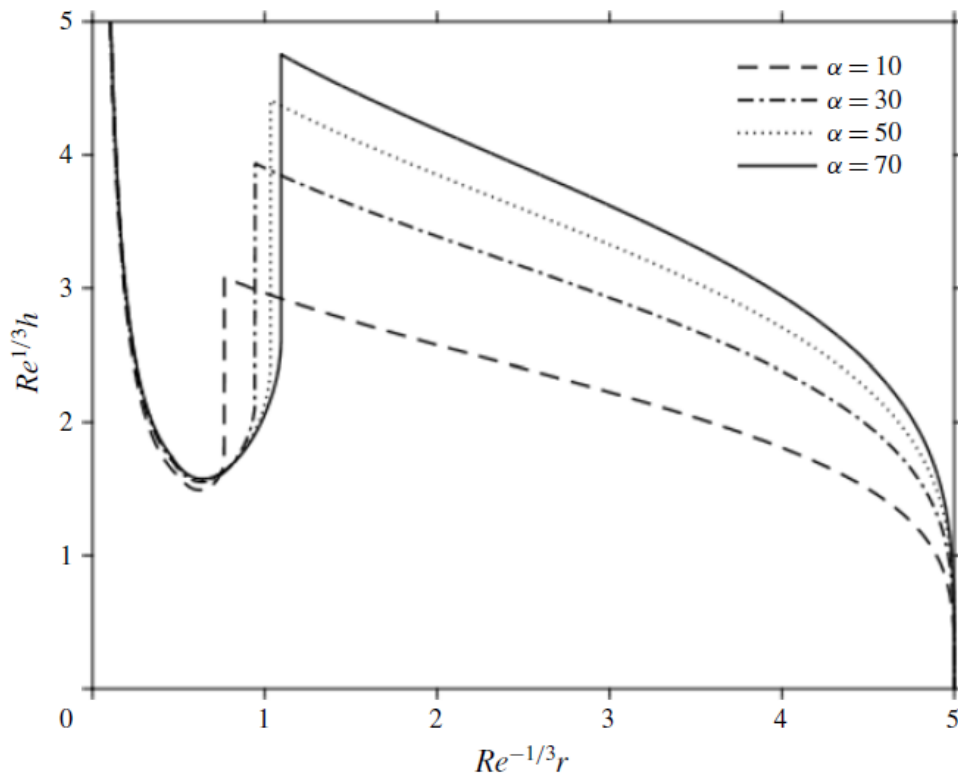


Figure 3-12: Influence of gravity on the film thickness plotted against radial distance in regions (ii), (iii) and (iv).

While the use of Equation (3.4.4) or (3.4.9) is imperative in the supercritical range ahead of the jump, allowing us to locate the jump, it is not necessarily so for the subcritical flow, where we have the choice to use different approximations. For instance, as the flow

slows down downstream of the shock, we saw that the lubrication assumption holds well between the jump and the edge of the disk, yielding a good agreement with experiment (see Figures 3-10 and 3-11). Our calculations of the subcritical flow so far are based on the asymptotic Equation (3.5.11) of (3.4.4) or (3.5.16) of (3.4.9) for large r as it is convenient to use, given the analytical distribution of the thickness (and velocity) downstream of the jump and its direct relation to the edge thickness and the disk radius. Alternatively, we now consider using Equation (3.4.4), and apply it directly to capture the subcritical flow, which should allow us to assess the validity of Equation (3.5.11). Simultaneously, we examine the effect of the disk radius. The comparison is reported in Figure 3-13 for the film thickness distribution with distance in the super- and subcritical ranges for three different values of the disk radius. We take $Re = 628$, $Fr = 63$, $Bo = 1.1$ and $\theta_Y = 55^\circ$. In this case, the values of the thickness at the edge of the disk are determined from Equation (3.5.12) are $h_\infty = 1.24$, 1.2 and 1.18 , corresponding to $r_\infty = 70, 80$ and 90 , respectively.

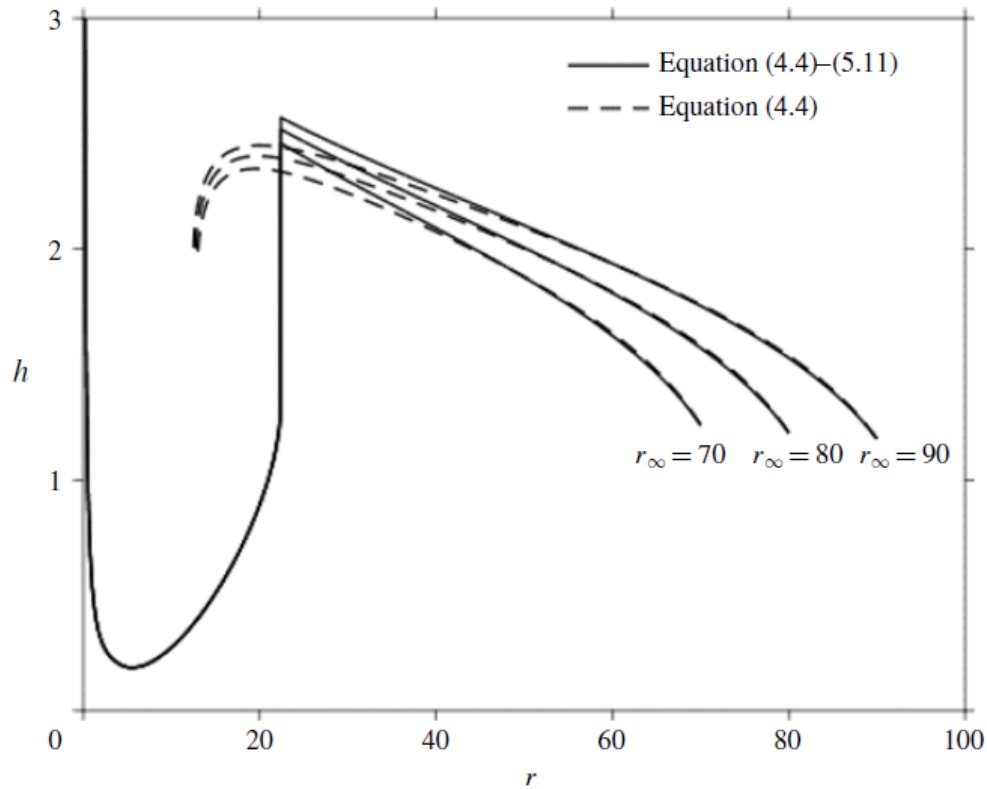


Figure 3-13: Influence of the disk radius on the film thickness plotted against the radial distance in regions (ii), (iii) and (iv). Solution in solid line based on Equations (3.4.4) and (3.5.11). Dashed line shows the subcritical profile based on (3.4.4).

Several observations are worth making here. Figure 3-13 shows that the subcritical branches exhibit a turning point corresponding to the singularity of Equation (3.4.4), which occurs slightly upstream of the jump location. As expected, the profile of the asymptotic Equation (3.5.11) collapses onto the profile based on Equation (3.4.4) at a distance not too far from the jump. This distance, nevertheless, increases with the disk radius. The asymptotic solution yields a jump height h_j^+ that is slightly above the one based on the exact solution of Equation (3.4.4). Finally, despite the important spread in the values of the disk radius, the location of the singularity reached by the subcritical branches is essentially the same, as reflected in the saturation near the turning point. This seems to suggest that the location of the jump in reality, if it were to fall half-way, say, between the two locations of the singularity, is independent of downstream conditions.

We seem to reach this observation regardless of which branch, super- or subcritical, we are referring to.

Next, we pursue our assessment of the validity of Equation (3.4.4) and the asymptotic form Equation (3.5.11) against experiment. The comparison is reported in Figure 3-14 for the film thickness distribution with distance in the super- and subcritical regions against the measurements of Duchesne *et al.* (2014) for silicon oil (20 cSt). The data are reproduced here in dimensionless form from their figure 2, corresponding to $Re = 169$, $Fr = 14.88$, $Bo = 1.19$, $\theta_Y = 55^\circ$ and $r_\infty = 94$. In this case, the value of the thickness at the edge of the disk is determined from Equation (3.5.12) as $h_\infty = 0.95$. Several observations are worth making here. Figure 3-14 shows that the theoretical predictions, based on the solution of Equation (3.4.4), are generally in good agreement with the experiment of Duchesne *et al.* (2014), slightly underestimating their measurements. The location of the jump is predicted to be close to the level of the turning point or the singularity of the supercritical branch upstream of the jump. The subcritical branch also exhibits a turning point corresponding to the singularity of Equation (3.4.4), occurring slightly downstream of the jump location (see Figure 3-13). The behaviour of the two branches is in close (qualitative) agreement with the theoretical predictions of Kasimov (2008) who incorporated the shape of the bottom (flat disk with a sharp cut off at the edge). The reader is particularly referred to figure 3(a) from Kasimov (2008). The asymptotic solution cannot mimic the downward turning trend observed in the experiment, yielding a jump height h_j^+ that is slightly above the one based on the exact solution of Equation (3.4.4). Interestingly, there is no need here to integrate from a critical point coinciding with at the edge of the disk to obtain the subcritical branch as Kasimov (2008) did. Kasimov estimated the location of the jump to be somewhere between the upstream and downstream singularities, which seems to be case here. However, this may not always be the case. Based on the agreement between theory and experiment in previous figures, we saw that the location of the jump coincides rather with the upstream singularity of the averaged momentum equation.

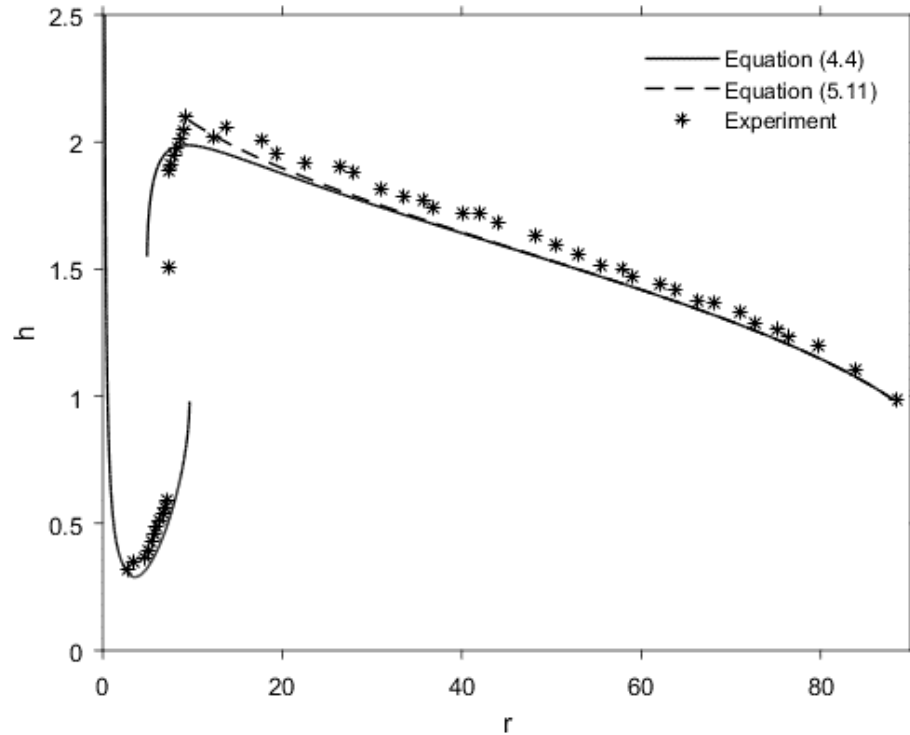


Figure 3-14: Free surface profile. Comparison between theoretical predictions and the measurements of Duchesne *et al.* (2014) for silicon oil (20 cSt). Results plotted in dimensionless form with $Re = 169$, $Fr = 14.88$, $Bo = 1.19$, $\theta_Y = 55^\circ$ and $r_\infty = 94$. Theoretical profiles based on current theory or Equation (3.4.4) (solid lines) and asymptotic subcritical Equation (3.5.11) (dashed line).

Finally, an interesting observation can be made regarding the (constant) value of Fr_J and its independence of Fr (or the flow rate). The measurements of the film profile for heavily viscous liquids seem to give a rough estimate of the height h_J^+ immediately downstream of the relative to the height h_J^- upstream of the jump. More precisely, experiment suggests that $h_J^+ \approx 2h_J^-$ (see, for instance, the measurements of Ellegaard *et al.* 1996, and those in figure 2 of Duchesne *et al.* 2014). By substituting $h_J^- = h_J^+ / 2$ in Equation (3.4.8) and recalling that $Fr_J = Fr / 2r_J (h_J^+)^{3/2}$, we deduce that

$$\text{Fr}_J = \frac{\text{Fr}}{2^{5/2} r_J h_J^{-3/2}} = \frac{1}{16} \sqrt{\frac{875}{34}} \approx 0.32, \quad (3.5.17)$$

which is very close to 0.33, the value measured by Duchesne *et al.* (2014). Another way of obtaining the same result is to assume that the singularity yielding Equation (3.4.8) occurs at a height half-way along the jump, where we expect the slope to be largest (infinite). In this case, one would replace h_J^- in Equation (3.4.8) by the average height, which, in turn, can be approximated as $h_J^+ / 2$ if one assumes that thickness before the jump is much smaller than the thickness after the jump (Watson 1964), and obtain Equation (3.5.17). The estimated value in Equation (3.5.17) confirms the important observation in this study that the jump characteristics appear to be dictated only by the supercritical flow and upstream conditions (for type I jump of course).

3.6 Concluding remarks and discussion

In this study, the flow of a high-viscosity jet impinging on a circular disk is examined theoretically. The present study focuses on the role of gravity in the prediction of both the location and height of the circular hydraulic jump and is restricted to laminar circular steady jump. Despite the numerous theoretical and numerical studies in the literature, this prediction remains somewhat difficult to achieve through a simple and practical theoretical model. This issue was partly addressed in Chapter 2 but was limited to low-viscosity liquids. In the present study, we show how a closure to the problem can be brought by establishing a simple relation between the jump location and pre-jump height by including the effect of gravity in the developing boundary-layer region and the fully-viscous region of the flow domain. We show that the jump Froude number for high-viscosity liquid is constant confirming again the finding of Duchesne *et al.* (2014).

The flow is assumed to remain steady and axisymmetric. A model is developed based on the Kármán-Pohlhausen integral approach to describe the behaviour of the flow in the developing boundary-layer region (ii) and the fully-viscous region (iii). The integral form of the continuity and momentum equations, governing the flow of a thin film, is treated numerically separately in each region, and the flow is matched at the transition point.

Unlike the flow in the absence of gravity, the problem does not admit a similarity solution. However, a self-similar cubic profile is nevertheless assumed for the velocity, which is commonly used and was previously shown to be accurate. Although two dimensionless parameters are involved in the absence of surface tension, namely the Reynolds number Re and the Froude number Fr defined in terms of the jet radius and the flow rate, we show that the problem can be cast in terms of only one parameter: $\alpha = Re^{1/3} Fr^2$.

We find that gravity tends to enhance inertia, leading to a drop in the boundary-layer height as well as the film thickness in region (ii). Near the stagnation point, the boundary layer departs from the $\sqrt{r/Re}$ behaviour to grow increasingly linearly with distance like $\delta \approx \sqrt{3} \left(Fr / \sqrt{Re} \right) r$ under the influence of gravity. The transition point, where the outer edge of the boundary layer intersects the film surface, moves towards the perimeter of the disk with increasing gravity while the film thickness at the transition location diminishes (Figures 3-2 and 3-3).

In the fully-viscous region (iii), the shallow-water equations are reduced to a first-order equation for the thickness (3.4.4) or (3.4.9). We show that this equation exhibits an essential singularity in the presence of gravity at a distance identified as the jump location. As the flow slows down, inertia weakens, and friction increases with radial distance. At some distance gravity and viscous effects become equal, causing the singularity and therefore the jump to occur.

The numerical solution indicates that the film thickness decreases rapidly near impingement and exhibits a minimum that strengthens with gravity (Figure 3-4), accompanied by an increase in the surface velocity that decays at a slower rate with radial distance (Figures 3-5). The shear stress along the wall exhibits a weak maximum that shifts downstream as the effect of gravity increases, which we believe is an artificial effect due to the matching of the flow (Figure 3-6).

We show that, for a flat disk, the jump radius can be determined independently of its height or downstream conditions, in agreement with experimental observations. Based on

their measurements, Brechet & Neda (1999) concluded that ‘the boundary conditions on a perfectly flat plate do not influence the radius of the hydraulic jump.’ These findings are validated against existing experimental data and numerical simulation. Comparison between the predicted and measured jump locations in Figure 3-8 confirm that, for a circular jump, the jump radius is independent of the subcritical flow downstream of the jump, nor is it affected by the radius of the disk or the thickness at the edge of a flat disk. Despite the simplicity of the present approach, the predicted jump location shows surprisingly close agreement with existing numerical results based on a spectral methodology.

We consider two alternatives to determine the jump height and assess the empirical claim of Duchesne *et al.* (2014) concerning the constancy of the jump Froude number Fr_j based on the jump radius and height, and its independence of the flow rate. The first approach, following Watson and many others, consists of applying a momentum balance across the (infinitely thin) hydraulic jump, yielding Equation (3.5.3). We demonstrate theoretically that for both uniform and lubrication flows downstream of the jump, the jump Froude number is indeed constant as Duchesne *et al.* (2014) claimed. However, the predicted values in both cases are higher than their measured value. This simultaneously suggests that the discretized momentum balance approach is not adequate, which is not surprising given the finite width of the jump for high-viscosity liquids. This brings us to the second alternative, which consists of solving the film Equation (3.4.4) by deducing an asymptotic form far from impingement, taking the thickness h_∞ of the film at the edge of the disk as the boundary condition and integrating (upstream) towards the jump location to determine the height. This approach yields close agreement with the measured jump Froude number for silicon oil (see Figure 3-10). The value of h_∞ is determined theoretically as a combined static and dynamic contributions as was done for low-viscosity liquids (Chapter 2) but turns out to be negligible for high-viscosity liquids. Finally, the influence of gravity on the film shape in the entire flow domain is assessed (Figure 3-13).

Generally, once the flow field of impinging jet flow fully is established, the thermal field can be directly incorporated without modifying the flow field if constant fluid properties are assumed. In other words, as the momentum equations decouple themselves, the flow field can be solved independently. This is indeed a common practice in existing theoretical studies and even many numerical works due to its computational efficiency. However, this method becomes less accurate in the presence of large temperature variation in the domain since viscosity strongly depends on temperature. The difficulty in the inclusion of the dependence of viscosity on temperature is that the nonlinear two-way coupling usually requires numerical iteration. Consequently, it suffers not only from large computational time but also the danger of potential divergence. It is therefore desirable to design an efficient two-way coupled approach that is capable of accounting for the temperature-dependent viscosity but free from numerical iteration. This will be covered in the next chapter.

3.7 References

- Avedisian, C. T. & Zhao, Z. 2000 The circular hydraulic jump in low gravity. *Proc. R. Soc. Lond. A* **456**, 2127–2151.
- Baonga, J.B. , Gualous, H.L., Imbert, M. 2006 Experimental study of hydrodynamic and heat transfer of free liquid jet impinging a flat circular heated disk. *Applied Thermal Eng.* **26**, 1125-1138.
- Bhagat, R. K., Jha, N. K., Linden, P. F. & Wilson, D. I. 2018 On the origin of the circular hydraulic jump in a thin liquid film. *J. Fluid Mech.* **851**, R5 1-11.
- Bohr, T., Dimon, P. & Putzkaradze, V. 1993 Shallow-water approach to the circular hydraulic jump. *J. Fluid Mech.* **254**, 635-648.
- Bohr, T., Ellegaard, C., Hansen, A. E. & Haaning, A. 1996 Hydraulic jumps, flow separation and wave breaking: An experimental study. *Physica B* **228**, 1-10.

- Bohr, T., Putkaradze, V. & Watanabe, S. 1997 Averaging theory for the structure of hydraulic jumps and separation in laminar free-surface flows. *Phys. Rev. Lett.* **79**, 1038-1041.
- Brechet, Y. & Neda, Z. 1999 On the circular hydraulic jump. *Am. J. Phys.* **67**, 723–731.
- Bush, J. W. M. & Aristoff, J. M. 2003 The influence of surface tension on the circular hydraulic jump. *J. Fluid Mech.* **489**, 229-238.
- Bush, J.W.M., Aristoff, J.M., & Hosoi, A.E. 2006. An experimental investigation of the stability of the circular hydraulic jump. *J. Fluid Mech.* **558**, 33-52.
- Craik, A., Latham, R., Fawkes, M. & Gibbon, P. 1981 The circular hydraulic jump. *J. Fluid Mech.* **112**, 347-362.
- Diversified Enterprises (2009) Surface Energy Data for PDMS (Polydimethylsiloxane): http://www.accudynetest.com/polymer_surface_data/polydimethylsiloxane.pdf
- Dressaire, E., Courbin, L., Crest, J. & Stone H. A. 2010 Inertia dominated thin-film flows over microdecorated surfaces. *Phys. Fluids* **22**, 073602-07
- Duchesne, A., Lebon, L. & Limat, L. 2014 Constant Froude number in a circular hydraulic jump and its implication on the jump radius selection. *Europhys. Lett.* **107**, 54002.
- Ellegaard, C., Hansen, A., Haaning, A., Hansen, K. & Bohr, T. 1996 Experimental results on flow separation and transitions in the circular hydraulic jump. *Phys. Scr.* **T67**, 105–110.
- Ellegaard, C, Hansen, A.E., Haaning, A., Marcussen, A., Bohr, T., Hansen, J.L. & Watanabe, S. 1998 Creating corners in kitchen sink flows. *Nature* **392**, 767-768.
- Ellegaard, C, Hansen, A.E., Haaning, A., Hansen, K., Marcussen, A., Bohr, T., Hansen, J.L. & Watanabe, S. 1999 Polygonal hydraulic jumps. *Nonlinearity* **12**, 1-7.

- Hansen, S. H., Horluck, S., Zauner, D., Dimon, P., Ellegaard, C. & Creagh, S. C. 1997 Geometric orbits of surface waves from a circular hydraulic jump. *Phys. Rev. E* **55**, 7048-7061.
- Kasimov, A. R. 2008 A stationary circular hydraulic jump, the limits of its existence and its gasdynamic analogue. *J. Fluid Mech.* **601**, 189–198.
- Khayat, R. E. 2016 Impinging planar jet flow and hydraulic jump on a horizontal surface with slip. *J. Fluid Mech.* **808**, 258-289.
- Khayat, R. E. & Kim, K. 2006 Thin-film flow of a viscoelastic fluid on an axisymmetric substrate of arbitrary shape. *J. Fluid Mech.* **552**, 37-71.
- Lienhard, J. 2006 Heat transfer by impingement of circular free-surface liquid jets. *18th National & 7th ISHMT-ASME Heat and Mass Transfer Conference* (IIT Guwahati, India) 1-17.
- Liu, X. & Lienhard, J. 1993 The hydraulic jump in circular jet impingement and in other thin liquid films. *Experiments in Fluids* **15**, 108-116.
- Liu, X., Gabour, L. A. & Lienhard, J. 1993 Stagnation-point heat transfer during impingement of laminar liquid jets: Analysis including surface tension. *ASME J. Heat Transfer* **115**, 99-105.
- Lubarda, V. & Talke, K. A. 2011 Analysis of the equilibrium droplet shape based on an ellipsoidal droplet Model. *Langmuir.* **27**, 10705–10713.
- Mohajer, B. & Li, R. 2015 Circular hydraulic jump on finite surfaces with capillary limit. *Phys. Fluids* **27**, 117102.
- Ozar, B., Cetegen, B. M. & Faghri, A. 2003 Experiments on the flow of a thin liquid film over a horizontal stationary and rotating disk surface. *Experiments in Fluids* **34**, 556–565.
- Passandideh-Fard, M., Teymourtash, A. R. & Khavari, M. 2011 Numerical study of circular hydraulic jump using volume-of-fluid method. *J. Fluids Eng.* **133**, 011401.

- Prince, J. F., Maynes, D. & Crockett, J. 2012 Analysis of laminar jet impingement and hydraulic jump on a horizontal surface with slip. *Phys. Fluids* **24**, 102103.
- Rao, A. & Arakeri, J. H. 1998 Integral Analysis Applied to Radial Film Flows. *Int. J. Heat Mass Transfer* **41**, 2757–2767.
- Rayleigh, Lord 1914 On the theory of long waves and bores. *Proc. R. Soc. Lond. A* **90** (619), 324–328.
- Rojas, N., Argentina, M. & Tirapegui, E. 2010 Inertial lubrication theory. *Phys. Rev. Letts.* **104**, 187801-4.
- Rojas, N., Argentina, M. & Tirapegui, E. 2013 A progressive correction to the circular hydraulic jump scaling. *Phys. Fluids* **25**, 042105-9
- Rojas, N. & Tirapegui, E. 2015 Harmonic solutions for polygonal hydraulic jumps in thin fluid films. *J. Fluid Mech.* **780**, 99-119.
- Stevens, J. & Webb, B. W. 1992 Measurements of the free surface flow structure under an impinging, free liquid jet. *ASME J. Heat Transfer* **114**, 79-84.
- Schlichtling, H. & Gersten, K. 2000 *Boundary-layer theory* (Springer, Berlin).
- Tani, I. 1949 Water Jump in the Boundary Layer. *J. Phys. Soc. Japan.* **4**, 212-215.
- Vicente, C. M. S., Andre, P. S. & Ferreira, R. A. S. 2012 Simple measurement of surface free energy using a web cam. *Rev. Brasil. Ens. Fisica* **34**, 3312-1-5
- Watanabe, S., Putkaradze, V. & Bohr, T. 2003 Integral methods for shallow free-surface flows with separation. *J. Fluid Mech.* **480**, 233–265.
- Watson, E. 1964 The spread of a liquid jet over a horizontal plane. *J. Fluid Mech.* **20**, 481-499.
- White, F. 2006 *Fundamentals of Fluid Mechanics*. McGraw-Hill.

Yang, S. & Chen, C. 1992 Laminar film condensation on a finite-size horizontal plate with suction at the wall. *Appl. Math. Modelling* **16**, 325-329.

Yang, Y., Chen, C. & Hsu, P. 1997 Laminar film condensation on a finite-size wavy disk. *Appl. Math. Modelling* **21**, 139-144.

Zhao, J. & Khayat, R.E. 2008 Spread of a non-Newtonian liquid jet over a horizontal plate. *J. Fluid Mech.* **613**, 411-443.

Chapter 4

4 The influence of heat transfer on liquid jet spreading and hydraulic jump formation

As pointed out at the end of Chapter 3, under the assumption of constant fluid properties, the accuracy of both the flow and the thermal field will drop in the presence of large temperature variation. On the other hand, incorporating the two-way coupling (temperature-dependent viscosity) generally requires non-linear iteration that suffers from large amounts of computing time and the potential danger of divergence. In this regard, we devote this chapter to design an iteration-free model to enhance the efficiency. More importantly, it makes investigating the influence of the heat transfer on the jet spreading and the hydraulic jump theoretically feasible.

4.1 Introduction

When a circular liquid jet impacts a solid surface, it spreads out radially as a thin film until reaching a critical radius at which the thickness of the liquid layer rises abruptly, forming a circular hydraulic jump as illustrated in Figure 4-1. The domains before and after the jump are formally known as the supercritical and subcritical regions, respectively. Impinging liquid jet is widely used in industrial cooling processes and hydraulic jump can significantly affect the performance. Consequently, the prediction of its location (radius) and the quantitative information of the flow and thermal fields are crucial in the design of such cooling applications.

For the hydrodynamics of impinging jet flow, Watson (1964) solved the flow field in the supercritical region using the boundary-layer theory. Gravity was neglected before the jump due to the small film thickness. Based on the balance of forces, the location of the jump was obtained with an imposed downstream depth. Watson's theory was tested in many experiments, including those of Watson himself, Craik *et al.* (1981), Bush & Aristoff (2003) and Baonga *et al.* (2006). The effect of surface tension was neglected in Watson's work, and was later included by Bush & Aristoff (2003), yielding a better prediction.

Watson's method requires an imposed downstream depth which is often controlled by downstream barrier. In practical applications, however, the target surface is often free of such controlled height. In this regard, Duchesne *et al.* (2014) found that the jump Froude number based on the jump height and depth-averaged velocity remains constant when the flow rate is varied. Consequently, they were able to determine the jump radius based on this constant jump Froude number, thus eliminating the need to impose a jump height. In Chapter 2, we have established a coherent model by connecting the super- and subcritical flows through a shock. The thickness near the disk edge was also derived. Consequently, we have also proved the constancy of the jump Froude number (see Chapter 2).

Bhagat *et al.* (2018) highlighted the importance of the role of surface tension. Based on their analysis and experiments, they concluded that, for a circular hydraulic jump, surface tension is the major cause of hydraulic jump, and gravity plays little role. However, their findings are not conclusive as per Chapter 3. Duchesne *et al.* (2019) very recently also pointed out that the approach of Bhagat *et al.* (2018) has some flaws that can overestimate the role of surface tension (see also Scheichl 2018, 2019). In fact, the role of gravity can be crucial, at least for a fluid of high viscosity. In Chapter 3, we derived a method specifically for high-viscosity liquids and showed that the location of the jump can be well predicted without surface tension.

However, since the liquids involved in jet cooling are generally low-viscosity fluids and thus the force and momentum balance method remains accurate, the hydraulic jump in the current heat transfer problem will be treated following the development of Chapter 2, which is based in part on the original approach of Watson (1964).

As to the thermal field of an impinging liquid jet, most existing studies focused only on the effect of the flow on the heat transfer. Chaudhury (1964) obtained a similarity solution for the case of constant wall temperature. He showed that the heat transfer rate decreases monotonically with radial distance. Chaudhury (1964) assumed constant fluid properties and zero heat loss from the free surface due to the dominance of convection. These assumptions became the basis for most of the later studies. Brdlik & Savin (1965) solved the energy equation for the same problem using an integral approach. They

assumed that the ratio of the thermal boundary layer to hydrodynamic boundary layer is $Pr^{-1/3}$, thus the momentum equation was conveniently eliminated. Saad *et al.* (1977) numerically investigated a submerged jet impinging on a surface of constant temperature using an upwind finite-difference scheme. It was found that, for a parabolic velocity inlet, the maximum Nusselt number is larger and closer to the impingement point when compared to a flat velocity profile.

Wang *et al.* (1989a) first considered the heat transfer in the stagnation region and obtained a nearly constant Nusselt number. Later Wang *et al.* (1989b) also considered the heat transfer outside the stagnation region and extended their study to the case of distributed (varying with distance) wall temperature and heat flux. Liu *et al.* (1993) numerically analyzed the influence of surface tension on stagnation heat transfer for inviscid liquids. They observed that at low flow rate, surface tension can slightly increase the Nusselt number. But this effect is negligible for practical configurations. The effect of surface roughness was studied by Gabour & Lienhard (1994) with experiments. The flow was found to be turbulent and the local Nusselt can be increased by 50% compared to a smooth surface.

Searle *et al.* (2017) considered impinging flow on slippery surface of constant temperature. They found that both the thermal and hydrodynamic boundary layer thicknesses decrease with increasing slip and temperature jump length. Hydraulic jump was not considered. Rohlf's *et al.* (2014) in their numerical work reported that a maximum Nusselt number can occur depending on the inlet velocity profile and the nozzle-to-plate distance. Kuraan *et al.* (2017) observed that at low nozzle-to-disk distance, the heat transfer will be enhanced with decreasing nozzle-to-disk distance.

We emphasize here that all these studies introduced above have assumed constant fluid properties. Even though for most liquids, the heat capacity and thermal conductivity do not change significantly with temperature (Okhotin *et al.* 1992, Granato 2002), their viscosities decrease moderately or even significantly with temperature as a result of the decrease in the molecular cohesive forces (Kundu *et al.* 2016). Variations of multiple orders of magnitude is common for liquids (Seeton 2006). This will be demonstrated later

when the viscosity models are introduced. Although surface tension is generally less sensitive to temperature variation, and therefore is not expected to have a significant effect on the normal stress for a thin film, its influence can be important on the surface shear stress (Marangoni effect) for a large temperature gradient. This effect is also largely missing in existing theoretical works due to difficulty of thermal coupling.

For pure boundary-layer flow (i.e. infinite domain without a free surface) on a flat plate of constant temperature, the two-way coupling can be treated using a similarity or Blasius approach (Miller *et al.* 2018). However, the similarity solution is generally not possible to find even for boundary-layer flow as in the presence of gravity or for an imposed heat flux. Earlier, Kafoussius & Williams (1995) examined the heated boundary-layer flow in the presence of gravity, using the so-called local similarity approach. A similarity approach is clearly unfeasible for the current free-surface problem in the presence of Marangoni effect and general heating conditions at the disk. Due to these limitations, the two-way coupling has largely been ignored in the literature for free-surface impinging jet and hydraulic jump problem, which is the focus of the current chapter.

The first major theoretical contribution to the two-way coupling problem for an impinging jet was due to Liu & Lienhard (1989). They adopted an integral approach to solve the energy equation and obtained the thermal boundary layer thickness based on the velocity and viscous boundary layer thickness. To account for the change of viscosity with temperature, they implemented an iterative algorithm to solve the coupled problem. The viscosity was evaluated based on the locally averaged temperature. Surface tension or Marangoni effect was ignored. They observed that the thermal boundary layer would not reach the free surface when the Prandtl number is greater than a critical value: 4.859. This value should however only be valid for a small temperature variation since the Prandtl number was obtained by assuming constant fluid properties. We note that the influence of heat transfer on the hydraulic jump region was not included in the work of Liu & Lienhard (1989). In this regard, Sung *et al.* (1999), adopting a finite-element implementation, and solved the coupled problem and investigated the influence of heat transfer on the location and height of the hydraulic jump. The location of the jump was found to move downstream with increased wall temperature. In addition, a sharp drop in

the Nusselt number was reported in the hydraulic jump region. We shall compare our predictions based on the thin-film approach against their finite-element results.

To the best of our knowledge, a simple two-way coupling is still not available theoretically by far. In this case, we propose an approximate iteration-free model to address the coupling problem for a heated impinging jet. Thus, the influence of the coupling on the location and height of the circular hydraulic jump, as well as on the sub-critical thermal field can be investigated theoretically. As will be seen, the advantage of the K-P approach provides a surprisingly convenient way to incorporate the temperature-dependent viscosity and surface tension approximately through the thickness of the viscous layer. More importantly, the present approach enhances our physical understanding of the effects of heat transfer on the axisymmetric thin-film flow and hydraulic jump structure resulting from the nonlinear two-way coupling. The current approach inherently eliminates the potential possibility of divergence in iterative schemes. Due to the variation of free-surface temperature, we also explore the effect of Marangoni stress that is largely missing in existing theoretical studies. It turns out that the current model, despite its approximate nature (like all the K-P approaches in the literature), predicts well the flow and thermal fields since, as we shall see, a reasonably good agreement is found when compared with existing experimental, theoretical and numerical studies.

In current chapter, the development of the hydrodynamic and thermal boundary layers, the influence of heating on the location and height of hydraulic jump are comprehensively explored. Additional important phenomena such as the difference between wall flux heating and wall temperature heating and the shock-type drop in the Nusselt number at the jump will also be investigated. The governing equations and boundary conditions as well as the viscosity model are presented in Section 4.2. The integral equations and the profiles for the velocity and temperature are detailed in Section 4.3. Results on the influence of the temperature and the heat flux are also presented, along with comparison with existing measurements and numerical data. We devote Section 4.4 to the hydraulic jump and the subcritical flow and thermal fields. In the presence of the two-way coupling, solving solely the momentum balance across the jump

is not sufficient to yield the location of the jump. Therefore, we resort to an energy balance as an additional relation to close the problem.

4.2 Physical domain and problem statement

Consider the steady laminar liquid jet of radius a , impinging at a volume flow rate Q and temperature \hat{T}_0 on a heated disk, lying normal to the jet direction. A hat is used to designate a dimensional variable or parameter when necessary. The liquid viscosity $\hat{\nu}$ and surface tension $\hat{\gamma}$ are assumed to depend on the temperature \hat{T} . The flow configuration is depicted schematically in Figure 4-1, where dimensionless variables are used. As the flow is assumed to be axisymmetric, the problem is formulated in the (r, z) plane, with the origin coinciding with the disk center, r and z being the dimensionless radial and vertical coordinates. The r -axis is taken along the disk radius and the z -axis is taken in upwards direction parallel to the jet. In this case, $u(r, z)$ and $w(r, z)$ are the corresponding dimensionless velocity components, and $T(r, z)$ is the dimensionless temperature. The length and velocity scales are taken to be a and $W \equiv Q / (\pi a^2)$ in both the radial and vertical directions. The temperature and heat flux are scaled by \hat{T}_0 and $k\hat{T}_0/a$, respectively, where k is the thermal conductivity, assumed to be constant. The two-way coupling is in principle ensured by adopting the temperature-dependent kinematic viscosity $\nu(T)$ and surface tension $\gamma(T)$, scaled by their reference values $\nu_0 = \hat{\nu}(\hat{T}_0)$ and $\gamma_0 = \hat{\gamma}(\hat{T}_0)$.

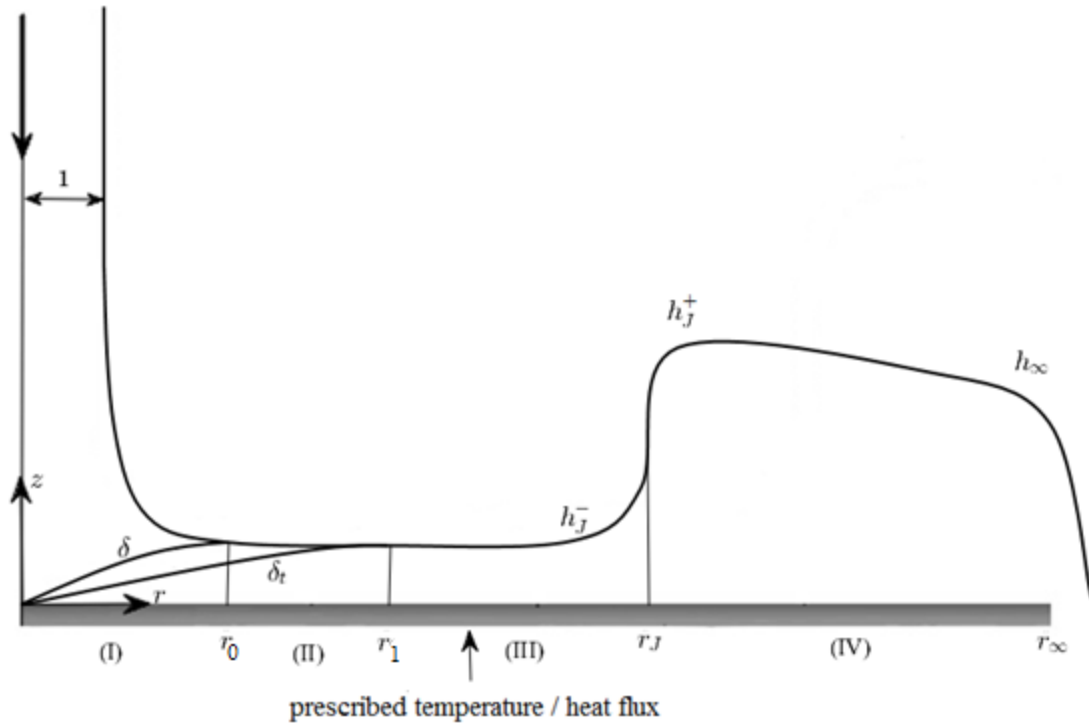


Figure 4-1: Schematic illustration of the axisymmetric jet flow impinging on a heated disk. The four sub-regions of the physical domain are also shown. All notations are dimensionless.

Upstream of the hydraulic jump, the variation of the film thickness with the radius is expected to be smooth and gradual, so that the radial variation of the hydrostatic pressure and Laplace pressure (caused by surface tension) are also small and thus negligible. Downstream of the jump, gravity is included due to the larger film thickness and serves as the driving force of the flow which is predominantly of lubrication type (Duchesne *et al.* 2014). Surface tension effect is also included at the jump and near the trailing edge of the disk when seeking the boundary condition for the flow downstream.

Under these assumptions, five similarity groups emerge, namely the Reynolds number $Re = Wa / \nu_0$, the Froude number $Fr = W / \sqrt{ag}$, the Peclet number $Pe = Wa / \kappa$, where $\kappa = k / (\rho C_p)$ is the thermal diffusivity, C_p being the heat capacity, and the capillary number $Ca = \rho \nu_0 W / \gamma_0$. In this work, the thermal diffusivity is assumed to be constant. Additional related groups are also introduced, namely the Prandtl number

$Pr = \nu_0 / \kappa = Pe / Re$. The Nusselt number is then defined as $Nu(r) = \tilde{h}a / k = \hat{q}_w a / (k(\hat{T}_w - \hat{T}_0)) = q_w(r) / (T_w(r) - 1)$, given in terms of the (dimensionless) transverse heat flux at the wall, $q_w(r) = -(\partial T / \partial z)|_{z=0}$, and the wall temperature, $T_w(r)$. In this study, either the heat flux $q_w(r)$ or the temperature $T_w(r)$ can be prescribed along the disk, and the proposed methodology developed here is equally applicable for constant and varying wall conditions.

4.2.1 The physical domain

Following the treatments of Watson (1964) (see also Liu & Lienhard 1989, Searle *et al.* 2017) and neglecting the stagnation region, we identify four distinct flow regions for the impinging jet heating problem. In region (I), both the hydrodynamic and the thermal boundary layers are below the liquid surface, growing until the former reaches the liquid surface at $r = r_0$. It is worth noting that for non-metallic liquids, the kinematic viscosity is generally larger than the thermal diffusivity (i.e. Prandtl number larger than unity), leading to the thermal boundary layer remaining thinner than the hydrodynamic boundary layer until it reaches the liquid-air interface. Region (II) begins from r_0 , where the viscous effect is appreciable up to the liquid surface, but the thermal boundary layer continues to grow. In the first two regions, the velocity and temperature outside their respective boundary layers remain essentially constant and unaffected by the viscous and thermal effects, and thus retain the same values as the incoming jet. Region (III) is identified when the thermal boundary layer merges with the free surface at $r = r_1$ where both the viscous and thermal effects have invaded the film thickness. The circular hydraulic jump emerges at a radius $r = r_j$, which separates region (III) and region (IV). We observe that Marangoni effect is consequently present only in regions (III) and (IV) ($r_1 < r < r_\infty$) where variation in the surface temperature is expected. The jump radius r_j is generally larger than r_0 as the jump typically occurs after the film becomes fully viscous, but not necessarily larger than r_1 . However, the tested cases in the present work are limited to the scenario when r_j is greater than r_1 for the ease of mathematical

demonstration. Referring to Figure 4-1, the height immediately upstream of the jump is denoted by h_j^- , and the height immediately downstream of the jump is denoted by h_j^+ . The subcritical height $h(r > r_j)$ is generally not constant and is different from the jump height h_j^+ . This variation can be large for high-viscosity liquids (Duchesne *et al.* 2014). In this study, the fluid is assumed to be drained at the edge of the disk at $r = r_\infty$, and the flow remains steady, with the film thickness denoted by $h_\infty = h(r = r_\infty)$. The edge thickness h_∞ is not expected to depend heavily on the flow rate (Dressaire *et al.* 2010, Rojas *et al.* 2013, Duchesne *et al.* 2014, Mohajer & Li 2015).

4.2.2 Governing equations and boundary conditions

Unless otherwise specified, the Reynolds number is assumed to be large but without causing turbulence. Consequently, for steady axisymmetric flow, the mass and momentum conservation equations are formulated using a thin-film or Prandtl boundary-layer approach, which amounts to assuming that the radial flow varies much slower than the vertical flow (Schlichting & Gersten 2000). To account for the two-way coupling, the temperature dependent kinematic viscosity is incorporated in the formulation. In this case, the reduced dimensionless conservation equations for mass, radial momentum, transverse momentum and energy become

$$\frac{\partial u}{\partial r} + \frac{u}{r} + \frac{\partial w}{\partial z} = 0, \quad (4.2.1a)$$

$$\text{Re} \left(u \frac{\partial u}{\partial r} + w \frac{\partial u}{\partial z} \right) = -\frac{\text{Re}}{\text{Fr}^2} \frac{\partial p}{\partial r} + \frac{\partial}{\partial z} \left(\nu \frac{\partial u}{\partial z} \right), \quad (4.2.1b)$$

$$\frac{\partial p}{\partial z} = -1, \quad (4.2.1c)$$

$$\text{Pe} \left(u \frac{\partial T}{\partial r} + w \frac{\partial T}{\partial z} \right) = \frac{\partial^2 T}{\partial z^2}. \quad (4.2.1d)$$

These boundary-layer type equations are often used to model the spreading of thin-film flow and heat transfer (Chaudhury 1964, Liu & Lienhard 1989, Searle *et al.* 2017). We observe that the pressure for a thin film is hydrostatic as a result of its vanishing at the free surface in the absence of large surface curvature. In addition, upstream of the jump, the variation of the film thickness with the radius is expected to be smooth and gradual so that the radial variation of the hydrostatic pressure is negligible. Indeed, according to Prince *et al.* (2012), the hydrostatic term has at most a 0.4% cumulative influence on the flow dynamics. At the disk, the no-slip and no-penetration conditions are assumed to hold for any r :

$$u(r, z = 0) = w(r, z = 0) = 0. \quad (4.2.2a,b)$$

In addition, the boundary condition for the temperature of the liquid at the disk surface is introduced as

$$\frac{\partial T}{\partial z}(r, z = 0) = -q_w(r), \quad (4.2.3a)$$

when the wall heat flux is imposed, and

$$T(r, z = 0) = T_w(r), \quad (4.2.3b)$$

when the wall temperature is imposed. We note that Equation (4.2.3b) is violated in the presence of slip, which automatically induces a temperature jump (Maynes & Crockett 2014, Searle *et al.* 2017). At the free surface $z = h(r)$, the kinematic condition and the balance between fluid stress and surface tension effect yield:

$$w(r, z = h) = u(r, z = h)h'(r), \quad (4.2.4a)$$

$$p(r, z = h) = 0, \quad (4.2.4b)$$

$$\frac{\partial u}{\partial z}(0 < r < r_1, z = h) = 0, \quad (4.2.4c)$$

$$v_s(r) \frac{\partial u}{\partial z}(r_1 < r < r_\infty, z = h) = \text{Ca}^{-1} \frac{d\gamma}{dT_s} T'_s(r), \quad (4.2.4d)$$

where $T_s(r) = T(r, z = h)$ and $v_s(r) \equiv v[T = T_s(r)]$ are the temperature and viscosity at the film surface. We also let $d\gamma/dT_s \equiv d\gamma/dT|_{T=T_s(r)}$ denote the derivative of the surface tension with respect to the surface temperature. In general, a prime denotes total differentiation with respect to the independent variable. We observe that the Marangoni effect, reflected in (4.2.4d), is only present downstream of the second transition location where the surface temperature varies.

Neglecting the heat loss (i.e. evaporation, radiation and air conduction) at the liquid-air interface (Chaudhury 1964, Liu & Lienhard 1989, Searle *et al.* 2017), the condition for temperature at the free surface becomes

$$\frac{\partial T}{\partial z}(r, z = h) = 0. \quad (4.2.5)$$

The flow field is sought separately in the four regions and the leading edge of the boundary layer in region (I) is taken to coincide with the disk centre. Consequently, the additional boundary conditions are as follows. In region (I), the flow is assumed to be sufficiently inertial for inviscid flow to prevail between the boundary-layer outer edge and the free surface. In this case, the following conditions at the outer edge of the boundary layer and beyond must hold:

$$\frac{\partial u}{\partial z}(r < r_0, z = \delta) = 0, \quad u(r < r_0, \delta \leq z < h) = 1. \quad (4.2.6a,b)$$

Similar conditions are established in regions (I) and (II) for the temperature, which remains the same as the incoming jet temperature above the thermal boundary layer (see Figure 4-1):

$$\frac{\partial T}{\partial z}(r < r_1, z = \delta_t) = 0, \quad T(r < r_1, \delta_t \leq z < h) = 1. \quad (4.2.7a,b)$$

Finally, the conservation of mass at any location yields the following relation in dimensionless form:

$$\frac{1}{2r} = \int_0^{h(r)} u(r, z) dz. \quad (4.2.8)$$

In liquid jet impingement problems, it is well established that under the assumption of constant fluid properties, similarity solutions exist for both the fluid flow (Watson 1964) and the heat transfer (Chaudhury 1964). However, the presence of coupling between hydrodynamics and heat transfer causes the failures of such self-similar solutions. Therefore, approximate solutions are sought in the current study in each region. Consequently, a two-way coupled integral approach of the Kármán-Pohlhausen (K-P) type (Schlichting & Gersten 2000) is designed and adopted upstream of the jump, serving as a new extension to existing integral approaches (Watanabe *et al.* 2003, Prince *et al.* 2012, Searle *et al.* 2017). The necessity to include a temperature-dependent viscosity is the result of the large change in value over a small temperature range as we shall see next.

4.2.3 The viscosity and surface tension model

Among a variety of temperature-dependent viscosity models available in the literature. The classical viscosity model proposed by Fulcher (1992) is commonly recommended as it gives fairly satisfying fits with experimental data (Mauro *et al.* 2009) except at very low temperature (Scherer 1992). Fulcher's model is known as the Vogel–Tamman–Fulcher (VTF) or the Vogel-Fulcher-Tamman (VFT) equation (Rampp *et al.* 2000). The kinematic viscosity of liquids using the VFT equation can be written in the dimensional form: $\hat{\nu}(\hat{T}) = \hat{A} \times 10^{\hat{B}/(\hat{T} - \hat{C})}$, with \hat{A} , \hat{B} and \hat{C} being the fitting parameters from experiments. We report in Figure 4-2 the fitting of viscosity data for three common liquids. The experimental data are taken from various sources. The fitting parameters are given in Table 1.

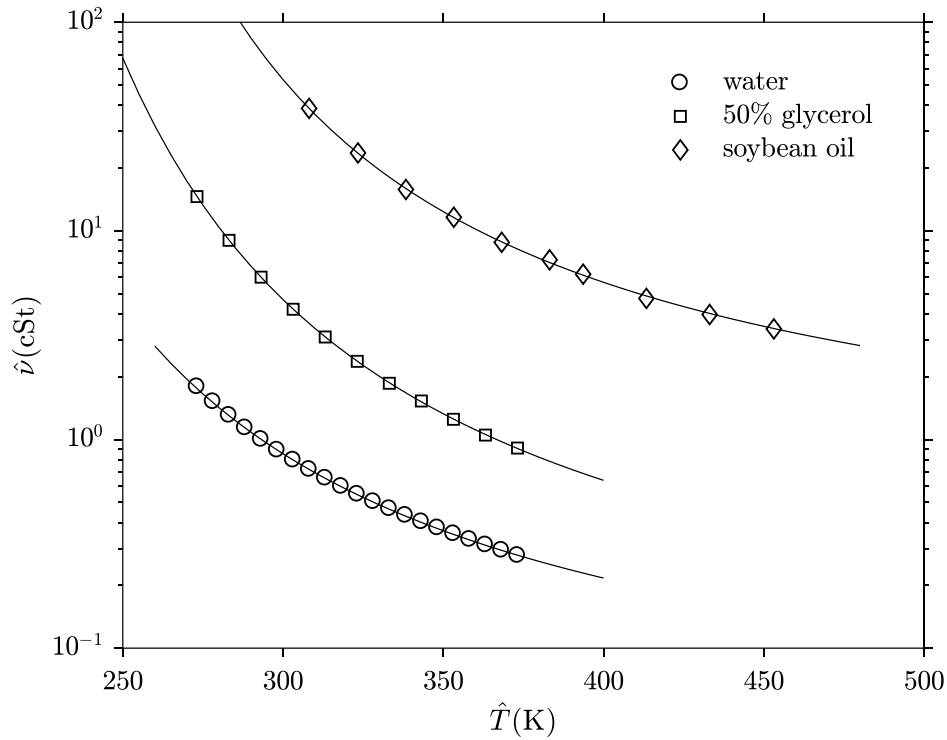


Figure 4-2: The dependence of viscosity on temperature for three common liquids. Solid lines indicate the fitting using the parameters in Table 1. The markers are experimental data from various sources (Korson et al. 1969 for water, Segur & Oberstar 1951 for glycerol, and Peleg 2017 for soybean oil).

Table 1: Viscosity and surface tension fitting parameters for three common liquids.

Liquid	\hat{A} (cSt)	\hat{B} (K)	\hat{C} (K)	\hat{D} (N/mK)	\hat{E} (N/m)
Water	0.02414	247.8	140.0	-0.0001669	0.1216
50% glycerol	0.03925	290.1	160.3	-0.0001049	0.09986
Soybean oil	0.43260	240.2	180.5	-0.00005	0.0463

The VFT model, when scaled by a reference kinematic viscosity at \hat{T}_0 (here taken to correspond to the temperature of the impinging jet), is written in dimensionless form as a two-parameter expression:

$$v(T) = 10^{B(1-T)/[(1-C)(T-C)]}, \quad (4.2.9)$$

with T scaled by \hat{T}_0 . Here $B = \hat{B}/\hat{T}_0$ and $C = \hat{C}/\hat{T}_0$ are dimensionless parameters.

As to the surface tension, Figure 4-3 depict the temperature dependence for the same liquids, all reflecting a linear dependence of the form $\hat{\gamma}(\hat{T}) = \hat{D}\hat{T} + \hat{E}$. The values of the two parameters are reported in Table 1. In dimensionless form, we have

$$\gamma(T) = DT + E, \quad (4.2.10)$$

where $D = \hat{D}\hat{T}_0 / (\hat{D}\hat{T}_0 + \hat{E})$ and $E = \hat{E} / (\hat{D}\hat{T}_0 + \hat{E})$ are dimensionless parameters.

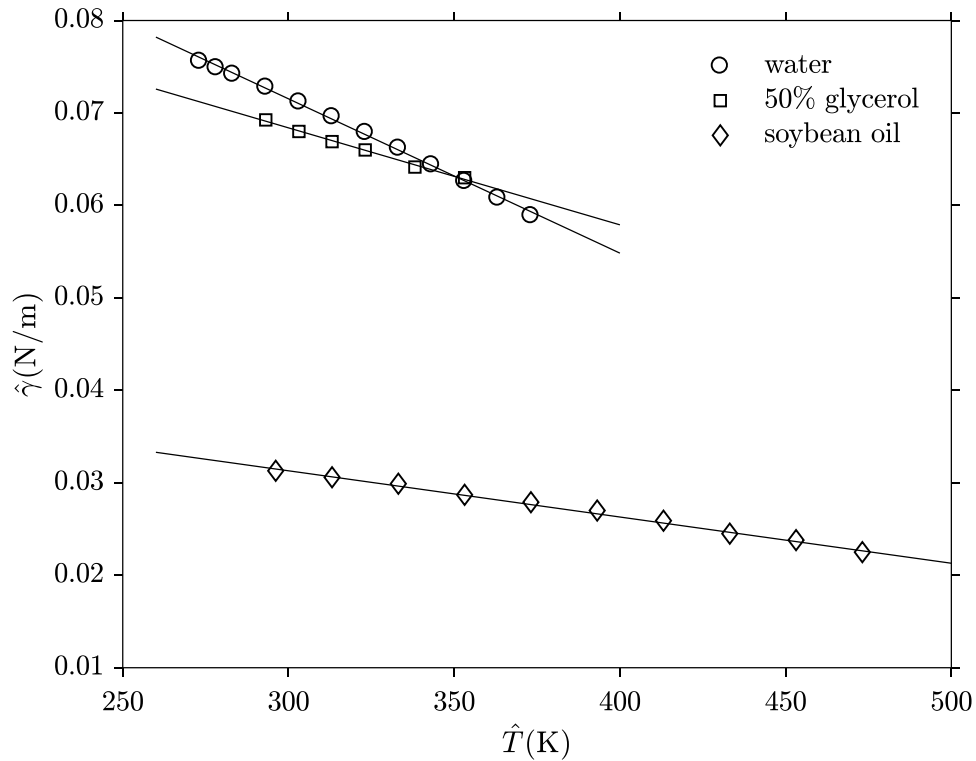


Figure 4-3: The dependence of surface tension on temperature for three common liquids. Solid lines indicate the fitting using the parameters T_n in table 1. The markers are experimental data from various sources (Agrawal & Menon 1992 for water, Takamura *et al.* 2012 for glycerol, Sahasrabudhe *et al.* 2017 for soybean oil).

For other popular models and their applicable liquids, the reader is referred to the paper of Seeton (2006) and the references therein. With the advantage of the integral approach, as we shall see, the resulting equations can be solved for any model of viscosity and surface tension given explicitly in terms of the temperature. The dimensionless kinematic viscosity and surface tension will be incorporated in the current formulation. Only the case of water will be considered in the present study. The temperature of the impinging jet will be specified, allowing the deductions of the values of the dimensionless parameters from Table 1.

4.3 The influence of heat transfer on the flow in the supercritical region and transition locations.

As mentioned earlier, either the heat flux or the temperature can be imposed at the wall. We shall examine both conditions. We formulate the general problem first

4.3.1 The general supercritical integral formulation

In region (I), where the inviscid flow dominates the upper layer ($\delta \leq z < h$) of the film, the radial velocity above the boundary layer remains equal to unity. The boundary-layer height δ is determined by considering the mass and momentum balance over the boundary-layer region. Consequently, upon integrating Equation (4.2.1b) across the hydrodynamic boundary-layer thickness and using Equation (4.2.1a) to eliminate w , we obtain the integral form of the momentum equation in the boundary-layer region:

$$\frac{\text{Re}}{r} \frac{d}{dr} \left(r \int_0^{\delta(r)} u(u-1) dz \right) = -v_w(r) \frac{\partial u}{\partial z} \Big|_{z=0}, \quad r < r_0, \quad (4.3.1)$$

Here $v_w(r) \equiv \nu [T = T_w(r)]$ denotes the value of the viscosity at the wall (disk). Similarly, by integrating Equation (4.2.1d) across the thermal boundary layer and using Equation (4.2.1a), we obtain the thermal integral equation:

$$\frac{Pe}{r} \frac{d}{dr} \left(r \int_0^{\delta_t(r)} u(T-1) dz \right) = - \frac{\partial T}{\partial z} \Big|_{z=0}, \quad r < r_1. \quad (4.3.2)$$

Inherent to the integral approach is the proper choice of the velocity and temperature profiles needed to solve the integral equations. A variety of profiles are of choice: parabolic velocity (Tani 1949, Bohr, *et al.* 1993, Basu & Cetegen 2007, Kasimov 2008), cubic velocity (Bohr *et al.* 1997, Prince *et al.* 2012), and even quartic velocity (Bohr *et al.* 1996). In the current study, we choose a cubic profile which is considered to be the leading-order solution in a comprehensive spectral approach when inertia is included (Khayat 2006, Rojas *et al.* 2010). The cubic profile seems to be amply adequate as it leads to a close agreement with Watson's (1964) similarity solution for a jet impinging on a circular disk (Prince *et al.* 2012, Chapter 2). Khayat (2016) also found that the cubic profile yields a good agreement with his numerical solution for slipping flow. The corresponding velocity profile, in region (I), is thus given by

$$u(r < r_0, z) = \frac{3}{2} \frac{z}{\delta} - \frac{1}{2} \left(\frac{z}{\delta} \right)^3, \quad (4.3.3)$$

which satisfies Equations (4.2.2a) and (4.2.6). Similarly, we also approximate the temperature by a cubic profile in the pre-jump jump region. Using conditions (4.2.3) and (4.2.7), the temperature in region (I) and (II) is given by

$$T(r < r_1, z) = T_w(r) - 3 \frac{T_w(r) - 1}{2} \frac{z}{\delta_t} + \frac{T_w(r) - 1}{2} \left(\frac{z}{\delta_t} \right)^3, \quad (4.3.4)$$

We note that the temperature profile (4.3.4) satisfies the energy Equation (4.2.1d) at the wall. Upon inserting Equation (4.3.3) and Equation (4.3.4) into Equation (4.3.1) and Equation (4.3.2), we obtain a pair of coupled differential equations for the hydrodynamic and thermal boundary-layer thickness over the range $0 < r \leq r_0$:

$$\frac{d\delta}{dr} = \frac{140}{13Re} \frac{v_w}{\delta} - \frac{\delta}{r}, \quad (4.3.5)$$

$$\frac{d\delta_t}{dr} = -\frac{\delta_t(14\delta^2 - \delta_t^2)}{4(T_w - 1)(7\delta^2 - \delta_t^2)} \frac{dT_w}{dr} + \frac{\text{Pe}\delta_t^3 r(14\delta^2 - 3\delta_t^2) \frac{d\delta}{dr} - 14\text{Pe}\delta^3 \delta_t^3 + \text{Pe}\delta\delta_t^5 + 140\delta^4 r}{4\text{Pe}\delta_t^2 \delta r(7\delta^2 - \delta_t^2)}. \quad (4.3.6)$$

These equations are solved subject to $\delta(r=0) = \delta_t(r=0) = 0$. In the isothermal limit ($v=1$), one recovers the solution of Equation (4.3.1) as $\delta(r < r_0) = 2\sqrt{(70/39)r/\text{Re}}$, which agrees with the $\delta \sim \sqrt{r/\text{Re}}$ behaviour established from dimensional argument of Equation (4.2.1b).

Originating from the disk centre, both the hydrodynamic and thermal boundary layers grow with the radial distance, eventually invading the entire film thickness. As the hydrodynamic boundary layer grows faster (see Section 4.2), it first reaches the jet free surface at $r = r_0$. For $r < r_0$, the free surface at some height $z = h(r) > \delta(r)$ lies above the boundary-layer outer edge. The height of the free surface in region (I) is then determined from mass conservation inside and outside the boundary layer. Therefore,

$$\int_0^{\delta(r)} u(r, z) dz + h(r) - \delta(r) = \frac{1}{2r}, \quad r < r_0. \quad (4.3.7)$$

The transition location r_0 where the hydrodynamic boundary layer first reaches the film surface is computed by equating $h(r_0)$ and $\delta(r_0)$. The corresponding transition heights for the thermal boundary layer and liquid film are given by $\delta_{t0} \equiv \delta_t(r_0)$ and $h_0 \equiv h(r_0)$ respectively, which serve as the initial conditions for the next region.

In region (II), the potential flow in the radial direction ceases to exist, with the velocity $u_s(r) = u(r, z = h)$ at the free surface becoming dependent on r . Integrating the momentum equation between the disk surface and the free surface, and using the mass conservation Equation (4.2.8), the momentum integral equation is obtained as

$$\frac{\text{Re}}{r} \frac{d}{dr} \left(r \int_0^{h(r)} u^2 dz \right) = -v_w(r) \left. \frac{\partial u}{\partial z} \right|_{z=0}, \quad r_0 < r < r_1. \quad (4.3.8)$$

We note that both the temperature profile and the energy integral equation in region (II) remain the same as in region (I), given by Equations (4.3.4) and (4.3.2) since the thermal boundary layer is still below the liquid-air interface. However, the cubic velocity profile subject to conditions (4.2.2a) and (4.2.4b) takes a different form:

$$u(r_0 < r < r_1, z) = \frac{1}{2} u_s(r) \left(3 \frac{z}{h} - \frac{z^3}{h^3} \right), \quad (4.3.9)$$

We observe that the shear stress at the film surface remains zero since the surface temperature $T_s(0 < r < r_1) = 1$. The surface velocity $u_s(r)$ is determined from the mass conservation Equation (4.2.8) to yield:

$$u_s(r_0 < r < r_1) = \frac{4}{5hr}, \quad (4.3.10)$$

which agrees with Prince *et al.* (2012) when setting their slip parameter equal to zero.

The validity of the cubic velocity profiles (4.3.3) and (4.3.9) is assessed in Figure 4-4, which provides a comparison between the parabolic and cubic profiles for the isothermal flow. Also shown in the figure is the exact similarity solution (Watson 1964). It is clear from Figure 4-4 that the cubic profile is more accurate as it almost coincides with the exact solution.

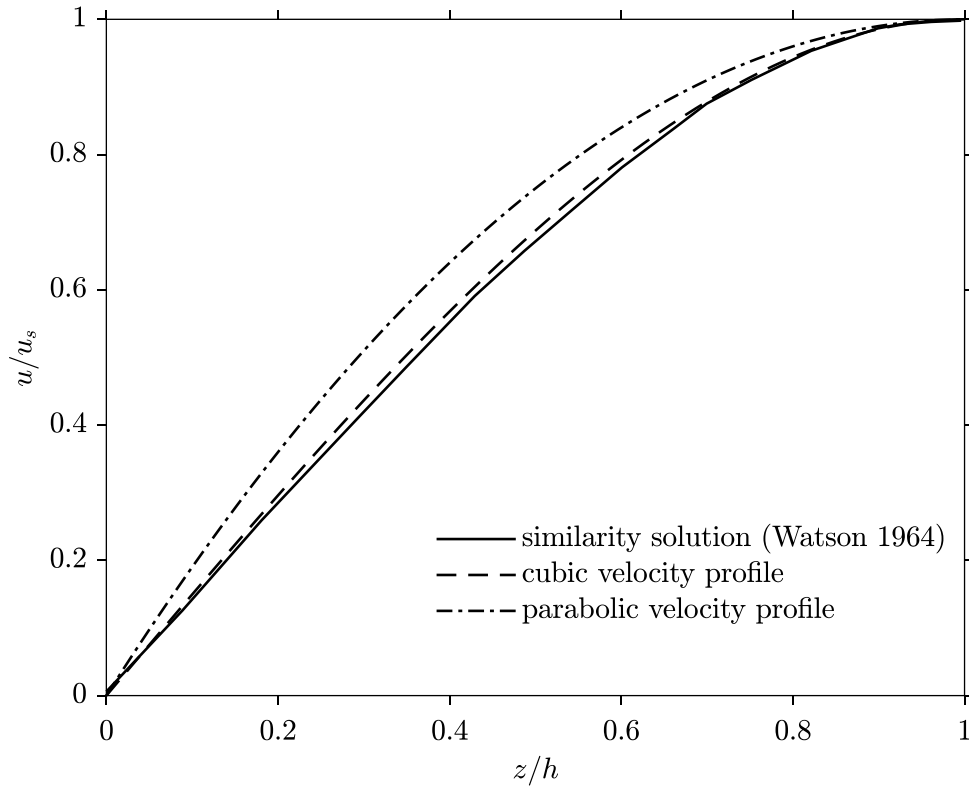


Figure 4-4: Comparison of Watson's similarity solution with the cubic and parabolic velocity profiles.

Substituting Equation (4.3.4) and Equation (4.3.9) into Equation (4.3.2) and Equation (4.3.8), and eliminating $u_s(r)$ using Equation (4.3.10), the pair of differential equations governing the film thickness and thermal boundary layer height in region (II) read ($r_0 < r < r_1$):

$$\frac{dh}{dr} = \frac{525}{136\text{Re}} r v_w - \frac{h}{r}, \quad (4.3.11)$$

$$\frac{d\delta_t}{dr} = -\frac{\delta_t(14h^2 - \delta_t^2)}{4(T_w - 1)(7h^2 - \delta_t^2)} \frac{dT_w}{dr} + \frac{175rh^4}{4\text{Pe}\delta_t^2(7h^2 - \delta_t^2)} + \frac{\delta_t}{h} \frac{dh}{dr}, \quad (4.3.12)$$

which are solved simultaneously subject to $h(r=r_0)=\delta(r_0)$ and $\delta_t(r=r_0)=\delta_{t0}$. The second transition location r_1 , which separates region (II) and (III) are obtained by equating $h(r_1)=\delta_t(r_1)$. The corresponding film thickness is defined as $h_1 \equiv \delta_t(r_1)$, which in turn, serves as the initial condition for region (III), where both the hydrodynamic and thermal boundary layer thickness have reached the free surface. In the isothermal case, the solution of Equation (4.3.11) reduces to $h(r_0 < r < r_J) = (1/4) \left(2/r + \sqrt{(210/13)r/Re} \right)$ and $r_0 = ((78/875)Re)^{1/3}$.

In region (III), the heights of the two boundary layers are the same and equal to that of the liquid film. Moreover, the free-surface temperature $T_s(r)$, serving as a new variable, begins to vary as it becomes a function of radial location for $r > r_1$. Consequently, the surface tension varies as well, yielding Marangoni induced flow. In this case, Equations (4.3.8)-(4.3.12) must be updated. Integrating Equation (4.2.1) and using (4.2.4d), we obtain ($r_1 < r < r_J$)

$$\frac{Re}{r} \frac{d}{dr} \left(r \int_0^{h(r)} u^2 dz \right) = Ca^{-1} \frac{d\gamma}{dT_s} T'_s(r) - v_w(r) \left. \frac{\partial u}{\partial z} \right|_{z=0}. \quad (4.3.13)$$

The corresponding velocity profile reads

$$u(r_1 < r < r_J, z) = \frac{1}{2} \left(3u_s - Ca^{-1} h \frac{d\gamma}{dT_s} \frac{T'_s}{v_s} \right) \frac{z}{h} - \frac{1}{2} \left(u_s - Ca^{-1} h \frac{d\gamma}{dT_s} \frac{T'_s}{v_s} \right) \frac{z^3}{h^3}. \quad (4.3.14)$$

The free-surface velocity is obtained from (4.2.8):

$$u_s(r_1 < r < r_J) = \frac{1}{5} \left(\frac{4}{hr} + Ca^{-1} h \frac{d\gamma}{dT_s} \frac{T'_s}{v_s} \right). \quad (4.3.15)$$

The temperature profile in this region is updated by replacing 1 by T_s and δ_t by h in (4.3.4), yielding

$$T(r_1 < r < r_J, z) = T_w - 3 \frac{T_w - T_s}{2} \frac{z}{h} + \frac{T_w - T_s}{2} \left(\frac{z}{h} \right)^3. \quad (4.3.16)$$

The corresponding integral equation of energy is obtained by integrating (4.2.1d) between $z = 0$ and $z = h(r)$, taking the following form

$$\frac{Pe}{r} \frac{d}{dr} \left(r \int_0^{h(r)} u(T-1) dz \right) = - \frac{\partial T}{\partial z} \Big|_{z=0}, \quad r_1 < r < r_J. \quad (4.3.17)$$

By substituting profiles (4.3.14) and (4.3.16) into (4.3.13) and (4.3.17), eliminating $u_s(r)$ using (4.3.15), we obtain the following equations for the range $r_1 < r < r_J$:

$$\begin{aligned} Re \frac{d}{dr} \left(\frac{272}{875} \frac{1}{hr} + \frac{16}{875} Ca^{-1} h \frac{d\gamma}{dT_s} \frac{T'_s}{v_s} + \frac{11}{2625} Ca^{-2} r h^3 \left(\frac{d\gamma}{dT_s} \right)^2 \frac{T_s'^2}{v_s^2} \right) \\ = Ca^{-1} r \frac{d\gamma}{dT_s} T'_s \left(1 + \frac{1}{5} \frac{v_w}{v_s} \right) - \frac{6}{5} \frac{v_w}{h^2}. \end{aligned} \quad (4.3.18)$$

$$Pe \frac{d}{dr} \left[\frac{39T_w + 136T_s}{350} + \frac{2}{175} Ca^{-1} r h^2 \frac{d\gamma}{dT_s} \frac{T'_s}{v_s} (T_s - T_w) \right] = \frac{3}{2} \frac{r}{h} (T_w - T_s). \quad (4.3.19)$$

Equations (4.3.18) and (4.3.19) govern the thickness $h(r)$ and the surface temperature $T_s(r)$, are solved subject to conditions $h(r = r_1) = h_1$, $T_s(r = r_1) = 1$ and $T'_s(r = r_1) = 0$. We observe that until now, all the resulting differential equations can be solved for any specific models for the viscosity and surface tension explicitly given as a function of the temperature, for any specified distribution of the temperature or heat flux along the wall. As it stands, the formulation above is readily implementable when $T_w(r)$ is specified. If, on the other hand, the wall heat flux $q_w(r) = -\partial T / \partial z|_{z=0}$ is imposed, then $T_w(r)$ is determined from the following relations between the wall temperature and heat flux, which are obtained from (4.3.4) and (4.3.16) as

$$T_w(0 < r < r_1) = \frac{2}{3} q_w(r) \delta_t(r) + 1, \quad (4.3.20a)$$

$$T_w(r_1 < r < r_J) = \frac{2}{3} q_w(r) h(r) + T_s(r). \quad (4.3.20b)$$

We shall examine separately the flow response when the temperature or heat flux are imposed along the disk in this section for super-critical flow, and in Section 4.4 for sub-critical flow. Finally, we observe that the number of parameters can be reduced by introducing the following rescaled variables as $\bar{r} = \text{Re}^{-1/3} r$, $\bar{q}_w = \text{Re}^{-1/3} q_w$ and $(\bar{h}, \bar{\delta}, \bar{\delta}_t) = \text{Re}^{1/3} (h, \delta, \delta_t)$, and parameters as $\bar{\text{Ca}} = \text{Ca} \text{Re}^{2/3}$ and $\bar{\text{Fr}} = \text{Re}^{1/6} \text{Fr}$. Other variables remain unchanged.

4.3.2 The influence of wall temperature

The formulation in Section 4.3.1 is readily applicable once $T_w(r)$ is specified. We shall only consider an imposed constant wall temperature, although the case of variable temperature is easily treated. The constant wall temperature condition usually corresponds to the cooling of boilers and condensers. The influence of the wall temperature on the boundary and thermal layers and liquid film thickness is displayed in Figure 4-5 for $\text{Ca} \text{Re}^{2/3} = 10$. Both boundary layers and the film height decrease with increased wall temperature as expected since the increase in the wall temperature leads to a decrease in the viscosity, which in turn reduces the wall resistance. The figure shows that the first transition location r_0 moves downstream with higher wall temperature, whereas the second transition location r_1 moves upstream towards the disk center. The mechanisms and causes for this behaviour will be discussed in detail when the influence of the wall heat flux is covered.

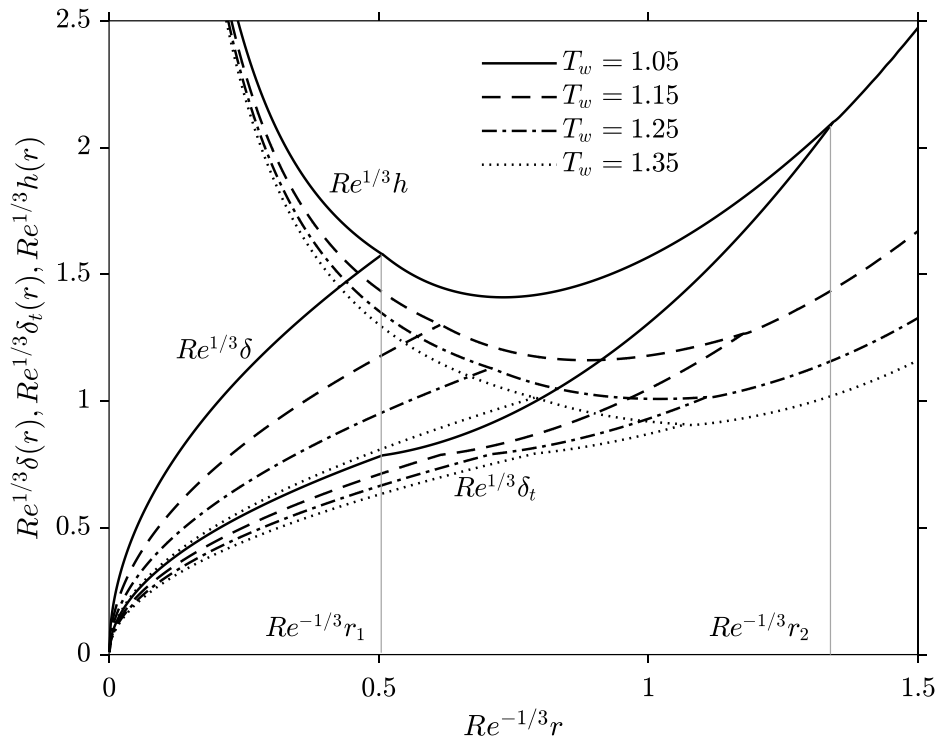


Figure 4-5: Influence of the wall temperature on the film thickness and boundary-layer heights for $\hat{T}_0 = 278\text{K}$ and $\text{Ca Re}^{2/3} = 10$ in the super-critical region. Also indicated are the values of (rescaled) transition locations in light vertical lines for $T_w = 1.05$.

Figure 4-6 depicts the influence of the wall temperature on the temperature and velocity along the film surface. For a given wall temperature, while the surface velocity decays with distance as the film thickens (resisting the flow), the surface temperature increases with distance as a result of sustained convective effect. In fact, Equations (4.3.15) and (4.3.16) suggest that $T_s \sim T_w + (1 - T_w)(r/r_1)^{-1/2\nu}$, indicating that $T_s \sim T_w$ at large distance as reflected in Figure 4-6; the liquid should indeed eventually acquire the same temperature as the solid surface far away. The figure also shows that the surface temperature is more sensitive to the change in the wall temperature than the surface velocity. When T_w increases, u_s increases as a result of lower viscosity and ease of fluid movement, and T_s increases as well as a result of the increased heating from the wall.

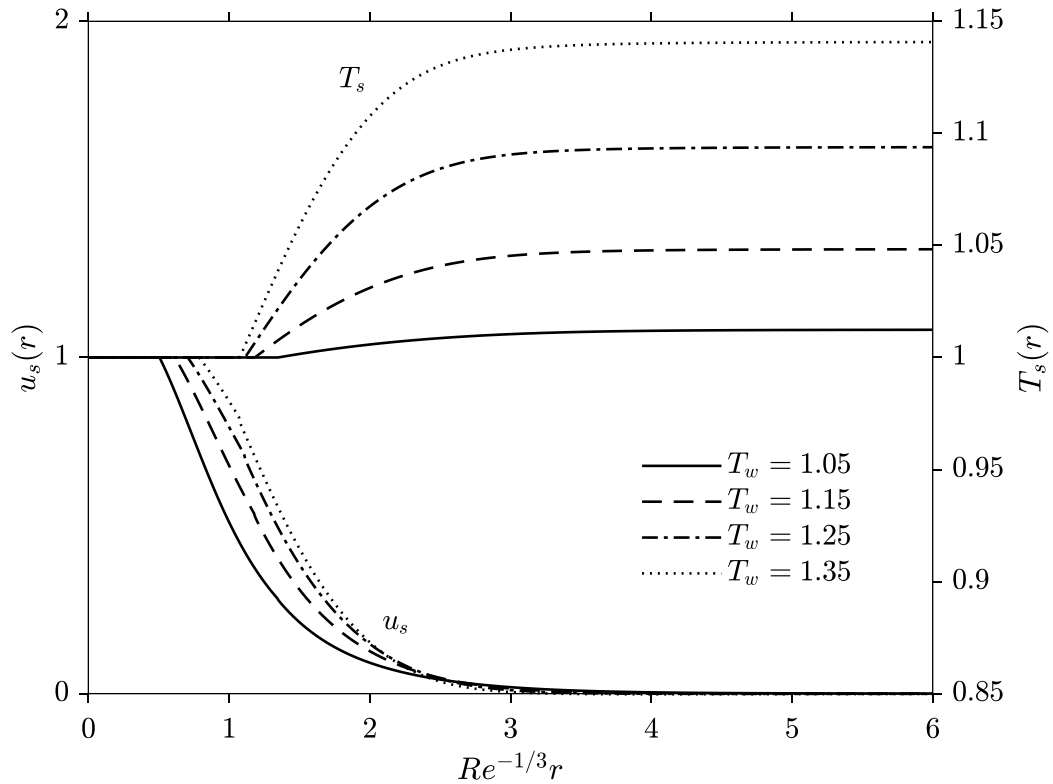


Figure 4-6: Influence of the wall temperature on the surface temperature and velocity in the super-critical region for $\hat{T}_0 = 278\text{K}$ and $\text{Ca Re}^{2/3} = 10$.

Figure 4-7 displays the influence of the wall temperature on the wall shear stress and the shear (Marangoni) stress along the free surface for $\text{Ca Re}^{2/3} = 10$. All shear stresses tend to decrease with distance as a result of weakening flow and rising temperature. At impingement, the wall shear stress is singular, decaying rapidly with distance like $1/\delta \sim \sqrt{\text{Re}/r}$. In regions (I) and (II) ($0 < r < r_1$), the wall shear stress decreases with the wall temperature, but this trend reverses downstream of the second transition location when Marangoni effect becomes palpable. At this point, the wall shear is typically one to two orders of magnitude larger than the Marangoni stress, but decays at a faster rate. We note that the shear stress is negative at the free surface (denoted by the negative sign in Figure 4-7) as the temperature decreases with radial distance. At the second transition location, the Marangoni stress rises rapidly from 0 to a non-zero value even though we

have imposed $T'_s(r=r_1)=0$, and the solution turns out to be not sensitive to this condition. Eventually, both stresses become of comparable magnitudes as they weaken, especially for the higher wall temperature.

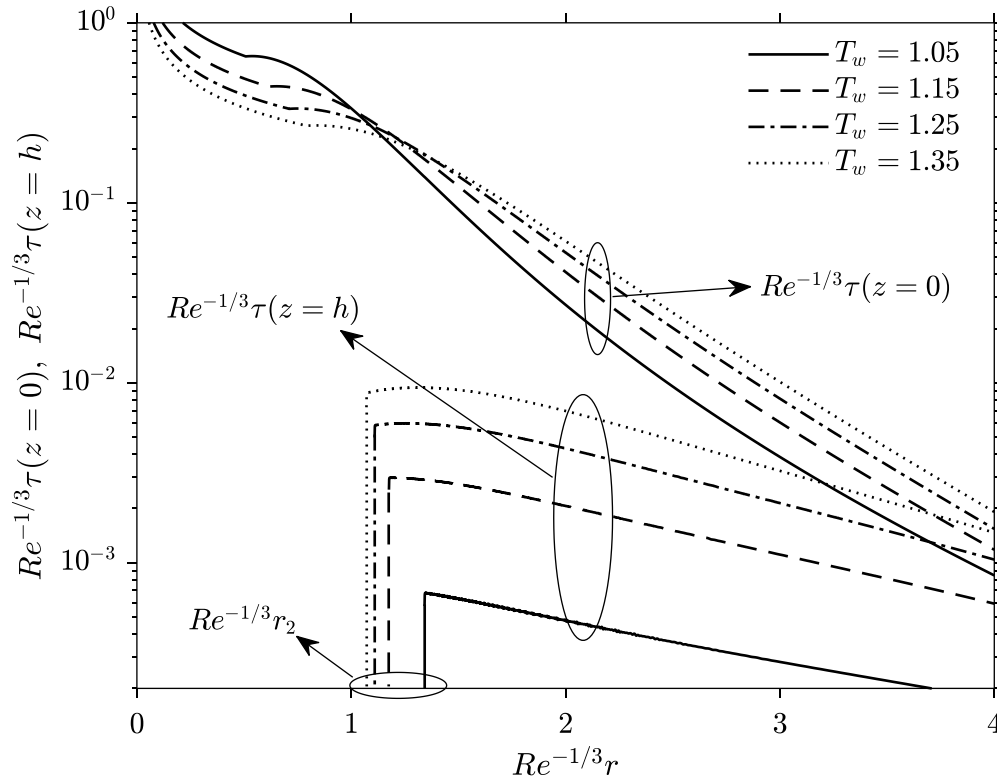


Figure 4-7: Influence of the wall temperature on the wall shear stress and Marangoni stress (surface shear stress) in the super-critical region for $\hat{T}_0 = 278$ K and $Ca Re^{2/3} = 10$. Vertical lines indicate second transition locations.

Chaudhury (1964) considered the heat transfer for a constant viscosity, for a jet and a disk held at different but constant temperatures. Watson's (1964) similarity profile was used for the velocity along with an integral approach and a similarity profile for the temperature in the thermal boundary layer. In particular, he examined the distribution of the averaged Nusselt number: $\langle Nu \rangle(r) = 2\pi \int_0^r q_w r / (T_w - 1) dr$ defined at a given radial location. To illustrate the effect of viscosity variation with temperature, we compare our predictions with those of Chaudhury in Figure 4-8 for two different Prandtl numbers (Pr

= 3 and 10) in the absence of Marangoni effect. While our results almost merge with the constant-viscosity prediction when the temperature of the wall is close to that of the incoming jet (corresponding to $T_w = 1.01$), the deviation grows significantly as the wall temperature departs from the jet temperature. This comparison suggests that the inclusion of the two-way coupling is crucial in the presence of large temperature change.

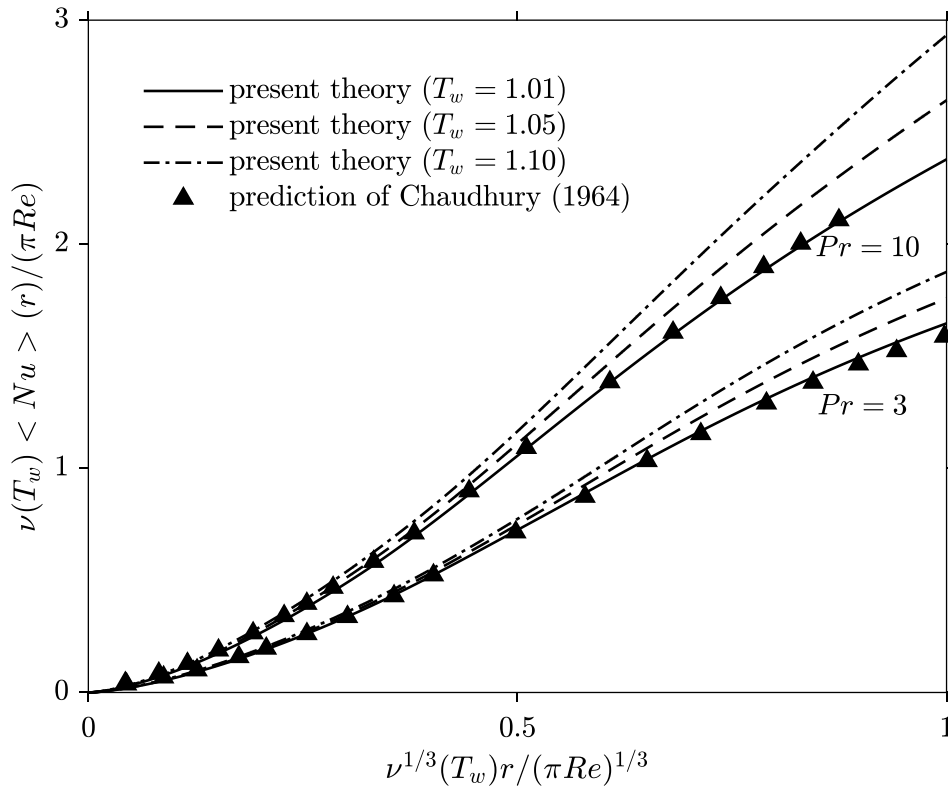


Figure 4-8: Influence of the wall temperature on the average Nusselt number (no surface tension effect). Also shown in the figure is the predictions of Chaudhury (1964) for water without surface tension effect. Here, $Pr=3$ corresponds to

$$\hat{T}_0 = 329.45 \text{ K and } Pr=10 \text{ corresponds to } \hat{T}_0 = 279.15 \text{ K} .$$

The influence of the wall temperature on the Nusselt number is illustrated in Figure 4-9 where a monotonic decay with radial distance is observed as a result of the flow deceleration and thermal accumulation. Following Chaudhury's approach, Searle *et al.* (2017) examined the heat transfer for a slipping flow of a fluid of constant viscosity and

the same properties as the incoming jet. Figure 4-9 shows the distribution of the Nusselt number for different wall temperatures, including the results of Searle *et al.* (2017) for the no-slip case, which we mimic here by taking $T_w = 1.01$. The deviation again worsens when the wall temperature is increasingly different from that of the impinging jet. Therefore, we conclude that the constant viscosity assumption is only reasonable when the temperature of the wall is close to that of the incoming jet.

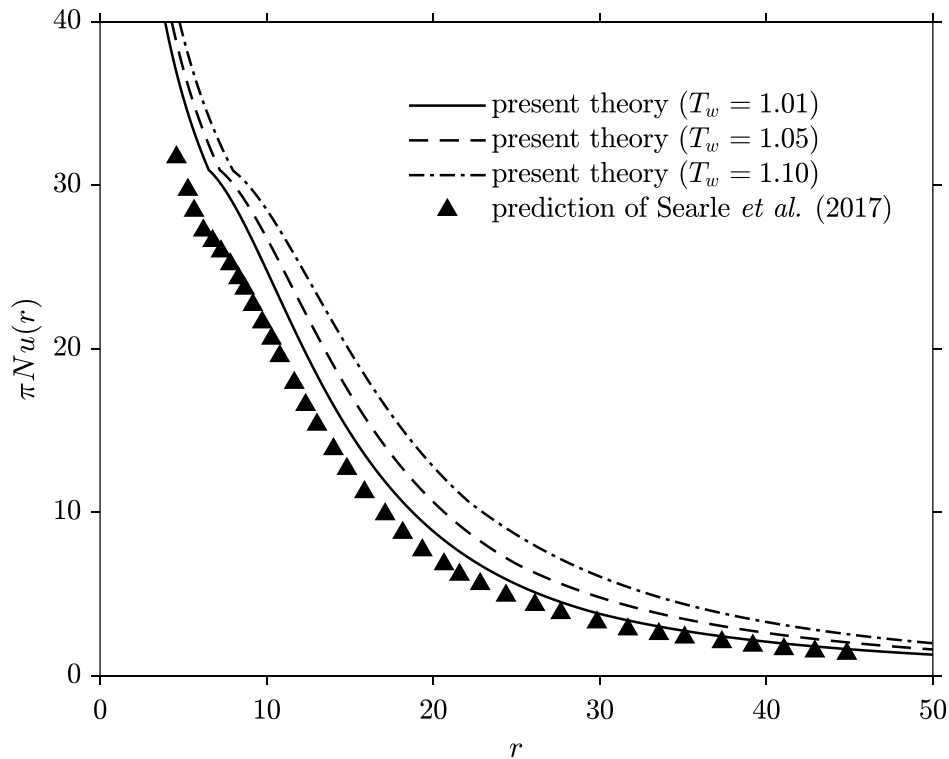


Figure 4-9: Influence of the wall temperature on the Nusselt number (no surface tension effect). The data for constant fluid property is from Searle *et al.* (2017). The Reynolds number is maintained at $Re = 4300$, $\hat{T}_0 = 278\text{ K}$.

4.3.3 The influence of constant wall heat flux on the flow

We now consider the influence of heat transfer on the super-critical flow field when the heat flux is imposed at the wall. The constant wall heat flux condition is usually encountered when a constant heat load is specified in practical applications. In this case, the wall temperature is directly deduced using (4.3.20). We shall examine the influence

of a constant wall heat flux for a water jet impinging at 300 K (see Table 1 for the viscosity and surface tension parameters).

For a constant wall heat flux, the hydrodynamic and thermal boundary layers, as well as the film thickness, all simultaneously decrease with increased wall heat flux, as reported in Figure 4-10. The response appears to be less sensitive to the variation of the heat flux compared to the influence of the wall temperature, especially near impingement. This congestion near the origin is expected since some accumulation distance is needed for the wall heat flux to cause a significant change in the wall temperature and hence the viscosity.

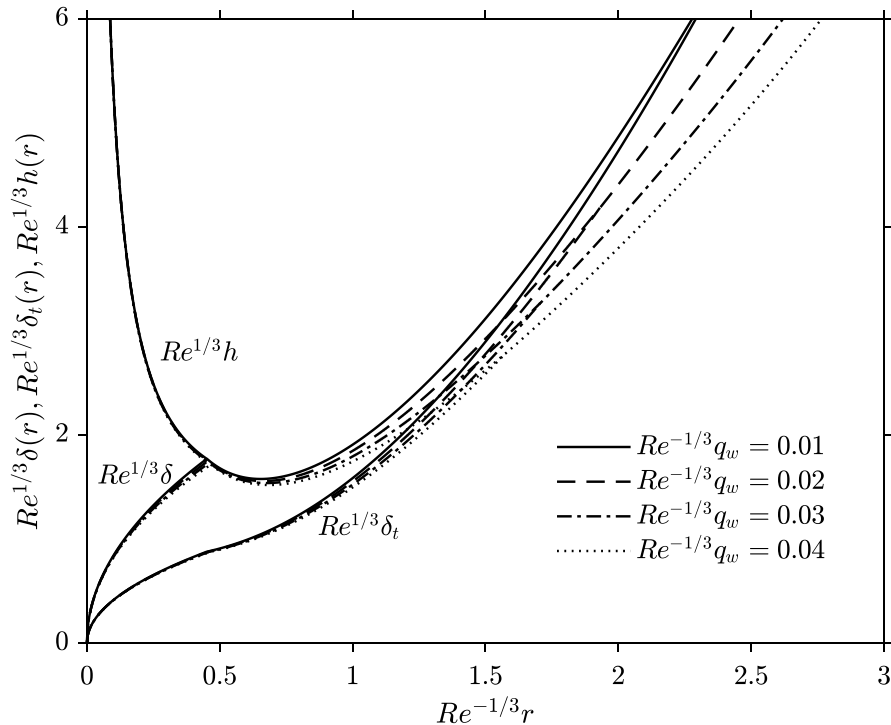


Figure 4-10: Influence of the wall heat flux on the boundary-layer heights and the film thickness for $\hat{T}_0 = 300\text{ K}$ and $Ca Re^{2/3} = 10$.

Figure 4-10 indicates that the thermal boundary layer appears to always reach the free surface as long as the disk is sufficiently large. This seems to contradict the finding of Liu & Lienhard (1989) that the thermal boundary layer cannot reach the free surface for a

Prandtl number greater than 4.859. However, this critical Prandtl number is based on the assumption of a constant viscosity. We report in Figure 4-11 the influence of the wall heat flux on the distribution of the *effective* Prandtl number $\nu[T_w(r)]Pr$ at the wall and along the free surface $\nu[T_s(r)]Pr$. As the liquid travels downstream, the Prandtl number should continue to decrease due to the increase in the wall temperature, and hence decrease in viscosity and surface tension, and the thermal boundary layer will eventually reach the free surface (unless a hydraulic jump forms upstream of the transition location or the disk is not sufficiently large). Consequently, the critical Prandtl number criterion is only applicable when the heat flux is weak, with insignificant temperature variation. In fact, Figure 4-11 indicates that the Prandtl number at the wall can be less than 4.859.

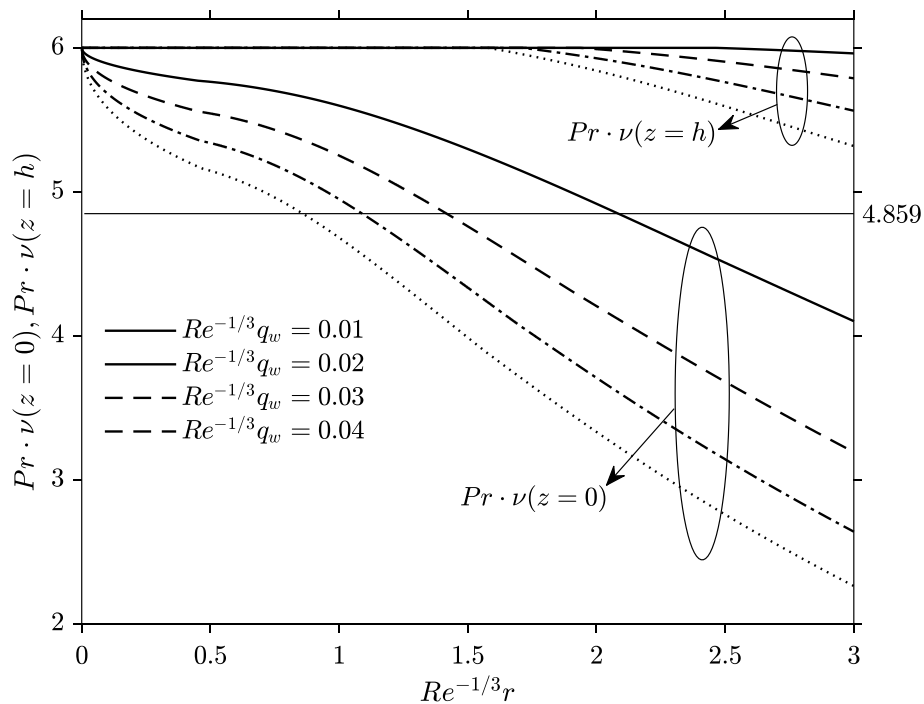


Figure 4-11: Influence of the wall-heat flux on the effective Prandtl number along the wall and the free surface for super-critical flow for $\hat{T}_0 = 300\text{ K}$ and

$$Ca Re^{2/3} = 10.$$

Interestingly, while both transition locations move downstream with increasing inertia (not obvious from Figures 4-5 and 4-10 because of the rescaling with respect to $Re^{1/3}$), they move in opposite directions with increasing wall temperature and heat flux. Figure 4-12 summarises the influence of the wall heat flux and inertia on the transition locations. The first transition location moves downstream with higher wall heat flux (or wall temperature in Figure 4-5), whereas the second transition location moves upstream towards the disk center. This is largely due to the dependence of the viscosity on the temperature. For common fluids, the viscosity can significantly decrease with temperature, while the thermal properties (thermal conductivity and heat capacity) remain relatively constant. This behaviour in turn causes an earlier second transition as the thermal boundary layer remains almost unchanged but the hydrodynamic boundary layer and the film thickness are moderately decreased. In other words, the free surface meets with the thermal boundary layer earlier.

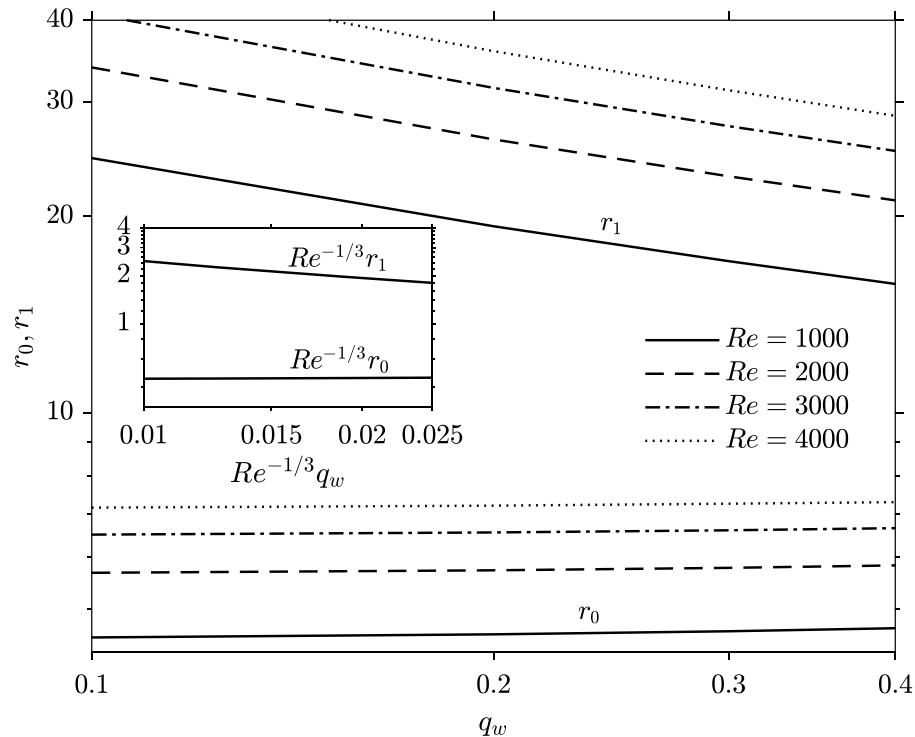


Figure 4-12: Influence of inertia and the wall heat flux on the transition locations for $\hat{T}_0 = 300\text{ K}$. Inset shows the rescaled transition locations.

In fact, the inset in Figure 4-12 suggests that the location of the first transition is essentially constant, with $r_0 \approx 0.454 \text{Re}^{1/3}$. It is not surprising that the increase of r_0 is very weak due to the curve congestion as discussed in Figure 4-10. The location of the second transition follows closely $r_1 \approx 0.524 \text{Re}^{4/9} q_w^{-1/3}$.

In any practical application with a constant heat load, it is the temperature at the solid surface T_w that needs to be controlled and monitored, making crucial the investigation of the influence of heat flux on the local wall temperature and Nusselt number $\text{Nu}(r) = q_w(r) / (T_w(r) - 1)$. Figure 4-13 depicts the influence of the Reynolds number on the Nusselt number distribution. Also shown in the figure are the corresponding experimental measurements from Liu & Lienhard (1989) and their numerical predictions using an iterative scheme. Here the liquid is water, and the temperature of the incoming jet is $\hat{T}_0 = 288.15\text{K}$. The value of the applied (dimensionless) heat flux is 0.09. The second transition location is not reached under these Reynolds numbers. Our predictions generally agree with their measurements and iterative solution. We emphasize that although the present method may not be as accurate as an iterative numerical approach, the high computational efficiency and the simplicity of implementation of the present approach far outweigh the relatively small inaccuracy, especially in the presence of a large temperature variation.

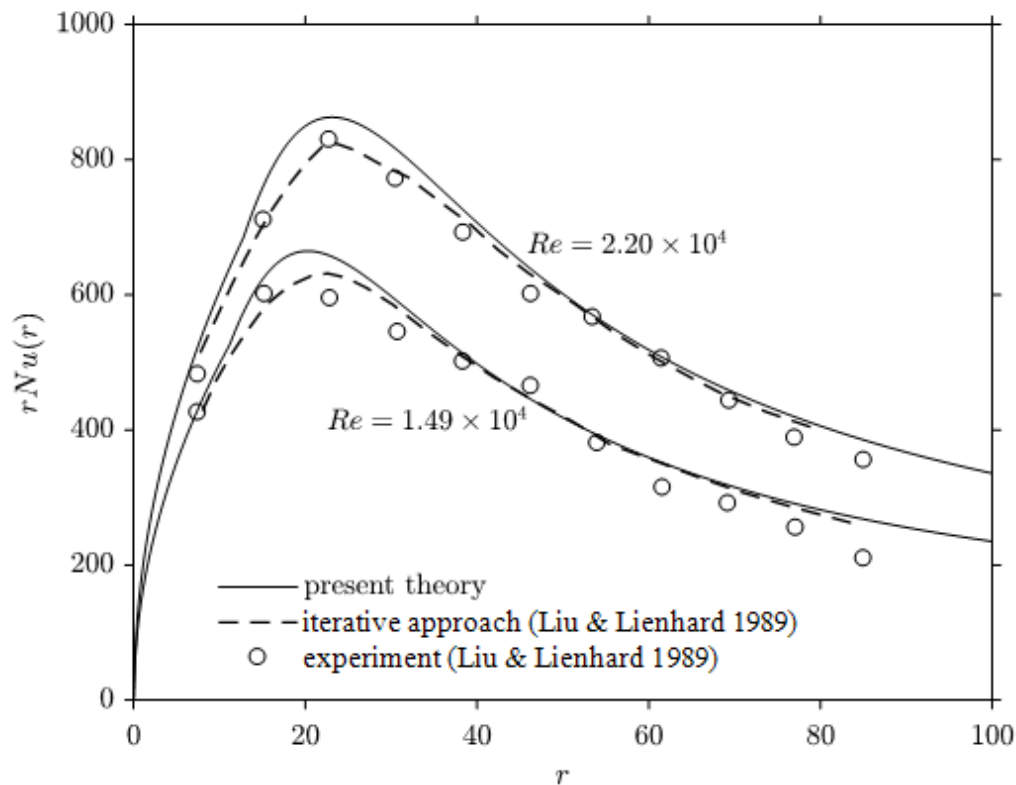


Figure 4-13: Influence of the Reynolds number on the local Nusselt number distribution). The comparison with the measurements and numerical results of Liu & Lienhard (1989) is also included.

4.4 The influence of heat transfer on the hydraulic jump and subcritical flow

In this section, we consider the flow in region (IV), the hydraulic-jump region. Although the flow field downstream of the jump may be assumed to be inviscid (Watson 1964) or viscous, only the viscous flow will be examined as it seems to represent better the real flow (Duchesne *et al.* 2014). In the absence of thermal coupling, the hydraulic jump can be examined using solely the discretized momentum equation with Watson's method. In other words, the thermal field in the subcritical region can be obtained after the hydraulic jump and downstream flow field are fully determined. For a temperature-dependent viscosity, however, solving the momentum equation is not sufficient to yield the location of the jump. In this case, we resort to an energy balance across the jump as an additional

relation to close the problem as we shall see. The determination of the subcritical velocity and temperature profiles is discussed in Section 4.4.1. The location and height of the hydraulic jump will be discussed separately for the constant wall temperature and wall heat flux conditions in Section 4.4.2 and 4.4.3, respectively.

4.4.1 The subcritical velocity and temperature profiles

When the effect of gravity is included, the integral form of Equation (4.2.1b) at any location can be written as

$$\frac{d}{dr} r \int_0^h u^2 dz = -\frac{r}{Fr^2} \int_0^h \frac{\partial p}{\partial r} dz - \frac{r}{Re} v_w(r) \left. \frac{\partial u}{\partial z} \right|_{z=0}. \quad (4.4.1)$$

We recall $r = r_J$ as being the position of the hydraulic jump. Across the jump, Equation (4.4.1) is applied to a control volume of width Δr in the radial direction, yielding

$$\int_0^{h_J^+} u_J^{+2} dz - \int_0^{h_J^-} u_J^{-2} dz = -\frac{1}{Fr^2} \left(\int_0^{h_J^+} p_J^+ dz - \int_0^{h_J^-} p_J^- dz \right) - \Delta r \left. \frac{v_w(r)}{Re} \frac{\partial u_J^-}{\partial z} \right|_{z=0}. \quad (4.4.2)$$

From here on, a ‘-’ and a ‘+’ superscript denotes a value immediately upstream and downstream of the jump, respectively. Integrating Equation (4.2.1c) subject to condition (4.2.4c), the pressure becomes $p(r, z) = h(r) - z$, reflecting its hydrostatic nature. Since the width of the jump Δr is assumed to be small, the viscous term in Equation (4.4.2) becomes negligible. In addition, the effect of surface tension resulting in a Hoop stress can be included following Bush & Aristoff (2003) so that Equation (4.4.2) reduces to

$$\frac{1}{2} (h_J^{+2} - h_J^{-2}) + \frac{Fr^2}{Ca Re} \frac{h_J^+ - h_J^-}{r_J} \gamma(T_J) = Fr^2 \left(\int_0^{h_J^-} u_J^{-2}(z) dz - \int_0^{h_J^+} u_J^{+2}(z) dz \right). \quad (4.4.3)$$

Here $T_J = (T_s^- + T_s^+)/2$ is taken to be the average free-surface temperature of the values immediately up- and downstream of the jump. We observe that the effect of heat transfer

is reflected implicitly in (4.4.3) in the height and velocity upstream and downstream of the jump since the heat transfer has a tangible effect on the flow velocity as well as the film thickness as we saw earlier. Here h_J^- and u_J^- (as functions of r_j) are directly obtained from the solution in the pre-jump region while the solution for h_J^+ and u_J^+ will be discussed next as they are both related to the thermal character downstream of the jump. For this, another relation is needed to obtain the temperature field after the jump, which naturally leads us to the consideration of the energy balance across the jump.

Integrating Equation (4.2.1d) between the disk and the free surface leads to

$$\frac{d}{dr} r \int_0^{h(r)} u T dz = - \frac{r}{Pe} \left. \frac{\partial T}{\partial z} \right|_{z=0}. \quad (4.4.4)$$

If a thermal balance is applied to a control volume of an infinitely small width Δr across the jump, we obtain

$$\int_0^{h_J^-} u_J^-(z) T_J^-(z) dz = \int_0^{h_J^+} u_J^+(z) T_J^+(z) dz. \quad (4.4.5)$$

It is clear by now that the super-critical flow and thermal fields are completely known at any given r , whereas the sub-critical flow and thermal structures are yet to be determined. Some assumptions are typically made regarding the nature of the flow downstream of the jump, ranging from the inviscid (Watson 1964) to the fully viscous (Duchesne *et al.* 2014) character. Although the current formulation accommodates various assumptions on the flow and heat transfer, we shall focus on a relatively slow flow of the lubrication type downstream of the jump, with gravity becoming significant. In this case, the solution of the Stokes equation is sufficiently manageable to accommodate a velocity profile that is explicitly dependent on the viscosity. We observe that the influence of the viscosity on the vertical velocity distribution should be fully accounted while before the jump the influence of the viscosity on the velocity profile is not as crucial given the dominance of inertia since the shearing is mostly concentrated near the wall. On the other hand, for the

sub-critical flow, inertia effect is small, and the influence of viscosity is consequently significant. As to temperature, the same cubic profile is still reasonable to use since thermal convection remains in balance with conduction. Again, the formulation for the flow and heat transfer is valid for any temperature-dependent viscosity and surface tension.

Consequently, the velocity will not be parabolic in z as is isothermal lubrication flow. In this case, neglecting the inertia terms in Equation (4.2.1b) and integrating twice the remaining terms $-\left(\text{Re}/\text{Fr}^2\right)h' + \partial/\partial z(v\partial u/\partial z) = 0$ subject to conditions (4.2.2a) and (4.2.4d), the velocity becomes

$$u(r > r_J, z) = \frac{\text{Re}}{\text{Fr}^2} h' \int_0^z \frac{y dy}{v[T(y)]} + \left(\text{Ca}^{-1} \frac{d\gamma}{dT_s} T'_s - \frac{\text{Re}}{\text{Fr}^2} h h' \right) \int_0^z \frac{dy}{v[T(y)]}. \quad (4.4.6)$$

As to the sub-critical temperature and heat flux at the wall, we adopt the same cubic profile (4.3.16), which is reproduced here as

$$T(r > r_J, z) = T_w - 3 \frac{T_w - T_s}{2} \frac{z}{h} + \frac{T_w - T_s}{2} \left(\frac{z}{h} \right)^3. \quad (4.4.7)$$

Inserting (4.4.6) into the mass conservation Equation (4.2.8), we obtain the following equation:

$$\frac{\text{Re}}{\text{Fr}^2} h' \int_0^h \int_0^z \frac{y dy dz}{v[T(y)]} + \left(\text{Ca}^{-1} \frac{d\gamma}{dT_s} T'_s - \frac{\text{Re}}{\text{Fr}^2} h h' \right) \int_0^h \int_0^z \frac{dy dz}{v[T(y)]} = \frac{1}{2r}. \quad (4.4.8)$$

Similarly, on inserting (4.4.6) and (4.4.7) into the energy Equation (4.4.4), we obtain

$$\begin{aligned} \frac{d}{dr} r \int_0^h \left[\frac{\text{Re}}{\text{Fr}^2} h' \int_0^z \frac{y dy}{v[T(y)]} + \left(\text{Ca}^{-1} \frac{d\gamma}{dT_s} T'_s - \frac{\text{Re}}{\text{Fr}^2} h h' \right) \int_0^z \frac{dy}{v[T(y)]} \right] \\ \times \left[T_w - 3 \frac{T_w - T_s}{2} \frac{z}{h} + \frac{T_w - T_s}{2} \left(\frac{z}{h} \right)^3 \right] dz = \frac{3}{2\text{Pe}} \frac{r}{h} (T_w - T_s). \end{aligned} \quad (4.4.9)$$

Once $T(y)$ is inserted from (4.4.7) into the temperature-dependent viscosity model, Equations (4.4.8) and (4.4.9) are used to determine $h(r)$ and $T_s(r)$. They are integrated subject to $h(r=r_\infty)=h_\infty$, the thickness at the edge of the disk. Another boundary condition, namely $T_s(r=r_j^+)$ is provided through relation (4.4.5), where use is made of the super- and sub-critical velocity and temperature profiles (4.3.14) and (4.3.16), and (4.4.6) and (4.4.7), respectively. The location of the jump (radius) is determined through (4.4.3), where use is made of (4.3.14) and (4.4.6).

The value of the edge thickness h_∞ was considered in Chapter 2 for the flow on stationary and rotating disks. We suggested that, as the flow has sufficiently decelerated, the film thickness at the edge of the disk should be essentially a value close to the film thickness the liquid exhibits under static conditions. De Gennes *et al.* (2004) proposed an expression for this static thickness as $h_s = 2\sqrt{\hat{\gamma}/\rho g} \sin(\theta_Y/2)$ using a force balance approach. Lubarda & Talke (2011) later obtained the same expression based on the minimum free energy principle. Here θ_Y is the contact angle, which depends on both the liquid and the solid, and may then be deduced from experiment. Apart from the static contribution, a weak dynamic contribution is also derived using a mechanical energy minimization theory. The dimensionless edge thickness is finally given by

$$h_\infty(T) = 2 \frac{Fr}{\sqrt{Ca Re}} \sqrt{\gamma(T)} \sin\left(\frac{\theta_Y}{2}\right) + \left(\frac{3}{40}\right)^{\frac{1}{3}} \left(\frac{Fr}{r_\infty}\right)^{\frac{2}{3}}. \quad (4.4.10)$$

Clearly, in the presence of relatively strong surface tension and a large disk radius, the second term tends to be dominated by the static contribution. For more details, the reader is referred to Chapter 2. Our predictions essentially confirmed the findings of Duchesne *et al.* (2014). Their direct measurements of the edge thickness give a nearly constant value on the order of the capillary length $\sqrt{\hat{\gamma}/\rho g}$ with a small power-law variation. h_∞ can be neglected for a liquid of high viscosity (Duchesne *et al.* 2014). The dynamic variation is not considered in the present calculation since it is suggested to be negligibly

small by many experiments (Dressaire *et al.* 2010, Duchesne *et al.* 2014, Mohajer & Li 2015).

For our purpose here, we shall report on further results below for water. The thickness at the edge of the disk using a generic hydrophilic situation with $\theta_Y = 35$ degree.

Finally, although the numerical implementation does not pose any major challenge, the downstream formulation becomes significantly more manageable if we adopt the inverse linear model for the kinematic viscosity dependence on the temperature, namely the following two parameter model: $\hat{\nu} = \hat{M}(\hat{T} - \hat{L})^{-1}$. For water, as in the current study, $\hat{M} = (1/29830)\text{m}^2\text{K}/\text{s}$ and $\hat{L} = 258.6\text{K}$. Although slightly less accurate than the VFT model, especially in the low temperature range, this model is commonly used in the literature (see, for instance, the studies of Ling & Dybbs 1992 and Kafoussias & Williams 1993 on forced convection, and the more recent treatment of Miller *et al.* 2018 on the boundary-layer flow over a heated plate). Here, \hat{M} is a constant, positive for liquids. In dimensionless form, we write the kinematic viscosity as

$$\nu(T) = [1 + L(T - 1)]^{-1}, \quad (4.4.11)$$

where $L = 1 / (1 - \hat{L} / \hat{T}_0)$ is the only dimensionless parameter. In this case, the velocity profile (4.4.6) reduces to a fifth-order polynomial:

$$\begin{aligned} u(r > r_J, z) = & \frac{\text{Re}}{\text{Fr}^2} h' \left[\frac{L(T_w - T_s)}{2h} \left(\frac{z^5}{5h^2} - \frac{z^4}{4h} + z^3 \right) + \frac{5LT_w - 3LT_s - 2L + 2}{4} z^2 \right] \\ & + \left[\frac{LT_s + 1 - L}{\text{Ca}} \frac{dy}{dT_s} T'_s - \frac{\text{Re}}{\text{Fr}^2} h' (LT_w - L + 1) h \right] z. \end{aligned} \quad (4.4.12)$$

Similarly, the double integrals in (4.4.8) and (4.4.9) can be carried out explicitly. In this case, (4.4.8) reduces to

$$\frac{\text{Re}}{\text{Fr}^2} \text{rh}^3 (7\text{LT}_s + 13\text{LT}_w - 20\text{L} + 20) \text{h}' - 30\text{Ca}^{-1} \text{rh}^2 (\text{LT}_s + 1 - \text{L}) \frac{\text{d}\gamma}{\text{d}\text{T}_s} \text{T}'_s = 30. \quad (4.4.13)$$

The second equation governing h and T_s is similarly deduced from (4.4.9):

$$\frac{\text{d}}{\text{d}r} \left(\frac{19535 \left(\text{LT}_s^2 + \frac{\text{T}_s (7138\text{LT}_w - 10248\text{L} + 10248) + \text{T}_w (2395\text{LT}_w - 3192\text{L} + 3192)}{3907} \right)}{-\text{Ca}^{-1} \text{h}^2 (719\text{LT}_s - 3239\text{LT}_w + 2520\text{L} - 2520) (\text{LT}_s + 1 - \text{L}) (\text{T}_s - \text{T}_w) r \frac{\text{d}\gamma}{\text{d}\text{T}_s} \text{T}'_s} \right) = \frac{10080}{\text{Pe}} \frac{r}{h} (\text{T}_w - \text{T}_s). \quad (4.4.14)$$

Model (4.4.11) is used to determine the sub-critical flow and thermal fields below for the case of a water jet. The flow and thermal fields are obtained iteratively using a shooting method. An initial value for r_j is guessed, and h_j^+ and T_s^+ are obtained from (4.4.3) and (3.4.5). Equations (4.4.13) and (4.4.14) are then solved simultaneously subject to $h(r=r_j) = h_j^+$, $\text{T}_s(r=r_j) = \text{T}_s^+$ and $\text{T}'_s(r=r_j) = 0$, aiming to match the boundary condition at the edge of the disk, namely $h(r=r_\infty) = h_\infty$.

4.4.2 The influence of the wall temperature on the hydraulic jump

Figure 4-14 illustrates the influence of the wall temperature on the film profiles in the super- and sub-critical regions. As observed from the figure, the jump height decreases with increased wall temperature, and the jump location is pushed downstream away from the centre of the disk at an almost constant rate. It is worth observing that the development of the shape of the jump under the influence of wall temperature is very similar to that under the effect of disk rotation (see Chapter 2); in both cases, the response is the result of enhanced convective effect. In fact, this similarity is not unexpected since a larger wall temperature lowers the wall resistance, reducing the loss of inertia. The

corresponding wall heat flux (not shown) experiences a drop that is relatively much sharper than the jump experienced by the surface height. This drop in the wall heat flux in turn leads to a drop in the Nusselt number as we shall see shortly. We recall that the effect of surface tension reflects both the Marangoni and hoop stresses. In an effort to isolate the Marangoni effect, we neglected the effect of surface tension except through the Hoop stress in (4.4.3), and the resulting plots are reported in included in Figure 4-14 as dashed curves. The Marangoni effect is therefore reflected in the difference between the solid and dashed curves.

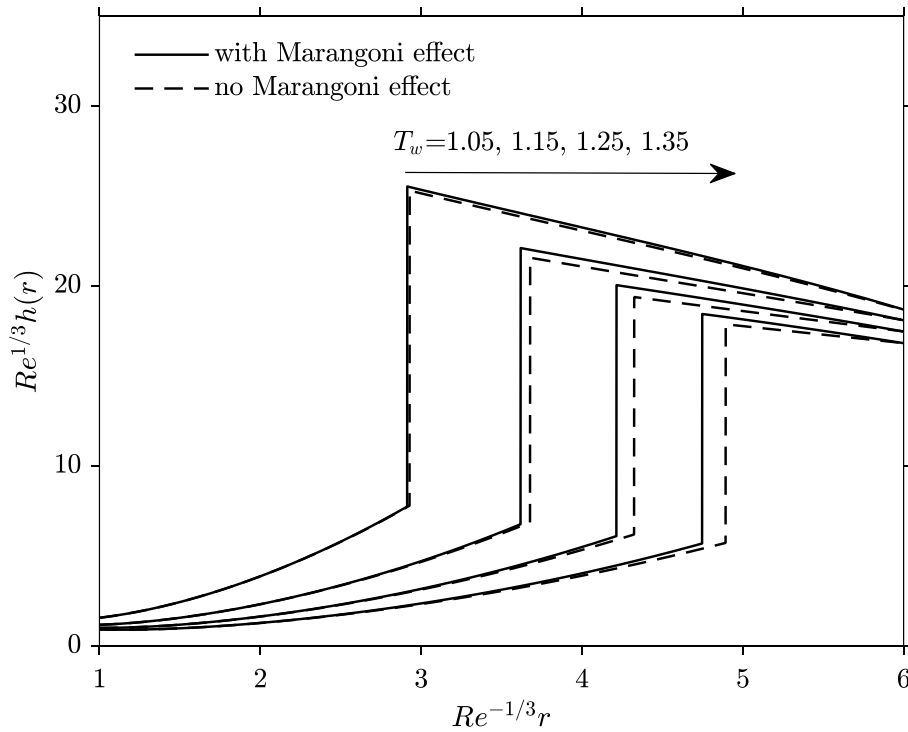


Figure 4-14: Influence of the wall temperature on the film height in the super- and sub-critical regions for $\hat{T}_0 = 300\text{ K}$. Here $\text{Ca Re}^{2/3} = 100$, $\text{Fr Re}^{-1/2} = 3$ and $r_\infty \text{Re}^{-1/3} = 6$.

As expected, Figure 4-14 suggests that the Marangoni effect tends to increase with the wall temperature, enhancing the jump height at an earlier location. This is also depicted in Figure 4-15, where the jump location and height are plotted against the wall

temperature for three levels of surface tension. The wall temperature causes the jump radius to increase and the jump height to decrease almost linearly (see also Figure 4-14). There is a significant influence of the surface tension in the lower Ca range. The jump location and height are less sensitive for large Ca where a saturation appears for liquids of very weak surface tension. It is not surprising to see that the Marangoni effect (and surface tension, in general) tends to reduce the jump radius since it acts as a resistance to the flow. Simultaneously, this effect decreases with the radial distance as the surface temperature levels off.

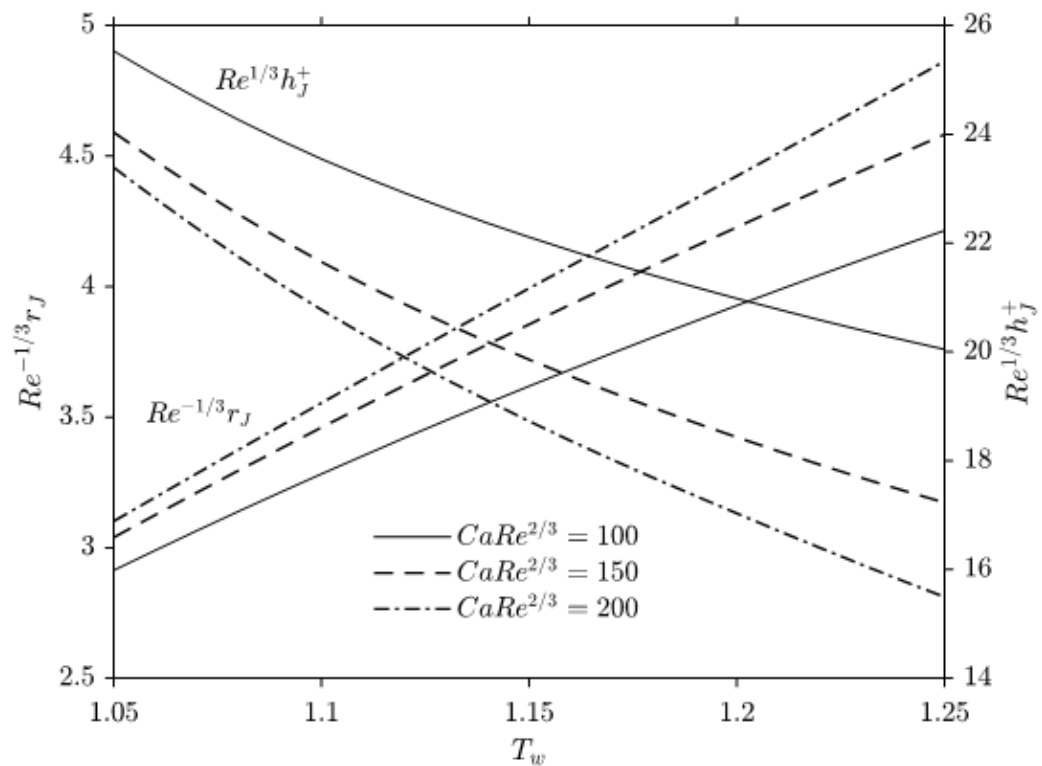


Figure 4-15: Influence of the wall temperature on the jump location and height for

$$\hat{T}_0 = 278 \text{ K}, \text{ Fr Re}^{-1/2} = 3 \text{ and } r_\infty \text{ Re}^{-1/3} = 6.$$

Sung *et al.* (1999) investigated numerically the heat transfer of a circular hydraulic jump using the finite-element method. We report a comparison in Figure 4-16 between our predictions for the hydraulic jump under the influence of the wall temperature against the numerical results of Sung *et al.* (1999). Our predictions generally agree with their results

on the location of the jump as well as the film thickness upstream and far downstream. The shape and height of the jump are different since we have assumed a shock-type transition whereas their numerical solution was obviously resolved continuously. Moreover, their nozzle to disk distance is very small, making the initial jet velocity not uniform and the inviscid flow assumption above the boundary layer not exactly satisfied. Therefore, the agreement is reasonably acceptable considering all the approximations we have made.

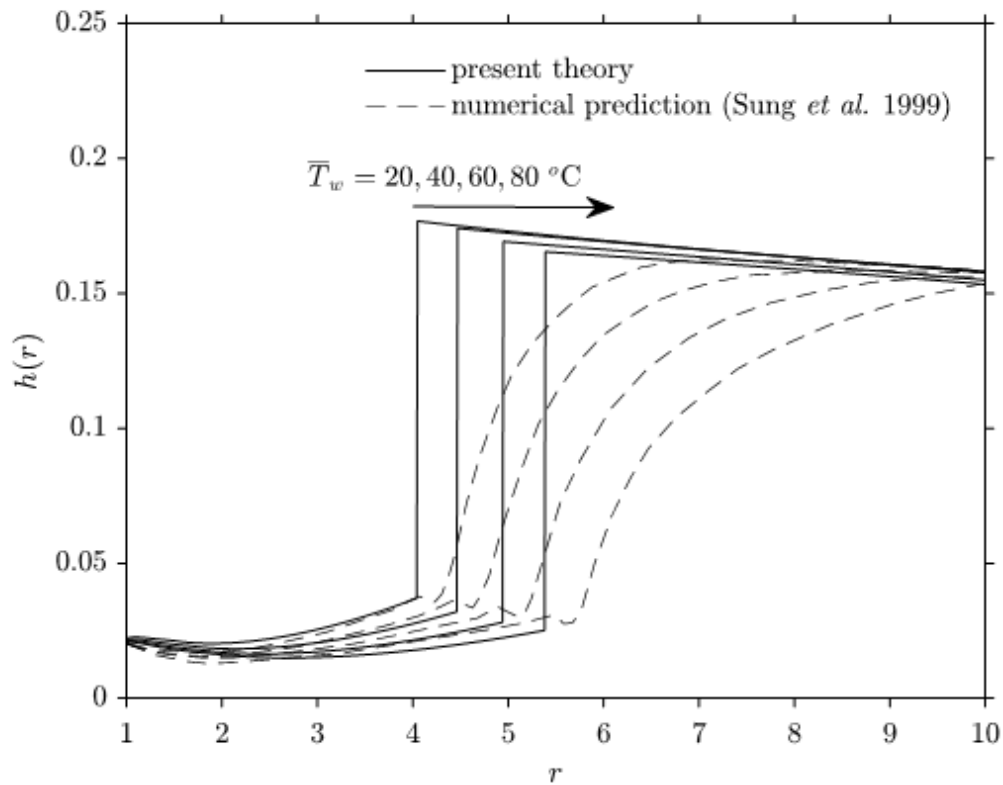


Figure 4-16: . Comparison of the film thickness over the entire domain with the predictions of Sung *et al.* (1999) for different wall temperatures

$$\left(\hat{T}_0 = 293\text{K}, \text{Re} = 16000, \text{Pe} = 112000, \text{Fr} = 5, \text{Ca} = 0.022 \right).$$

Figure 4-16 indicates that the numerical profiles of Sung *et al.* (1999) shows a small dip in the film surface at the bottom of the jump, which is not captured by our thin-film approach. Although the discrepancy is insignificant, the presence of these mild

depressions becomes more consequential when the heat transfer is examined. Indeed, Sung *et al.* (1999) also examined the influence of the flow rate on the distribution of the Nusselt number for a fluid of constant viscosity. They reported a sharp drop of the Nusselt number in the hydraulic jump region, which we also capture in our solution, as reported in Figure 4-17. We note here that h_i is the initial film thickness in their flow domain. As can be seen, both the sharp-drop and downstream values of the Nusselt number are recovered overall. Our solution does not recover the undershoot predicted by Sung *et al.* (1999), resulting from the formation of a flow separation, which in turn impedes the convective heat transfer. We emphasize that numerical approaches to some extent do give us better local predictions of the hydrodynamic and heat transfer character of the flow even though they can be time consuming. Our model is computationally efficient but may sacrifice some accuracies as already seen. This is usually the limitations of theoretical models.

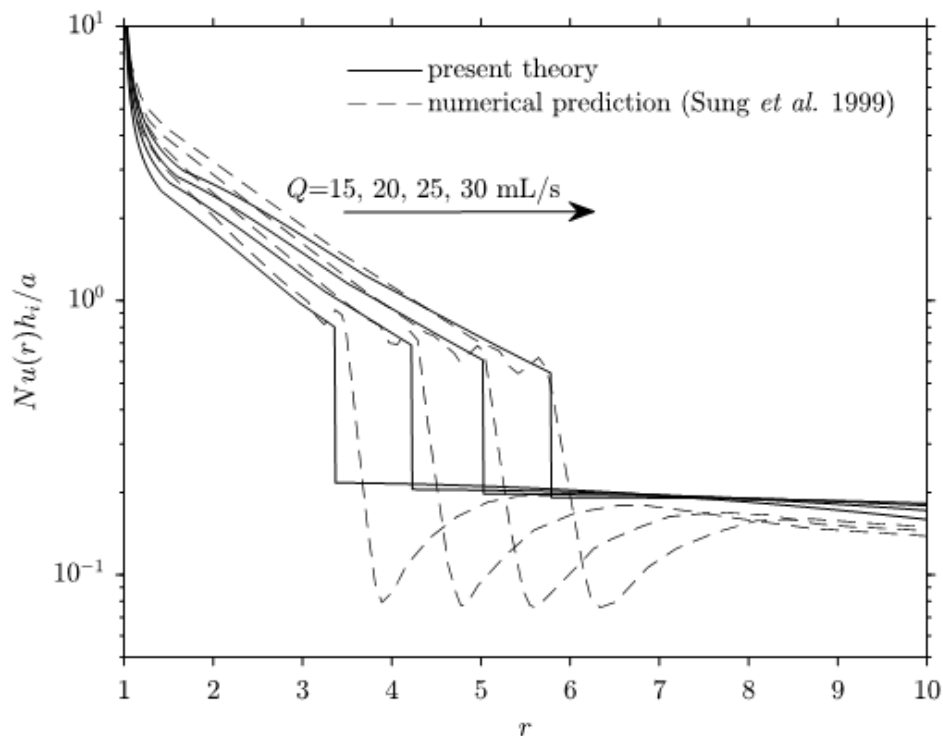


Figure 4-17: Influence of the jet flow rate on the profiles of the Nusselt number. Comparison between our results and the predictions of Sung *et al.* (1999).

It is important to observe that Sung *et al.* (1999) did not provide the value of the wall temperature when generating their results reproduced here in Figure 4-17. It turns out that the Nusselt number is not influenced by the wall temperature for a fluid of constant viscosity. This important property is discussed here by means of the following statement:

The Nusselt number for the super- and sub-critical regions is independent of the (constant) wall temperature for a fluid of constant properties.

We prove this statement by first considering the flow of a fluid of constant viscosity. In this case, $\nu(T) = \gamma(T) = 1$, and the flow is decoupled from the heat transfer so that both $\delta(r)$ and $h(r)$ are everywhere independent of the wall temperature. We need to show in this case that $Nu(r) = q_w(r)/(T_w - 1)$ is independent of T_w for any r . Equation (4.3.20a) indicates that $Nu(0 < r \leq r_1) = (3/2)(1/\delta_t)$. On the other hand, for constant $T_w > 1$, the solution of Equations (4.3.5) gives $\delta(r < r_0) = 2\sqrt{(70/39)r/Re}$ and Equation (4.3.6) reduce to

$$\frac{d\delta_t}{dr} = \frac{\delta_t^3 r (14\delta_t^2 - 3\delta_t^2) \delta_t' - 14\delta_t^3 \delta_t^3 + \delta\delta_t^5 + 140Pe^{-1}\delta_t^4 r}{4\delta_t^2 \delta (7\delta_t^2 - \delta_t^2) r}. \quad (4.4.15)$$

indicating that $\delta_t(0 < r \leq r_0)$ is independent of T_w . Similarly (4.3.12) yields $h(r_0 < r < r_1) = (1/4)(2/r + \sqrt{(210/13)r/Re})$ and (4.3.13) reduce to

$$\frac{d\delta_t}{dr} = \frac{175Pe^{-1}rh^4}{4\delta_t^2 (7h^2 - \delta_t^2)} + \frac{\delta_t}{h} h', \quad (4.4.16)$$

indicating that $\delta_t(r_0 \leq r < r_1)$ is also independent of T_w . This shows, in turn, that $Nu(0 < r \leq r_1)$ is independent of T_w . Closer to the jump, Equation (4.3.20b) yields $Nu(r_1 \leq r < r_j) = (3/2)[(T_w - T_s)/(h(T_w - 1))]$. Simultaneously, Equation (4.3.19) reduces to

$$\frac{dT_s}{dr} = -\frac{d(T_w - T_s)}{dr} = \frac{525}{136Pe} \frac{(T_w - T_s)r}{h}. \quad (4.4.17)$$

By dividing both sides of Equation (4.4.17) by $T_w - 1$, we deduce that $(T_w - T_s)/(T_w - 1)$ is independent of T_w . Finally, in the sub-critical region, by setting $\nu = \gamma = 1$, Equation (4.4.8) can be integrating to give the thickness independent of the temperature:

$$h(r > r_J) = \left(h_\infty^4 + 6 \frac{Fr^2}{Re} \ln \left(\frac{r}{r_\infty} \right) \right)^{\frac{1}{4}}. \quad (4.4.18)$$

In this case, upon noting from Equation (4.4.7) that $q_w(r > r_J) = 3(T_w - T_s)/(2h)$, then the equation for the heat flux is obtained from the reduced Equation (4.4.9):

$$\frac{dq_w}{dr} = -\frac{q_w}{h} \left(\frac{5}{Pe} r - \frac{3}{2} \frac{Fr^2}{Re} \frac{h^{-3}}{r} \right), \quad (4.4.19)$$

which is solved subject to $q_w(r = r_J) = q_w^+$. Clearly, (4.4.18) and (4.4.19) indicate that both the thickness and wall heat flux are independent of the wall temperature. Consequently, $Nu(r_J < r \leq r_\infty)$ is independent of T_w . This concludes the proof of our statement.

4.4.3 The influence of the wall heat flux on the hydraulic jump

Figure 4-18 illustrates the influence of the wall heat flux on the location and the height of the hydraulic jump, depicting the film profiles for different flux values. Similar to the influences of the wall temperature, the heat flux causes the jump radius to increase and the jump height to drop. The Marangoni effect is also reflected in the difference between the solid and dashed curves. As can be seen, the influence of the Marangoni stress is more dominant for an imposed wall heat flux than for an imposed wall temperature. This is not unexpected since the surface temperature increases with the radial distance (not

reported) caused by the constant heat addition from the wall. In contrast, when a constant wall temperature is imposed, the surface temperature invariably levels off since it cannot surpass the temperature of the wall. In fact, it should eventually saturate to the wall temperature level far downstream.

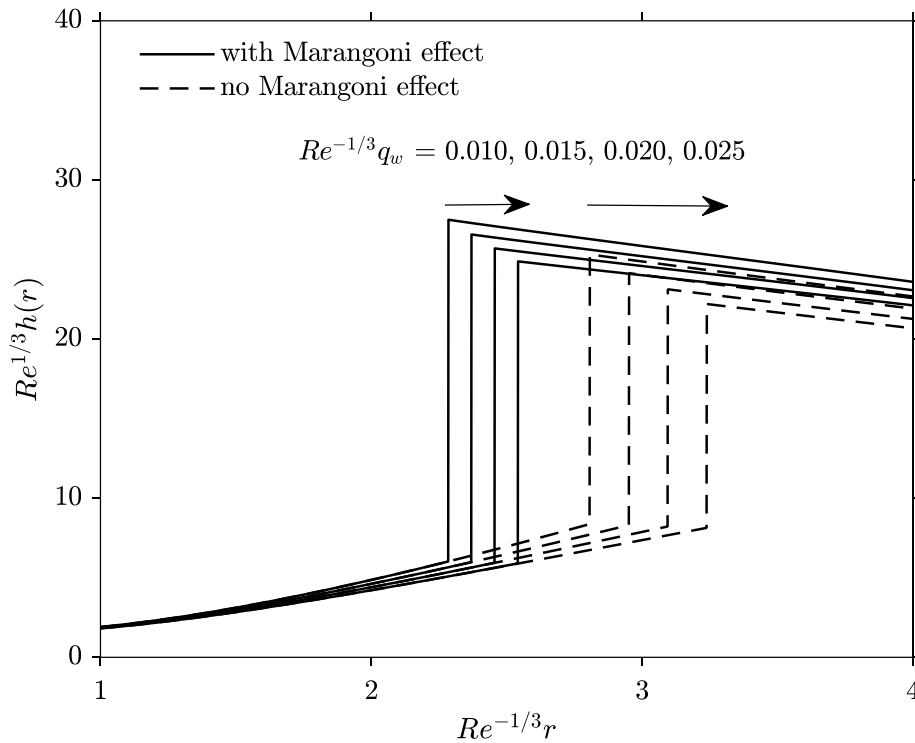


Figure 4-18: Influence of the wall heat flux on the film profile in the super- and sub-critical regions for $\hat{T}_0 = 300\text{ K}$. Here $\text{Ca Re}^{2/3} = 100$, $\text{Fr Re}^{-1/2} = 3$ and $r_\infty \text{Re}^{-1/3} = 6$

Finally, we report in Figure 4-19 on the influence of the wall heat flux on the Nusselt number profiles. We recall $\text{Nu} = q_w / (T_w - 1)$ for a given constant wall heat flux. Thus, the drop in Nu reflects a jump in the wall temperature. The figure indicates that the wall heat flux causes a significant jump in the wall temperature. However, the drop in Nu or the jump in T_w is not affected significantly by the increasing heat flux. This behaviour should be contrasted with the drop in the wall heat flux when the wall temperature is imposed.

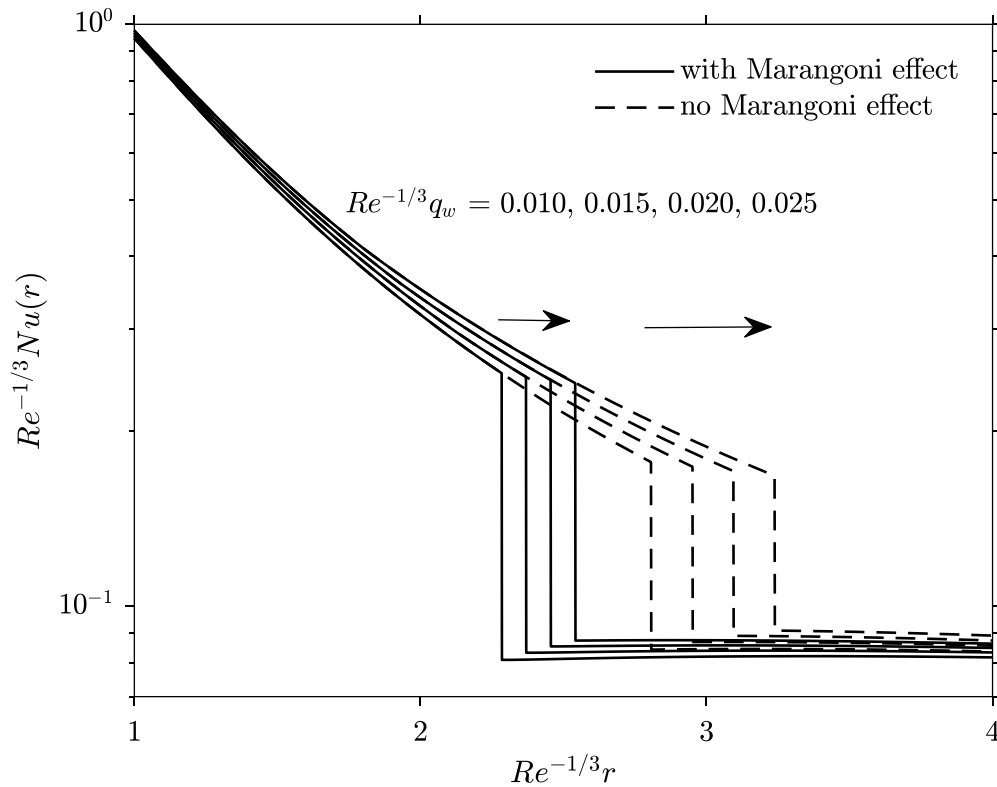


Figure 4-19: Influence of the wall heat flux on the Nusselt number in the super- and sub-critical regions for $\hat{T}_0 = 300\text{K}$. Here $\text{Ca Re}^{2/3} = 100$, $\text{Fr Re}^{-1/2} = 3$ and $r_\infty \text{Re}^{-1/3} = 6$.

4.5 Conclusion

We examine theoretically the influence of heat transfer on the axisymmetric spreading and structure of the hydraulic jump of a liquid jet impinging on a circular heated disk (Figure 4-1). The disk is maintained at either an imposed heat flux or temperature. The liquid viscosity and surface tension are assumed to depend on the temperature. The viscosity is taken to follow the well-established VFT model, whereas the surface tension is assumed to decrease linearly with temperature. Both models are validated by fitting existing measurements for various liquids (Figures 4-2 and 4-3). A Kármán–Pohlhausen (K-P) integral approach is adopted to capture the flow and heat transfer in the super-critical region upstream of the jump. We develop an iteration-free model to incorporate

the temperature-dependent viscosity and surface tension, therefore eliminate the potential divergence of iterative schemes. With this approach, we investigate the super-critical flow and thermal fields by solving the boundary-layer equations approximately. The Marangoni stress is also considered, which manifests itself downstream after the temperature varies along the film free surface. At the hydraulic jump, we extend the method of Watson (1964) and develop an energy balance across the jump as an additional condition to close the system so that the hydraulic and thermal jumps, as well as the downstream flow and thermal fields can be simultaneously determined. Our approach is validated against existing experimental and numerical results.

We find that both the hydrodynamic and thermal boundary layers grow with distance, with the former reaching the free surface first as our study is confined to non-metallic liquids which possess a higher kinematic viscosity than the thermal diffusivity. We find that both the wall heat flux and the wall temperature tend to enhance convection, leading to a drop in the height of boundary layers as well as the film thickness (Figures 4-5 and 4-10). When a constant wall flux is imposed, the thermal boundary layer always reaches the free surface, which to some extent contradicts an earlier study. This contradiction is the result of the constant Prandtl number and decoupling typically assumed in the literature.

The two transition locations r_0 and r_1 where the hydrodynamic and thermal boundary layers reach the free surface, respectively, behave differently under the influence of inertia and thermal effects (Figure 4-12). While both r_0 and r_1 move downstream with increased Reynolds number, they travel in opposite directions under enhanced wall heating regardless of the heating form (wall temperature or heat flux). With a larger thermal input at the disk, the first transition location r_0 moves downstream whereas the second transition location r_1 shifts upstream. The velocity and temperature at the free surface remain constant and equal to those of the incoming jet until reaching the first and second transition locations, respectively. Downstream of the transition locations, the surface velocity drops whereas the surface temperature begins to rise (Figure 4-6).

Consequently, the Marangoni stress emerges downstream of r_1 where the thermal effects reach the free surface. Although it decreases with radial distance as the temperature at the free surface flattens, it becomes relatively more dominant downstream since the wall shear stress decreases at a higher rate (Figure 4-7). The Marangoni stress is negative in the jet cooling problem since the free-surface temperature increases with radial distance. Consequently, it represents an additional resistance to the flow.

At the disk (wall), either the temperature $T_w(r)$ or the heat flux $q_w(r)$ can be prescribed (constant or r dependent), and the non-prescribed variable is calculated. Interestingly, when q_w is imposed and constant, $T_w(r)$ increases with the radial direction. On the other hand, $q_w(r)$ decreases with the radial distance if a constant T_w is imposed. Both behaviours reflect the drop of the cooling efficiency of the jet as the liquid travels downstream. Although the stagnation zone is not accounted for in the present formulation, our predictions of the Nusselt number distribution are in good agreements with existing experimental and theoretical studies (Figures 4-8, 4-9 and 4-13).

To locate the hydraulic jump in the presence of the hydrodynamic-thermal coupling, an additional energy balance across the jump is derived, allowing the jump radius and the sub-critical thermal field to be simultaneously determined. The jump is found to move outwards with increasing higher wall temperature and heat flux (Figures 4-14, 4-16 and 4-18). On the other hand, the jump height decreases with enhanced thermal input at the wall. Our prediction of the influence of heating on the location and height of the hydraulic jump corroborate well existing numerical studies (Figure 4-16). The hydraulic jump induces shock-type drops in the Nusselt number, confirming existing numerical studies (Figure 4-17).

The Marangoni stress tends to push the jump upstream as it induces further resistance to the flow in addition to the wall shear stress (Figure 4-14 and 4-18). Consequently, its effect decreases with capillary number as the viscous effect strengthens (Figure 4-15).

Finally, we show that the Nusselt number is independent of the wall temperature for a fluid of constant properties under the K-P approximation (Section 4.4.2).

4.6 References

Agrawal, D. C. & Menon, V. J. 1992 Surface tension and evaporation: An empirical relation for water. *Phys. Rev. A* **46**, 2166-2169.

Baonga, J.B. , Gualous, H.L., Imbert, M. 2006 Experimental study of hydrodynamic and heat transfer of free liquid jet impinging a flat circular heated disk. *Applied Thermal Eng.* **26**, 1125-1138.

Basu, S. & Cetegen, B. M. 2007 Effect of hydraulic jump on hydrodynamics and heat transfer in a thin liquid film flowing over a rotating disk analyzed by integral method. *J. Heat Transfer* **129**, 657-663.

Bhagat, R. K., Jha, N. K., Linden, P. F. & Wilson, D. I. 2018 On the origin of the circular hydraulic jump in a thin liquid film. *J. Fluid Mech.* **851**, R5 1-11.

Bohr, T., Dimon, P. & Putzkaradze, V. 1993 Shallow-water approach to the circular hydraulic jump. *J. Fluid Mech.* **254**, 635-648.

Bohr, T., Ellegaard, C., Hansen, A. E. & Haaning, A. 1996 Hydraulic jumps, flow separation and wave breaking: An experimental study. *Physica B* **228**, 1-10.

Bohr, T., Putkaradze, V. & Watanabe, S. 1997 Averaging theory for the structure of hydraulic jumps and separation in laminar free-surface flows. *Phys. Rev. Lett.* **79**, 1038-1041.

Brdlik, P. M. & Savin, V. K. 1965 Heat transfer between an axisymmetric jet and a plate normal to the flow. *J. Engng Phys.* **8**, 91-98.

Bush, J. W. M. & Aristoff, J. M. 2003 The influence of surface tension on the circular hydraulic jump. *J. Fluid Mech.* **489**, 229-238.

Chaudhury, Z. H. 1964 Heat transfer in a radial liquid jet. *J. Fluid Mech.* **20**, 501-511.

- Craik, A., Latham, R., Fawkes, M. & Gibbon, P. 1981 The circular hydraulic jump. *J. Fluid Mech.* **112**, 347-362.
- De Gennes, P. G., Brochard-Wyart, F. & Quere, D. 2004 *Capillarity and Wetting Phenomena*. Springer.
- Dressaire, E., Courbin, L., Crest, J. & Stone H. A. 2010 Inertia dominated thin-film flows over microdecorated surfaces. *Phys. Fluids* **22**, 073602-07.
- Duchesne, A., Lebon, L. & Limat, L. 2014 Constant Froude number in a circular hydraulic jump and its implication on the jump radius selection. *Europhys. Lett.* **107**, 54002.
- Duchesne, A., Andersen, A. & Bohr, T. 2019 Surface tension and the origin of the circular hydraulic jump in a thin liquid film (APS Fluid Div. March 2019). [arXiv:1903.11495](https://arxiv.org/abs/1903.11495)
- Fulcher, G. S. 1992 Analysis of recent measurements of the viscosity of glasses. *J. Am. Ceram. Soc.* **75**, 1043–1055.
- Gabour, L. A. & Lienhard, J. 1994 Wall roughness effects on stagnation-point heat transfer beneath an impinging liquid jet. *ASME J. Heat Transfer* **116**, 81–87.
- Granato, A. V. 2002 The specific heat of simple liquids. *J. Non-Cryst. Solids* **307–310**, 376-386.
- Kafoussius N. G. & Williams, E.W. 1995 The effect of temperature-dependent viscosity on the free convective laminar boundary layer flow past a vertical isothermal flat plate. *Acta Mech.* **110**, 123–137.
- Kasimov, A. R. 2008 A stationary circular hydraulic jump, the limits of its existence and its gas dynamic analogue. *J. Fluid Mech.* **601**, 189–198.
- Khayat, R. E. 2016 Impinging planar jet flow and hydraulic jump on a horizontal surface with slip. *J. Fluid Mech.* **808**, 258-289.

- Khayat, R. E. & Kim, K. 2006 Thin-film flow of a viscoelastic fluid on an axisymmetric substrate of arbitrary shape. *J. Fluid Mech.* **552**, 37-71.
- Korson, L., Dorst-Hansen, W. & Millero, F. J. 1969 Viscosity of Water at Various Temperatures. *J. Phys. Chem.* **73**, 34-39.
- Kundu, P.K., Cohen, I.M. & Bowling, D.R. 2016 *Fluid Mechanics*. 6th edn. Elsevier.
- Liu, X. & Lienhard, J. 1989 Liquid jet impingement heat transfer on a uniform flux surface. *ASME Heat Transfer Phenomena in Radiation, Combustion, and Fires* **106**, 523-530.
- Liu, X., Gabour, L. A. & Lienhard, J. 1993 Stagnation-point heat transfer during impingement of laminar liquid jets: Analysis including surface tension. *ASME Heat Transfer* **115**, 99-105.
- Lubarda, V. & Talke, K. A. 2011 Analysis of the equilibrium droplet shape based on an ellipsoidal droplet Model. *Langmuir*. **27**, 10705–10713.
- Mauro, J. C., Yue, Y., Ellison, A. J., Gupta, P.K. & Allan, D. C. 2009 Viscosity of glass-forming liquids. *PNAS*. **106**(47), 19780-19784.
- Maynes, D., Crockett, J. 2014 Apparent temperature jump and thermal transport in channels with streamwise rib and cavity featured superhydrophobic walls at constant heat flux. *ASME Heat Transfer* **136**, 011701.
- Miller, R. Garrett, S. J., Griffiths, P. T. & Hussain, Z. 2018 Stability of the Blasius boundary layer over a heated plate in a temperature-dependent viscosity flow. *Phys. Rev. Fluids* **3**, 113902.
- Mohajer, B. & Li, R. 2015 Circular hydraulic jump on finite surfaces with capillary limit. *Phys. Fluids* **27**, 117102.

Okhotin, A. S., Zhmakin, L. I. & Ivanyuk, A. P. 1992 Universal temperature dependence of the thermal conductivity and viscosity coefficients. *Int. J. Heat Mass Transfer* **35**, 3059–3067.

Peleg, M. 2017 Temperature–viscosity models reassessed. *Crit Rev Food Sci Nutr.* 1-10.

Prince, J. F., Maynes, D. & Crockett, J. 2012 Analysis of laminar jet impingement and hydraulic jump on a horizontal surface with slip. *Phys. Fluids* **24**, 102103.

Rampp, M., Buttersack, C. and Ludeman, H. D. 2000 c,T-Dependence of the viscosity and the self-diffusion coefficients in some aqueous carbohydrate solutions. *Carbohydr. Res.* **328**, 561–572.

Rojas, N., Argentina, M. & Tirapegui, E. 2010 Inertial lubrication theory. *Phys. Rev. Letts.* **104**, 187801-4.

Rojas, N., Argentina, M. & Tirapegui, E. 2013 A progressive correction to the circular hydraulic jump scaling. *Phys. Fluids* **25**, 042105

Saad, N. R., Douglas, W. J. M. & Mujumdar, A. S. 1977 Prediction of heat transfer under an axisymmetric laminar impinging jet. *Ind. Eng Chem., Fundam.* **16**, 148–154.

Sahasrabudhe, S.N., Rodriguez-Martinez, V., O’Meara, M. & Farkas, B. E. 2017 Density, viscosity, and surface tension of five vegetable oils at elevated temperatures: Measurement and modeling. *Int. J. Food Properties* **20**, 51965-51981.

Scheichl, B. “Centred splash of a vertical jet on a horizontal rotating disc: the thin radial film in the parabolic and weakly elliptic limit”; accepted as talk for: BAIL 2018 - International Conference on Boundary and Interior Layers, University of Strathclyde, Glasgow, UK; 2018-06-18 - 2018-06-22; in: "Boundary and Interior Layers, Computational and Asymptotic Methods - BAIL 2018", G. Barrenechea et al. (ed.); Springer, Lecture Notes in Computational Science and Engineering / ?? / Berlin, Heidelberg (2019), ISSN: 1439-7358.

Schlichting, H. & Gersten, K. 2000 *Boundary-layer theory* (Springer, Berlin).

- Scherer, G. W. 1992 Editorial comments on a paper by Gordon S. Fulcher. *J Am Ceram Soc.* **75**, 1060–1062.
- Searle, M., Maynes, D. & Crockett, J. 2017 Thermal transport due to liquid jet impingement on super hydrophobic surfaces with isotropic slip. *Int. J. Heat Mass Transfer* **110**, 680–691.
- Seeton, C. J. 2006 Viscosity–temperature correlation for liquids. *Tribol Lett.* **22**, 67-78.
- Segur, J. B. & Oberstar, H. E. 1951 Viscosity of glycerol and its aqueous solutions. *Ind. Eng. Chem.* **43**, 2117–2120.
- Sung, J., Choi, H. G. & Yoo, J. Y. 1999 Finite element simulation of thin liquid film flow and heat transfer including a hydraulic jump. *Int. J. Numer. Methods Eng.* **46**, 83-101.
- Takamura, K., Fischer, H. & Morrow, N. R. 2012 Physical properties of aqueous glycerol solutions. *J. Petro Sci & Eng.* **98-99**, 50-60.
- Tani, I. 1949 Water Jump in the Boundary Layer. *J. Phys. Soc. Japan* **4**, 212-215.
- Wang, X. S., Dagan, Z. & Jiji, L. M. 1989a Heat transfer between a circular free impinging jet and a solid surface with nonuniform wall temperature or wall heat flux—1. solution for the stagnation region. *Int. J. Heat Mass Transfer* **32**, 1351-1360.
- Wang, X. S., Dagan, Z. & Jiji, L. M. 1989b Heat transfer between a circular free impinging jet and a solid surface with nonuniform wall temperature or wall heat flux—2. solution for the boundary layer region. *Int. J. Heat Mass Transfer* **32**, 1361-1371.
- Watanabe, S., Putkaradze, V. & Bohr, T. 2003 Integral methods for shallow free-surface flows with separation. *J. Fluid Mech.* **480**, 233–265.
- Watson, E. 1964 The spread of a liquid jet over a horizontal plane. *J. Fluid Mech.* **20**, 481-499.

Chapter 5

5 Conclusions and recommendations for future works

In this chapter, the conclusions of the current thesis are given, followed by some recommendations for future work.

5.1 Conclusions

The flow field and heat transfer of an impinging jet flow with a circular hydraulic jump are studied theoretically using boundary-layer approaches. Improved approaches on the circular hydraulic jumps for both low- and high-viscosity liquids are designed. An iteration-free model capable of incorporating the temperature-dependent viscosity is proposed for impinging jet problem. The effects of inertia, rotation, gravity and heat transfer are comprehensively explored.

The boundary-layer heights and film thickness are found to diminish with inertia. The wall shear stress is found to decrease with radial distance for on a stationary impingement surface but can increase for a rotary surface for large rotation speeds. It is found that rotation tends to enhance inertia, leading to a drop in the boundary layer height as well as the film thickness. Interestingly, when the surface is in rotation, a maximum liquid thickness appears in the flow domain, reflecting the competition between convective and centrifugal effects. The maximum thickness moves downstream with higher inertia but moves upstream with stronger rotation. With higher rotating rates, the hydraulic jump is found to move downstream and its height diminishes (Chapter 2).

The location of the hydraulic jump is determined for both low- and high-viscosity liquids. For low-viscosity liquid, the location of the jump is determined subject to the thickness near the trailing edge under static condition, reflecting the dominance of surface tension effect. For high high-viscosity liquids, the gravitational effect is more important, and the jump coincides with a singularity in the thin-film equation. The jump height decreases with increasing gravity, simultaneously as the jump location is pushed upstream toward the impingement point. Downstream of the hydraulic jump, the recent finding of a

constant ‘jump Froude number’ is also justified. As the jump location can be well predicted without the inclusion of the surface tension for high-viscosity liquids, it invalidates part of the recent argument of in Bhagat *et al.* (2018) who claimed that surface tension is the only dominant effect in circular hydraulic jump and gravity plays little role (Chapter 2 & 3).

In the heat transfer analysis, to consider the non-linear two-way coupling caused by the dependence of viscosity on temperature, an iteration-free model is designed and applied. This method inherently shortens the computing time and eliminate the potential danger of divergence due to numerical iteration. Both the hydrodynamic and thermal boundary layers are found to decrease with heat input at the solid surface. At the hydraulic jump, we develop an energy balance across the jump as an additional condition to close the system so that the hydraulic and thermal jumps, as well as the downstream flow and thermal fields can be simultaneously determined. A higher heat input is also found to push the hydraulic jump downstream. The Marangoni stress is found to push the hydraulic jump upstream due to the increase of free-surface temperature with radial distance. The wall temperature and heat flux discontinuities at the hydraulic jump are observed. Such discontinuities lead to shock-type drops in the Nusselt number, confirming previous findings in the literature (Chapter 4).

Here we emphasize that in some scenarios numerical approaches to some extent do give us better predictions of the hydrodynamic and heat transfer character of the flow even though they can be time consuming. Therefore cautions should definitely be exercised when choosing the proper method. Our presented models are computationally efficient but may sacrifice some accuracies as some comparisons have indicated, which is usually the limitations of theoretical models.

5.2 Recommendations for future works

For a hydraulic jump on a rotating surface, we have presented a method to determine the downstream thickness based on the analogy with spin coating. In fact, the measurements for the subcritical flow is still rare. To understand the downstream flow and hydraulic jump on a rotating surface better, some serious experimental measurements of the flow

field after the hydraulic jump are needed. In addition, the method we develop for high-viscosity liquid can be also applied to a rotating flow, which can be done in future works.

Surface tension effects can be dominant on hydraulic jump especially for low-viscosity liquids as discussed in Chapter 2. Interestingly, the hydraulic jump can be observed on a vertical wall. This reason for this phenomenon is still missing theoretically. Though Bhagat *et al.* (2018) proposed a method to emphasize the effect of surface tension, no conclusive agreement has been reached yet. Duchesne *et al.* (2019) also pointed out that the method of Bhagat *et al.* (2018) is wrong. In this case, the effects of surface tension deserve more rigorous treatments, which perhaps begs combined theoretical, numerical and experimental efforts.

We finally emphasize that the flow separation is not captured in the present thesis. Even though Bohr *et al.* (1997) and Watanabe *et al.* (2003) adopted a non-self-similar cubic profile for the velocity that allowed them to force the solution cross the jump, two experimental points are needed in their solution to fix the boundaries and some prior knowledge of the location of the jump was required. More importantly, the boundary layer equations do not hold exactly at the jump. In fact, the flow very close to the hydraulic jump is of strongly two-dimensional character which is also the reason the current thesis did not explicitly solve the flow near the jump as it is based on the boundary layer equations. Ideally, the flow in the jump region should be solved using the full Navier-Stokes equations. This is can be done in future works with the fully inclusion of the non-linear two-way coupling on heat transfer.

Appendices

Appendix A: The thin-film equations and boundary conditions

In this appendix, we derive equations (2.2.1a-d) from the full Navier-Stokes equations. These equations govern the motion of the thin film on the rotating disk. Consequently, we assume the film thickness to be small relative to its (horizontal) length. We therefore take the jet radius a as the length scale in the vertical direction and L as the length scale in the radial direction. Here L may correspond to the radius of the disk. In this case, we let $\bar{r} = \varepsilon r$ be the radial coordinate in the current analysis. Thus, the jet radius is assumed to be small relative to L so that $\varepsilon \equiv a/L \ll 1$ becomes the small perturbation parameter in the problem. The radial and azimuthal velocity components, u and v , are scaled by $Q/\pi a^2$, while the vertical velocity component, w , is scaled by $(Q/\pi a^2)\varepsilon$, where Q is the jet flow rate. The pressure is scaled by $\rho g a$. The full Navier-Stokes equations for axisymmetric flow are given by Schlichting & Gersten (2000) in the (r, z) plane, and are recast here in dimensionless form:

$$u_{\bar{r}} + \frac{u}{\bar{r}} + w_z = 0, \quad (\text{A1a})$$

$$\varepsilon \text{Re} \left(uu_{\bar{r}} + wu_z - \frac{v^2}{\bar{r}} \right) = -\varepsilon \frac{\text{Re}}{\text{Fr}^2} p_{\bar{r}} + \varepsilon^2 \left(u_{\bar{r}\bar{r}} + \frac{u_{\bar{r}}}{\bar{r}} - \frac{u}{\bar{r}^2} \right) + u_{zz}, \quad (\text{A1b})$$

$$\varepsilon \text{Re} \left(uv_{\bar{r}} + wv_z + \frac{uv}{\bar{r}} \right) = \varepsilon^2 \left(v_{\bar{r}\bar{r}} + \frac{v_{\bar{r}}}{\bar{r}} - \frac{v}{\bar{r}^2} \right) + v_{zz}, \quad (\text{A1c})$$

$$\varepsilon^2 \text{Re} (uw_{\bar{r}} + ww_z) = -\frac{\text{Re}}{\text{Fr}^2} p_z + \varepsilon^3 \left(w_{\bar{r}\bar{r}} + \frac{w_{\bar{r}}}{\bar{r}} \right) + \varepsilon w_{zz} - \frac{\text{Re}}{\text{Fr}^2} \begin{cases} 0 & \bar{r} < \bar{r}_j \\ 1 & \bar{r} > \bar{r}_j \end{cases}. \quad (\text{A1d})$$

These equations are subject to adherence and no-penetration at the disk:

$$u(\bar{r}, z=0) = 0, \quad v(\bar{r}, z=0) = \bar{\Omega} \bar{r} = \Omega r, \quad w(\bar{r}, z=0) = 0. \quad (\text{A2a-c})$$

the kinematic condition:

$$w(\bar{r}, z = h) = u(\bar{r}, z = h)h'(\bar{r}), \quad (\text{A3})$$

and the vanishing of the traction components at the film surface $z = h(\bar{r})$:

$$-\varepsilon \frac{\text{Re}}{\text{Fr}^2} h' p + 2\varepsilon^2 h' u_{\bar{r}} + u_z + \varepsilon^2 w_{\bar{r}} = 0, \quad (\text{A4a})$$

$$\varepsilon^2 h' \left(v_{\bar{r}} + \frac{v}{\bar{r}} \right) + v_z = 0, \quad (\text{A4b})$$

$$-\frac{\text{Re}}{\text{Fr}^2} p + \varepsilon h' \left(u_z + \varepsilon^2 w_{\bar{r}} \right) + 2\varepsilon w_z = 0. \quad (\text{A4c})$$

Various levels of approximation can be envisaged, depending on the values of ε , Re and Fr . In this study, we follow the commonly adopted boundary-layer or thin-film formulation and assume that $\text{Re} = O(\varepsilon^{-1})$ and $\text{Fr} = O(\varepsilon^{-1/2})$ so that gravity and inertia effects are of the same strength. In this case, equations (A1b-d) reduce to

$$\varepsilon \text{Re} \left(uu_{\bar{r}} + wu_z - \frac{v^2}{\bar{r}} \right) = -\varepsilon \text{Re} p_{\bar{r}} + u_{zz}, \quad (\text{A5a})$$

$$\varepsilon \text{Re} \left(uv_{\bar{r}} + wv_z + \frac{uv}{\bar{r}} \right) = v_{zz}, \quad (\text{A5b})$$

$$p_z = - \begin{cases} 0 & \bar{r} < \bar{r}_j \\ 1 & \bar{r} \geq \bar{r}_j. \end{cases} \quad (\text{A5c})$$

As to the dynamic conditions, we note from (A4c) that the pressure term is of leading order, yielding $p(\bar{r}, z = h) = 0$, which, when inserted in (A4a), leads to $u_z(\bar{r}, z = h) = 0$. Also, $v_z(\bar{r}, z = h) = 0$ from (A4b). Finally, equation (A1a) and conditions (A2-A3)

remain the same. Upon setting $\bar{r} = \varepsilon r$, we recover equations (2.2.1) and conditions (2.2.2) - (2.2.4).

Curriculum Vitae

Name: Yunpeng Wang

Post-secondary Education and Degrees: Hebei university of technology
Tianjin, China
2008-2012 B.A.

Honours and Awards: National Encouragement Scholarship
2011

Outstanding Graduation Thesis
2012

Related Work Experience Mechanical Engineer
Technology Center of XCMG, China
2012-2015

Teaching Assistant
The University of Western Ontario
2016-2019

Publications and Conferences:

Wang, Y. & Khayat, R.E. 2018 Impinging jet flow and hydraulic jump on a rotating disk. *J. Fluid Mech.* **839**, 525-560.

Wang, Y. & Khayat, R.E. 2019 The role of gravity in the prediction of the circular hydraulic jump radius for high-viscosity liquids. *J. Fluid Mech.* **862**, 128-161.

Wang, Y. & Khayat, R.E. 2019 A fast two-way coupled integral approach for impinging jet heat transfer. *CSME-CFDSC Congress 2019*.

Wang, Y. & Khayat, R.E. 2019 A numerical investigation on the fundamentally different mechanisms of circular hydraulic jump for high and low-viscosity liquids. *CSME-CFDSC Congress 2019*.